PHD

Microwave photoelectrochemistry of silicon

Ushiroda, Shin

Award date:
2002

Awarding institution:
University of Bath

Microwave Photoelectrochemistry of silicon

Submitted by Shin Ushiroda

for the degree of

Doctor of Philosophy

of the University of Bath

2002

Shin Ushiroda

ProQuest LLC
789 East Eisenhower Parkway
P.O. Box 1346
Ann Arbor, MI 48106-1346

University of Bath

Department of Chemistry

Doctor of Philosophy

Microwave Photoelectrochemistry of silicon

by Shin Ushiroda

Abstract

Anodic and cathodic reactions of silicon in fluoride media were studied by conventional electrochemical and microwave reflectivity measurements. The technique is based on measuring a change of the microwave reflection of an electrode induced by electrical or optical perturbation. For a small change of conductivity, the relative microwave reflection, $\Delta P/P_{in}$, is linearly proportional to the change in the conductivity of the sample, $\Delta\sigma$,

$$\frac{\Delta P}{P_{in}} = S\Delta\sigma$$

where S is sensitivity factor.

There are two approaches to study an interfacial kinetics of photoinduced semiconductors; frequency- and time-resolved approaches. The kinetics of hydrogen evolution reaction at p-type Si was studied by Intensity Modulated Photocurrent Spectroscopy (IMPS), and Light Modulated Microwave Reflectance (LMMR). Time- resolved Potential Modulated Microwave Reflectance (PMMR) under illumination is an analogous technique as IMPS and LMMR to study the interfacial kinetics, which provides an new insight of the semiconductor electrochemistry. The experimental results were compared with the theoretical model, and the details are discussed.

It is known that $Ru(NH_3)_6^{2+/3+}$ couple is outer-sphere redox couple. The kinetics of photoreduction of $Ru(NH_3)_6^{3+}$ at p-type Si was studied to compare with Marcus theory. It is shown that the electron transfer reaction via reduction of $Ru(NH_3)_6^{3+}$ is slower than Marcus type outer-sphere reaction, and an alternative reaction route is proposed.

Frequency-resolved PMMR was combined with electrochemical impedance spectroscopy (EIS) to study anodic dissolution of p-Si in the electropolishing region, and the details are discussed.

Contents

0.1 Acknowledgement

I really enjoyed this work, which has given me new insight into semiconductor electrochemistry. I would like to thank my supervisor, Prof. L. M. Peter for his guidance through the project. Thanks to all the members of the Electrochemistry group for their assistance, especially, June, Upul, and Petra. I would like to also thank to Dr. M. Bailes for the QBasic programs, Mr. M. Cass for the theoretical modelling of Si, Dr. N. W. Duffy for his invaluable assistance for the time resolved measurements, and Dr. S. R. Pennock for the stack model and Mr. D. Hatten for the general microwave measurements. I also would like to thank Prof. H. J. Lewerenz for useful discussions of silicon electrochemistry. Finally, I also need to mention my colleagues, Oleg and Manosh, for general discussion of Physics and Mathematics.

0.2 List of symbols

a	width of a rectangular waveguide
A	area of the sample
A	electron affinity
b	height of a rectangular waveguide = a/2
c	speed of light = 2.998×10^8 ms^{-1}
c_{Ox}	concentration of oxidised species
c_{Red}	concentration of reduced species
C	coupling constant
C_{sc}	space charge capacitance
C_{acc}	accumulation capacitance
C_{ox}	oxide capacitance
C_H	Helmholtz capacitance
d	sample thickness
D	diffusion coefficient
E	electric field
E_c	bottom of the conduction band
E_i	Energy level in intrinsic semiconductor
E_v	top of the valence band
E_F	Fermi level
$E_{F,n}$	quasi Fermi level for electrons
$E_{F,p}$	quasi Fermi level for holes
E_g	Energy gap
f	frequency
f_0	operating frequency
f_c	cut-off frequency
F	Faraday constant = 9.6485×10^4 $C mol^{-1}$
G	generation rate of electron-hole pair
j_a	anodic current density
j_c	cathodic current density

j_{ch}	charging current density
j_{diff}	diffusion current density
j_{drift}	drift current density
j_G	generation current density
j_{rec}	recombination current density
j_{tr}	electron transfer current density
j_{photo}	photocurrent density
h	Planck's constant = 6.6261×10^{-34} J
H	magnetic field
k	propagation constant
k^o	standard rate constant
k_B	Boltzmann constant = 1.38×10^{-23} JK^{-1}
k_e	extinction coefficient
k_{tr}	rate constant for electron transfer reaction
k_{rec}	rate constant for surface recombination reaction
L	diffusion length
l	length of active region
m_0	free electron mass
n	concentration of electrons
N_A	concentration of acceptors
N_C	effective density of states in conduction band
N_D	concentration of donors
N_V	effective density of states in valence band
p	concentration of holes
P_r	reflected microwave
ΔP	change of microwave
Q	charge
QE	quantum efficiency
q	elementary charge = 1.6022×10^{-19} C
r	reflection coefficient
r′	complex conjugate of reflection coefficient

R	gas constant = 8.314 $JK^{-1}mol^{-1}$
S	sensitivity factor
S′	modified sensitivity factor
t	transmission coefficient
T	Temperature in Kelvin
V_a	applied potential
V_{fb}	flat-band potential
W	space-charge width
$W(E)_{Ox}$	energy distribution for oxidised species
$W(E)_{Red}$	energy distribution for reduced species
Y	admittance
Y_1	real part of admittance
Y_2	imaginary part of admittance
Z	impedance
Z_1	real part of impedance
Z_2	imaginary part of impedance
Z_{acc}	accumulation impedance
z_{Ox}	oxidation state of oxidised species
z_{Red}	oxidation state of reduced species

α	absorption coefficient
α_c	cathodic transfer coefficient
δ	tunnelling distance
η	overpotential
η_H	efficiency for hydrogen evolution
ε_0	permittivity of free space = 8.854×10^{-14} $J^{-1}C^2cm^{-1}$
ε_r	relative permittivity
λ	wavelength
λ_c	cut-off wavelength
λ_{re}	reorganisation energy
μ	permeability

μ_n	mobility of electrons
$\overline{\mu}_{\mathrm{n}}$	electrochemical potential of electron
$\overline{\mu}_{\mathrm{Ox}}$	electrochemical potential of oxidised species
μ_p	mobility of holes
$\overline{\mu}_{\mathrm{Red}}$	electrochemical potential of reduced species
ν_{th}	thermal velocity
ρ	resistivity
$\rho(\mathrm{x})$	charge density
σ	conductivity
$\Delta\sigma$	change of conductivity
τ_{n}	lifetime for electrons
τ_{p}	lifetime for holes
ω	angular frequency
Φ_{m}	work function for metals
Φ_{sc}	work function for semiconductors

Chapter 1

Historical Survey and Aims of the Project

1.1 Introduction

The electrochemistry of silicon has been the subject of many investigations. The anodic behaviour of silicon electrodes has been studied extensively due to its importance in applications such as passivation, oxide film growth, etching, cleaning, photochemical cells, and porous silicon formation [1–3, 5]. Similarly, the cathodic behaviour of silicon electrodes has also been studied by the number of researchers. The main effort on the cathodic reactions is the hydrogen production on semiconductors with/without the surface modification [6–13].

1.2 Anodic dissolution

The anodic dissolution of silicon in fluoride media was first reported by Turner [14] in 1958, and since then a wide range of phenomena have been characterised such as current multiplication and the change of dissolution valence, the occurrence of passivation and current oscillation [15–19]. The primary characteristics of the anodic behaviour of silicon can be seen in the schematic current-voltage curve below

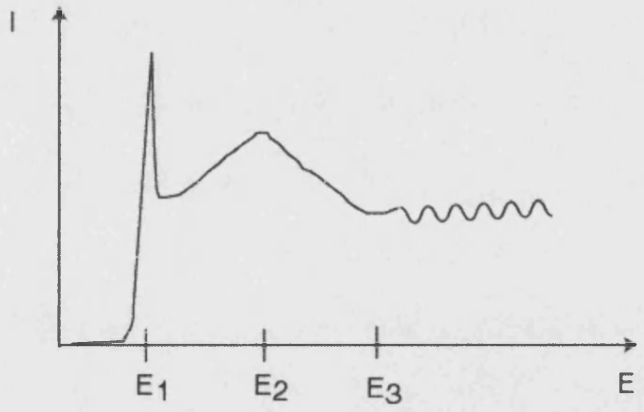

Figure 1.1: General i-V curve of Si at anodic potentials.

The anodic i-V curves of p-Si in the dark or strongly illuminated n-Si in fluoride solutions are typically characterised by two current peaks. At anodic potentials up to E_1, the electrode behaviour is characterised by an exponential dependence of current on potential and by uneven dissolution of the silicon surface. This corresponds to the

formation of porous silicon. At potentials more positive than E_1, it is characterised by the formation and dissolution of a surface oxide film resulting in a smooth surface, and this region is referred to as electropolishing. At potentials more positive than E_3, current oscillation may occur. The current in the voltammogram is independent of doping type but depends on solution composition.

The exact dissolution chemistry of silicon is not clearly understood although it is generally accepted that holes are required in the initial oxidation steps for both pore formation and electropolishing. This means that significant dissolution occurs only under illumination for n-type Si, whereas the dissolution of p-type Si does not require illumination since holes are already accumulated at the surface under anodic potentials. Fig 1.2 shows i-V curve of Si in fluoride media. It is seen that the current increases with increasing the light intensity for n-Si and it behaves like p-Si under strong illumination.

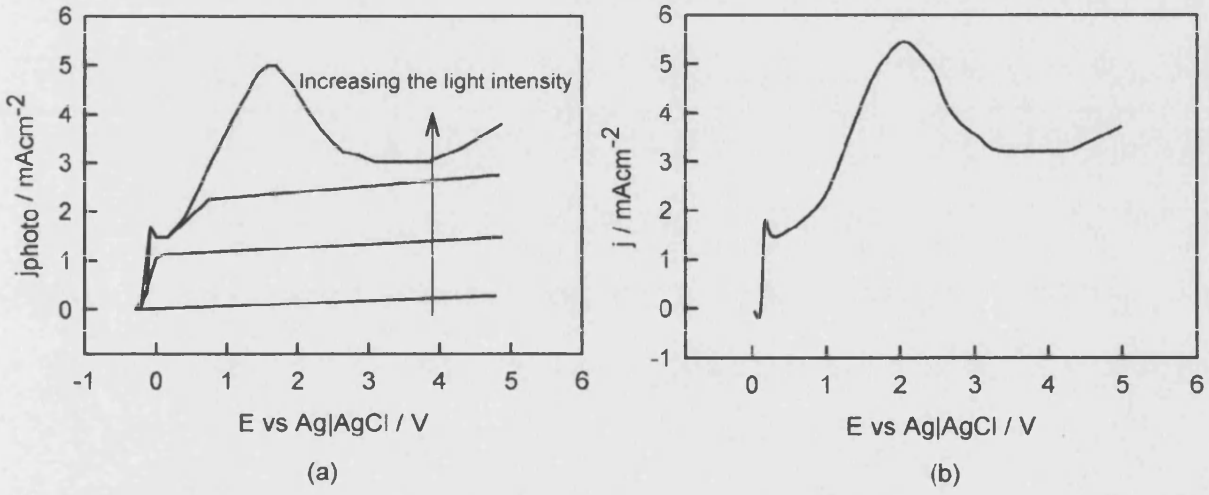

Figure 1.2: i-V curve a) n-type Si under illumination b) p-type Si in the dark in 0.2M HF[20].

The overall reaction is commonly written as

$$Si + 6HF + mh^+ \longrightarrow SiF_6^{2-} + (4-n)H^+ + \frac{n}{2}H_2 + (4-m-n)e^- \qquad (1.1)$$

For n-Si, the quantum efficiency, Q, and the efficiency η for hydrogen evolution are

given by

$$\mathrm{QE} = \frac{4-n}{m} \tag{1.2}$$

$$\eta_{\mathrm{H}} = \frac{n}{4-n} \tag{1.3}$$

In the case of tetravalent dissolution of n-Si, m = 2 and n = 0, which give 2 for the quantum efficiency [21]. The fact that the quantum efficiency depends on the light intensity and photocurrent multiplication during the photodissolution of n-Si was first reported by Matsumura and Morrison [22]. They showed that the quantum efficiency is light intensity dependent. Peter *et al.* [23] reported that the quantum efficiency is 4 at low light intensity and decreases to 2 as increasing the light intensity as shown in Fig 1.3.

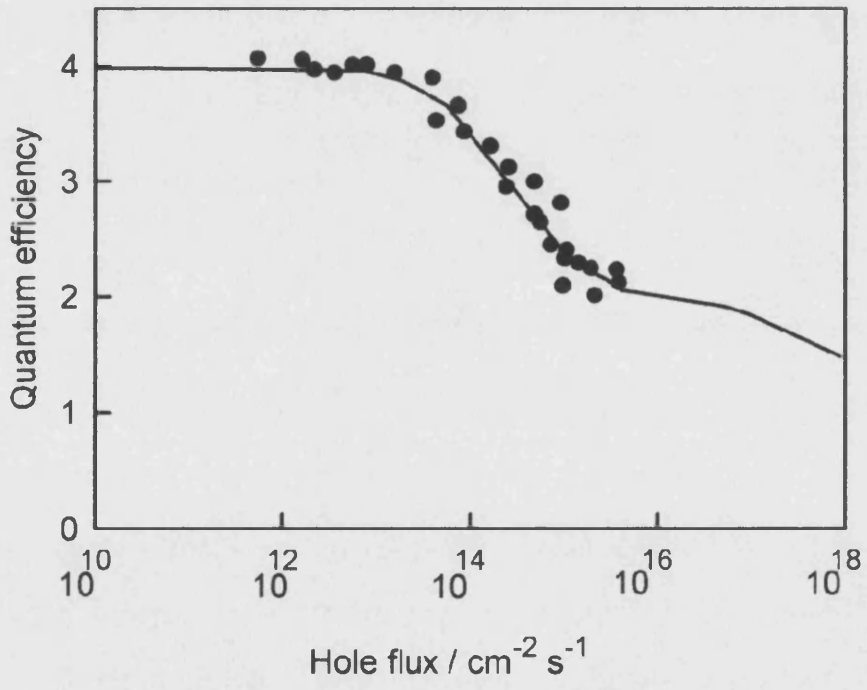

Figure 1.3: Light intensity dependence of quantum efficiency for n-type Si [23].

Several mechanisms of the photodissolution of silicon has been proposed by a number of researchers [25–30, 34]. Two proposed mechanisms are shown in Fig 1.4 and Fig 1.5. The first mechanism was proposed by Lehmann *et al.* [27] and the second

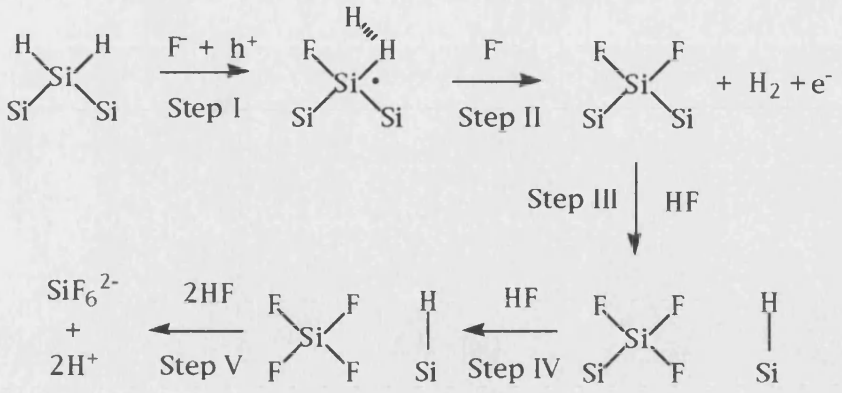

Figure 1.4: Anodic dissolution mechanism by Lehmann *et al.* [27].

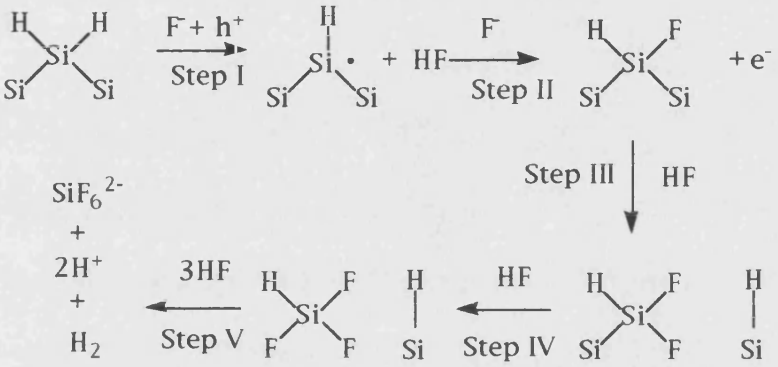

Figure 1.5: Anodic dissolution mechanism by Gerischer *et al.* [28].

one by Gerischer *et al.* [28]. Both mechanisms consist of five steps where step I is hole capture, step II is electron injection, step III, IV and V are chemical steps, and are valid for strong illumination (QE = 2). Hydrogen gas is produced at electron injection step followed by three chemical steps in the first mechanism. On the other hand, the reaction intermediate $SiHF_3$ is involved and the production of hydrogen gas occurs at the end of the chemical step in the second mechanism.

It is generally assumed that the first step in the reaction sequence is hole capture and a simplified reaction scheme is shown below [30]

$$Si + h^+ \longrightarrow Si(I) \tag{1.4}$$

where Si(I) is a dissolution intermediate with an oxidation state of +1.

The rest of the reaction sequence takes place either by electron injection or hole cap-

ture, which depends on the light intensity.

$$Si(I) + h^+ \longrightarrow Si(II) \quad \text{or} \quad Si(I) \longrightarrow Si(II) + e^- \tag{1.5}$$

$$Si(II) + h^+ \longrightarrow Si(III) \quad \text{or} \quad Si(II) \longrightarrow Si(III) + e^- \tag{1.6}$$

$$Si(III) + h^+ \longrightarrow Si(IV) \quad \text{or} \quad Si(III) \longrightarrow Si(IV) + e^- \tag{1.7}$$

Here Si(II) is a dissolution intermediate with an oxidation state of +2

Si(III) is a dissolution intermediate with an oxidation state of +3

Si(IV) is the final product, which is soluble SiF_6^{2-}.

The one hole capture and three electron injection pathway gives a quantum efficiency of 4 whereas two hole capture and two electron injection pathway gives a quantum efficiency of 2.

Cattarin *et al.* [4] showed that the electron injection was also observed during dissolution of p-Si. They proposed the mechanism for the porous silicon region

$$Si + h^+ \longrightarrow Si(I) \tag{1.8}$$

$$Si(I) \longrightarrow Si(II) + e^- \tag{1.9}$$

$$Si(II) + 2H^+ \longrightarrow Si(IV) + H_2 \tag{1.10}$$

1.3 Photoelectrochemical hydrogen evolution

The electrochemical hydrogen evolution reaction on metal electrodes is a multi-step process involving an adsorbed hydrogen intermediate that can be desorbed either by a chemical or electrochemical route.

$$H^+ + e^- \longrightarrow H_{ads}^{\cdot} \tag{1.11}$$

followed either by

$$H^+ + H_{ads}^{\cdot} + e^- \longrightarrow H_2 \tag{1.12}$$

or

$$H_{ads}^{\cdot} + H_{ads}^{\cdot} \longrightarrow H_2 \tag{1.13}$$

In principle, hydrogen evolution on semiconductors should also involve some form of adsorbed intermediate. Schlichthörl *et al.* [33] studied the kinetics of hydrogen evolution reaction on p-Si using intensity modulated photocurrent spectroscopy (IMPS) and light modulated microwave reflectivity (LMMR) and showed that hydrogen evolution reaction is a slow process. The hydrogen evolution reaction can be catalysed either by the presence of redox species or deposition of metals onto semiconductor surfaces. Wrighton and coworkers [7, 36, 37] studied the reduction of methyl viologen (MV) on p-Si. Its structure is shown below

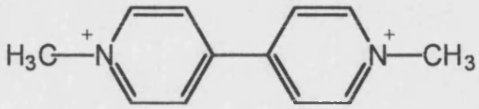

Fig 1.6 shows that the presence of methyl viologen shifts the i-V curve to the right, which indicates that the rate constant of the electron transfer reaction is increased.

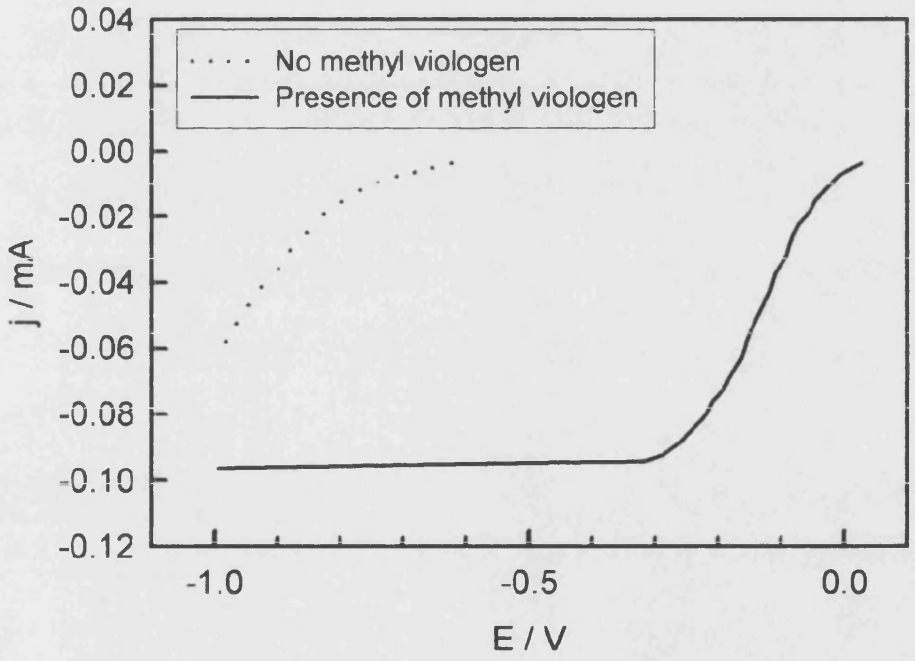

Figure 1.6: Effect of redox species (25 mM of methyl viologen) on p-Si under illumination [7].

The reaction scheme is as follows

$$h\nu \longrightarrow h^{+}_{vb} + e^{-}_{cb}$$

$$MV^{2+} + e^{-}_{cb} \longrightarrow MV^{+\cdot}$$

$$2H_2O + 2MV^{+\cdot} \xrightarrow{\Delta} 2MV^{2+} + H_2 + 2OH^{-}$$

It is noted that the last step requires a catalyst such as PtO_2, Pt/asbestos, Pd/asbestos etc.

The same authors observed that platinisation of p-Si also shifts the i-V curve to the right as shown in Fig 1.7. It is predicted that the rate of electron transfer reaction is enhanced by the presence of platinum.

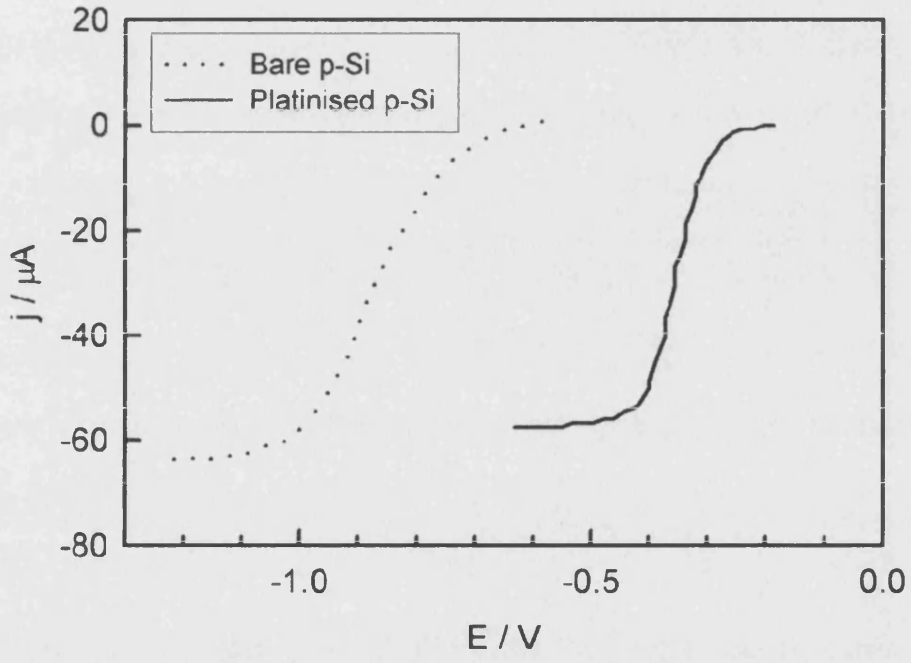

Figure 1.7: Effect of platinum on p-Si under illumination [7].

Fig 1.8 shows a plot of the exchange current density for the hydrogen evolution reaction as a function of a free energy of adsorption of the hydrogen atom for a series of metals. It is seen that the largest rate of hydrogen evolution occurs at platinum electrodes.

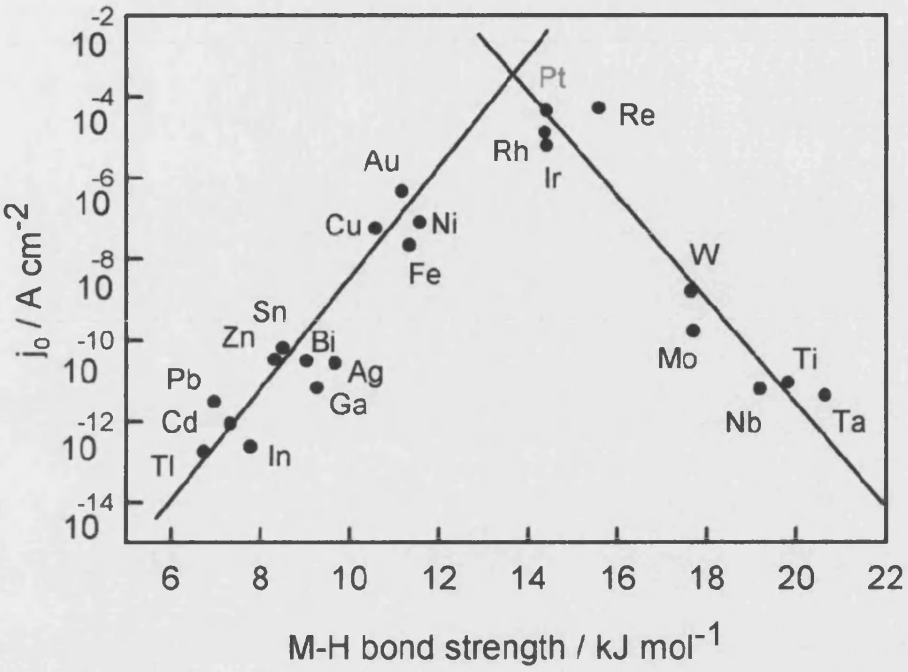

Figure 1.8: Catalytic activities of metals for hydrogen evolution [40].

Dominey *et al.* [7] showed that the coverage of 5×10^{-8} mol of Pt on p-Si is optimum for hydrogen evolution and proposed the reaction scheme

$$2h\nu \longrightarrow 2h^{+}_{\nu b} + 2e^{-}_{cb}$$

$$Pt + 2e^{-}_{cb} \longrightarrow Pt^{2-}$$

$$2H_2O + Pt^{2-} \longrightarrow Pt + H_2 + 2OH^{-}$$

It is seen that the hydrogen evolution processes involve photoexcitation of electron-hole pairs followed by charging of the small Pt islands. The reduction of oxygen and carbon dioxide on p-Si was also studied by several researchers [41–44]. The reduction of oxygen on p-Si did not show the current doubling, whereas the current doubling is observed from p-GaAs and p-GaP. Peter and coworkers [45–47] suggested the reaction scheme

$$O_2 + H^{+} + e^{-} \longrightarrow HO_2^{\cdot}$$

$$HO_2^{\cdot} + H^{+} \longrightarrow H_2O_2 + h^{+}$$

It is seen that current doubling involves injection of holes by reaction intermediates.

1.4 Microwave reflectivity measurements and the aim of the current study

Microwave reflectivity measurements are well established in semiconductor science and technology to obtain information about minority carrier lifetimes and surface recombination velocities, whereas the use of microwave methods in semiconductor electrochemistry is less common [50–52]. Microwave photoelectrochemistry was pioneered by Tributsch and coworkers at the Hahn-Meitner Institute in Germany to study charge transfer kinetics in semiconductors, and their approach was extended by Peter and coworkers [53–60]. Tributsch and coworkers used photoinduced microwave conductivity (PMC) and focused on the time and potential dependence of PMC with simultaneous measurements of photocurrent. For the time-resolved microwave conductivity (TRMC), their interest is non-steady state condition using a laser pulse and the time scale is between pico seconds and micro seconds. They also developed photoinduced microwave conductivity image to characterise properties of materials.

Schlichthörl *et al.* [61–63] combined potential modulated microwave reflectivity (PMMR) with impedance spectroscopy and measured the flat band potential of n-Si. They showed that flat band potentials obtained from PMMR agree with those obtained from conventional capacitance measurements. Searson *et al.* [65, 66] have also used the PMMR to study n-Si in fluoride media after Schlichthörl and Peter. Schlichthörl *et al.* [33] also studied the kinetics of the hydrogen evolution reaction on p-Si and showed that the rate constants derived from Light Modulated Microwave Reflectivity (LMMR) are consistent with those derived from Intensity Modulated Photocurrent Spectroscopy (IMPS). Lewis *et al.* [67, 68] have employed radio frequency and microwave methods to study the photoelectrochemical behaviour of Si in non-aqueous media. We have extended Schlichthörl and Peter's work and use frequency- and time-resolved microwave reflectivity methods under steady state conditions with simultaneous measurements of photocurrent (cf. Tributch and Lewis). Initially we used an X band microwave (f = 10 GHz) system since almost all work published so far refers to X-band microwave systems. The major problem for the microwave measurements was that signal/noise ratio was low and the solution of this problem is to use a Ka band microwave system (f

= 33 GHz) with signal averaging. Because of this development, we are able to obtain microwave data at low photocurrent ranges in a few microamps. The main aims of the present quantitative analysis of Si|fluoride system were

- to use microwave methods to study the kinetics of electrode reactions at silicon
- to relate frequency- and time-resolved microwave methods
- to relate microwave response and photocurrent response
- to relate microwave response and model of the semiconductor|electrolyte system

References

[1] Belaidi, A.; Chazalviel, J. N.; Ozanam, F.; Gorochov, O.; Chari, A.; Fotouhi, B.; Etman, M. Journal of Electroanalytical Chemistry **1998**, 444, 55-60.

[2] Belaidi, A.; Safi, M.; Ozanam, F.; Chazalviel, J. N.; Gorochov, O. Journal of the Electrochemical Society **1999**, 146, 2659-2664.

[3] Cattarin, S.; Chazalviel, J. N.; DaFonseca, C.; Ozanam, F.; Peter, L. M.; Schlichthörl, G.; Stumper, J. Journal of the Electrochemical Society **1998**, 145, 498-502.

[4] Cattarin, S.; Peter, L. M.; Riley; D. J. Journal of Physical Chemistry B 101 **1997**, 4071-4076.

[5] Chazalviel, J. N.; Etman, M.; Ozanam, F. Journal of Electroanalytical Chemistry **1991**, 297, 533-540.

[6] Y. Nakato, Y.; Tonomura, S.; H. Tsubomura, H. Berichte Der Bunsen-Gesellschaft-Physical Chemistry Chemical Physics **1976**, 80, 1289-1293.

[7] Dominey, R. N.; Lewis, N. S.; Bruce, J. A.; Bookbinder, D. C.; Wrighton, M. S. Journal of the American Chemical Society **1982**, 104, 467-482.

[8] Morisawa, K.; Ishida, M.; Yae, S.; Nakato, Y. Electrochimica Acta **1999**, 44, 3725-3729.

[9] Nakato, Y.; Tsubomura, H. Berichte Der Bunsen-Gesellschaft-Physical Chemistry Chemical Physics **1987**, 91, 405-408.

[10] Nakato, Y.; Tsubomura, H. Electrochimica Acta **1992**, 37, 897-907.

[11] Nakato, Y.; Yano, H.; Nishiura, S.; Ueda, T.; Tsubomura, H. Journal of Electroanalytical Chemistry **1987**, 228, 97-108.

[12] Yae, S.; Inakanishi, I.; Nakato, Y.; Toshima, N.; Mori, H. Journal of the Electrochemical Society **1994**, 141, 3077-3081.

[13] Yae, S. J.; Fujitani, M.; Nakanishi, I.; Uetsuji, M.; Tsuda, R.; Nakato, Y. Solar Energy Materials and Solar Cells **1996**, 43, 311-318.

[14] Turner, D. R. Journal of the Electrochemical Society **1958**, 105, 402-408.

[15] Allongue, P.; Costakieling, V.; Gerischer, H. Journal of the Electrochemical Society **1993**, 140, 1009-1018.

[16] Allongue, P.; Costakieling, V.; Gerischer, H. Journal of the Electrochemical Society **1993**, 140, 1018-1026.

[17] Allongue, P.; Brune, H.; Gerischer, H. Surface Science **1992**, 275, 414-423.

[18] Allongue, P.; Kieling, V.; Gerischer, H. Journal of Physical Chemistry **1995**, 99, 9472-9478.

[19] Rao, A. V.; Ozanam, F.; Chazalviel, J. N. Journal of the Electrochemical Society **1991**, 138, 153-159.

[20] Chazalviel, J.N in Porous silicon science and technology, p17, Springer-Verlag, France, 1995.

[21] Blackwood, D. J.; Borazio, A.; Greef, R.; Peter, L. M.; Stumper, J. Electrochimica acta **1992**, 37, 889-896.

[22] Matsumura, M.; Morrison, S. R. Journal of Electroanalytical Chemistry **1983**, 147, 157-166.

[23] Peter, L. M.; Borazio, A. M.; Lewerenz, H. J.; Stumper, J. Journal of Electroanalytical Chemistry **1990**, 290, 229-248.

[24] Matsumura, M.; Morrison, S. R. Journal of Electroanalytical Chemistry **1983**, 144, 113-120.

[25] Memming, R.; Schwandt, G. Surface science **1966**, 4, 109-124.

[26] Allongue, P.; Kieling, V.; Gerischer, H. Electrochimica Acta **1995**, 40, 1353-1360.

[27] Lehmann, V; Gosele; U. Applied Physics Letter **1991**, 58, 856-858.

[28] Gerischer, H.; Allongue, P.; Kieling, V. C. Berichte Der Bunsen-Gesellschaft-Physical Chemistry Chemical Physics **1993**, 97, 753-756.

[29] Gerischer, H.; Lubke, M. Journal of the Electrochemical Society **1988**, 135, 2782-2786.

[30] Peter, L. M. Chemical Reviews **1990**, 90, 753-769.

[31] Cattarin; S.; Peter; L. M.; Riley; D. J. Journal of Physical Chemistry B **1997**, 101, 4071-4076.

[32] Gerischer, H.; Lubke, M. Berichte Der Bunsen-Gesellschaft-Physical Chemistry Chemical Physics **1988**, 92, 573-577.

[33] Schlichthörl, G.; Ponomarev, E. A.; Peter, L. M. Journal of the Electrochemical Society **1995**, 142, 3062-3067.

[34] Gerischer, H.; Lubke, M. Berichte Der Bunsen-Gesellschaft-Physical Chemistry Chemical Physics **1987**, 91, 394-398.

[35] Forbes, M. D. E.; Lewis, N. S. Journal of the American Chemical Society **1990**, 112, 3682-3683.

[36] Bookbinder, D. C; Lewis, N. S; Bradlet, M. G; Bocarsly, A. B; Wrighton, M. S Journal of the American Chemical Society **1979**, 101, 7721-7723.

[37] Bocarsly, A. B.; Bookbinder, D. C.; Dominey, R. N.; Lewis, N. S.; Wrighton, M. S. Journal of the American Chemical Society **1980**, 102, 3683-3688.

[38] Rappich, J.; Lewerenz, H. J.; Gerischer, H. Journal of the Electrochemical Society **1993**, 140, L187-L189.

[39] Decker, F.; Fracastorodecker, M.; Badawy, W.; Doblhofer, K.; Gerischer, H. Journal of the Electrochemical Society 1983, 130, 2173-2179.

[40] Trasatti, S. Journal of Electroanalytical Chemistry, **1972**, 39, 163-184.

[41] Ogata, Y. H.; Ikeda, T.; Sakka, T.; Kobayashi, T. Electrochimica Acta **2000**, 45, 2219-2225.

[42] Liu, J. F.; Baozhu, C. Y. Journal of Electroanalytical Chemistry **1992**, 324, 191-200.

[43] Hirota, K.; Tryk, D. A.; Yamamoto, T.; Hashimoto, K.; Okawa, M.; Fujishima, A. Journal of Physical Chemistry B **1998**, 102, 9834-9843.

[44] Hinogami, R.; Mori, T.; Yae, S. J.; Nakato, Y. Chemistry Letters **1994**, 1725-1728.

[45] Li, J.; Peat, R.; Peter, L. M. Journal of Electroanalytical Chemistry **1984**, 165, 41-59.

[46] Peat, R.; Peter, L. M. Electrochimica Acta 1986, 31, 731-734.

[47] Peat, R.; Peter, L. M. Journal of Electroanalytical Chemistry **1986**, 209, 307-321.

[48] Blackwood, D. J.; Peter, L. M. Electrochimica Acta **1990**, 35, 1073-1080.

[49] Searson, P. C.; Macdonald, D. D.; Peter, L. M. Journal of the Electrochemical Society **1992**, 139, 2538-2543.

[50] Ramsa, A. P.; Jacobs, H.; Brand, F. A. Journal of Applied Physics **1959**, 30, 1054-1060.

[51] Atwater, H. A. Journal of Applied Physics **1960**, 31, 938-939.

[52] Deb, S.; Nag, B. R. Journal of Applied Physics **1962**, 33, 1604.

[53] Bogomolni, R. A.; Tributsch, H.; Petermann, G.; Klein, M. P. Journal of Chemical Physics **1983**, 78, 2578-2584.

[54] Kunst, M.; Beck, G.; Tributsch, H. Journal of the Electrochemical Society **1984**, 131, 954-956.

[55] Kunst, M.; Tributsch, H. Chemical Physics Letters **1984**, 105, 123-126.

[56] Messer, B.; Tributsch, H. Journal of the Electrochemical Society **1986**, 133, 2212-2213.

[57] Messer, B.; Tributsch, H. Chemical Physics Letters **1987**, 142, 546-550.

[58] Schlichthörl, G.; Tributsch, H. Electrochimica Acta **1992**, 37, 919-931.

[59] Tributsch, H.; Schlichthörl, G.; Elstner, L. Electrochimica Acta **1993**, 38, 141-152.

[60] Tributsch, H. in Modern aspects of electrochemistry. Vol. 33, p.435, Kluwer Academic/Plenum publishers, New York, 1999.

[61] Schlichthörl, G.; Peter, L. M. Journal of the Electrochemical Society **1994**, 141, L171-L173.

[62] Schlichthörl, G.; Peter, L. M. Journal of Electroanalytical Chemistry **1995**, 381, 55-61.

[63] Schlichthörl, G.; Peter, L. M. Journal of the Electrochemical Society **1995**, 142, 2665-2669.

[64] Searson; P. C. in advances in electrochemical science and engineering, vol. 4, VCH, 1995.

[65] Natarajan, A,; Oskam, G.; Searson, P. C. Journal of Applied Physics, **1998**, 83, 2112-2121.

[66] Natarajan, A.; Nellore, A.; Searson, P. C. Journal of Applied Physics, **1999**, 85, 1631-1636.

[67] Kenyon, C. N.; Ryba, G. N.; Lewis, N. S. Journal of Physical Chemistry **1993**, 1298-12936.

[68] Forbes, M. D. E.; Lewis, N. S. Journal of the American Chemical Society **1993**, 112, 3682-3683.

Chapter 2

Overview of Semiconductor Electrochemistry

2.1 Band Theory

Solids can be classified into 3 classes: metals, semiconductors and insulators. Metals tend to conduct electric current very well, whereas insulators do not. Semiconductors have intermediate properties. The electrical properties of solids can be explained by using a band diagram.

When two atomic orbitals (AOs) overlap, two molecular orbitals (MOs) are formed. In general, the number of MOs is the same as the number of atoms coming together to make the solid. For example, if n atoms are built up in a linear chain, n MOs are made up, as shown in Figure 2.1. If each AO supplies one 's' electron, half of the band is filled by electrons.

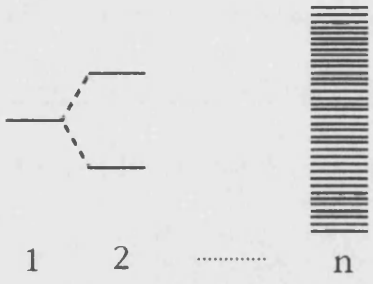

Figure 2.1: Band diagram of solids

An empty band of molecular orbitals is called a conduction band, and the occupied band is called a valence band. It is noted that a band should be partially filled by electrons for electrical conduction to occur. For metals, the valence band overlaps the conduction band and there are many empty allowed energy levels just above the valence band into which electrons can go if an electric field is applied. Even if small electric field is applied, it provides enough energy to promote electrons into the conduction band because there is no energy gap between valence and conduction bands. On the other hand, there is a energy gap between the valence and conduction bands for both insulators and semiconductors. If the valence band is totally filled with electrons leaving the conduction band empty, it is known as insulators. Semiconductors can be classified based on the electrical resistivity at room temperature with the range between 10^{-2} and 10^{9} Ωcm, whereas insulators have a resistivity above 10^{14} Ωcm [1]. The simplified diagram of solids are summarised in Fig 2.2

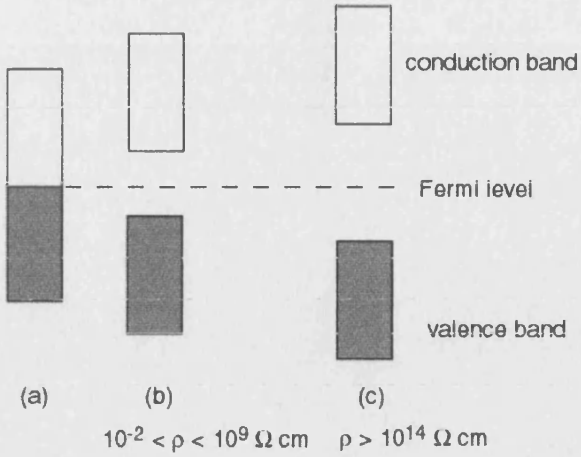

Figure 2.2: Simple band diagrams for (a) metals, (b) semiconductors, and (c) insulators.

The Fermi level, E_F, for semiconductors is defined as an energy level at which the probability occupied by electrons is half. The Fermi-Dirac function is given by

$$f(E) = \frac{1}{1 + \exp\left(\frac{E - E_F}{k_B T}\right)} \tag{2.1}$$

If $E - E_F = 0$, eq 2.1 becomes

$$\begin{aligned} f(E) &= \frac{1}{1 + \exp(0)} \\ &= \frac{1}{2} \end{aligned}$$

2.2 Doped silicon

Silicon is a semiconductor, and its conductivity can be increased by adding a small percentage of impurities into the structure, which is known as doping. In pure silicon, all the Si-Si bonds are regarded as covalent bonds since Si has four valence electrons and is bonded to four other Si atoms. If boron, which has only three valence electrons, is added as a dopant, one of the B-Si bonds must be deficient by one electron. The energy level associated with each B-Si bond does not form part of the valence band of silicon. Instead, it forms a discrete level just above the top of the valence band as shown in Fig 2.3 (a). This level is known as an acceptor level because it is capable of accepting an electron, and boron-doped silicon is p-type semiconductor.

If phosphorus is added as a dopant, there is one extra electron to form four Si-P co-valent bonds. This extra electron occupies a discrete level below the bottom of the conduction band, as shown in Fig 2.3 (b). This level acts as a donor level because the electrons in the donor level are donated to the conduction band where they are free to move. This kind of semiconductor is known as an n-type semiconductor.

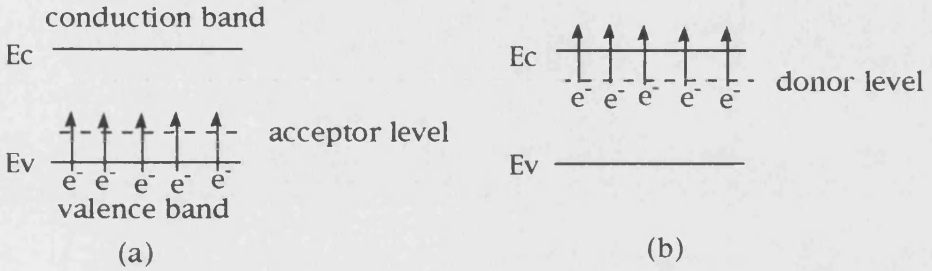

Figure 2.3: The band diagram for extrinsic semiconductors a) p-type semiconductors and b) n-type semiconductors.

The carrier densities can be expressed as

$$n = N_C \exp\left(-\frac{E_C - E_F}{k_B T}\right) \tag{2.2}$$

$$p = N_V \exp\left(-\frac{E_F - E_V}{k_B T}\right) \tag{2.3}$$

where N_C is effective density of states in the conduction band and N_V is effective density of states in the valence band.

Therefore the product of np is

$$\begin{aligned} np &= N_C \exp\left(-\frac{E_C - E_F}{k_B T}\right) N_V \exp\left(-\frac{E_F - E_V}{k_B T}\right) \\ &= N_C N_V \exp\left(-\frac{E_C - E_F + E_F - E_V}{k_B T}\right) \\ &= N_C N_V \exp\left(-\frac{E_C - E_V}{k_B T}\right) \\ &= N_C N_V \exp\left(-\frac{E_g}{k_B T}\right) \end{aligned} \tag{2.4}$$

For example, if the concentration of holes for p-type Si is 1×10^{15} cm^{-3}, the energy difference between Fermi level and the valence band is

$$E_F - E_V = -k_B T \ln\left(\frac{p}{N_V}\right)$$

$$= 0.0259 \ln\left(\frac{1 \times 10^{15}}{1.04 \times 10^{19}}\right)$$
$$= 0.240 \text{ eV}$$

From eq 2.4 the concentration of minority carriers is

$$n = \frac{N_C N_V}{p} \exp\left(-\frac{E_g}{k_B T}\right)$$
$$= \frac{2.8 \times 10^{19} \times 1.04 \times 10^{19}}{1 \times 10^{15}} \exp\left(-\frac{1.12}{0.026}\right)$$
$$= 5.7032 \times 10^4 \text{cm}^{-3}$$

2.3 Metal/semiconductor interface

When p-type semiconductors are contacted by metal, electrons flow from the metal into the valence band in the semiconductor in the case of $\Phi_m < \Phi_s$ where Φ_m and Φ_s are the work function of the metal and semiconductors, respectively. This flow occurs until the Fermi levels are aligned as as shown in Fig 2.4 for a p-type semiconductor.

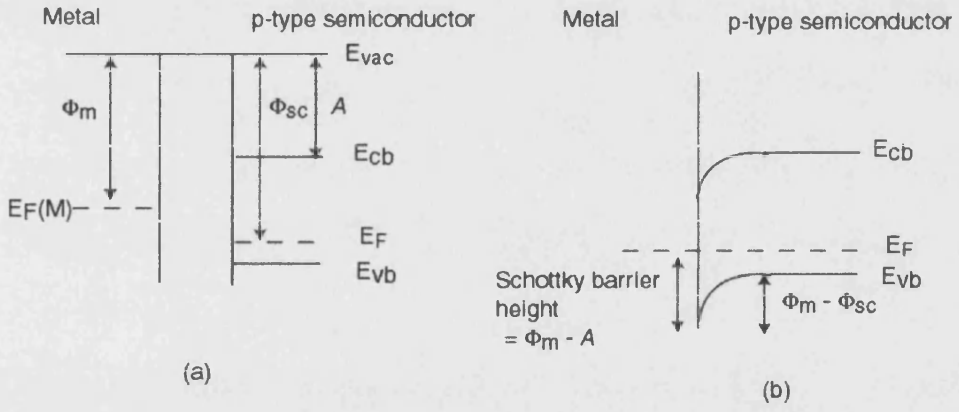

Figure 2.4: Metal/p-type semiconductor contact in the case of $\Phi_m < \Phi_{sc}$. (a) two materials isolated from each other (b) at thermal equilibrium after the contact is made.

The work function, Φ, is defined as the energy difference between the Fermi level and vacuum level, whereas the electron affinity, A, is the difference between the bottom of the conduction band and the vacuum level. The Schottky barrier height is the difference between work function and electron affinity.

A Schottky barrier can also be formed when a metal is in contact with n-type semiconductors. If Φ_m is greater than Φ_{sc}, the Fermi level of the semiconductor must be lowered in order to align the two Fermi level as shown in Fig 2.5.

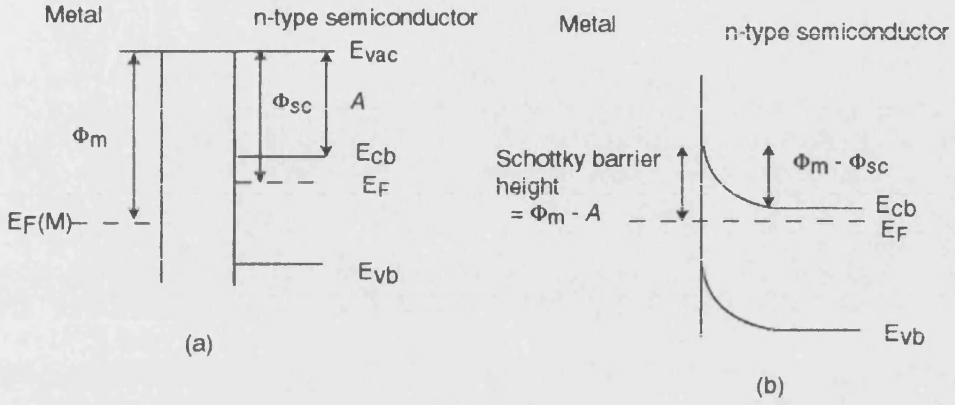

Figure 2.5: Metal/n-type semiconductor contact. (a) two materials isolated from each other (b) at thermal equilibrium after the contact is made.

Ohmic contacts are also important metal|semiconductor contacts. The condition to construct the ohmic contact is that Φ_m is greater than Φ_s for p-type semiconductors and that Φ_m is less than Φ_s for n-type semiconductors. For p-type semiconductors the Fermi levels are aligned at equilibrium by lowering the Fermi level on the semiconductor and holes easily flow across the interface as shown in Fig 2.6.

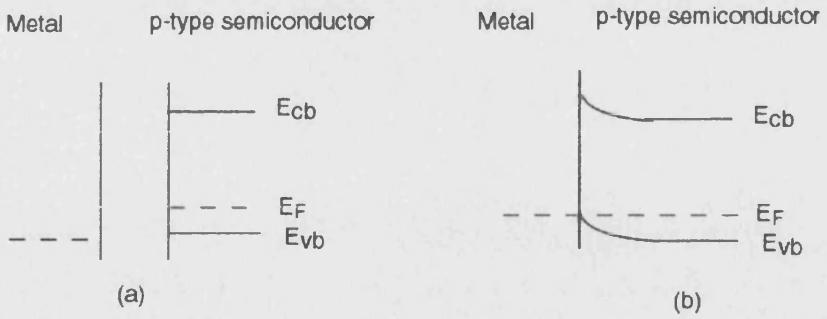

Figure 2.6: Ohmic contacts for p-type semiconductor. (a) two materials isolated from each other (b) at thermal equilibrium after the contact is made.

For n-type semiconductors the Fermi levels are aligned at equilibrium by transferring electrons from metals to the semiconductor. This raises the Fermi level on the semiconductor relative to the metal at equilibrium as shown in Fig 2.7.

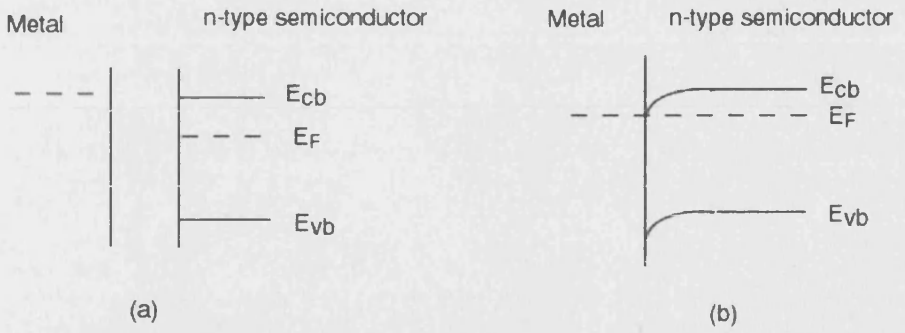

Figure 2.7: Ohmic contacts for n-type semiconductor. (a) two materials isolated from each other (b) at thermal equilibrium after the contact is made.

2.4 Semiconductor/electrolyte interface

The preceding discussion of metal/semiconductor interface can be extended to the semiconductor/electrolyte interface. For example, when p-type semiconductors are in contact with a redox electrolyte, electrons flow from the electrolyte into the valence band in the semiconductor in the case of $E_{redox} < E_F$. This flow occurs until E_F is in equilibrium with E_{redox}.

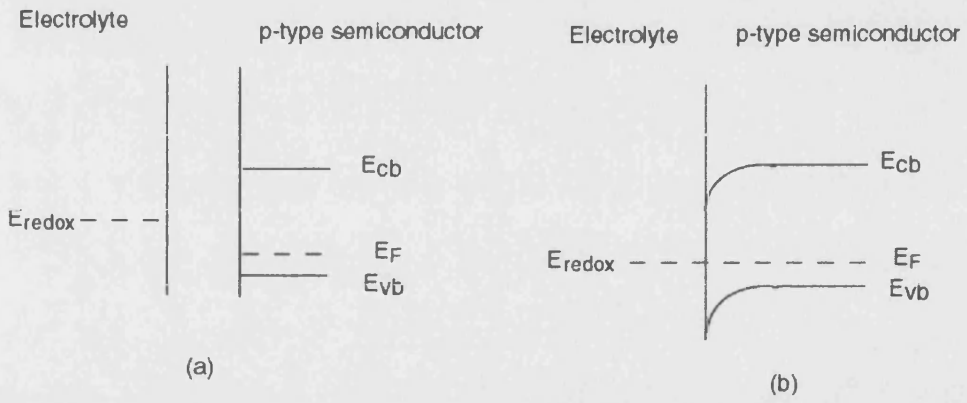

Figure 2.8: Electrolyte/p-type semiconductor contact. (a) two materials isolated from each other (b) at thermal equilibrium after the contact is made.

Similarly, when n-type semiconductors are in contact with a redox electrolyte, electrons flow from the conduction band to the electrolyte in the case of $E_{redox} > E_F$. This flow occurs until equilibrium is established, as shown in Fig 2.9.

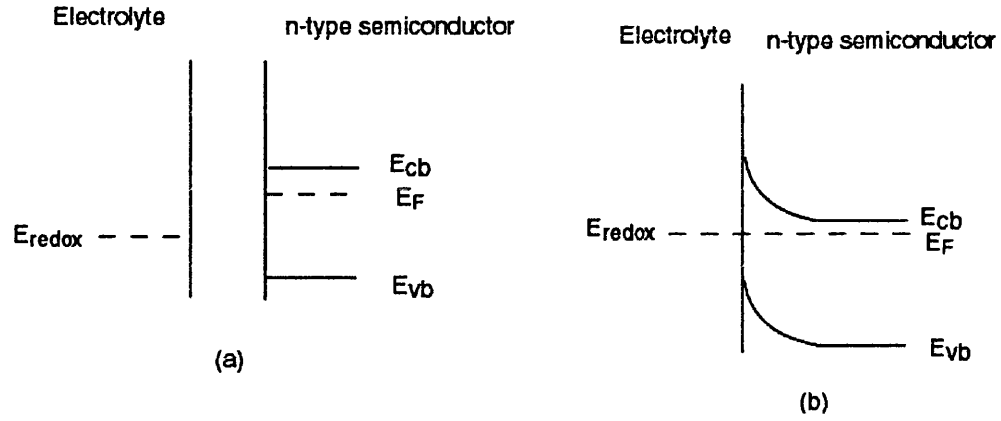

Figure 2.9: Electrolyte/n-type semiconductor contact. (a) two materials isolated from each other (b) at thermal equilibrium after the contact is made.

When a semiconductor is brought into contact with an electrolyte, an electric field is created in the solid, and the band energies become a function of position. The interfacial region in the solution is referred to as the double layer, and the interfacial region in the solid is referred to as the space charge layer. There are three types of space charge layers; accumulation, depletion, and inversion as shown in Figure 2.10. For p-type semiconductors, the bands bend upwards and the concentration of holes in the valence band is enhanced at the surface in the case of accumulation. The bands bend downwards for the depletion layer and the concentration of holes is reduced at the surface. For inversion layers, the bands bend also downwards, but the concentration of electrons is enhanced at the surface and is greater than that of holes. When the semiconductor has no excess charge, there is no space-charge and the bands are not bent. The electrode potential under this condition is called the flat-band potential.

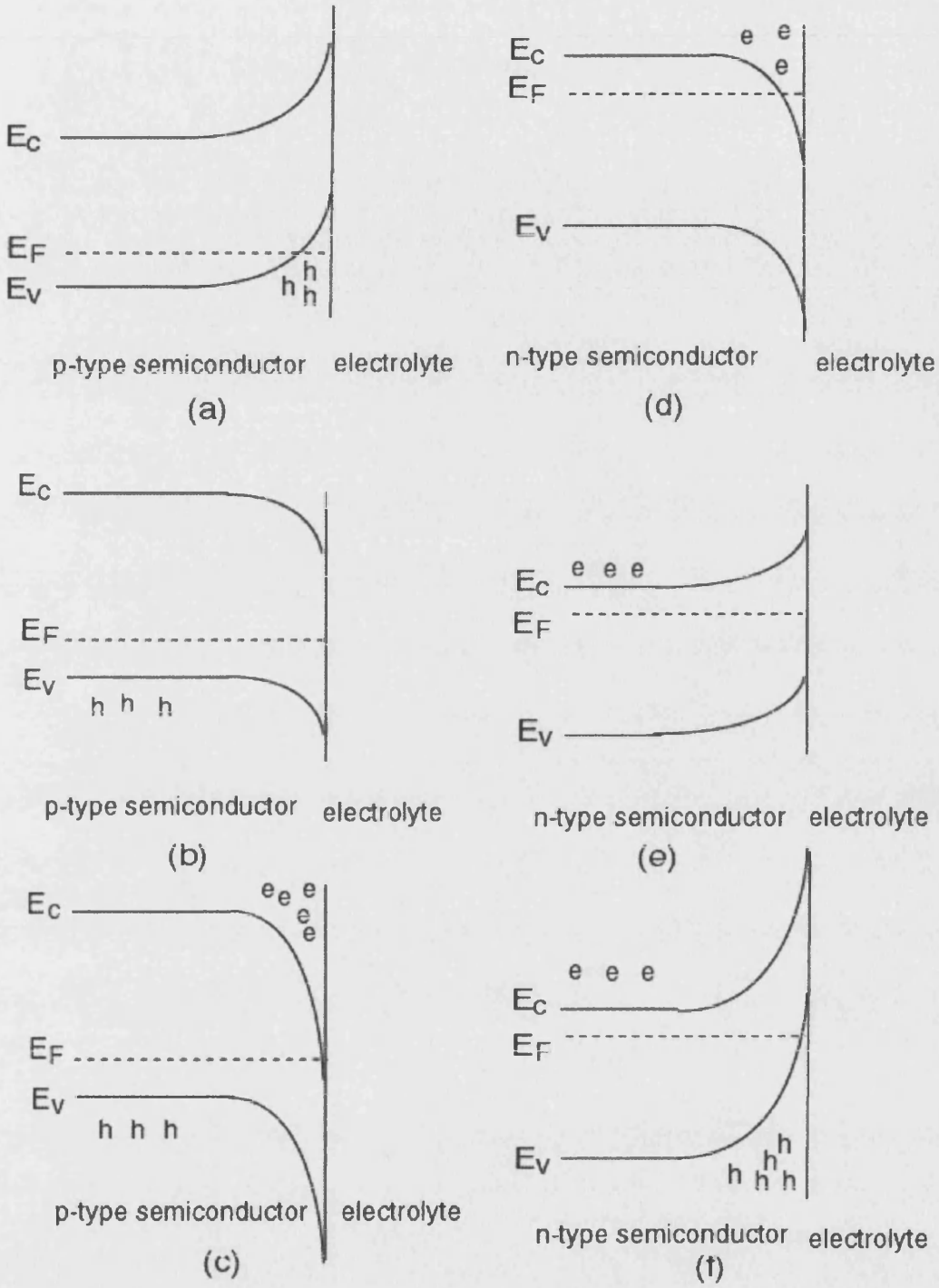

Figure 2.10: Space charge layers; (a) and (d) accumulation, (b) and (e) depletion, and (c) and (f) inversion layer for p-type and n-type semiconductors, respectively. Note that e and h represent electron and hole, respectively.

The potential drop across metal/electrolyte and semiconductor/electrolyte interface is schematically shown in Fig 2.11. The potential drop across metal/electrolyte occurs mainly in electrolyte, φ_H, whereas the potential drop across semiconductor/electrolyte occurs mainly at semiconductor, φ_{sc}. It is noted that the charge in both regions is equal but with opposite sign.

$$Q_{sc} + Q_{ss} = -Q_{sol} \quad \text{in the dark for semiconductors} \tag{2.5}$$

Here Q_{sc} is the charge in the space charge layer associated with ionised acceptor levels, Q_{ss} is the charge due to the surface state, and Q_{sol} is the charge due to the electrolyte.

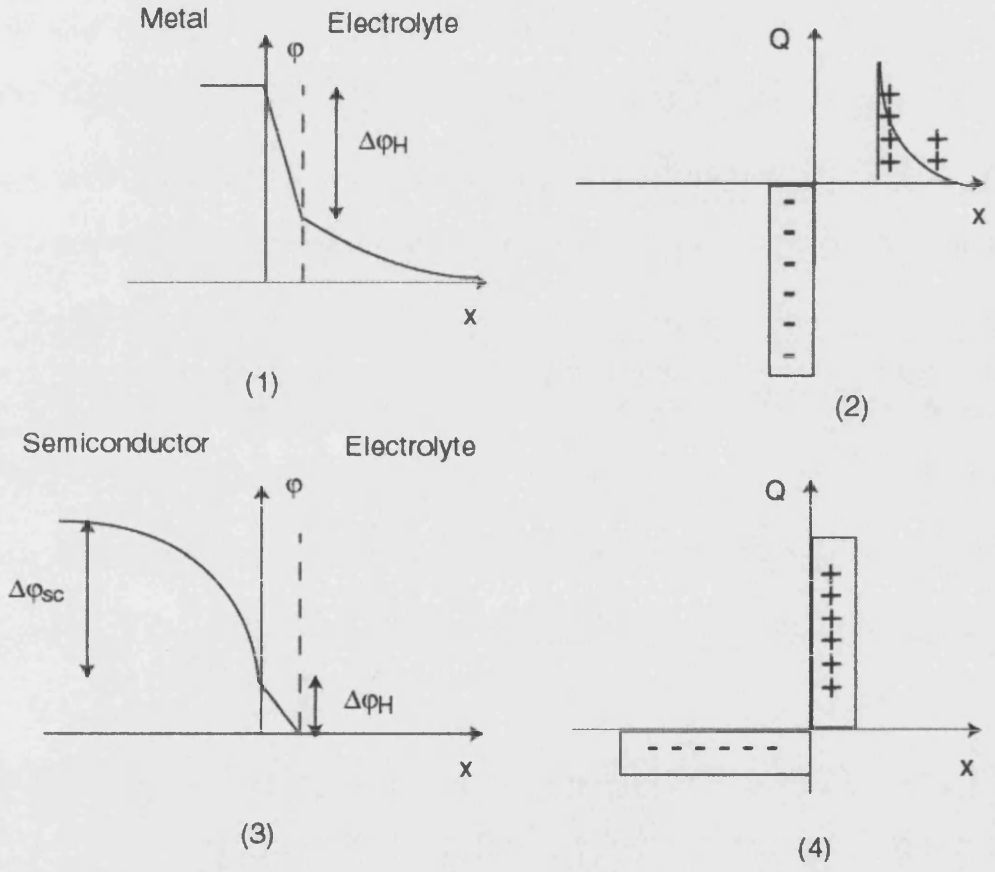

Figure 2.11: Potential distribution at (1) metal|electrolyte interface (3) semiconductor|electrolyte interface under depletion conditions. Charge distribution at (2) metal|electrolyte interface (4) semiconductor|electrolyte interface under depletion conditions. Note that φ_{sc} is potential drop across the semiconductor and φ_H is potential drop across the electrolyte.

A surface state is a energy level that located at the surface. The surface state causes an extra charge at the surface as shown in Fig 2.12. Before p-type semiconductor is in contact with electrolyte, the surface state is empty. The surface state is partially filled when the semiconductor is brought into the contact with electrolyte.

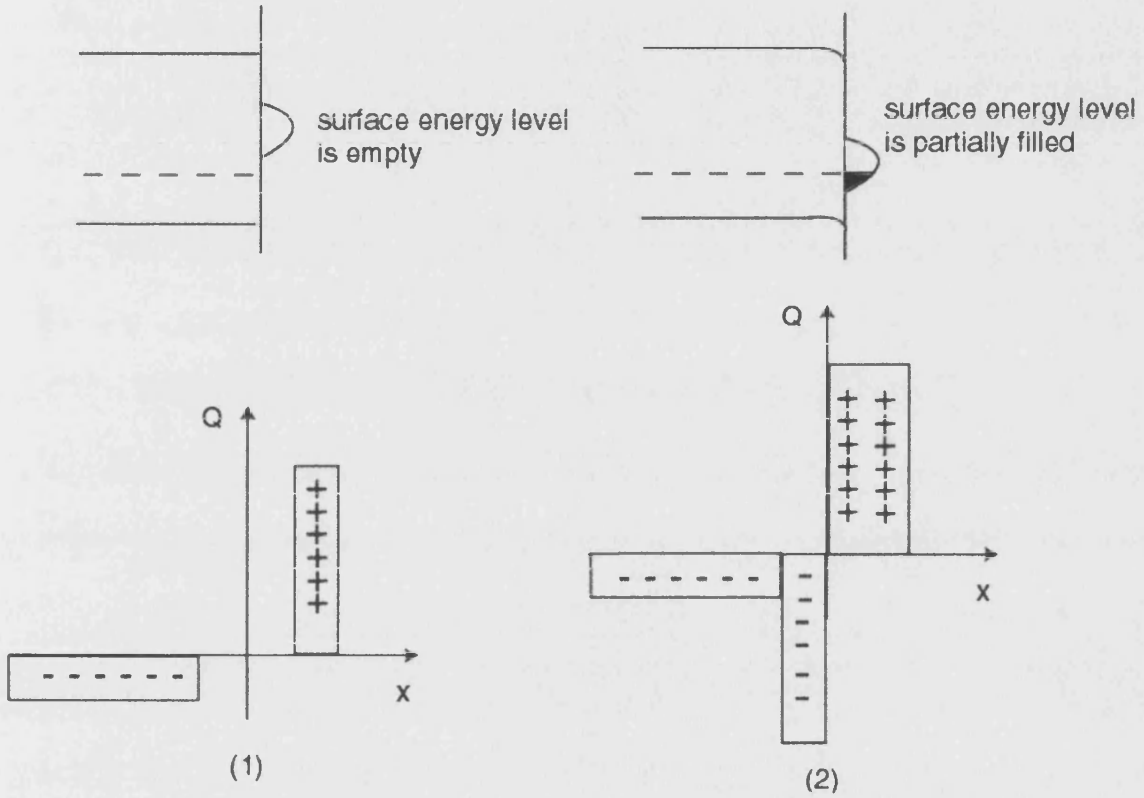

Figure 2.12: (1) Before contact with electrolyte (2) At equilibrium in the dark.

There are mainly two types of surface states; surface dangling and ion induced states. The surface dangling state is caused by dangling bonds, which is the unsaturated bond at the first surface layer. The ion induced state is caused by the potential difference from the internal lattice potential of ionic compound semiconductor. It is noted that both dangling state and ion induced states are characteristic of the semiconductor materials. This type of surface state is classified as intrinsic surface states. On the other hand, the extrinsic surface state is caused by adsorbed particles and surface films that depends on the environment in which the surface is exposed.

Potential drop as a function of overpotential is schematically shown in Fig 2.13. At flat band potential, surface state is empty. At weak depletion, surface state en-

ergy level starts to be filled by electrons. As increasing the band bending, the surface state energy level is more occupied by electrons. If there is no potential drop across the semiconductor (between E_2 and E_3 in Fig 2.13), it is referred to as Fermi level pinning.

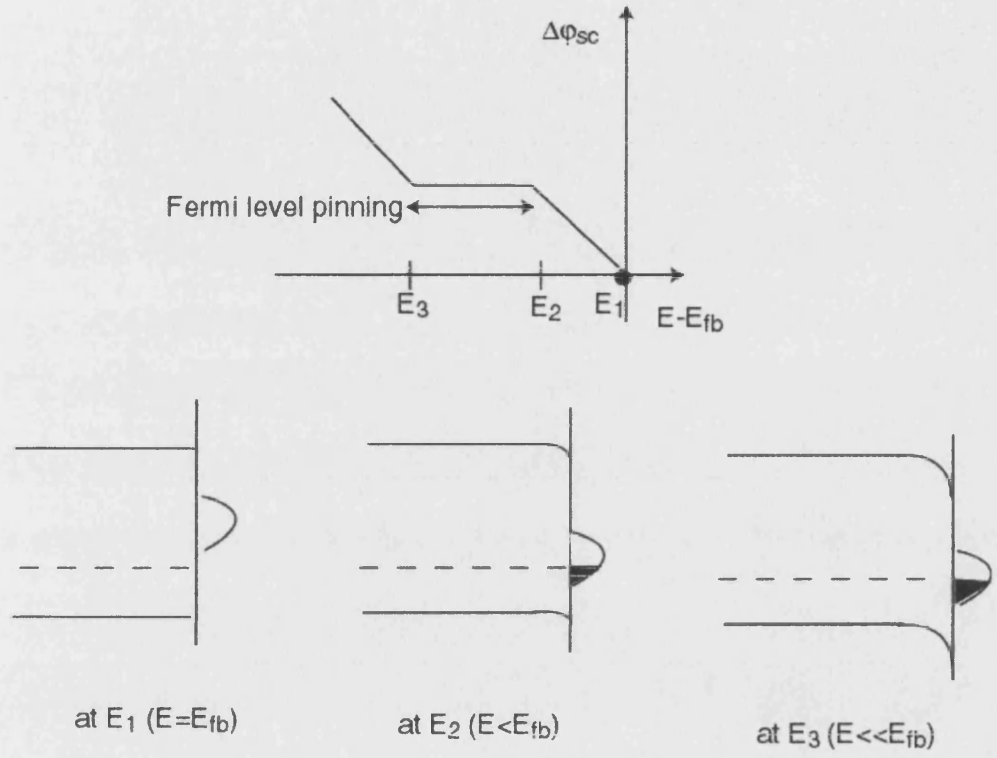

Figure 2.13: Potential drop as a function of potential for p-type semiconductors.

The interface between a semiconductor and an electrolyte behaves like a capacitor. The impedance of a semiconductor|electrolyte interface can be represented as follows

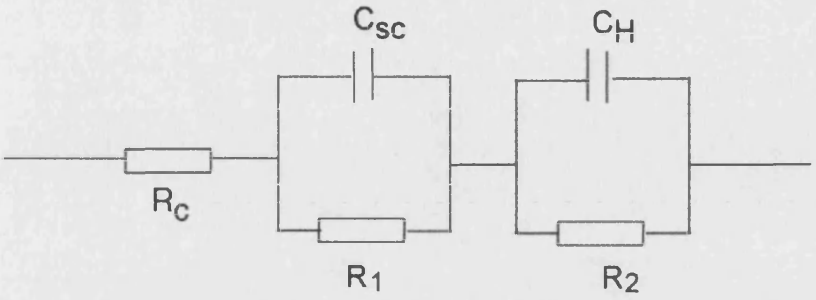

Figure 2.14: Impedance at semiconductor|electrolyte interface. R_c is contact and solution resistance, C_{sc} is space-charge capacitance, C_H is Helmholtz capacitance, R_1 is space-charge resistance, and R_2 is charge transfer resistance.

The total impedance is given by

$$Z = R_c + \frac{R_1}{1 + i\omega C_{sc}} + \frac{R_2}{1 + i\omega C_H} \tag{2.6}$$

If the doping density is low, it can be assumed that the space-charge capacitance is smaller than the Helmholtz capacitance, and eq 2.6 can be reduced to

$$Z = R_c + \frac{R_1}{1 + i\omega C_{sc}} \tag{2.7}$$

The simplified equivalent circuit is shown

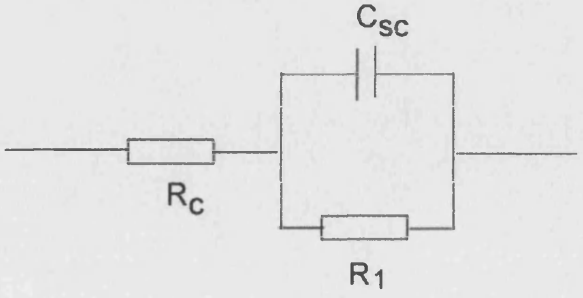

Figure 2.15: Simplified equivalent circuit.

2.5 Space-charge capacitance

2.5.1 Depletion layer width

The semiconductor consists of two layers; space-charge layer and bulk layer as shown in Fig 2.16,

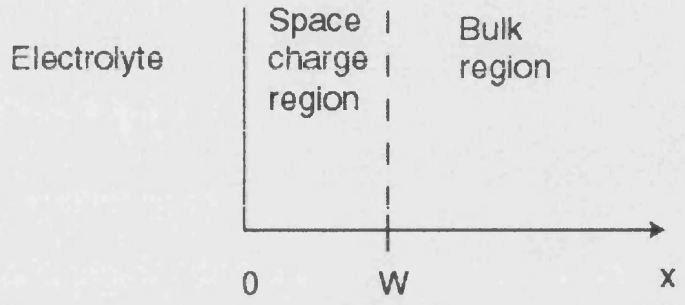

Figure 2.16: Schematic diagram of semiconductor.

There is electric field in the space-charge layer whereas there is no electric field outside the space-charge layer. The space charge width, W, can be derived from Poisson's equation, which describes the relationship between the electric field and charge density, $\rho(\mathrm{x})$. Poisson's equation for p-type semiconductors is given by

$$\frac{\mathrm{d}^2\phi}{\mathrm{dx}^2} = \frac{\rho(\mathrm{x})}{\varepsilon_0\varepsilon_\mathrm{r}} \tag{2.8}$$

where ϕ is potential across the semiconductor, and x is distance from the surface.
It is noted that the charge density is determined by the concentration of ionised acceptors and electrons. For $\mathrm{x} < \mathrm{W}$, the charge density can be approximated as

$$\rho(\mathrm{x}) = \mathrm{qN_A} \tag{2.9}$$

This approach is known as the abrupt depletion approximation.
Integrating eq 2.8 with respect to x gives the electric field in the space charge region

$$\begin{aligned} \int_0^\mathrm{W} \frac{\mathrm{d}^2\phi}{\mathrm{dx}^2} = \frac{\mathrm{d}\phi}{\mathrm{dx}} = \mathrm{E} &= \int_0^\mathrm{W} \frac{\rho(\mathrm{x})}{\varepsilon_0\varepsilon_\mathrm{r}}\mathrm{dx} \\ &= \frac{\rho(\mathrm{x})}{\varepsilon_0\varepsilon_\mathrm{r}}\mathrm{x} + \mathrm{C_1} \end{aligned} \tag{2.10}$$

where C_1 is an integration constant, and can be worked out using the boundary condition that there is no electric field at distance, W

$$\begin{aligned} 0 &= \frac{\rho(x)}{\varepsilon_0\varepsilon_r}W + C_1 \\ C_1 &= -\frac{\rho(x)}{\varepsilon_0\varepsilon_r}W \end{aligned} \tag{2.11}$$

Inserting eq 2.11 into eq 2.10 leads to

$$\begin{aligned} E &= \frac{\rho(x)}{\varepsilon_0\varepsilon_r}x - \frac{\rho(x)}{\varepsilon_0\varepsilon_r}W \\ &= \frac{\rho(x)}{\varepsilon_0\varepsilon_r}(x - W) \end{aligned} \tag{2.12}$$

Integration of eq 2.12 gives the potential distribution,

$$\begin{aligned} \int_0^x \frac{d\phi}{dx} = \Delta\phi &= \int_0^x \frac{\rho(x)}{\varepsilon_0\varepsilon_r}(x - W) \\ &= \frac{\rho(x)}{\varepsilon_0\varepsilon_r}\int_0^x (x - W) \\ &= \frac{\rho(x)}{\varepsilon_0\varepsilon_r}\left[\frac{x^2}{2} - Wx\right]_0^W \\ &= -\frac{\rho(x)W^2}{2\varepsilon_0\varepsilon_r} \end{aligned} \tag{2.13}$$

Rearranging eq 2.13 gives the depletion width for the p-type semiconductors

$$W = \sqrt{-\frac{2\varepsilon_0\varepsilon_r\Delta\phi}{\rho(x)}} \tag{2.14}$$

Similarly the depletion width for n-type semiconductors is

$$W = \sqrt{\frac{2\varepsilon_0\varepsilon_r\Delta\phi}{\rho(x)}} \tag{2.15}$$

2.5.2 Mott-Schottky relation

The depletion layer capacitance is defined as

$$C = \frac{dQ}{dV} = \frac{\varepsilon_0\varepsilon_r A}{W} \tag{2.16}$$

Inserting eq 2.15 into eq 2.16

$$\begin{aligned} C &= \frac{\varepsilon_0\varepsilon_r A}{W} \\ &= \varepsilon_0\varepsilon_r A \times \sqrt{-\frac{qN_A}{2\varepsilon_0\varepsilon_r\Delta\phi}} \\ &= \sqrt{-\frac{\varepsilon_0\varepsilon_r A^2 qN_A}{2\Delta\phi}} \end{aligned} \tag{2.17}$$

Rearranging eq 2.17 gives the Mott-Schottky equation;

$$\frac{1}{C^2} = -\frac{2}{q\varepsilon_0\varepsilon_r A^2 N_A}\Delta\phi \tag{2.18}$$

The relationship between the potential across the semiconductor and the applied potential, V_a is given by

$$\Delta\phi = V_a - V_{fb} + \frac{k_B T}{q} \tag{2.19}$$

where V_{fb} is flat band potential, and $\frac{k_B T}{q}$ is thermal voltage.

Similarly, the Mott-Schottky equation for n-type semiconductors is

$$\frac{1}{C^2} = \frac{2}{q\varepsilon_0\varepsilon_r A^2 N_D}\left(V_a - V_{fb} - \frac{k_B T}{q}\right) \tag{2.20}$$

2.6 Electron transfer at electrode/electrolyte interface

2.6.1 Metal electrodes

The general electron transfer reaction can be written as

$$O + ne^- \rightleftharpoons R \tag{2.21}$$

Fig 2.17 shows the energy diagram for 3 cases; i) reduction ii) equilibrium and iii) oxidation processes. If E is less than E_{eq}, the free energy of activation energy for the reduction is less than that for the oxidation and a cathodic current flows as shown in eq 2.22. Similarly if E is greater than E_{eq}, the free energy of activation energy for the oxidation is less than that for the reduction and an anodic current flows.

$$j = j_0\left[\exp\left(\frac{(1-\alpha_c)nF(E-E_{eq})}{RT}\right) - \exp\left(\frac{-\alpha_c nF(E-E_{eq})}{RT}\right)\right] \tag{2.22}$$

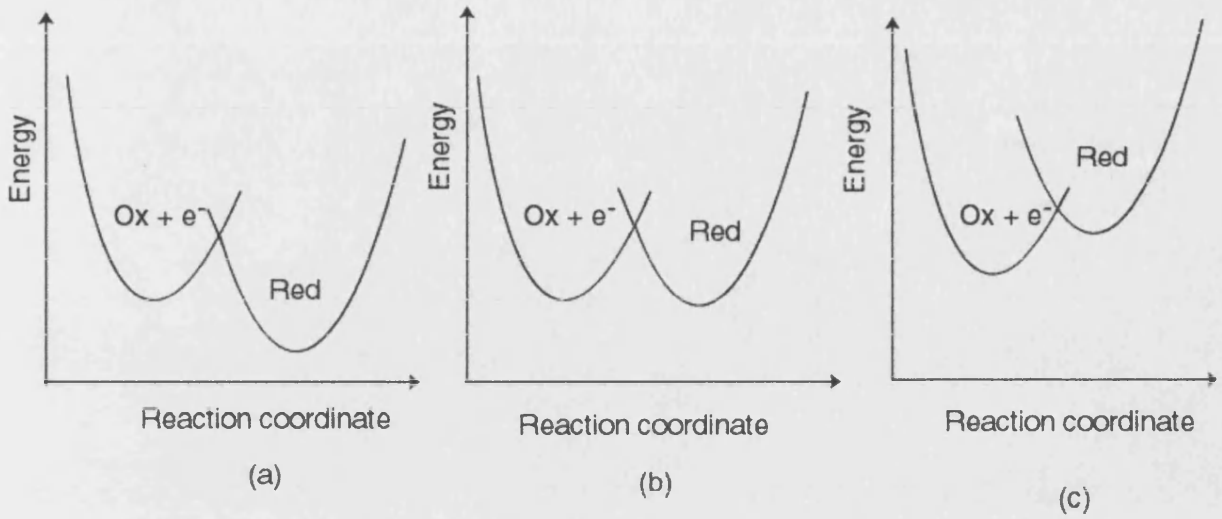

Figure 2.17: Energy diagram for a) reduction, b) equilibrium (c) oxidation.

According to the Frank-Condon principle, an electronic transition to an ion occurs for an extremely short time without changing the position of nucleus and the electron transfer at metal electrodes was quantitatively described by Marcus [4]. The distribution of energies for oxidised species is given by a Gaussian distribution [3]

$$W(E)_{Ox} = \frac{1}{\sqrt{4\pi\lambda_{re}k_BT}} \exp\left(-\frac{(E_{Ox} - E)^2}{4\lambda_{re}k_BT}\right) \tag{2.23}$$

Similarly, the distribution of energies for reduced species is given by

$$W(E)_{Red} = \frac{1}{\sqrt{4\pi\lambda_{re}k_BT}} \exp\left(-\frac{(E_{Red} - E)^2}{4\lambda_{re}k_BT}\right) \tag{2.24}$$

The general plot of eq 2.23 and eq 2.24 is shown in Fig 2.18.

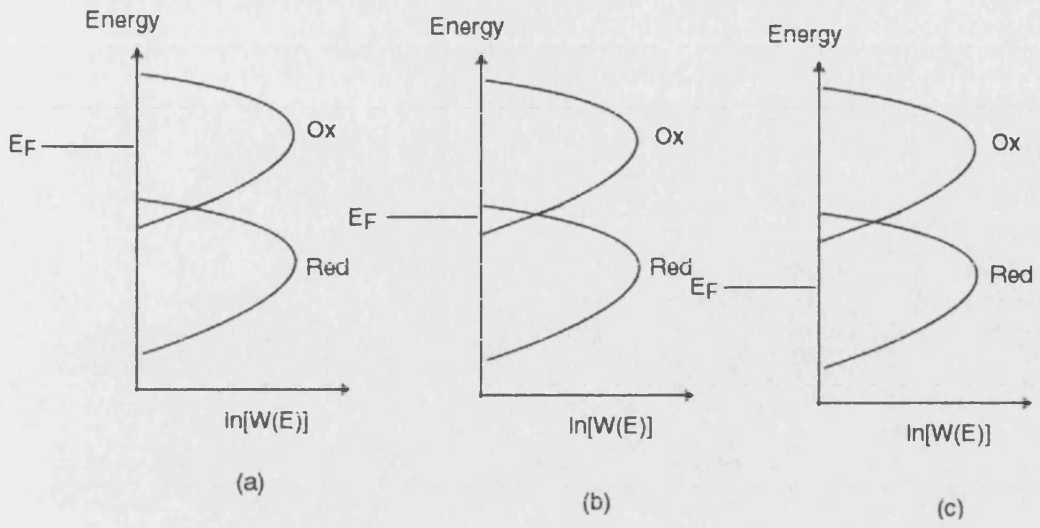

Figure 2.18: Energy distribution a) negative overpotential b) equilibrium c) positive overpotential.

The probability function for electron states in the redox electrolyte is the sum of occupied and unoccupied states

$$D_{Redox}(E) = D_{Red}(E) + D_{Ox}(E) \tag{2.25}$$

$D_{Red}(E)$ and $D_{Ox}(E)$ are represented by

$$D_{Red}(E) = c_{Red} W_{Red}(E) \tag{2.26}$$

$$D_{Ox}(E) = c_{Ox} W_{Ox}(E) \tag{2.27}$$

At equilibrium the occupation of these energy states is given by the Fermi-Dirac distribution

$$D_{Red}(E) = D_{Redox}(E) \cdot f(E - E_{F,Redox}) \tag{2.28}$$

$$D_{Ox}(E) = D_{Redox}(E) \cdot \{1 - f(E - E_{F,Redox})\} \tag{2.29}$$

The rate of electron transfer from the metal to the electrolyte in a range of energy level between E and E + dE must be proportional to the number of occupied states in the metal, $D_M(E) \cdot f(E - E_{F,M})$, and the number of unoccupied states in the electrolyte, $D_{Redox}(E) \cdot \{1 - f(E - E_{F,Redox})\}$.

$$j_c' = q \cdot k_a \cdot D_M(E) \cdot f(E - E_{F,M}) \cdot D_{Redox}(E) \cdot \{1 - f(E - E_{F,Redox})\} \tag{2.30}$$

A similar expression is obtained for the anodic current

$$j'_a = q \cdot k_a \cdot D_M(E) \cdot \{1 - f(E - E_{F,M})\} \cdot D_{Redox}(E) \cdot f(E - E_{F,Redox}) \quad (2.31)$$

The total current density is given by integration of eq 2.30 and eq 2.31 with respect to potential

$$j_c = q \cdot \int_{-\infty}^{+\infty} k_a \cdot D_M(E) \cdot f(E - E_{F,M}) \cdot D_{Redox}(E) \cdot \{1 - f(E - E_{F,Redox})\} dE \quad (2.32)$$

$$j_a = q \cdot \int_{-\infty}^{+\infty} k_a \cdot D_M(E) \cdot \{1 - f(E - E_{F,M})\} \cdot D_{Redox}(E) \cdot f(E - E_{F,Redox}) dE \quad (2.33)$$

Fig 2.19 shows the cathodic and anodic current.

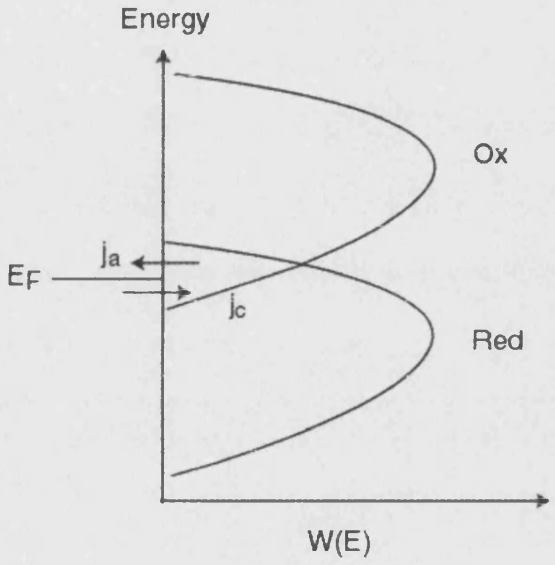

Figure 2.19: Anodic and cathodic currents at metal|electrolyte interface.

Nernst equation

The Fermi level is actually the electrochemical potential of electrons in solid. The electrochemical potential at equilibrium is given by [5, 6]

$$\overline{\mu}_{Ox} + \overline{\mu}_n = \overline{\mu}_{Red} \quad (2.34)$$

where $\overline{\mu}_{Ox}$ is electrochemical potential of oxidised species, $\overline{\mu}_n$ is electrochemical potential of electrons, and $\overline{\mu}_{Red}$ is electrochemical potential of reduced species.
Eq 2.34 can be rewritten as

$$\mu_{Ox} + z_{Ox}FE_{sol} + \mu_n - nFE_n = \mu_{Red} + z_{Red}FE_{sol} \quad (2.35)$$

where $\overline{\mu}_{Ox} = \mu_{Ox} + z_{Ox}FE_{sol}$

$\overline{\mu}_{n} = \mu_{n} - nFE_{n}$

$\overline{\mu}_{R} = \mu_{Red} + z_{Red}FE_{sol}$

It is noted that z_{Ox} and z_{Red} represent the oxidation state of oxidised and reduced species, respectively and $z_{Ox} - z_{Red}$ represent the number of transferred electrons. E_{sol} and E_{n} represent the Galvani potentials for the solution and electrode, respectively.

Eq 2.35 can be solved for the difference of the Galvani potentials for the solution and electrode, ΔE

$$\begin{aligned}(z_{Ox} - z_{Red})FE_{sol} - nFE_{n} &= \mu_{Red} - \mu_{Ox} - \mu_{n} \\ nF(E_{sol} - E_{n}) &= \mu_{Red} - \mu_{Ox} - \mu_{n} \\ \Delta E &= \frac{\mu_{Red} - \mu_{Ox} - \mu_{n}}{nF} \end{aligned} \tag{2.36}$$

Since $\mu_{Red} = \mu^{o}_{Red} + RT\ln\left(\frac{c_{Red}}{c^{o}}\right)$ and $\mu_{Ox} = \mu^{o}_{Ox} + RT\ln\left(\frac{c_{Ox}}{c^{o}}\right)$ eq 2.36 becomes

$$\begin{aligned}\Delta E &= \frac{1}{nF}\left[\mu^{o}_{Red} + RT\ln\left(\frac{c_{Red}}{c^{o}}\right) - \mu^{o}_{Ox} - RT\ln\left(\frac{c_{Ox}}{c^{o}}\right) - \mu_{n}\right] \\ &= \frac{1}{nF}(\mu^{o}_{Red} - \mu^{o}_{Ox} - \mu_{n}) + \frac{RT}{nF}\ln\left(\frac{c_{Ox}}{c_{Red}}\right) \\ &= E^{o}_{sol} + \frac{RT}{nF}\ln\left(\frac{c_{Ox}}{c_{Red}}\right) \end{aligned} \tag{2.37}$$

where $E^{o}_{sol} = \frac{1}{nF}(\mu^{o}_{Red} - \mu^{o}_{Ox} - \mu_{n})$. Eq 2.37 is known as Nernst equation.

Standard exchange rate constants

The cathodic and anodic currents are defined as [17]

$$j_{c} = -nFc_{Ox}k^{o}\exp\left(\frac{-\alpha_{c}nF(E - E_{eq})}{RT}\right) \tag{2.38}$$

$$j_{a} = nFc_{Red}k^{o}\exp\left(\frac{(1 - \alpha_{c})nF(E - E_{eq})}{RT}\right) \tag{2.39}$$

where α_{c} is cathodic transfer coefficient, k^{o} is standard rate constant, and $E - E_{eq}$ is overpotential = η.

The exchange current density is defined by

$$j_{0} = |j_{c}| = |j_{a}| \tag{2.40}$$

The Nernst equation is given by

$$E = E^{\circ} + \frac{RT}{nF} \ln\left(\frac{c_{Ox}}{c_{Red}}\right) \tag{2.41}$$

Rearranging eq 2.41

$$\ln \frac{c_{Ox}}{c_{Red}} = \frac{nF\eta}{RT} \tag{2.42}$$

Taking exponential for both sides, eq 2.42 becomes

$$\frac{c_{Ox}}{c_{Red}} = \exp\left(\frac{nF\eta}{RT}\right) \tag{2.43}$$

Taking power of $-\alpha_c$, eq 2.43 becomes

$$\left(\frac{c_{Ox}}{c_{Red}}\right)^{-\alpha_c} = \exp\left(\frac{-\alpha_c nF\eta}{RT}\right) \tag{2.44}$$

From eq 2.38, the exchange current density is given as

$$\begin{aligned} j_0 &= |j_c| \\ &= nFc_{Ox}k^0 \exp\left(\frac{-\alpha_c nF\eta}{RT}\right) \\ &= nFc_{Ox}k^0 \left(\frac{c_{Ox}}{c_{Red}}\right)^{-\alpha_c} \\ &= nFk^0 c_{Ox}^{1-\alpha_c} c_{Red}^{\alpha_c} \end{aligned} \tag{2.45}$$

2.6.2 Semiconductor electrodes

Photoinduced electron transfer reactions under steady illumination are observed at many semiconductor electrodes. For the simple case, minority carriers generated within space charge region are rapidly transferred to the surface. Carriers generated outside the space charge region can diffuse into the space charge region and then are collected and transported to the surface if they reach the edge of the space charge region. This model was developed by Gärtner [9]. The total photocurrent density for Gärtner model is given by

$$j_{photo} = j_G + j_{diff}$$

where j_G is generation current and j_{diff} is diffusion current.

The generation current is dominated in the space-charge region where the electric field exists and the diffusion current is observed outside the space-charge layer. Fig 2.20 shows four characteristic length in the semiconductor; i) sample thickness, d, ii) penetration depth of the light, $1/\alpha$, iii) space-charge width, W, and iv) diffusion length, L, given by

$$\begin{aligned} L &= \sqrt{D\tau} \\ &= \sqrt{\frac{\mu k_B T \tau}{q}} \end{aligned} \tag{2.46}$$

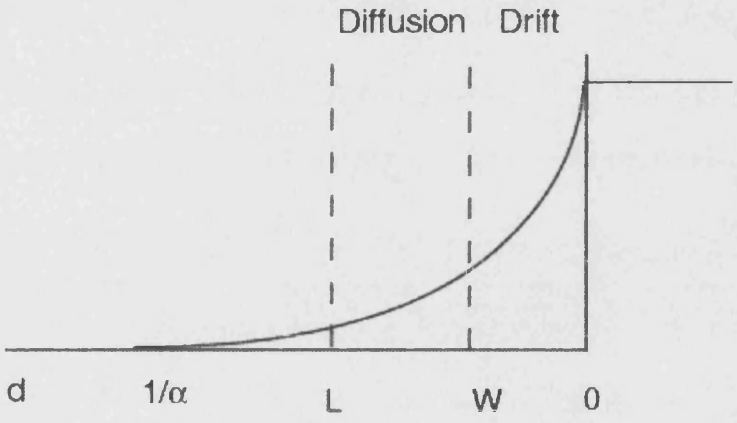

Figure 2.20: Characteristic length used to derive photocurrent response.

Generation current

The rate of generation of electron-hole pairs is given by the Beer-Lambert Law

$$G = I_0 \alpha \exp(-\alpha x) \tag{2.47}$$

where I_0 is incident photon flux corrected for reflection losses, α is absorption coefficient (See Appendix A.5), and x is distance from the surface.

If it is assumed that all carriers generated in the depletion region contribute to the photocurrent, this component is given by the integration of eq 2.47 within the space

charge width

$$\begin{aligned} j_G &= q\int_0^W G dx \\ &= q\int_0^W I_0\alpha \exp(-\alpha x) \\ &= q\left[\frac{I_0\alpha}{\alpha}\exp(-\alpha x)\right]_0^W \\ &= q\{I_0\exp(-\alpha W) - I_0\} \end{aligned} \tag{2.48}$$

Diffusion current

The continuity equation is given by

$$\frac{dn}{dt} = G + D\frac{d^2n}{dx^2} - \frac{n-n_0}{\tau} = 0 \quad \text{at steady state} \tag{2.49}$$

where τ is electron lifetime

Since the diffusion length, $L = \sqrt{D\tau}$, eq 2.49 can be rewritten as

$$\frac{dn}{dt} = G + D\frac{d^2n}{dx^2} - \frac{D(n-n_0)}{L^2} = 0 \tag{2.50}$$

The general solution to eq 2.50 in second order differential equation is

$$n(x \geq x_n) = A\exp\left(-\frac{x-x_n}{L}\right) + B\exp\left(\frac{x-x_n}{L}\right) \tag{2.51}$$

Applying the following boundary conditions

$$\begin{aligned} n &\longrightarrow 0 \qquad & x &\longrightarrow \infty \\ n &= 0 \qquad & x &= W \end{aligned}$$

The second boundary condition states that all carriers which reach the surface region (x = W) are immediately carried to the surface.

The solution of eq 2.50 is [13]

$$n = \alpha I_0 \frac{\{\exp\left(\frac{W-x}{L}\right)\exp(-\alpha W) - \exp(-\alpha x)\}}{\left(\alpha^2 - \frac{1}{L^2}\right)D} \tag{2.52}$$

Differentiating eq 2.52

$$\frac{dn}{dx} = -\frac{1}{L}\alpha I_0 \frac{\exp\left(\frac{W-x}{L}\right)\exp(-\alpha W)}{\left(\alpha^2 - \frac{1}{L^2}\right)D} + \alpha^2 I_0 \frac{\exp(-\alpha x)}{\left(\alpha^2 - \frac{1}{L^2}\right)D} \tag{2.53}$$

At x = W eq 2.53 becomes

$$\begin{aligned}\left(\frac{dn}{dx}\right)_{x=W} &= -\frac{1}{L}\alpha I_0 \frac{\exp(-\alpha W)}{\left(\alpha^2 - \frac{1}{L^2}\right)D} + \alpha^2 I_0 \frac{\exp(-\alpha W)}{\left(\alpha^2 - \frac{1}{L^2}\right)D} \\ &= \frac{\alpha I_0 \left(\alpha - \frac{1}{L}\right)\exp(-\alpha W)}{\left(\alpha - \frac{1}{L}\right)\left(\alpha + \frac{1}{L}\right)D} \\ &= \frac{\alpha I_0 \exp(-\alpha W)}{\left(\alpha + \frac{1}{L}\right)D} \\ &= \frac{\alpha I_0 L \exp(-\alpha W)}{D(\alpha L + 1)} \end{aligned} \tag{2.54}$$

The diffusion current outside the space-charge layer is therefore given by

$$\begin{aligned} j_{diff} &= -qD\left(\frac{dn}{dx}\right)_{x=W} \\ &= -qD\frac{I_0}{D}\exp(-\alpha W)\frac{1}{1+\frac{1}{\alpha L}} \\ &= -qI_0 \exp(\alpha W)\frac{\alpha L}{\alpha L + 1} \end{aligned} \tag{2.55}$$

Gärtner equation

The total photocurrent is, therefore, the sum of eq 2.48 and 2.55

$$\begin{aligned} j_{photo} &= j_G + j_{diff} \\ &= q\left(I_0 \exp(-\alpha W) - I_0\right) - qI_0 \exp(\alpha W)\frac{\alpha L}{\alpha L + 1} \\ &= qI_0\left(1 - \frac{\alpha L}{1+\alpha L}\right)\exp(-\alpha W) - qI_0 \\ &= qI_0\left(\frac{1+\alpha L - \alpha L}{1+\alpha L}\right)\exp(-\alpha W) - qI_0 \\ &= qI_0\frac{\exp(-\alpha W)}{1+\alpha L} - qI_0 \\ &= -qI_0\left(1 - \frac{\exp(-\alpha W)}{1+\alpha L}\right) \quad \text{for p-type semiconductors} \end{aligned} \tag{2.56}$$

Eq 2.56 is known as the Gärtner equation.

Electron transfer reactions [7, 14, 15]

In the case of semiconductor electrodes, two types of redox reactions are possible; electron and hole transfers

$$O + e_{cb}^{-} \rightleftharpoons R \quad \text{or} \quad O \rightleftharpoons R + h_{vb} \tag{2.57}$$

Fig 2.21 illustrates the anodic and cathodic currents at semiconductor electrodes. It is seen that the Fermi level is split into two energy levels for electrons and holes respectively. The quasi Fermi level describes the occupation of energy levels at non equilibrium conditions.

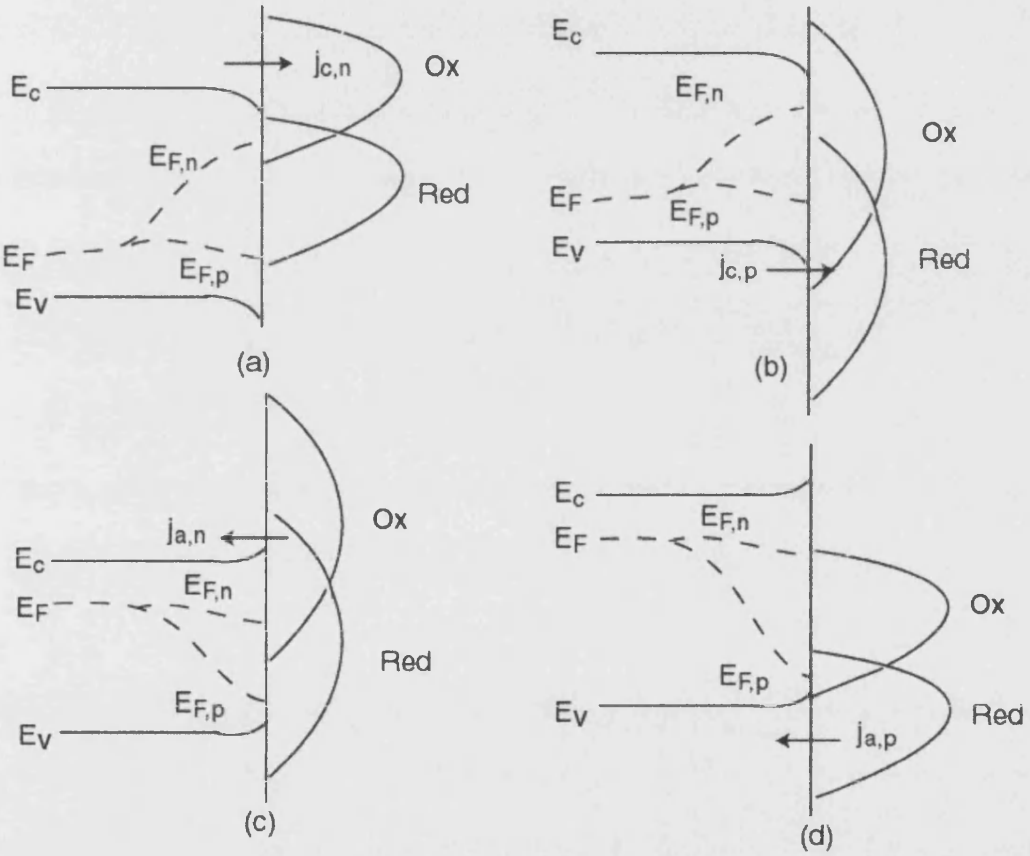

Figure 2.21: Anodic and cathodic currents at semiconductor|electrolyte interface under illumination. Note that $E_{F,n}$ and $E_{F,p}$ are quasi Fermi level for electron and hole, respectively.

The quantitative description of electron transfer at semiconductor electrodes was gen-

eralised by Gerischer [11]. The cathodic current for electron transfer in the conduction band is given by the number of occupied states in semiconductors and the number of unoccupied states of the redox species, and vice versa for anodic current

$$j'_{c,n} = qk_cD_{sc}f(E - E_F)D_{Ox} \quad (2.58)$$

$$j'_{a,n} = qk_aD_{sc}(1 - f(E - E_F))D_{Red} \quad (2.59)$$

Similarly, the cathodic current for hole transfer in the valence band is represented by the number of unoccupied states by holes on semiconductors and the number of occupied states of oxidised species, and vice versa for the anodic current. It is noted that the current flows in the opposite direction as holes are transferred.

$$j'_{c,p} = qk_cD_{sc}f(E - E_F)D_{Ox} \quad (2.60)$$

$$j'_{a,p} = qk_aD_{sc}\{1 - f(E - E_F)\}D_{Red} \quad (2.61)$$

Therefore, the total current density is obtained by integration of those expressions.

$$j_{c,n} = q\int_{-\infty}^{+\infty} k_cD_{sc}f(E - E_F)D_{Ox}dE \quad (2.62)$$

$$j_{a,n} = q\int_{-\infty}^{+\infty} k_aD_{sc}\{1 - f(E - E_F)\}D_{Rcd}dE \quad (2.63)$$

$$j_{c,p} = q\int_{-\infty}^{+\infty} k_cD_{sc}f(E - E_F)D_{Ox}dE \quad (2.64)$$

$$j_{a,p} = q\int_{-\infty}^{+\infty} k_aD_{sc}\{1 - f(E - E_F)\}D_{Red}dE \quad (2.65)$$

2.7 Space charge recombination

Recombination is the process where electrons and holes are destroyed. There are three types of recombination; Hall-Schockley-Read (HSR), radiative and Auger recombinations, as shown in Figure 2.22.

The recombination lifetime is determined by the three mechanisms

$$\frac{1}{\tau_{rec}} = \frac{1}{\tau_{HSR}} + \frac{1}{\tau_{radiative}} + \frac{1}{\tau_{Auger}} \quad (2.66)$$

During HSR recombination, electron hole pairs recombine via recombination center. This process causes a lattice vibration to release the energy. On the other hand, for radiative recombination, electron hole pairs recombine directly from band to band with

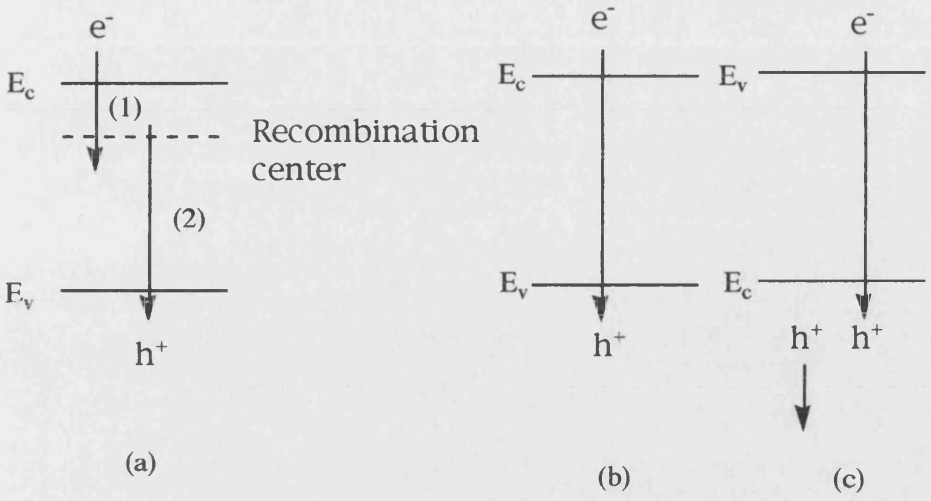

Figure 2.22: 3 types of recombination; (a) Hall-Schockley-Read, (b) radiative and (c) Auger recombination.

the photon emission. During Auger recombination, the recombination energy is absorbed by a third carrier. The general plot of the recombination lifetime of Si is shown in Fig 2.23. At high carrier densities, the lifetime is controlled by Auger recombination, whereas at low carrier densities, it is controlled by HSR. Radiative recombination is not important for Si since silicon is an indirect band gap semiconductor (c.f. GaAs) [18]. We used a low doped Si ($N_A = 1 \times 10^{15}$ cm^{-3}) and therefore Hall-Shockley -Read recombination is dominant.

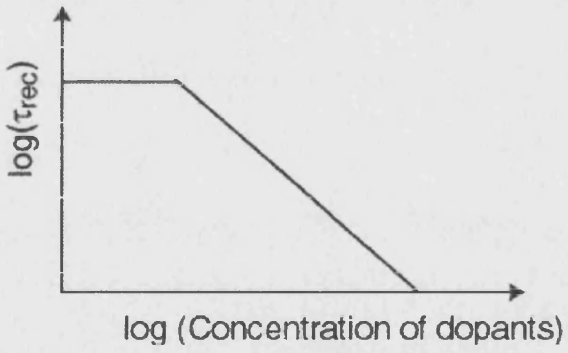

Figure 2.23: Recombination lifetime for Si.

Hall-Shockley-Read statistics [18, 20–22]

Fig 2.24 shows 4 processes of indirect recombination through intermediate states

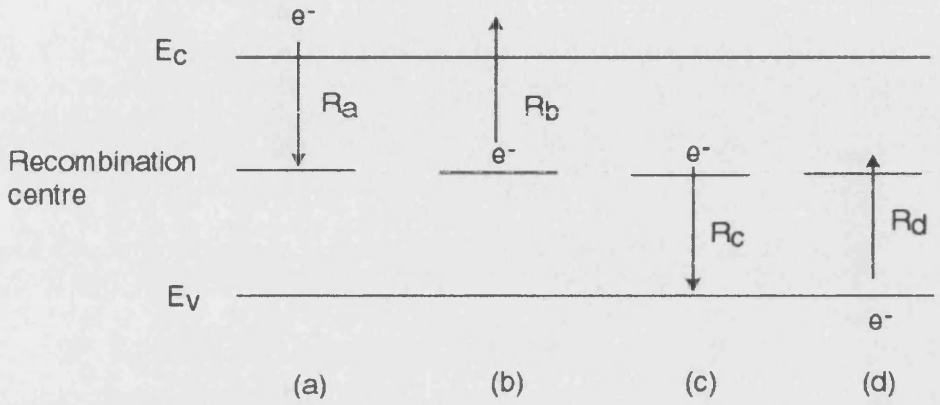

Figure 2.24: Indirect recombination processes (a) electron capture (b) electron emission (c) hole capture and (d) hole emission

The probability for electrons that occupy the state is given by Fermi distribution

$$f(E) = \frac{1}{1 + \exp\left(\frac{E_t - E_F}{k_B T}\right)} \tag{2.67}$$

Here E_t is the energy level of the centre. The rate of electron capture is proportional to the concentration of centres that are not occupied, $N_t(1 - f(E))$.

$$R_a = \nu_{th}\sigma_n n N_t\,(1 - f(E)) \tag{2.68}$$

where ν_{th} is thermal velocity of electrons and σ_n is capture cross section of electrons.

The rate of emission of electrons from the centre is the inverse of the electron capture process. The rate is proportional to the concentration of centers occupied by electrons, $N_t f(E)$, and given by

$$R_b = e_n N_t f(E) \tag{2.69}$$

where e_n is proportionality constant given by

$$e_n = \nu_{th}\sigma_n n_i \exp\left(\frac{E_t - E_i}{k_B T}\right) \tag{2.70}$$

The details are described in Appendix A1.

The rate of hole capture is proportional to the concentration of centers occupied by electrons and the concentration of holes

$$R_c = \nu_{th}\sigma_p p N_t f(E) \tag{2.71}$$

where σ_p is capture cross section of holes

The rate of hole emission is

$$R_d = e_p N_t\,(1 - f(E)) \tag{2.72}$$

where e_p is proportionality constant given by

$$e_p = \nu_{th}\sigma_p n_i \exp\left(\frac{E_i - E_t}{k_B T}\right) \tag{2.73}$$

Details are described in Appendix A1.

The net rate at which electrons are captured from the conduction band is simply the difference between electron capture and emission.

$$\begin{aligned} R_n &= R_a - R_b \\ &= \nu_{th}\sigma_n n N_t\,(1 - f(E)) - e_n N_t f(E) \\ &= \nu_{th}\sigma_n n N_t\,(1 - f(E)) - \nu_{th}\sigma_n n' N_t f(E) \\ &= \nu_{th}\sigma_n N_t\,(n(1 - f(E)) - n' f(E)) \end{aligned} \tag{2.74}$$

where $n' = n_i \exp\left(\frac{E_t - E_i}{k_B T}\right)$

Similarly the net rate at which holes are captured from the valence band is expressed as

$$\begin{aligned} R_p &= R_c - R_d \\ &= \nu_{th}\sigma_p p N_t f(E) - e_p N_t\,(1 - f(E)) \\ &= \nu_{th}\sigma_p N_t\,(p f(E) - p'(1 - f(E))) \end{aligned} \tag{2.75}$$

where $p' = n_i \exp\left(\frac{E_i - E_t}{k_B T}\right)$

If electron-hole pairs are generated at a constant rate, R, the net rate of electron capture is equal to the net rate of hole capture

$$R = R_n = R_p \tag{2.76}$$

$$\nu_{th}\sigma_n N_t\left(n(1-f(E))-n'f(E)\right) = \nu_{th}\sigma_p N_t\left(pf(E)-p'(1-f(E))\right)$$

$$f(E) = \frac{\sigma_n n+\sigma_p p'}{\sigma_n(n+n')+\sigma_p(p+p')} \tag{2.77}$$

Inserting eq 2.77 into eq 2.76

$$\begin{aligned} R &= R_n \\ &= \nu_{th}\sigma_n N_t\left[n\left(1-\frac{\sigma_n n+\sigma_p p'}{\sigma_n(n+n')+\sigma_p(p+p')}\right)-n'\left(\frac{\sigma_n n+\sigma_p p'}{\sigma_n(n+n')+\sigma_p(p+p')}\right)\right] \\ &= \nu_{th}\sigma_n N_t\left[n\left(\frac{\sigma_n n'+\sigma_p p}{\sigma_n(n+n')+\sigma_p(p+p')}\right)-n'\left(\frac{\sigma_n n+\sigma_p p'}{\sigma_n(n+n')+\sigma_p(p+p')}\right)\right] \\ &= \nu_{th}\sigma_n N_t \times \frac{\sigma_p\left(np-n'p'\right)}{\sigma_n(n+n')+\sigma_p(p+p')} \end{aligned} \tag{2.78}$$

since $n'p' = n_i^2$, eq 2.78 can be rewritten as

$$R = \frac{\nu_{th}\sigma_n N_t\sigma_p\left(np-n_i^2\right)}{\sigma_n(n+n')+\sigma_p(p+p')} \tag{2.79}$$

The same answer is obtained if eq 2.77 is inserted to R_p in eq 2.76. We define lifetimes for electron and holes as

$$\tau_n = \frac{1}{\nu_{th}\sigma_n N_t} \tag{2.80}$$

$$\tau_p = \frac{1}{\nu_{th}N_t\sigma_p} \tag{2.81}$$

Eq 2.79 can be rewritten as

$$R = \frac{np-n_i^2}{\tau_p(n+n')+\tau_n(p+p')} \tag{2.82}$$

Dividing eq 2.82 by p

$$R = \frac{n-\frac{n_i^2}{p}}{\tau_p\left(\frac{n}{p}+\frac{n'}{p}\right)+\tau_n\left(1+\frac{p'}{p}\right)} \tag{2.83}$$

If p is greater than n, eq 2.83 can be reduced to

$$\begin{aligned} R &= \frac{n-\frac{n_i^2}{p}}{\tau_n} \\ &= \frac{n-\frac{n_0 p_0}{p}}{\tau_n} \end{aligned} \tag{2.84}$$

Under low injection condition ($p \approx p_0$), the final simplified form is

$$R = \frac{n-n_0}{\tau_n} \tag{2.85}$$

It is noted that eq 2.85 is valid in neutral region as discussed later.

2.8 Theoretical analysis of the semiconductor|electrolyte interface

2.8.1 Numerical analysis

In order to obtain potential distribution, electric field, carrier concentration of electron and holes, current density of electron and holes (6 unknowns), 6 equations are required at least: Poissons equation ($\frac{d^2\phi}{dx^2}$ and $\frac{d\phi}{dx}$), continuity equations for electron and holes and current density equations for electrons and holes. These equations can be expressed in finite difference form.

Finite difference

2nd order derivative can be expressed in finite difference form

$$\frac{d^2f(x)}{dx^2} = \frac{df(x)^+ - df(x)^-}{dx} \tag{2.86}$$

where $\frac{df(x)^+}{dx} = \frac{f(x+dx)-f(x)}{dx}$

$\frac{df(x)^-}{dx} = \frac{f(x)-f(x-dx)}{dx}$

Hence eq 2.86 becomes

$$\begin{aligned}\frac{d^2f(x)}{dx^2} &= \frac{\frac{f(x+dx)-f(x)}{dx} - \frac{f(x)-f(x-dx)}{dx}}{dx} \\ &= \frac{f(x+dx) - 2f(x) + f(x-dx)}{dx}\end{aligned} \tag{2.87}$$

Eq 2.87 can be applied to Poisson's equation

$$\frac{\phi_{i+1} - 2\phi_i + \phi_{i-1}}{dx^2} = \frac{\rho(x)}{\varepsilon_0\varepsilon_r} \tag{2.88}$$

Similarly, the current density and continuity equations can be expressed in finite difference form

$$j_n = q\mu_n n\frac{\phi(x+dx)-\phi(x)}{dx} + qD_n\frac{n(x+dx)-n(x)}{dx} \quad \text{for electrons} \tag{2.89}$$

$$j_p = q\mu_p p\frac{\phi(x+dx)-\phi(x)}{dx} - qD_n\frac{n(x+dx)-n(x)}{dx} \quad \text{for holes} \tag{2.90}$$

$$-\frac{1}{q}\frac{j_n(x+dx)-j_n(x)}{dx} = \alpha I_0\exp(-\alpha x) - \frac{np-n_i^2}{\tau_p(n+n_i)+\tau_n(p+n_i)} \quad \text{for electrons} \tag{2.91}$$

$$\frac{1}{q}\frac{j_p(x+dx)-j_p(x)}{dx} = \alpha I_0\exp(-\alpha x) - \frac{np-n_i^2}{\tau_p(n+n_i)+\tau_n(p+n_i)} \quad \text{for holes} \tag{2.92}$$

Newton's method

The above equations can be iterated, applying 1st order Taylor expansion

$$f(x) = f(x_0) + f'(x_0)(x - x_0) \tag{2.93}$$

Eq 2.93 can be solved for x

$$x = x_0 - \frac{f(x_0)}{f'(x_0)} \tag{2.94}$$

Eq 2.94 can be rewritten as an iteration formula, and the graphical representation of Newton's method is shown in Fig 2.25

$$x_{n+1} = x_n - \frac{f(x_n)}{f'(x_n)} \tag{2.95}$$

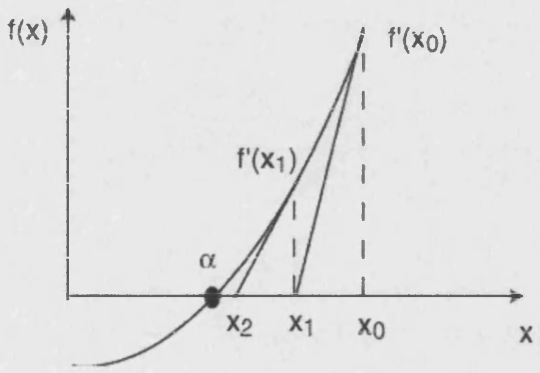

Figure 2.25: Graphical representation of Newton's method.

The initial guess starts at $x = x_0$ and tangent line can be drawn at $(x_0, f(x_0))$. The intercept with x axis is $x = x_1$. The tangent line can be drawn at $(x_1, f(x_1))$ and etc. This process is repeated until the approximation is within the error limit. Newton's method was used to improve the initial guess, and the solution of the above 6 equations are achieved by applying Gaussian elimination.

Gaussian elimination

It is quite hard to solve non-linear systems of equations, while linear systems are quite easy to study. There are numerical techniques which approximate nonlinear systems

with linear ones and it is assumed that the solutions of the linear systems are close enough to the solutions of the nonlinear systems.

For a simple case, 3 × 3 matrix is considered as an example

$$\begin{vmatrix} 1 & 1 & 1 \\ 1 & -2 & 2 \\ 1 & 2 & -1 \end{vmatrix} \begin{vmatrix} x \\ y \\ z \end{vmatrix} = \begin{vmatrix} 0 \\ 4 \\ 2 \end{vmatrix} \tag{2.96}$$

The idea is to keep the first equation and work on the last two. In doing that, one of the unknowns is eliminated and the other two can be solved.

Subtracting the first one from the last one, eq 2.96 becomes

$$\begin{vmatrix} 1 & 1 & 1 \\ 1 & -2 & 2 \\ 0 & 1 & -2 \end{vmatrix} \begin{vmatrix} x \\ y \\ z \end{vmatrix} = \begin{vmatrix} 0 \\ 4 \\ 2 \end{vmatrix} \tag{2.97}$$

Eliminating x via subtracting the first from the second, eq 2.97 becomes

$$\begin{vmatrix} 1 & 1 & 1 \\ 0 & -3 & 1 \\ 0 & 1 & -2 \end{vmatrix} \begin{vmatrix} x \\ y \\ z \end{vmatrix} = \begin{vmatrix} 0 \\ 4 \\ 2 \end{vmatrix} \tag{2.98}$$

From the second and the third equation, the same procedure is repeated, and one of the two unknowns (y or z) can be eliminated.

Adding the second to the third after multiplying it by 3, eq 2.98 becomes

$$\begin{vmatrix} 1 & 1 & 1 \\ 0 & -3 & 1 \\ 0 & 0 & -5 \end{vmatrix} \begin{vmatrix} x \\ y \\ z \end{vmatrix} = \begin{vmatrix} 0 \\ 4 \\ 10 \end{vmatrix} \tag{2.99}$$

Hence, z = -2 from the third equation, y = -2 from the second equation, and x = 4 from the first equation are obtained.

These equations (Poisson's equation, continuity equations, and current density equations) were self-consistently solved by applying the relaxation method (Finite difference method, Newton's method, and Gaussian elimination) that employs the initial guesses (I_0 = 0 and V = 0) and iterates to improve the approximation. The solution

of these equations gives the potential distribution and quasi Fermi level, which can be used to find the carrier concentrations.

$$n = N_C \exp\left(-\frac{E_C - E_{F,n}}{k_B T}\right) \tag{2.100}$$

$$p = N_V \exp\left(-\frac{E_{F,p} - E_V}{k_B T}\right) \tag{2.101}$$

2.8.2 Carrier concentration profile

The semiconductor electrodes possess a sum of charge density in the space charge layer, Q_{sc} associated with ionised acceptor atoms, charge density due to the surface state, Q_{ss}, and charge density due to excess carriers under illumination, Q_{excess}. In order to maintain electrical neutrality, the charge on the electrode must be matched in solution by opposite charge, Q_{sol}, as shown in Fig 2.26 .

$$Q_{sc} + Q_{ss} + Q_{excess} = -Q_{sol} \tag{2.102}$$

Figure 2.26: Charge neutrality at semiconductor|electrolyte interface.

The concentrations of majority and minority carriers were calculated, taking into account Hall-Schockley-Read (HSR) recombination (see from eq 2.89 to eq 2.92). In the Gärtner model, all electrons are transferred to the electrolyte, whereas in the HSR model, electrons are either transferred to the electrolyte or recombine with holes. Calculations were performed for p-Si using values of the doping density and minority carrier lifetimes that are relevant to our experiment. Fig 2.27 illustrates the carrier concentrations in the dark and under illumination. The program was written by M. Cass [16].

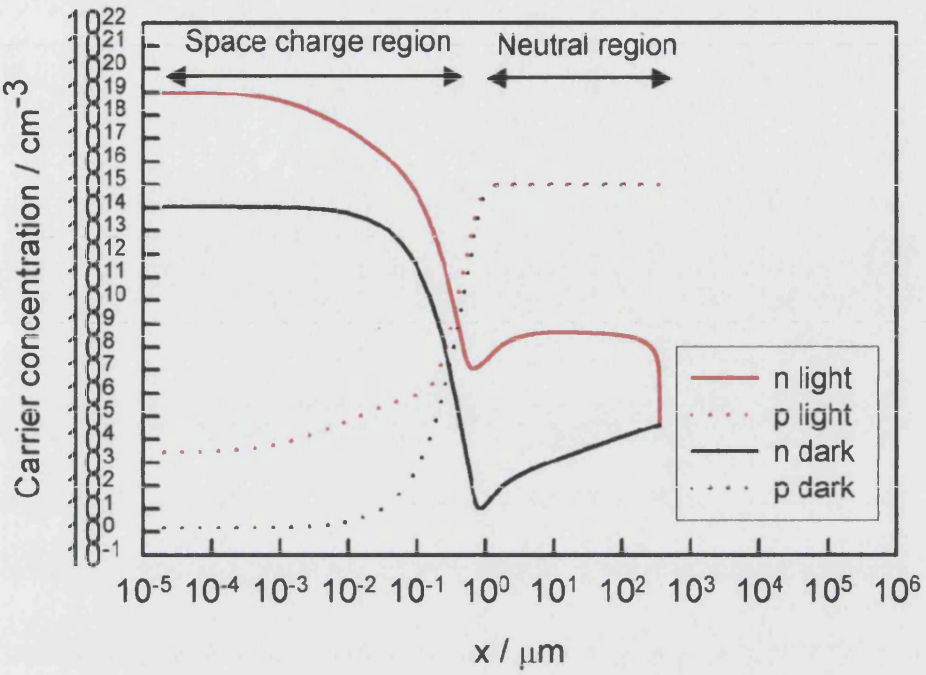

Figure 2.27: Carrier concentration profiles for p-Si in the dark and under illumination ($I_0 = 10^{14}$ $cm^{-2}s^{-1}$) at E – E_{fb} = -0.76 V.

The parameters for the simulation were

$N_c = 2.8 \times 10^{19}$ cm^{-3}

$N_V = 1.0 \times 10^{19}$ cm^{-3}

Band gap = 1.12 eV

$N_A = 1.0 \times 10^{15}$ cm^{-3}

Schottky barrier height = 0.5 eV

electron lifetime = 1×10^{-4} s

hole lifetime = 1×10^{-4} s

Electron mobility = 1350 $cm^2V^{-1}s^{-1}$

Hole mobility = 480 $cm^2V^{-1}s^{-1}$

Effective mass of electron = $1.02m_0$

Effective mass of hole = $0.52m_0$

Absorption coefficient = 4420 cm^{-1} at λ = 626 nm

Interfacial transfer velocity = 1×10^{-5} $cm\,s^{-1}$

The concentration of majority carriers is much greater than that of minority carriers in the dark. For example, for p-type Si with a doping density of 1×10^{15} cm^{-3}

$$\begin{aligned} n &= \frac{N_C N_V}{p} \exp\left(-\frac{E_c - E_v}{k_B T}\right) \\ &= \frac{2.8 \times 10^{19} \times 1.04 \times 10^{19}}{1 \times 10^{15}} \exp\left(-\frac{1.12}{0.026}\right) \\ &= 5.703 \times 10^4 cm^{-3} \end{aligned}$$

It is seen from Fig 2.27 that the concentration of holes is much greater than that of electrons in the neutral region ($x > W$). In this region the recombination rate can be expressed as pseudo 1st order

$$\begin{aligned} \frac{dn}{dt} &= -knp \\ &= -k'n \end{aligned} \tag{2.103}$$

where $k' = kp$

The solution of eq 2.103 is obtained by integration

$$n(t) = -n(0) \exp\left(\frac{t}{\tau_n}\right) \tag{2.104}$$

where τ_n is the electron lifetime in the bulk, given by

$$\tau_n = \frac{1}{k'} \tag{2.105}$$

On the other hand, the concentration of electrons is greater than that of holes in the space charge region ($x < W$), and recombination is no longer 1st order.

The excess carrier concentration is the difference between the carrier concentration under illumination and in the dark

$$\Delta n = n_{light} - n_{dark} \tag{2.106}$$

$$\Delta p = p_{light} - p_{dark} \tag{2.107}$$

Fig 2.28 shows the calculated excess carrier concentration profile for 3 light intensities (incident photon flux = 10^{13}, 10^{14}, and 10^{15} $cm^{-2}s^{-1}$ at $E - E_{fb}$ = -0.76 V).

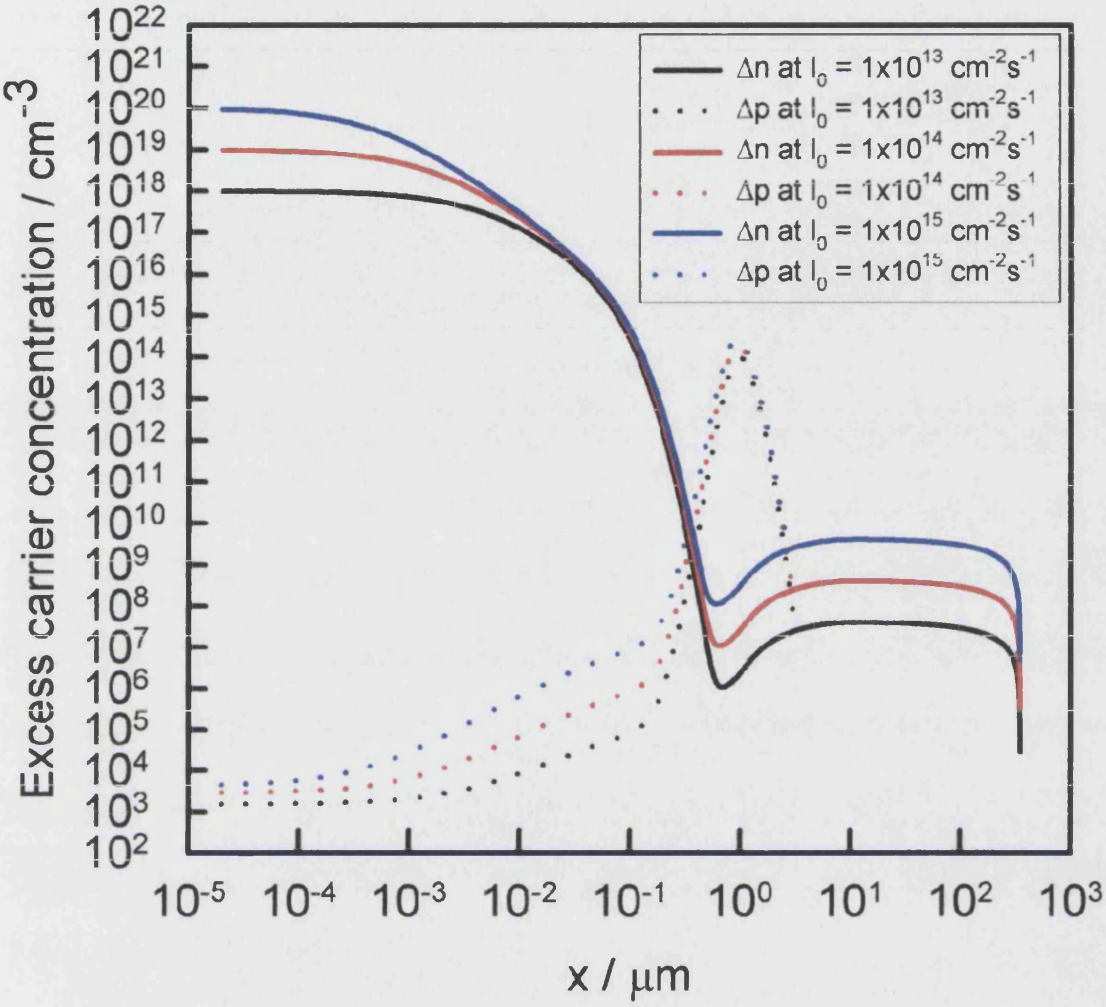

Figure 2.28: Light intensity dependence of excess carrier concentration profiles for p-Si at $E - E_{fb}$ = -0.76 V.

It is seen that the excess carrier concentrations of electrons and holes increases with increasing light intensity as expected. Fig 2.29 illustrates the generation profile of electrons at several light intensity, and shows that an intense illumination produces more minority carriers. Hence the excess carrier concentrations are increased with increasing the light intensity.

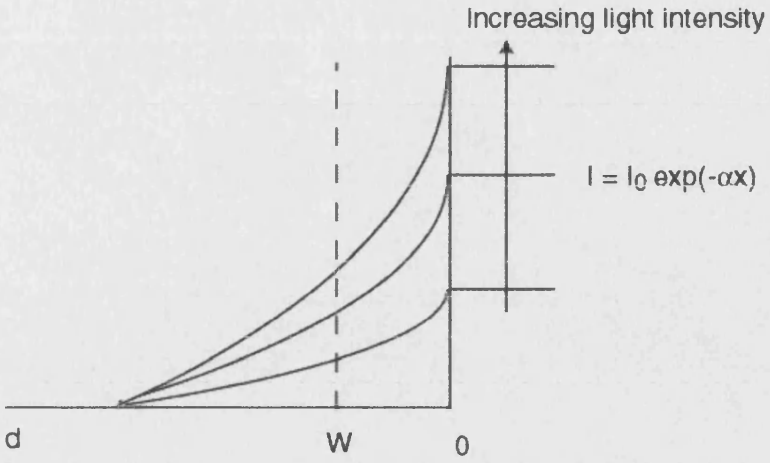

Figure 2.29: Generation profile at different light intensity.

The excess carrier concentration profiles at several potentials are shown in Fig 2.31. As the potential increases, the space charge width also increases and collects more electrons, whereas the concentration of holes decreases as increasing the space charge width as shown in Fig 2.30. It is noted that under depletion condition for p-type semiconductors, electrons move to the surface whereas holes move away from the surface.

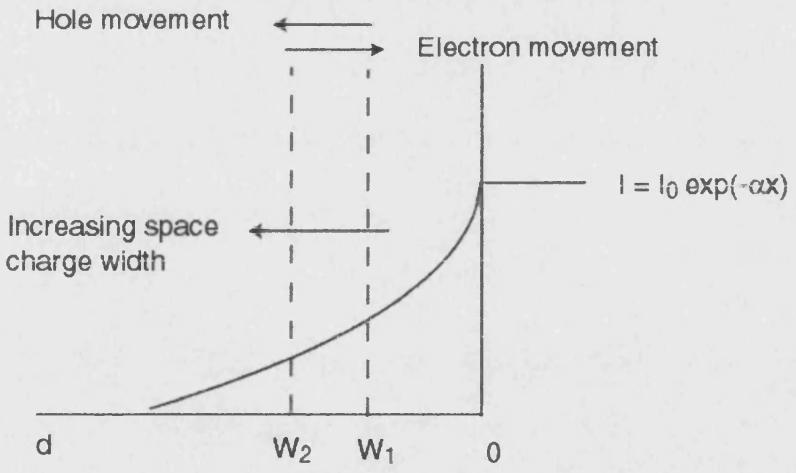

Figure 2.30: Generation profile at different potential.

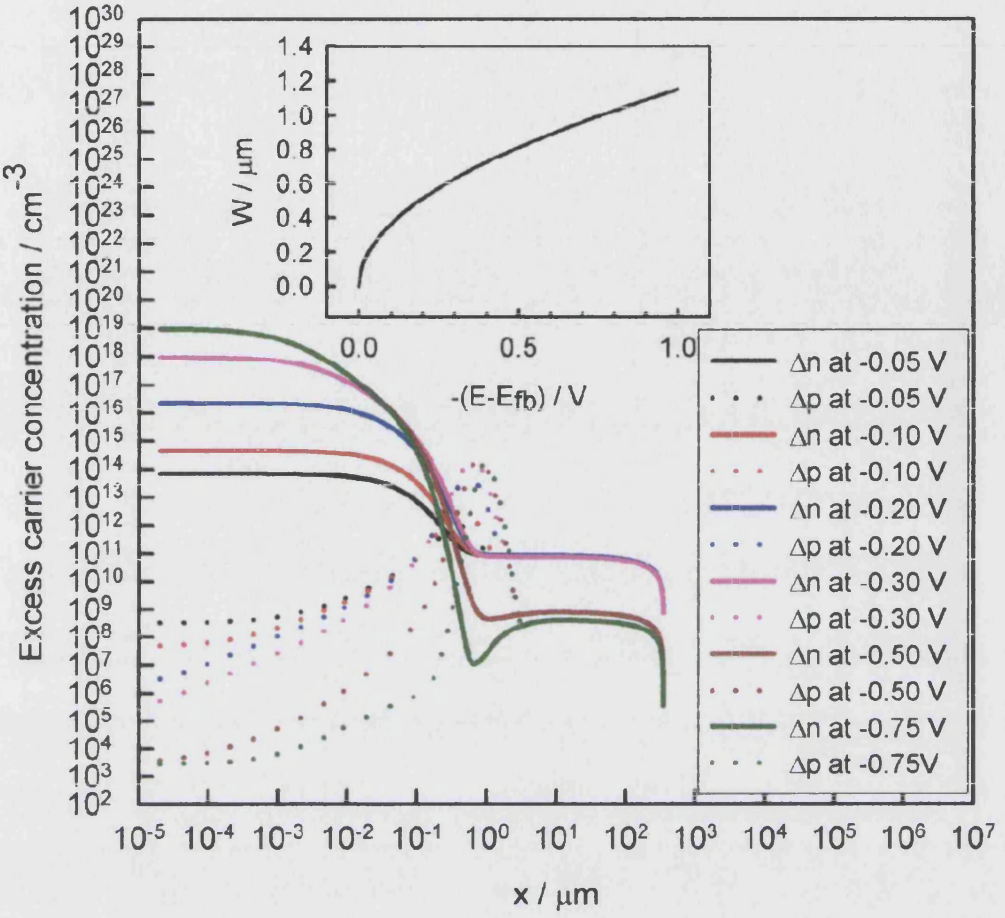

Figure 2.31: Potential dependent excess carrier concentration profiles for p-Si at I_0 = 1×10^{14} $cm^{-2}s^{-1}$. The inset shows the potential dependent space charge width. It is noted that the potential shown on the graph is the overpotential, i.e $E - E_{fb}$.

It is shown that a large concentration of electrons is accumulated at the surface if electron transfer is slow. The normalised excess carrier distribution was obtained by the ratio of integration from the surface to x and the integration from the surface to the sample thickness.

$$\text{Normalised } \Delta n = \frac{\int_0^x \Delta n(x)dx}{\int_0^d \Delta n(x)dx} \tag{2.108}$$

The normalised concentration of excess electrons is plotted in Fig 2.32. It is noted that the data is from Fig 2.31. The integrated values are proportional to the charge (or conductivity). Fig 2.32 shows that 70 - 80 % of electrons are located within 1 nm thickness from the surface. Therefore we can consider that the charge is essentially

surface charge.

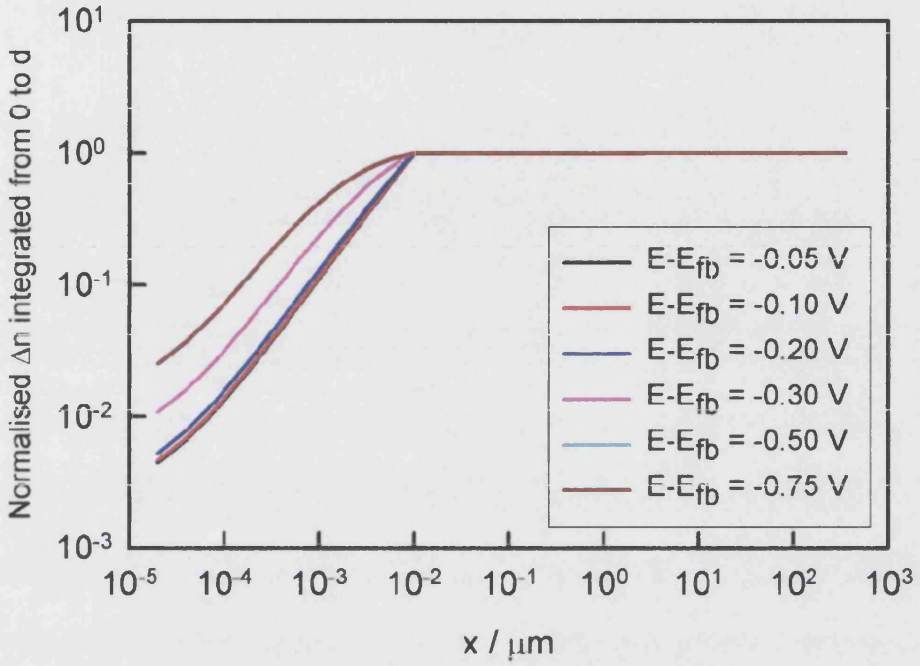

Figure 2.32: Normalised concentration of excess electrons. Data is based on Fig 2.31.

The calculated photocurrent-voltage curve which takes into account Hall-Schockley-Read (HSR) recombination at $I_0 = 10^{14}$ $cm^{-2}s^{-1}$ with $\tau_n = 1 \times 10^{-4}$ s and $k = 1 \times 10^{-5}$ $cm\,s^{-1}$ is shown in Fig 2.33. The normalised Gärtner plot under the same condition is also shown as a comparison. It is seen that the Gärtner plot is almost constant over the potential, whereas the photocurrent-voltage curve taken into account HSR recombination shows an onset region. This means that the reduction of the photocurrent is due to recombination, and the photocurrent can be generally expressed as

$$j_{photo} = j_{Gärtner} - j_{HSR} \tag{2.109}$$

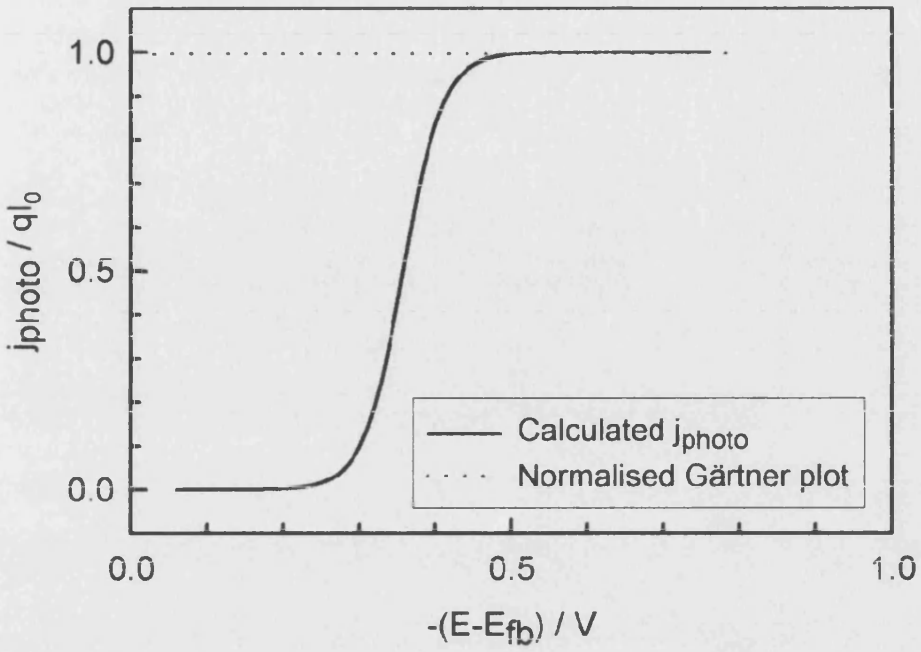

Figure 2.33: Calculated photocurrent-voltage curve at $I_0 = 10^{14}$ $cm^{-2}s^{-1}$ with $\tau_n = 1 \times 10^{-4}$ s and $k = 1 \times 10^{-5}$ $cm\,s^{-1}$.

The effect of the light intensity on the photocurrent-voltage plot in the case of $\tau_n = 1 \times 10^{-7}$ s is shown in Fig 2.34. In this case, the normalised photocurrent is less than unity. It is seen that the curve shifts to the left as increasing the light intensity. Initially we looked at the intensity dependence of photocurrent-voltage curve for $\tau_n = 1 \times 10^{-4}$ s, which does not show the shift at all. This result puzzles us since we observed experimentally the shift of the photocurrent-voltage curve with increasing the light intensity due to the change of Fermi level (cf experimental result in Fig 7.3). The reason for this is not clear at present but it could be said that the shift of the photocurrent-voltage curve arises from the HSR recombination, which changes the potential distribution of Si.

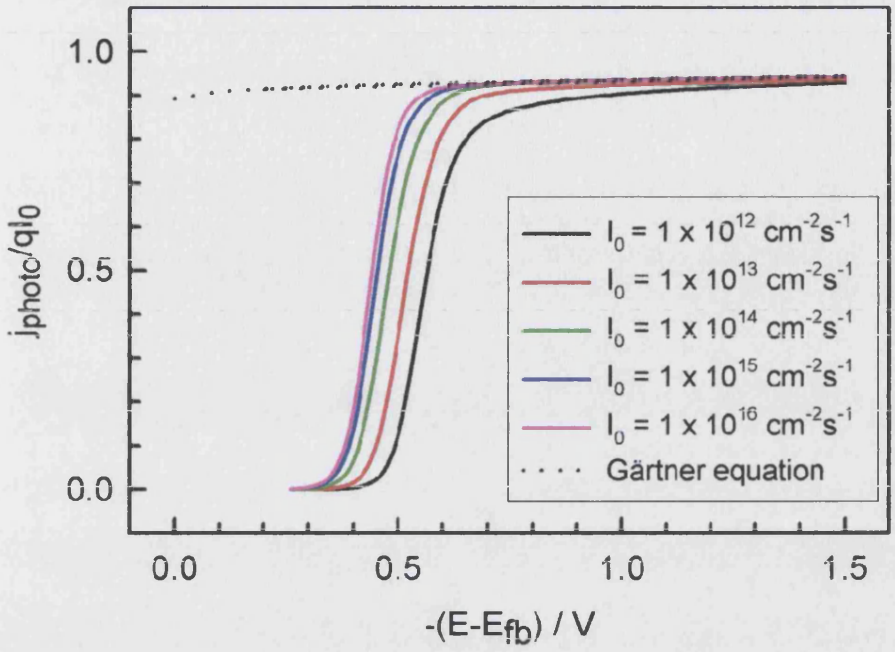

Figure 2.34: Effect of the light intensity on photocurrent-voltage curve in the case of $\tau_n = 1 \times 10^{-7}$ s, and $k_{tr} = 1 \times 10^{-5}$ cm s^{-1}.

Fig 2.35 shows the effect of the rate constant of the charge transfer under the same light intensity and lifetimes. As the rate constant is increased, the photocurrent-voltage curves shift to the left. It can be said that the system becomes ideal, i.e. approach the Gärtner model where the electron transfer rate is high. In the Gärtner model, electrons are immediately transferred to the interface and contribute to the photocurrent. In the HSR model, increasing the rate constant means that electrons are transferred through the interface rather than recombining with holes. Fig 2.36 shows the effect of charge transfer rate constant on the excess carrier profile at $E-E_{fb} = -0.8$ V. It is seen that electrons are accumulatedless with increasing the k_{tr}.

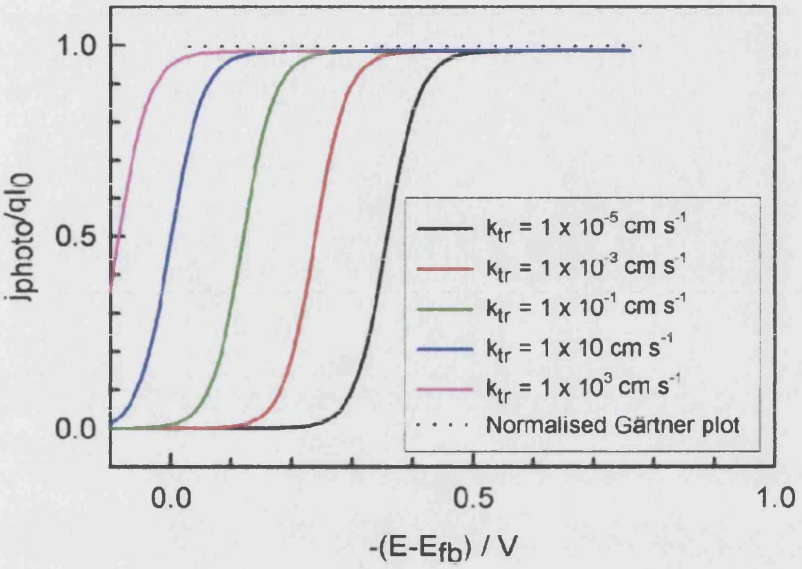

Figure 2.35: Effect of the charge transfer rate constant on the photocurrent-voltage curve. ($I_0 = 1 \times 10^{14}$ $cm^{-2}s^{-1}$ and $\tau_n = 1 \times 10^{-4}$ s^{-1}). Note that all plots approach the Gärtner limit at high band bending.

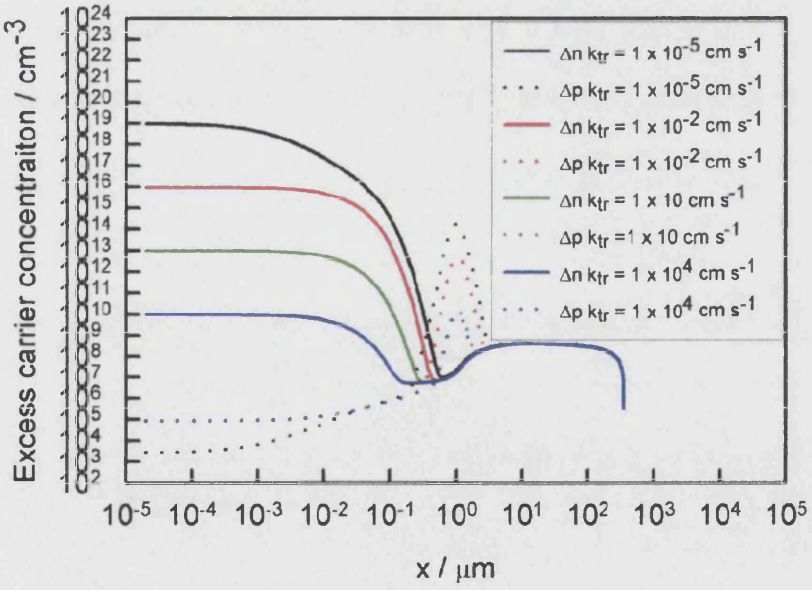

Figure 2.36: Effect of charge transfer rate constant on excess carrier concentration profiles at $E\text{-}E_{fb}$ = -0.8 V under the same illumination ($I_0 = 1 \times 10^{14}$ $cm^{-2}s^{-1}$).

Heterogeneous rate constants

An outer sphere redox reaction can be expressed as

$$Ox + ne \longrightarrow Red$$

The rate of first order heterogeneous reaction at a metal electrode is given by the flux, J

$$J = k_1[Ox] \tag{2.110}$$

It is noted that the units of k_1 are $cm\,s^{-1}$ since J is in $mol\,cm^{-2}s^{-1}$, and [Ox] is in $mol\,cm^{-3}$. For metal electrodes, electron transfer takes place at energy levels close to the Fermi level and the concentration of electrons is assumed to be large and constant. On the other hand, a redox reaction at p-type semiconductor electrodes under illumination can be expressed as

$$h\nu \longrightarrow e + h$$

$$Ox + ne \longrightarrow Red$$

In this case, the concentration of electrons depends on the light intensity and is variable. Hence we are dealing with a second order heterogeneous reaction.

$$J = k_1 n[Ox] \tag{2.111}$$

It is noted that units of k_1 are cm^4s^{-1} if J is in $cm^{-2}s^{-1}$, n is in cm^{-3} and [Ox] is in cm^{-3}. If [Ox] is constant, eq 2.111 can be expressed as pseudo first order

$$J = k_2 n \tag{2.112}$$

where $k_2 = k_1[Ox]$

The units of k_2 are $cm\,s^{-1}$ since k_1 is in cm^4s^{-1} and [Ox] is in cm^{-3}. The flux can be expressed in terms of concentration of electrons per unit area (cm^{-2})

$$J = k_3 n_{surf} \tag{2.113}$$

where n_{surf} is given by

$$n_{surf} = n \times \delta \tag{2.114}$$

where δ is a reaction length determined by the tunnelling distance as shown in Fig 2.37

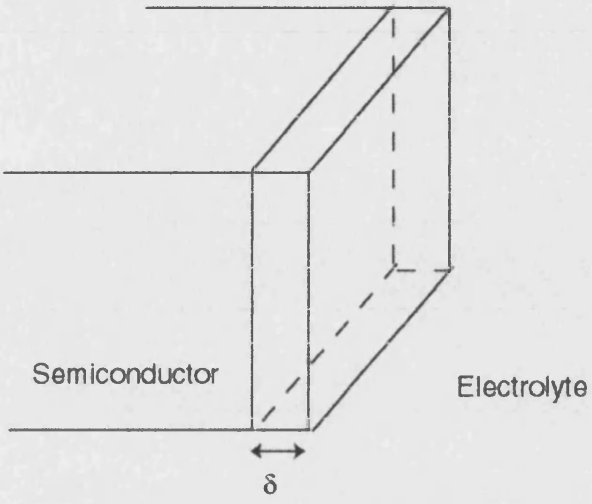

Figure 2.37: Reaction length at semiconductor|electrolyte interface.

From eq 2.112 and eq 2.113

$$\begin{aligned} J = k_2 \times n &= k_3 \times \delta \times n \\ k_2 &= k_3 \times \delta \end{aligned} \tag{2.115}$$

Lewis and coworkers [41–45] have argued that the upper limit to the second order heterogeneous rate constant of outer sphere redox reactions taking place at semiconductor electrodes is around 1×10^{-17} $cm^4 s^{-1}$. These authors expressed the rate constant for semiconductors as

$$k_{tr} = \nu \left[2\pi (r_A + r_e) \frac{1}{\sqrt[3]{\beta}} \right] \exp\left(\frac{-(\lambda_{re} + \Delta G)^2}{4\lambda_{re} k_B T} \right) \tag{2.116}$$

where ν is vibrational frequency for the charge transfer reaction, r_A is effective radius of the acceptor, r_e is effective radius of the electron in the semiconductor, λ_{re} is reorganisation energy of reactant near the surface of the semiconductor, ΔG is driving force for the interfacial charge transfer reaction, and β is an attenuation factor.

Estimating that $r_A = 3 \times 10^{-8}$ cm

$r_e = 1 \times 10^{-7}$ cm

$\nu = 1 \times 10^{13}$ s^{-1}

$\beta = 1 \times 10^{18}$ cm^{-1}

$$\exp\left(\frac{-(\lambda_{re}+\Delta G)^2}{4\lambda_{re}k_BT}\right) = 1 \text{ for optimal driving force}$$

the rate constant is

$$\begin{aligned} k_{tr} &= 1 \times 10^{13}\left[2\pi(3 \times 10^{-8} + 1 \times 10^{-7})\frac{1}{\sqrt[3]{1 \times 10^{18}}}\right] \\ &= 8.17 \times 10^{-18}\ \text{cm}^4\text{s}^{-1} \end{aligned} \tag{2.117}$$

In the case of [Ox] = 10 mM = 6×10^{18} cm^{-3}

$$\begin{aligned} k_2 &= 1 \times 10^{-17} \times 6 \times 10^{18} \\ &= 60\ \text{cm}\,\text{s}^{-1} \end{aligned} \tag{2.118}$$

The corresponding first order rate constant for a tunnelling distance of 1.5 nm is

$$\begin{aligned} k_3 &= \frac{k_2}{\delta} \\ &= \frac{60}{1.5 \times 10^{-7}} \\ &= 4 \times 10^8\ \text{s}^{-1} \end{aligned} \tag{2.119}$$

References

[1] Kittel, C. Introduction to solid state Physics, 7th edition, John Wiley, New York, 1996.

[2] Parker, G. Introductory semiconductor device physics, Prentice Hall, New York, 1994.

[3] Morrison, S. R. Electrochemistry at semiconductor and oxidised metal electrodes, Premium press, London, 1980.

[4] Marcus, R. A. Journal of Chemical Physics **1956**, 24, 966-978.

[5] Bockris, J. O'M; Reddy, A. K. V.; Gamboa-Aldeco, M. Modern Electrochemistry, volume 2A, Kluwer Academic/Plenum, New York, 2000.

[6] Hibbert, D. B. Introduction to electrochemistry Macmillan, London, 1993.

[7] Peter, L. M. in Porous silicon science and technology, Springer-Verlag, 1995.

[8] Nozik, A. J.; Memming, R. Journal of Physical chemistry, **1996**, 100, 13061-13078.

[9] Gärtner, W. W. Physical Review, **1959**, 116, 84-87.

[10] Butler, M. A. Journal of Applied Physics, **1977**, 48,1914-1920.

[11] Gerischer, H. Advances in electrochemistry and electrochemical engineering, vol. 1. John Wiley, New York. 1961.

[12] Schmickler, W. Interfacial electrochemistry, Oxford University Press, Oxford, 1996.

[13] Hamnet, A. in Comprehensive Chemical kinetics, Vol. 27, p.242, Elsevier, New York, 1987.

[14] Gerischer, H. in Advances in electrochemistry and electrochemical engineering, vol. 1, Interscience, 1961.

[15] Sato, N. Electrochemistry at metal and semiconductor electrodes, Elsevier, New York, 1998.

[16] Cass, M.; Duffy, N. W.; Pennock, S. R.; Peter, L. M.; Ushiroda, S.; Walker, A. Journal of Electroanalytical Chemistry, 2002 in press.

[17] Southampton Electrochemistry group, Instrumental methods in electrochemistry, Horwood, Chichester, 2001.

[18] Sze, S. M. Semiconductor devices: Physics and technology, John Wiley, New York, 1985.

[19] Sze, S. M. Physics of semiconductor devices, 2nd ed, John Wiley, New York, 1981.

[20] McKelvey, J. P. Solid state and semiconductor physics, Harper, New York, 1966.

[21] Bube, R. H. Photoconductivity of solids, John Wiley, New York, 1960.

[22] Fehrenbruch, A. L.; Bube, R. H. Fundamentals of solar cells, Academic press, New York, 1982.

[23] Parker, G. Introductory Semiconductor Physics Prentice Hall, New York, 1994.

[24] Streetman, B. G. Solid state electronic devices, 4th edition, Prentice-Hall, New Jersey, 1995.

[25] Chapra, S. C.; Canale, R. P. Numerical methods for engineers, 3rd ed., Mc-Graw Hill, New York, 1998.

[26] Burden, R. L.; Fairs, J. D. Numerical analysis, 7th ed., Books/cole, 2001.

[27] Rutishauser, H. Lectures on numerical mathematics, Birkhäuser, Berlin, 1990.

[28] De Vahl Davis, G. Numerical methods in engineers and science, Allen & Unwin, London, 1986.

[29] Shriver, D. F.; Atkins, P. W.; Langford, C. H. Inorganic chemistry, 2nd edition, Oxford university press, Oxford, 1994.

[30] Owen, S.; Brooker, A. T. A guide to modern inorganic chemistry, Longman, 1991.

[31] Purcell, K. F.; Kotz, J. C. Inorganic chemistry, W. B. Saunders, London, 1977.

[32] Atkins, P. W. Physical chemistry, 5th edition, Oxford university press, Oxford, 1994.

[33] Atkins, P. W.; Beran, J. A. General chemistry, 2nd edition, Scientific american books, New York, 1992.

[34] Bard, A. J.; Faulkner, L. R. Electrochemical methods, John Wiley, New York, 1980.

[35] Pierret, R. F. Semiconductor fundamentals, 2nd edition, Addison-Wesley publishing, Reading, 1989.

[36] Pierret, R. F. Modular series on solid state devices, Addison-Wesley publishing, Reading, 1987.

[37] Brett, C. M. A.; Brett, A. M. O. Electrochemistry, Oxford science publications, Oxford, 1993.

[38] West, A. R. Basic solid state chemistry, John Wiley, New York, 1984.

[39] Mahajan, S.; Harsha, K. S. S. Principles of growth and processing of semiconductors, McGraw-Hill, London, 1999.

[40] Fisher, A. C. Electrode dynamics, Oxford science, Oxford, 1996.

[41] Lewis, N. S. Solar Energy Materials and Solar Cells **1995**, 38, 323-325.

[42] Pomykal, K. E.; Fajardo, A. M.; Lewis, N. S. Journal of Physical Chemistry **1996**, 100, 3652-3664.

[43] Fajardo, A. M.; Lewis, N. S. Journal of Physical Chemistry B **1997**, 101, 11136-11151.

[44] Pomykal, K. E.; Lewis, N. S. Journal of Physical Chemistry B **1997**, 101, 2476-2484.

[45] Lewis, N. S. Journal of Physical Chemistry B **1998**, 102, 4843-4855.

Chapter 3

Fundamental aspects of microwaves

3.1 Introduction

Electromagnetic waves in frequency above 300 MHz and below 300 GHz are referred to as microwaves, and the electromagnetic spectrum is shown below

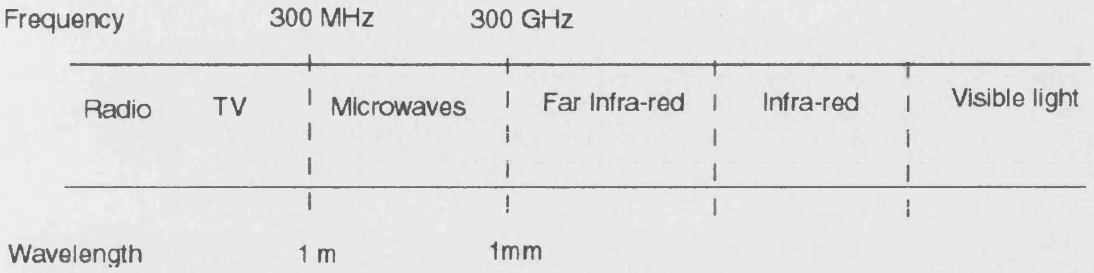

Figure 3.1: Electromagnetic spectrum

Band	Frequency / MHz
HF	3-30
VHF	30-300
UHF	300-1000
L	1000-2000
S	2000-4000
C	4000-8000
X	8000-12000
Ku	12000-18000
K	18000-27000
Ka	27000-40000
Millimeter	40000-300000

Table 3.1: Bands specification in microwaves.

The microwave reflectivity method is relatively new approach in electrochemistry and each microwave component needs to be considered.

3.2 Microwave components

The experimental set-up for a Ka band microwave system is shown below

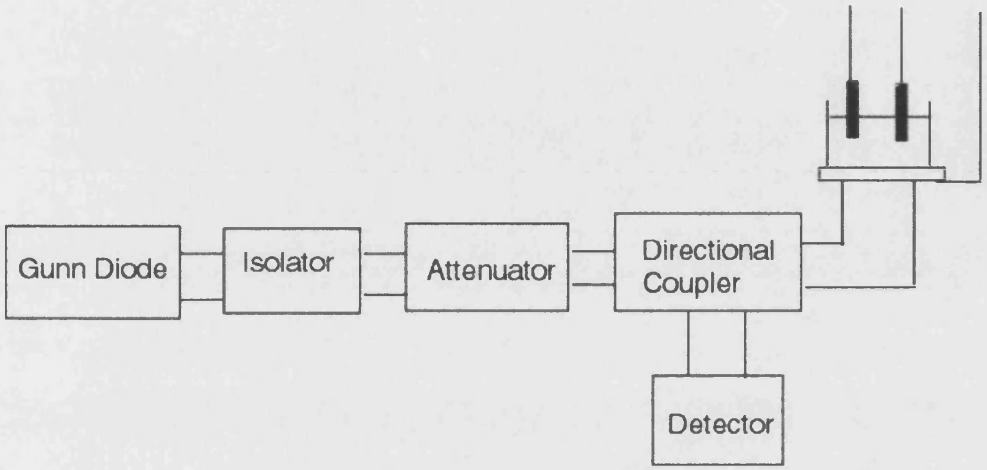

Figure 3.2: Microwave set-up

Microwaves generated by Gunn diode are directed to the sample, which is mounted at the end of the waveguide, and the reflected microwave is directed to the detector via directional coupler. In this setup, the reflected microwave power is detected. Each microwave component is described in the next section.

3.2.1 Gunn diode

The Gunn diode is a transferred electron device that provides negative resistance, and is used as a microwave oscillator. In negative resistance devices, there is a certain range of applied potential in which the current decreases with increasing potential, as shown in Fig 3.3 (a), and the Gunn diode is composed of GaAs and the schematic diagram is shown in Fig 3.3 (b).

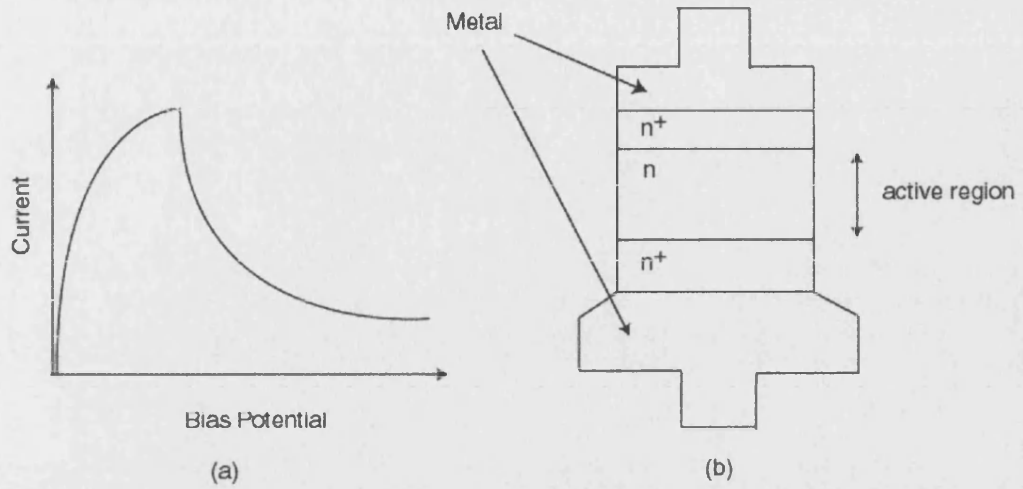

Figure 3.3: (a) I-V characteristic for a negative resistance device. (b) Schematic diagram of a Gunn diode. Note that n^+ is heavily doped n-type GaAs and n is n-type GaAs.

When a dc voltage is applied to the diode, electrons flow from one side of n^+ to the other side via the active region due to the electric field. This current flows causes the periodic fluctuation of electrons, which produces microwaves with an operating frequency that is given by

$$f_0 = \frac{\nu_d}{l}$$

where ν_d is a velocity of majority carrier in $cm\,s^{-1}$ and l is a length of active region in cm. It is noted that the length of the active region controls the operating frequency and for example, the length of active region for 33 GHz microwaves is

$$\begin{aligned} l &= \frac{10^7}{33 \times 10^9} \\ &= 3 \times 10^{-4} \text{ cm} \end{aligned}$$

3.2.2 Crystal detector

A microwave detector rectifies the received signal and produce a current. It consists of a fine tungsten wire which is pointed and brought in contact with a semi-

conductor such as silicon or germanium. Fig 3.4 represents a schematic diagram of a crystal detector.

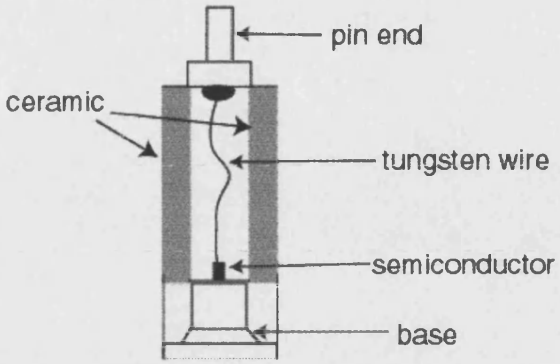

Figure 3.4: Schematic diagram of a microwave detector.

The tungsten wire is soldered to a stud connected to the pin. The crystal shell is usually low loss ceramic. The semiconductor is soldered to a brass screw base. The current-voltage relationship for a diode is expressed as

$$i = I_s\left(\exp\left(\frac{qv}{k_BT}\right) - 1\right) \tag{3.1}$$

Using Taylor expansion, eq 3.1 becomes

$$i = I_s\left[\frac{qv}{k_BT} + \frac{1}{2!}\left(\frac{qv}{k_BT}\right)^2 + \frac{1}{3!}\left(\frac{qv}{k_BT}\right)^3 + \cdots\right] \tag{3.2}$$

For a small signal, eq 3.3 can be approximated to

$$i \approx I_s\left[\frac{qv}{k_BT} + \frac{1}{2!}\left(\frac{qv}{k_BT}\right)^2\right] \tag{3.3}$$

If v is a microwave signal given by

$$v = v_0 \cos\omega t \tag{3.4}$$

eq 3.3 becomes

$$i = I_s\left[\frac{qv_0\cos\omega t}{k_BT} + \frac{1}{2!}\left(\frac{qv_0\cos\omega t}{k_BT}\right)^2\right] \tag{3.5}$$

Using the trigonometric identity

$$\cos^2\omega t = \frac{1+\cos 2\omega t}{2} \tag{3.6}$$

eq 3.5 becomes

$$\begin{aligned} i &= I_s \left[\frac{qv_0 \cos \omega t}{k_B T} + \frac{1 + \cos 2\omega t}{4} \left(\frac{qv_0}{k_B T} \right)^2 \right] \\ &= \frac{I_s q^2 v_0^2}{4k_B^2 T^2} + \frac{qv_0 I_s \cos \omega t}{k_0 T} + \frac{I_s q^2 v_0^2 \cos 2\omega t}{4k_B^2 T^2} \end{aligned} \tag{3.7}$$

Eq 3.7 shows dc and ac components. The ac component is normally filtered off by a capacitor in the diode and is not outputted. The dc term is proportional to v_0^2 and is proportional to the input power since $P = \frac{v_0^2}{R}$. Because of this, the detector is said to be a square law detector.

3.2.3 Waveguide

Waveguides are hollow metal conductors that can be rectangular or circular in cross section and are normally made of brass or aluminium. The inside of the waveguide is covered with silver to minimise the energy loss of microwaves. Silver is used for the coating since it has a characteristic of low penetration depth of microwaves. They are used to transfer electromagnetic waves from one point to another with minimum energy loss, as shown in Fig 3.5.

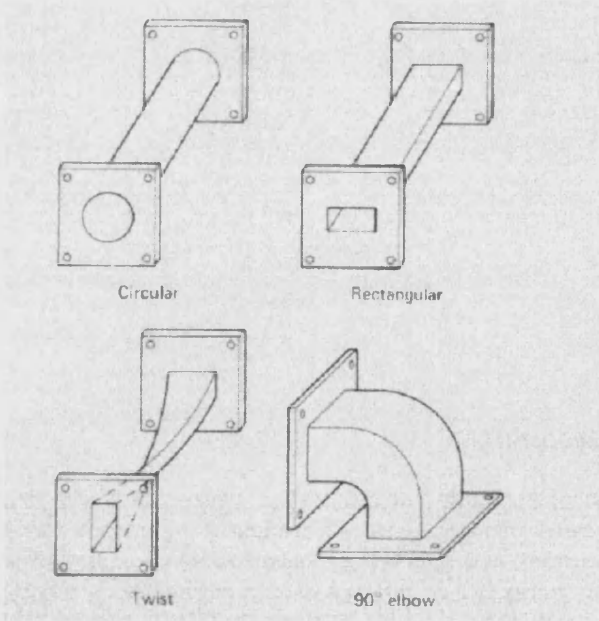

Figure 3.5: Common waveguides

Waveguides may be bent to some angle or twisted to some desired angle. At each end of the waveguide section is a metal flange to allow one section to be bolted to the other.

The mode describes the various electromagnetic energy pattern that are propagated down the interior of a waveguide. In the transverse electric (TE) mode, the electric field is perpendicular to the direction of propagation and the magnetic field is parallel to the direction of propagation.

A waveguide acts as a high pass filter. It will support waves above a certain cut-off frequency. The mode with the lowest cut-off frequency is called the dominant mode. For the commonly used rectangular waveguide, TE_{10} is the dominant mode. The two subnumbers following TE indicate the number of half wavelength patterns of the transverse field in the x and y direction, respectively. When a TE mode is discussed, the two subscripts refer to the number of electric field patters. The TE_{10} states that there is one half wavelength pattern in the x direction, and zero half wavelength patterns in the y direction.

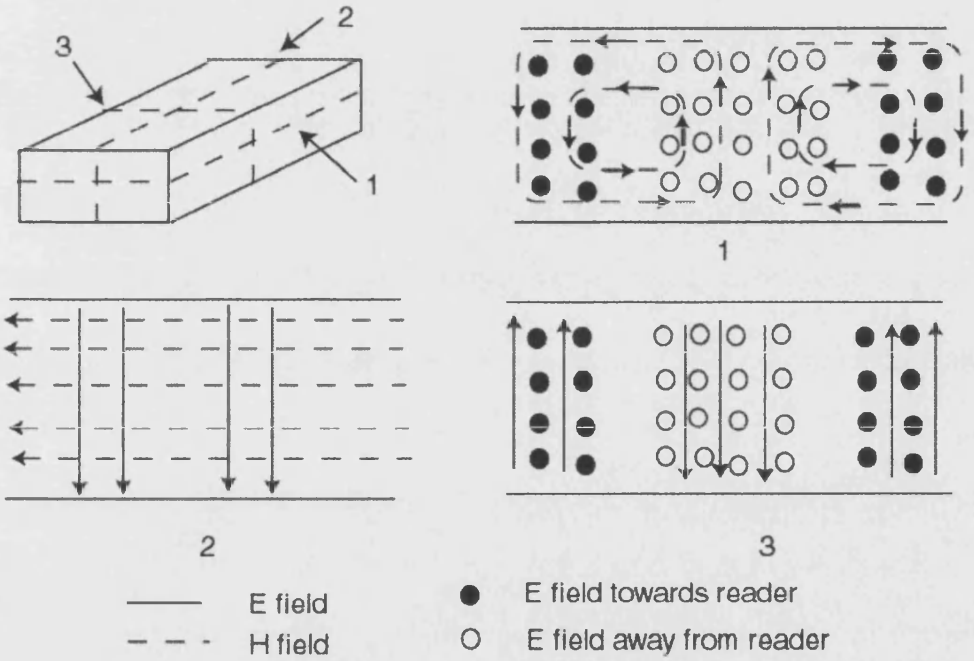

Cut-off frequency

The cut-off frequency for TE_{mn} mode of a rectangular waveguide is given by

$$f_c = \frac{1}{2\sqrt{\mu\varepsilon}}\sqrt{\left(\frac{m}{a}\right)^2 + \left(\frac{n}{b}\right)^2} \tag{3.8}$$

where a is width of waveguide and b is height of waveguide.

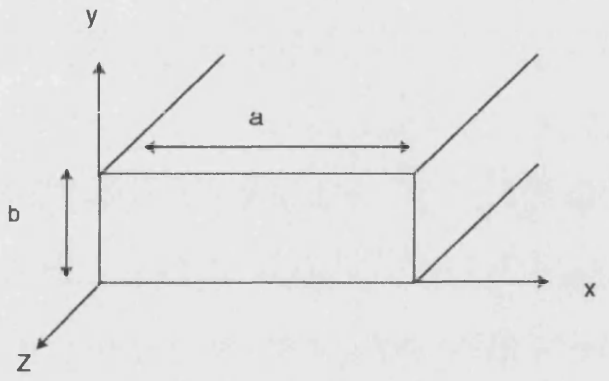

Figure 3.6: Rectangular waveguide dimensions

Eq 3.8 can be rewritten in terms of the speed of light

$$f_c = \frac{c}{2}\sqrt{\left(\frac{m}{a}\right)^2 + \left(\frac{n}{b}\right)^2}$$

Since $\mu = \mu_0$ and $\varepsilon = \varepsilon_0$ for air dielectrics

$$c = \frac{1}{\sqrt{\mu_0\varepsilon_0}}$$

The cut-off wavelength is then

$$\begin{aligned} \lambda_c &= \frac{c}{f_c} \\ &= \frac{2}{\sqrt{\left(\frac{m}{a}\right)^2 + \left(\frac{n}{b}\right)^2}} \end{aligned}$$

For example, a Ka band microwave guide has dimensions of 0.7×0.3 cm. The TE_{10} mode cut-off frequency is

$$\begin{aligned} f_c &= \frac{c}{2a} \\ &= \frac{3 \times 10^8}{2 \times 0.7 \times 10^{-2}} \\ &= 2.14 \times 10^{10} \\ &= 21.4\,\text{GHz} \end{aligned}$$

Therefore, waves in the frequencies below 21.4 GHz are not propagated in the waveguide.

The cut-off wavelength for a Ka band microwaves is

$$\begin{aligned} \lambda_c &= \frac{3 \times 10^8}{2.14 \times 10^{10}} \\ &= 1.4 \times 10^{-2} \\ &= 1.4\ \text{cm} \end{aligned}$$

3.2.4 Attenuator

The attenuator is a device used to reduce the microwave signal and consists of thin resistive sheet that can be moved from the side wall to the center of the guide. The resistive sheet absorbs the microwave power and effects attenuation. The minimum attenuation is observed when the resistive sheet is at the side wall, whereas the maximum of the attenuation is observed when it is at the center. The mechanical drive for the sheet is fitted with a micrometer control so that fine adjustment of attenuation can be made as shown in Fig 3.7

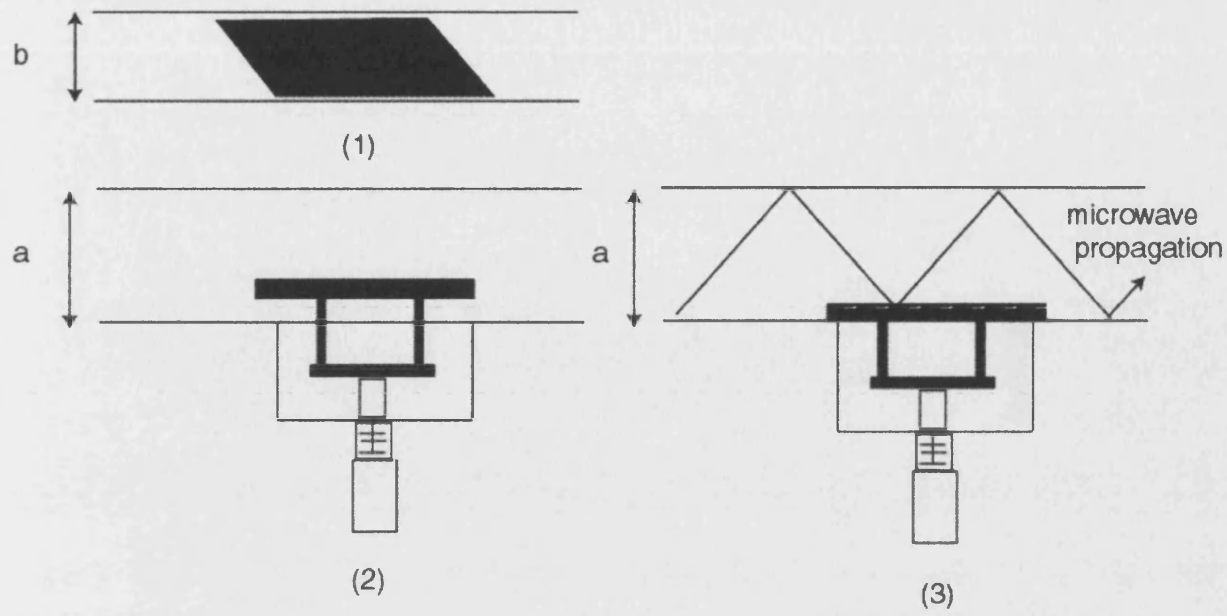

Figure 3.7: Schematic diagram of attenuator (1) side view and (2) top view (3) minimum attenuation.

3.2.5 Isolator

An isolator is a ferrite device which passes microwave signals with low loss in the forward direction but absorbs energy in the reverse direction. One application of an isolator is to prevent power being reflected back to a source. A common type of isolator is based on Faraday rotation. When an electromagnetic wave travels through a ferrite material in a direction parallel to an applied magnetic field, the wave polarisation is rotated. The basic principle is shown in Fig 3.8. Resistive attenuator vanes are placed parallel to the x direction of the waveguide. The input electric vector is perpendicular to the input attenuator vane and is not affected by it. Polarisation of wave incident is shifted clockwise 45^o in passing through the magnetised ferrite. The emerging electric field is also perpendicular to the second resistive vane and passes out of the device through a rectangular waveguide which is oriented to correspond to the emerging polarisation as shown in Fig 3.8 (a). Fig 3.8 (b) illustrates the operation of the device for a signal reflected back through the device. The reflected wave is rotated 45^o in the same direction in which the forward wave was shifted and absorbed since the electric field is in parallel with the resistive vane.

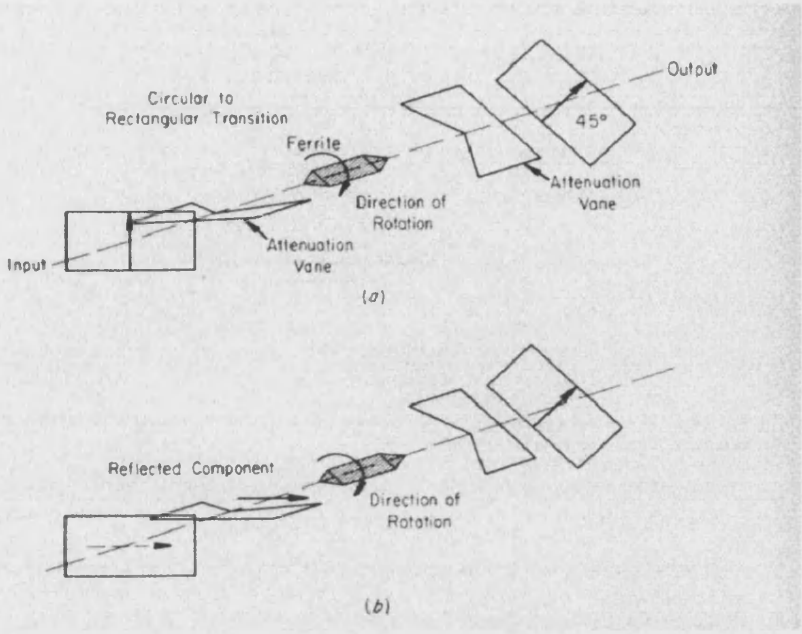

Figure 3.8: Faraday rotation; a) forward direction and b) reverse direction

The ferrite is located approximately one half the distance from the side to the center of the guide and the permanent magnet is placed outside the waveguide to provide the magnetic field through the ferrite as shown in Fig 3.9.

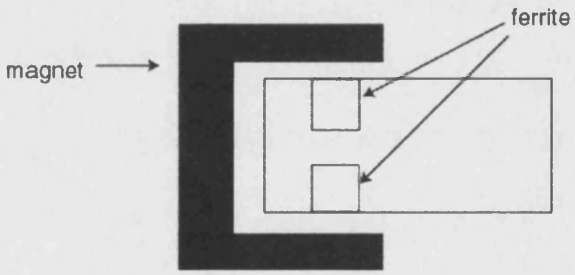

Figure 3.9: Schematic diagram of isolator

3.2.6 Directional coupler

Directional couplers are four port components containing of two waveguides joined together through a number of openings in a common wall, as shown in Fig 3.10 and a simplified diagram of the directional coupler is shown in Fig 3.11.

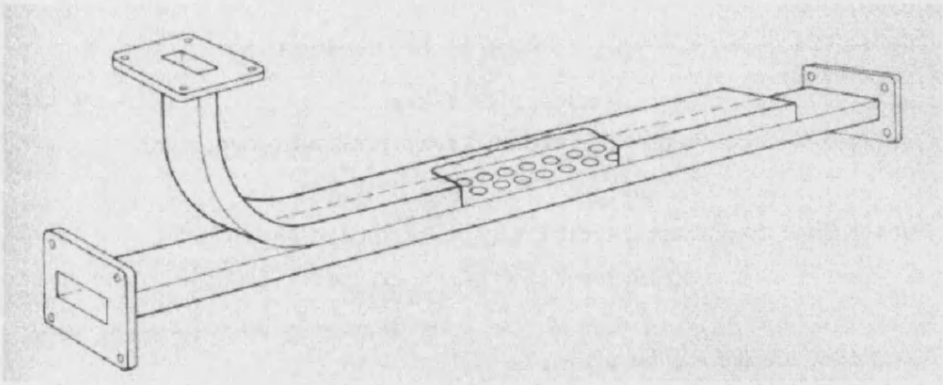

Figure 3.10: Common type of a directional coupler

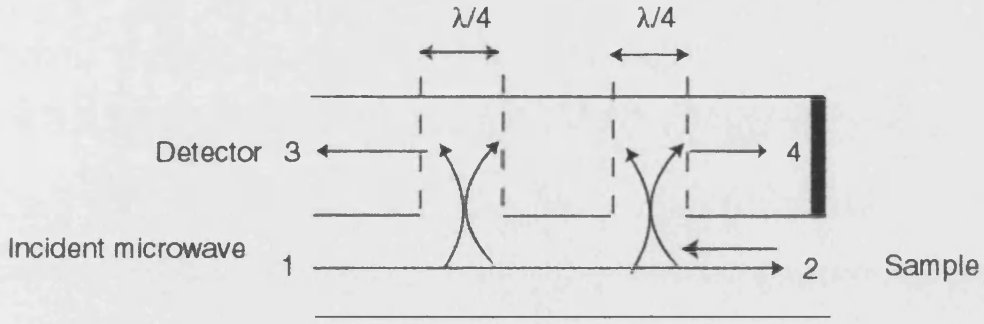

Figure 3.11: Simplified diagram of directional coupler

The incident microwave comes from Port 1 and goes to Port 2. The reflected microwave by the sample is directed to Port 3 and Port 4 is normally terminated by absorber. Since the spacing of holes is $\lambda/4$, the coupled waves travelling towards Port 4 are out of phase.

Directional couplers are specified by their coupling, and coupling is defined as

$$C = 10 \log \left(\frac{P_2}{P_3} \right)$$

where C is coupling in dB, P_2 is reflected power at Port 2, and P_3 is output power at Port 3. For example, 10 dB directional coupler was used for our system

$$\begin{aligned} 10 &= 10 \log \left(\frac{P_2}{P_3} \right) \\ \frac{P_2}{P_3} &= 10 \end{aligned}$$

Therefore, 10% of the incident microwave is outputted to port 3.

3.3 Microwave reflection at Si/electrolyte

The dominant mode is TE_{10} in our system, and the amplitude of the electric field in the propagation direction, E(x), is given by

$$E(x) = E_0 \exp(-kx)$$

where E_0 is amplitude of the incident wave at x = 0 and k is complex propagation constant in a waveguide with inner dimensions of a × b, given by

$$k = \sqrt{\left(\frac{\pi}{a}\right)^2 - j\omega\mu(\sigma + j\omega\varepsilon)} \tag{3.9}$$

Here ω is the angular frequency of microwave source, σ is generalised conductivity of the medium, ε_0 is permittivity of free space, ε is relative permittivity of the medium, μ_0 is magnetic permittivity of vacuum. Details for the propagation constant are given in Appendix A2.

Fig 3.12 shows the reflection and transmission of electromagnetic waves in terms of electric and magnetic fields.

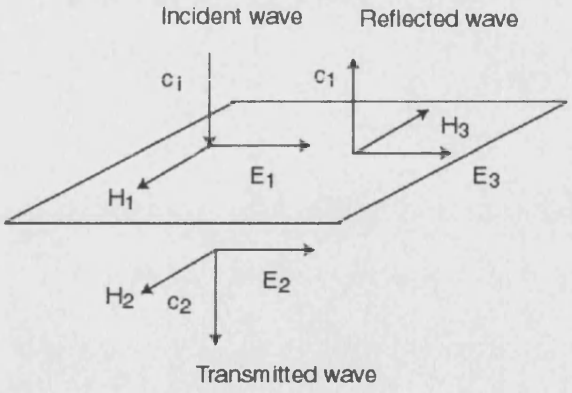

Figure 3.12: Reflection and transmission at two media.

The Fresnel reflection coefficient is defined as the ratio of electric field or magnetic field of an incident and reflected waves.

$$r = \left|\frac{E_3}{E_1}\right| = \left|\frac{H_3}{H_1}\right| \tag{3.10}$$

where E is electric field and H is magnetic field.

The reflection coefficients has the following characteristics

$$r_{mn} = -r_{nm} \tag{3.11}$$

$$t_{mn} = -t_{nm} \tag{3.12}$$

$$t_{mn} = 1 + r_{mn} \tag{3.13}$$

where r_{mn} is reflection coefficient from medium m to n, and t_{mn} is transmission coefficient from medium m to n.

The reflection coefficient and transmission coefficients can be expressed in terms of the propagation constant

$$r_{mn} = \frac{k_m - k_n}{k_m + k_n} \tag{3.14}$$

$$t_{mn} = \frac{2k_m}{k_m + k_n} \tag{3.15}$$

The reflectance is defined as

$$R = \left|\frac{E_3 H_3}{E_1 H_1}\right| \tag{3.16}$$

$$= \left|r^2\right| \tag{3.17}$$

$$= r \times r' \tag{3.18}$$

where r' is complex conjugate.

It is noted that EH represents the energy of the electromagnetic waves, referred to as a Poynting vector. The Poynting vector is given by

$$E \times H = EH \sin\theta \tag{3.19}$$

Since the electric and magnetic fields are perpendicular, eq 3.19 can be reduced to

$$E \times H = EH \tag{3.20}$$

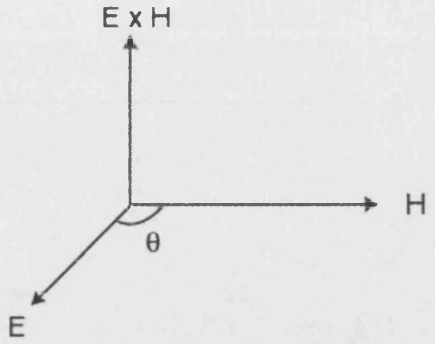

Figure 3.13: Graphical representation of Poynting vector.

3.3.1 3 layer model

The microwave reflection can be described by Fresnel's law. For multilayers, the reflection coefficient is derived from a reflection and transmission in each region. Our interest is to describe the effect of space charge layer to the microwave reflection. A 4-layer model is better than 3 layer one since the space charge region is included for the 4 layer model. However, the derivation of reflection coefficient for 4 layer model is based on the 3 layer model and 3 layer model is considered first. The corresponding 3 layers are i) air (waveguide), ii) semiconductor and iii) electrolyte.

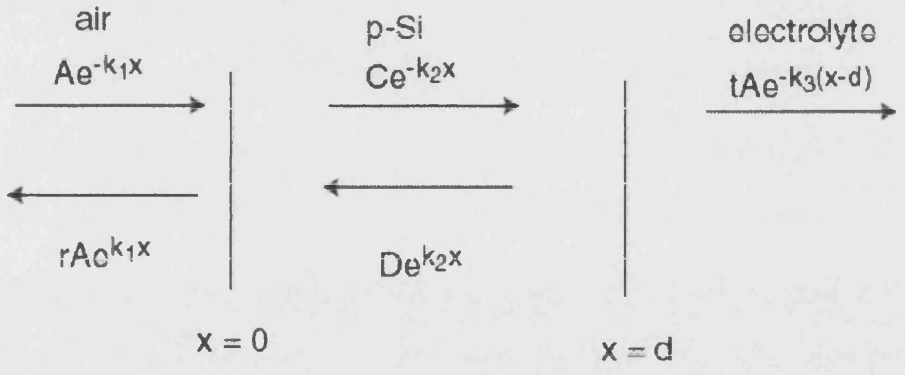

Figure 3.14: Reflection and transmission from 3 layer medium

The amplitude of those waves in Fig 3.14 are related

At x = 0

$$C = t_{12}A + r_{21}D \tag{3.21}$$

$$rA = r_{12}A + t_{21}D \tag{3.22}$$

At x = d

$$tA = t_{23}Ce^{k_2 d} \tag{3.23}$$

$$De^{k_2 d} = r_{23}Ce^{-k_2 d} \tag{3.24}$$

Using eq 3.11 to eq 3.13, eq 3.21 and 3.22 can be rewritten as

$$C = (1 + r_{12})A - r_{12}D \tag{3.25}$$

$$rA = r_{12}A + (1 - r_{12})D \tag{3.26}$$

Inserting eq 3.25 into eq 3.24

$$\begin{aligned} De^{k_2 d} &= r_{23}\left[(1 + r_{12})A - r_{12}D\right]e^{-k_2 d} \\ D &= \left[(1 + r_{12})r_{23}A - r_{12}r_{23}D\right]e^{-2k_2 d} \end{aligned} \tag{3.27}$$

Therefore, eq 3.27 can be solved for D

$$\begin{aligned} \left(1 + r_{12}r_{23}e^{-2k_2}\right)D &= (1 + r_{12})r_{23}A \\ D &= \frac{(1 + r_{12})r_{23}Ae^{-2k_2 d}}{1 + r_{12}r_{23}e^{-2k_2 d}} \end{aligned} \tag{3.28}$$

Inserting eq 3.28 into eq 3.26

$$\begin{aligned} rA &= r_{12}A + (1 - r_{12})\left(\frac{(1 + r_{12})r_{23}Ae^{-2k_2 d}}{1 + r_{12}r_{23}e^{-2k_2 d}}\right) \\ r &= r_{12} + (1 - r_{12})\left(\frac{(1 + r_{12})r_{23}e^{-2k_2 d}}{1 + r_{12}r_{23}e^{-2k_2 d}}\right) \\ &= \frac{r_{12}(1 + r_{12}r_{23}e^{-2k_2 d}) + (1 - r_{12}^2)r_{23}e^{-2k_2 d}}{1 + r_{12}r_{23}e^{-2k_2 d}} \\ &= \frac{r_{12} + r_{12}^2 r_{23}e^{-2k_2 d} + r_{23}e^{-2k_2 d} - r_{12}^2 r_{23}e^{-2k_2 d}}{1 + r_{12}r_{23}e^{-2k_2 d}} \end{aligned} \tag{3.29}$$

The final solution for 3 layered reflection coefficient is

$$r = \frac{r_{12} + r_{23}e^{-2k_2 d}}{1 + r_{12}r_{23}e^{-2k_2 d}} \tag{3.30}$$

3.3.2 4 layer model

A similar approach can be applied to 4 layer model and the corresponding 4 layers are i) air (waveguide), ii) semiconductor bulk iii) semiconductor space charge and iv) electrolyte as shown in Fig 3.15.

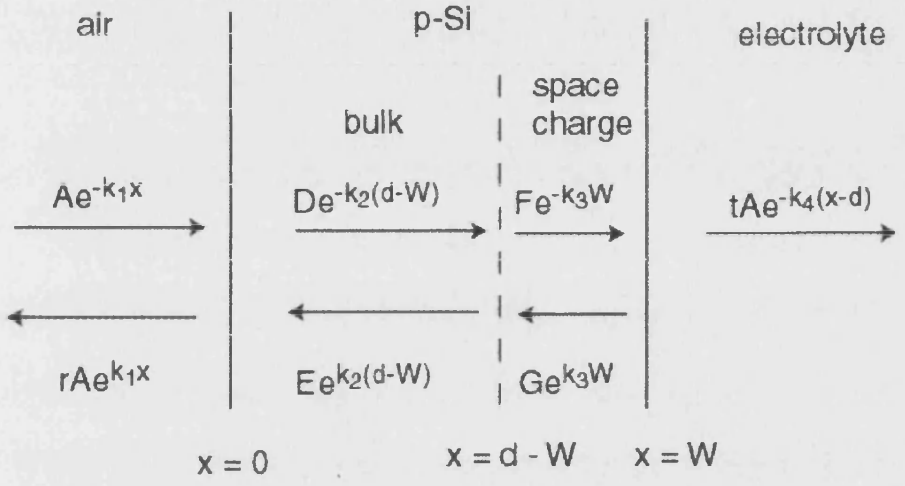

Figure 3.15: Reflection and transmission from 4 layer medium

The amplitude of those waves in Fig 3.15 are related

At x = 0

$$D = t_{12}A + r_{21}E \tag{3.31}$$

$$rA = r_{12}A + t_{21}E \tag{3.32}$$

At x = d - W

$$F = t_{23}De^{-k_2(d-W)} + t_{23}G \tag{3.33}$$

$$Ee^{k_2(d-W)} = r_{23}De^{-k_2(d-W)} + t_{23}G \tag{3.34}$$

At x = W

$$Ge^{k_3W} = r_{34}Fe^{-k_3W} \tag{3.35}$$

Rewriting eq 3.31 to eq 3.34 in terms of reflection coefficient

$$D = (1 + r_{12})A - r_{12}E \tag{3.36}$$

$$rA = r_{12}A + (1 - r_{12})E \tag{3.37}$$

$$F = (1 + r_{23})De^{-k_2(d-W)} - r_{23}G \tag{3.38}$$

$$Ee^{k_2(d-W)} = r_{23}De^{-k_2(d-W)} + (1 - r_{23})G \tag{3.39}$$

Rewriting eq 3.35

$$\begin{aligned} F &= \frac{Ge^{k_3W}}{r_{34}e^{-k_3W}} \\ &= \frac{G}{r_{34}}e^{2k_3W} \end{aligned} \tag{3.40}$$

Inserting eq 3.40 into eq 3.38

$$\begin{aligned} \frac{G}{r_{34}}e^{2k_3W} &= (1 + r_{23})De^{-2k_2(d-W)} - r_{23}G \\ (e^{2k_3W} + r_{23}r_{34})G &= r_{34}(1 + r_{23})De^{-k_2(d-W)} \\ G &= \frac{r_{34}(1 + r_{23})De^{-k_2(d-W)}}{e^{2k_3W} + r_{23}r_{34}} \end{aligned} \tag{3.41}$$

Inserting eq 3.41 into eq 3.39

$$\begin{aligned} Ee^{k_2(d-W)} &= r_{23}De^{-k_2(d-W)} + (1 - r_{23})\frac{r_{34}(1 + r_{23})De^{-k_2(d-W)}}{e^{2k_3W} + r_{23}r_{34}} \\ E &= \frac{r_{23}e^{2k_3W} + r_{34}}{e^{2k_3W} + r_{23}r_{34}}De^{-2k_2(d-W)} \end{aligned} \tag{3.42}$$

Inserting eq 3.36 into eq 3.42

$$E = \frac{r_{23}e^{2k_3W} + r_{34}}{e^{2k_3W} + r_{23}r_{34}}\left[(1 + r_{12})A - r_{12}E\right]e^{-2k_2(d-W)} \tag{3.43}$$

From eq 3.37

$$A = \frac{1 - r_{12}}{r - r_{12}}E \tag{3.44}$$

Inserting eq 3.44 into eq 3.43

$$\begin{aligned} E &= \frac{r_{23}e^{2k_3W} + r_{34}}{e^{2k_3W} + r_{23}r_{34}} \left[(1 + r_{12})\frac{1 - r_{12}}{r - r_{12}}E - r_{12}E\right] e^{-2k_2(d-W)} \\ 1 &= \frac{r_{23}e^{2k_3W} + r_{34}}{e^{2k_3W} + r_{23}r_{34}} \left[\frac{1 - r_{12}r}{r - r_{12}}\right] e^{-2k_2(d-W)} \end{aligned} \tag{3.45}$$

Therefore, the final solution for the reflection coefficient in the 4 layer system is

$$r = \frac{(r_{23}e^{2k_3W} + r_{34})e^{-2k_2(d-W)} + r_{12}(e^{2k_3W} + r_{23}r_{34})}{e^{2k_3W} + r_{23}r_{34} + (r_{23}e^{2k_3W} + r_{34})r_{12}e^{-2k_2(d-W)}} \tag{3.46}$$

If W = 0 and r_{34} = 0, eq 3.46 can be reduced to the 3 layer model. The relationship between Fresnel reflection coefficient and reflectance is

$$R = r \times r' \tag{3.47}$$

where r′ is complex conjugate.

In potential modulated microwave reflectivity, the change in the microwave reflectivity is caused by a change in the width of the space charge layer which is induced by a change in the band bending. Since the change in reflectivity is small, experimental measurements are performed in an ac mode by harmonically modulating the band bending. The time dependent space charge width for p-type semiconductors is given by

$$W(t) = \sqrt{-\frac{2\varepsilon_0\varepsilon_r(V + \Delta\overline{\phi}_{sc})}{qN_A}} \tag{3.48}$$

where $\Delta\overline{\phi}_{sc}$ is modulated potential given by

$$\Delta\overline{\phi}_{sc} = \Delta\phi_{sc}\sin(2\pi f) \tag{3.49}$$

The time dependence of the reflectance is shown in Fig 3.16. The following values were used for the calculation

$a = 0.7 \times 10^{-2}$ m

ε (air) = 1

ε (silicon bulk) = 12

ε (silicon space charge) = 12

ε (solution) = 20

$\mu_0 = 12.56 \times 10^{-7}\ \mathrm{NA}^{-2}$

$\mathrm{d} = 364 \times 10^{-6}\ \mathrm{m}$

f = 33 GHz

σ (air) = 0 $\mathrm{S\,m^{-1}}$

σ (silicon bulk) = 10 $\mathrm{S\,m^{-1}}$

σ (silicon space charge) = 0 $\mathrm{S\,m^{-1}}$

σ (solution) = 0.001 $\mathrm{S\,m^{-1}}$

$\mathrm{N_A} = 1 \times 10^{21}\ \mathrm{m^{-3}}$

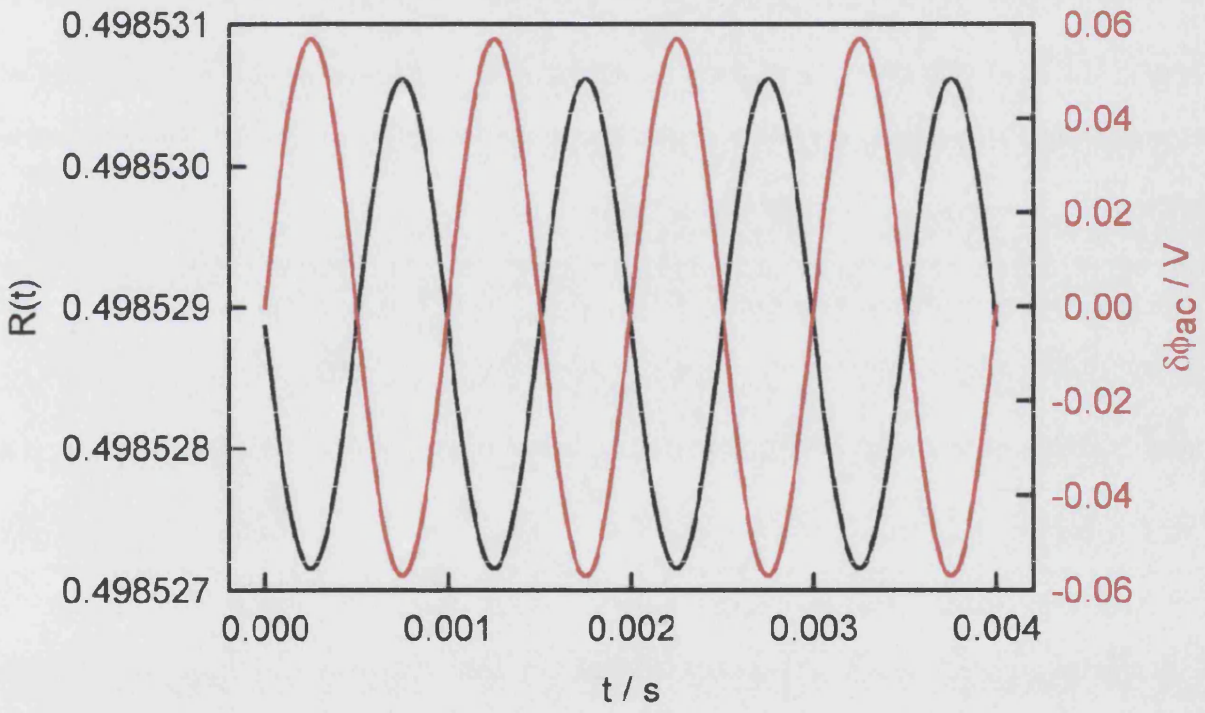

Figure 3.16: Time dependence of microwave reflectivity and modulation amplitude.

3.4 The change of the conductivity at Si/electrolyte

The integrated excess carrier concentrations are directly related to the change of mean conductivity, which determines the microwave response. The change of the conductivity can be expressed as

$$< \Delta\sigma >= \frac{q}{d}\int_0^d (\mu_n \Delta n + \mu_p \Delta p)\, dx \tag{3.50}$$

where d is the sample thickness. The details of the microwave response are discussed in the next chapter.

Fig 3.17 shows the conductivity and the change of the conductivity as a function of the potential where the calculation is based on the carrier concentration profile obtained in the previous chapter. The bulk conductivity is given by

$$\sigma = q\mu_n n + q\mu_p p \tag{3.51}$$

The first term is due to electrons and the second term is due to holes. Normally, one term can be neglected, and for p-type semiconductors holes are majority carriers. Eq 3.51 can be reduced to

$$\sigma = q\mu_p p \tag{3.52}$$

The conductivity of p-Si ($N_A = 1 \times 10^{15} cm^{-3}$) in the dark is

$$\begin{aligned} \sigma &= 1 \times 10^{-19} \times 480 \times 1 \times 10^{15} \\ &= 0.0768\ \Omega^{-1} cm^{-1} \end{aligned}$$

In Chapter 2, it is seen that the reduction of photocurrent arises from the space charge recombination of electron-hole pair. The similar behaviour is observed from a mean conductivity change as a function of potential plot. The initial increase in the mean conductivity change in the potential range between 0.2 and 0.4 V is due to the shift of Fermi level, decreasing the space charge recombination. After the mean conductivity change reaches to the maximum, it decreases slowly as space charge layer gets wider.

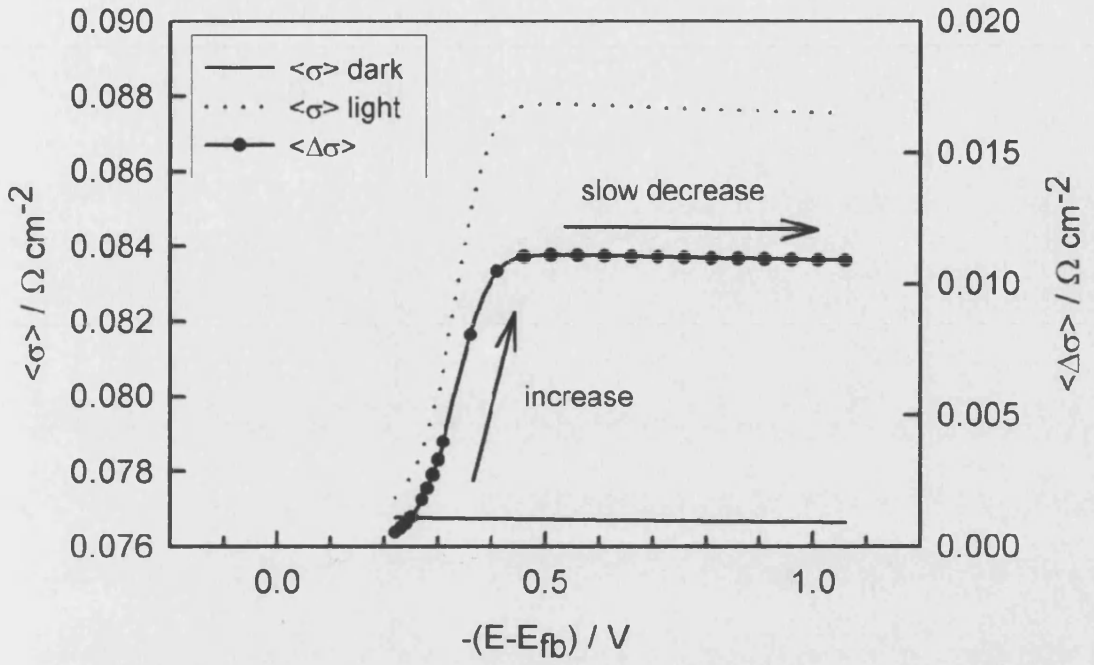

Figure 3.17: Mean conductivity and change of the mean conductivity as a function of potential for p-Si. $I_0 = 1 \times 10^{14}$ $cm^{-2}s^{-1}$.

Fig 3.18 shows the schematic diagram of the generation profile under illumination. It is noted that the area under the line of $I = I_0 \exp(-\alpha x)$ represents the generation profile of electrons. At low rate constant conditions, there is a competition between electron transfer and recombination. Increasing the rate constant decreases the build up of electrons in the space charge region. For high values of the electron transfer rate constant, the electron concentration in the space charge region becomes negligible. Under these circumstances, the microwave response originates only from the neutral region as shown in Fig 3.18.

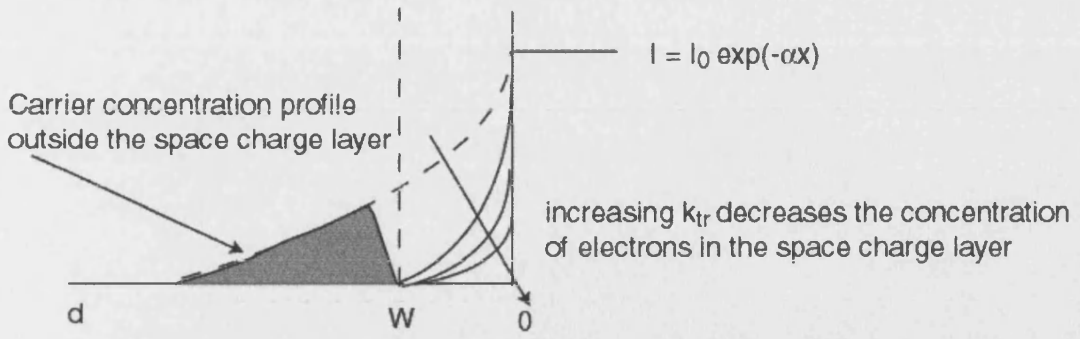

Figure 3.18: Generation profile outside and inside of the space charge region.

Fig 3.19 shows the effect of the rate constant of charge transfer on the change of conductivity.

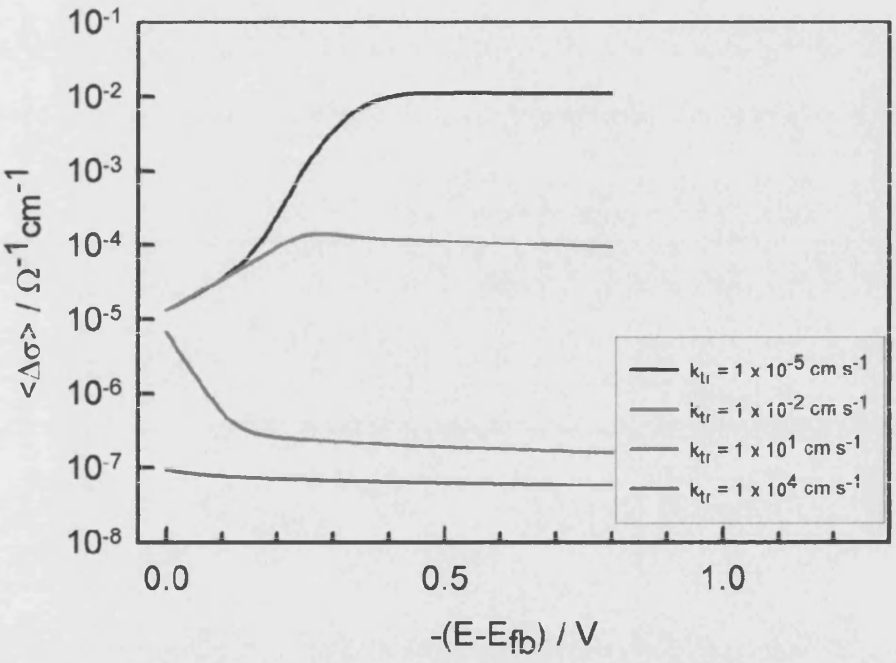

Figure 3.19: The photoinduced conductivity change as a function of potential at $I_0 = 1 \times 10^{14}$ $cm^{-2}s^{-1}$ and $\tau_n = 1 \times 10^{-4}$ s.

It is clear that the change of conductivity is reduced by increasing the rate constant. Therefore, a small microwave response is expected for fast electron transfer reactions. However, the change of conductivity is not linearly proportional to the rate constant as shown in Fig 3.20.

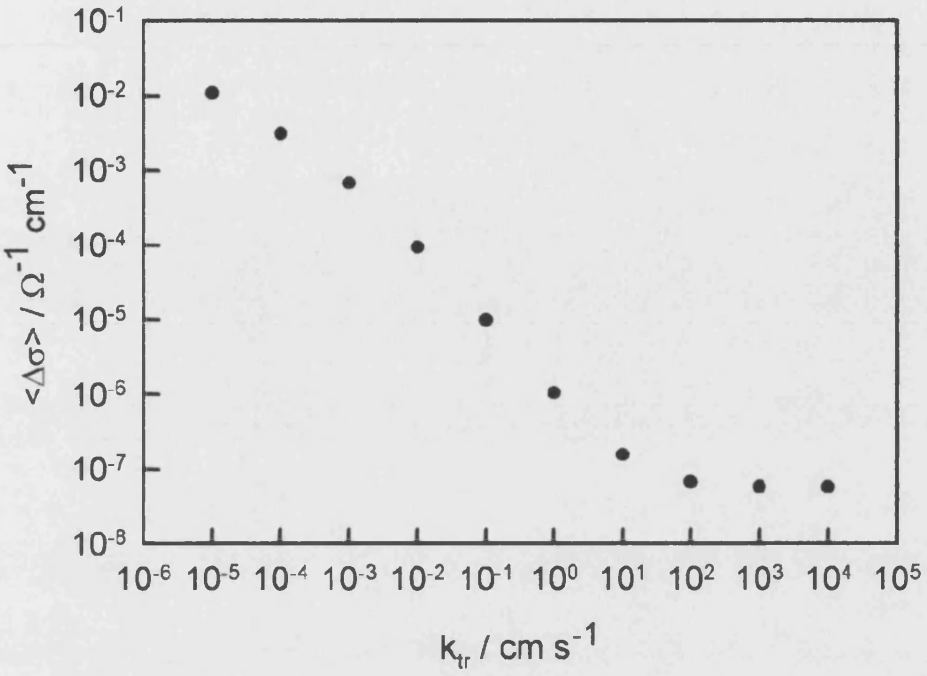

Figure 3.20: The photoinduced conductivity change as a function of k_{tr} at $E - E_{fb}$ = -0.8 V ($I_0 = 1 \times 10^{14}$ $cm^{-2}s^{-1}$ and $\tau_n = 1 \times 10^{-4}$ s).

In Chapter 2, the carrier concentration profile is discussed and it is seen that the carrier concentration profile strongly depends on the distance from the surface. The large carrier concentration of carriers in a very thin layer might affect the microwave response. Therefore, we used a stack model to obtain the theoretical microwave response. We used 9 layers for Si and 1 layer for electrolyte as shown in Fig 3.21 and each layer thickness is tabulated in Table 3.2. The program was written by Dr. S.R. Pennock.

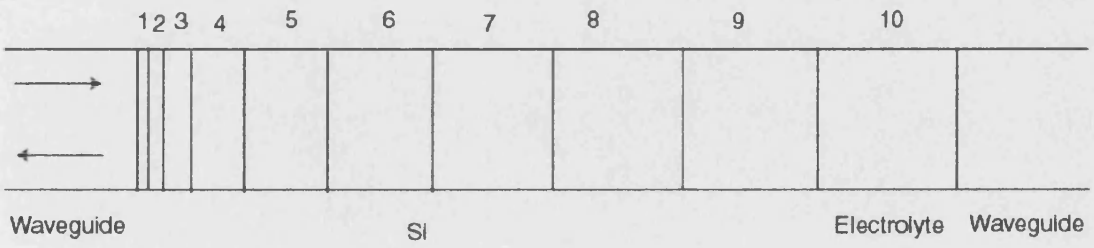

Figure 3.21: Stack model to calculate microwave response.

Layer	Thickness of layer	Layer	Thickness of layer
1	340 μm	6	50 nm
2	9 μm	7	40 nm
3	0.5 μm	8	9 nm
4	0.25 μm	9	1 nm
5	0.15 μm	10	1 cm

Table 3.2: Thickness of each layer to obtain a theoretical microwave response.

The microwave response was calculated at several k_{tr} ($E-E_{fb}$ = -0.8 V) under illumination ($I_0 = 1 \times 10^{14}$ $cm^{-2}s^{-1}$). It is noted that this condition is the same as in Fig 3.20. The normalised microwave response is obtained as follows

$$\frac{\Delta R}{R} = \frac{R_{light} - R_{dark}}{R_{dark}} = \frac{S\Delta\sigma}{R} \tag{3.53}$$

The normalised microwave response is shown in Fig 3.22. It is seen that the calculated microwave response from the stack model is superimposable with the change of conductivity.

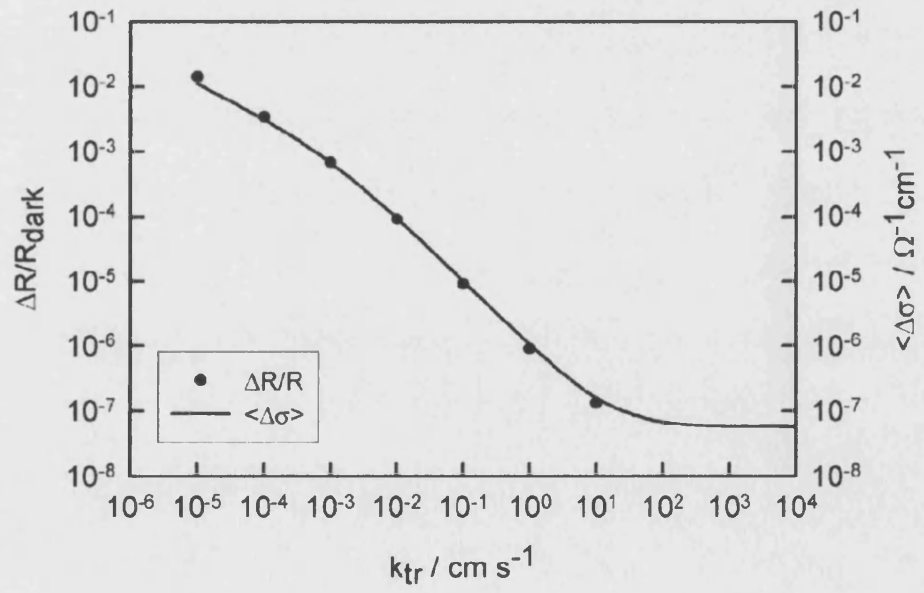

Figure 3.22: The effect of charge transfer rate constant on microwave response.

References

[1] Lance, A. L. Introduction to microwave theory and measurements, McGraw-Hill, New York, 1964.

[2] Fuller, A. J. B. Microwaves, 3rd edition, Pergamon press, Oxford, 1990.

[3] Car, J. J. Elements of microwave electronics technology, Harcourt Bruce Jonavovich, New York, 1989.

[4] Cook, N. P. Microwave principles and systems, Prentice-Hall, New Jersey, 1986.

[5] Seeger, J. A. Microwave theory, components and devices, Prentice-Hall, New Jersey, 1986.

[6] Sucher, M.; Fox, J. Handbook of microwave measurements, vol.1 and 3, Polytechnic press, New York, 1963.

[7] Collins, R. E. Foundations for microwave engineering, McGraw-Hill, New York, 1992.

[8] Roddy, D. Microwave technology, Prentice-Hall, New Jersey, 1986.

[9] Wheeler, G. J. Introduction to microwaves, Prentice-Hall, New Jersey, 1963.

[10] Natarajan, A.; Nellore, A.; Searson, P. C. Journal of Applied Physics, **1999**, 85, 1631-1636.

[11] Coué, E.; Chausse, J. P. Semiconductor science and technology, **2000**, 15, 178-183.

[12] P. Yeh, Optical waves in layered media, John Wiley, New York, 1988.

[13] Grant, I. S.; Phillips, W. R. Electromagnetism, 2nd edition, John Wiley, New York, 1990.

[14] Chatterjee, R. Elements of microwave engineering, John Wiley, New York, 1986.

[15] Dunlop, J.; Smith, D. G. Telecommunications engineering, 2nd edition, Van Norstrand Reinhold, Hong Kong, 1989.

[16] Sadiku, M. N. O. Elements of electromagnetics, 2nd edition, Oxford University Press, Oxford, 1995.

Chapter 4

Advanced aspects of microwaves

4.1 Reflected microwave

There are number of techniques to measure the physical properties of semiconductors such as the four-probe method. Mobility and surface recombination rate are normally measured by the technique based on the reflection of microwaves. The relative microwave signal, $\frac{\Delta P}{P_{in}}$, is proportional to the change of the conductivity, as shown below

$$\frac{\Delta P}{P_{in}} = S\Delta\sigma \tag{4.1}$$

The relative change of the reflected microwave power is given by

$$\frac{\Delta P(\sigma)}{P_{in}(\sigma)} = \frac{P_r(\sigma+\Delta\sigma) - P_r(\sigma)}{P_{in}} \tag{4.2}$$

$$R(\sigma) = \frac{P_r(\sigma)}{P_{in}} \tag{4.3}$$

where $P_r(\sigma)$ is reflected microwave power, P_{in} is incident microwave power, and $R(\sigma)$ is reflectance.

Inserting eq 4.3 into eq 4.2

$$\begin{aligned}\frac{\Delta P(\sigma)}{P_{in}} &= \frac{P_{in}R(\sigma+\Delta\sigma) - P_{in}R(\sigma)}{P_{in}} \\ &= R(\sigma+\Delta\sigma) - R(\sigma)\end{aligned} \tag{4.4}$$

Using Taylor's expansion, eq 4.4 becomes

$$\begin{aligned}\frac{\Delta P(\sigma)}{P_{in}} &= R(\sigma+\Delta\sigma) - R(\sigma) \\ &= \frac{\delta R}{\delta\sigma}(\sigma+\Delta\sigma-\sigma) \\ &= \left(\frac{\delta R}{\delta\sigma}\right)\Delta\sigma\end{aligned} \tag{4.5}$$

Rewriting eq 4.5 using sensitivity factor, S,

$$\frac{\Delta P(\sigma)}{P_{in}} = S\Delta\sigma \tag{4.6}$$

where $S = \left(\frac{\delta R}{\delta\sigma}\right)$

$\Delta\sigma$ is change of the conductivity, given by

$$\Delta\sigma = \frac{q}{d}\left[\int_0^d \mu_n \Delta n(x)\,dx + \int_0^d \mu_p \Delta p(x)\,dx\right] \tag{4.7}$$

4.2 Potential Modulated Microwave Reflectivity (PMMR) response

Eq 4.7 can be rewritten in terms of charge

$$\Delta\sigma = \frac{\mu_n Q_n}{d} + \frac{\mu_p Q_p}{d} \tag{4.8}$$

where Q_n is charge due to the electrons, and Q_p is charge due to the holes.
Under the potential modulated condition, the change of the conductivity is due to the majority carriers in the dark and the eq 4.8 can be reduced to

$$\Delta\sigma = \frac{\mu_p Q_p}{d} \quad \text{for p-type semiconductors} \tag{4.9}$$

A differential capacitance is given by

$$\Delta Q = C\Delta V$$

Experimentally, the change in the charge density in space charge layer is measured in an ac mode by harmonically modulating the applied potential. The modulated charge in the semiconductor space charge region can be expressed as

$$\Delta\overline{Q}_{sc} = C_{sc}\Delta\overline{\phi}_{sc} \tag{4.10}$$

where $\Delta\overline{\phi}_{sc}$ is modulation amplitude.
As inserting eq 4.9 and eq 4.10 into eq 4.6, the eq 4.6 becomes

$$\begin{aligned} \frac{\Delta P}{P_r} &= S\frac{\mu_p \overline{Q}_{sc}}{Rd} \\ &= S\frac{\mu_p C_{sc}\Delta\overline{\phi}_{sc}}{Rd} \end{aligned} \tag{4.11}$$

where C_{sc} is space charge capacitance, given by

$$C_{sc} = \sqrt{-\frac{q\varepsilon_0\varepsilon_r N_A A^2}{2\left(V_a - V_{fb} + \frac{k_B T}{q}\right)}} \tag{4.12}$$

Inserting eq 4.12 into eq 4.11 and rearranging it gives a Mott-Schottky like relation

$$\left(\frac{P_r}{\Delta P}\right)^2 = -\frac{2R^2d^2}{\left(S\mu_p\Delta\bar{\phi}_{sc}\right)^2 q\varepsilon_0\varepsilon_r N_A A^2}\left(V_a - V_{fb} + \frac{k_B T}{q}\right) \tag{4.13}$$

It is noted that eq 4.13 is for p-type semiconductors and sensitivity factor can be obtained from the slope if plotting $\left(\frac{P_r}{\Delta P}\right)^2$ vs V_a. In addition, the intercept with x axis gives the flat-band potential as described in the capacitance measurements.

4.3 Frequency resolved responses (optical perturbation)

4.3.1 IMPS response

Fig 4.1 shows the general reaction scheme for photogenerated electrons in p-type semiconductors.

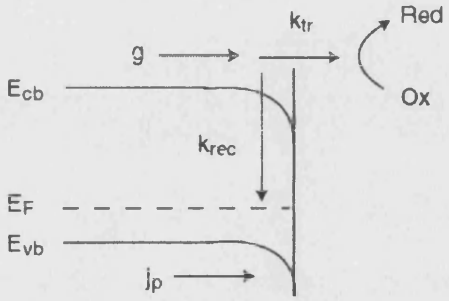

Figure 4.1: General scheme at semiconductor/electrolyte interface.

From Fig 4.1, the time dependence of the concentration of electrons are given by

$$\frac{dn}{dt} = g - k'_{tr}c_{Ox}n - k'_{rec}np = 0 \text{ at steady state} \tag{4.14}$$

Here g is Gärtner flux.

If both c_{Ox} and p are assumed to be constant,

$$\frac{dn}{dt} = g - k_{tr}n - k_{rec}n = 0 \tag{4.15}$$

where $k_{tr} = k'_{tr}c_{Ox}$

$k_{rec} = k'_{rec}p$

Hence

$$n = \frac{g}{k_{tr} + k_{rcc}} \tag{4.16}$$

The photocurrent density is given by

$$\begin{aligned} j_{photo} &= qk_{tr}n \\ &= qg\frac{k_{tr}}{k_{tr} + k_{rec}} \end{aligned} \tag{4.17}$$

Therefore, it is shown that the rate constants for electron transfer and recombination cannot be separated under steady state illumination. However, k_{tr} and k_{rec} can be separated under non-steady conditions. In this case, the measured photocurrent response is the sum of the charging and transfer components or the difference between the photogenerated minority carrier current density, qg, and the recombination current density, as shown below

$$j_{photo} = j_{ch} + j_{tr} \tag{4.18}$$

or

$$j_{photo} = qg - j_{rec} \tag{4.19}$$

where j_{ch} is charging current density, j_{tr} is electron transfer current density, and j_{rec} is surface recombination current density.

Each term can be written in terms of charge

$$j_{ch} = \frac{dQ}{dt} \tag{4.20}$$

$$j_{tr} = k_{tr}Q \tag{4.21}$$

$$j_{rec} = k_{rec}Q \tag{4.22}$$

Therefore, eq 4.18 becomes

$$j_{photo} = \frac{dQ}{dt} + k_{tr}Q \tag{4.23}$$

Since $\frac{d}{dt} = i\omega$, eq 4.23 becomes

$$j_{photo} = i\omega Q + k_{tr} Q \tag{4.24}$$

From eq 4.18 and eq 4.19

$$qg = j_{ch} + j_{tr} + j_{rec} \tag{4.25}$$

Eq 4.25 can be rewritten as

$$qg = i\omega Q + (k_{tr} + k_{rec})\, Q \tag{4.26}$$

Dividing eq 4.23 by eq 4.26

$$\begin{aligned} \frac{j_{photo}}{qg} &= \frac{i\omega Q + k_{tr} Q}{i\omega Q + (k_{tr} + k_{rec})\, Q} \\ &= \frac{i\omega + k_{tr}}{i\omega + (k_{tr} + k_{rec})} \end{aligned} \tag{4.27}$$

Multiplying by the complex conjugate eq 4.27 becomes

$$\begin{aligned} \frac{j_{photo}}{qg} &= \frac{(i\omega + k_{tr})\,[(k_{tr} + k_{rec}) - i\omega]}{[i\omega + (k_{tr} + k_{rec})]\,[(k_{tr} + k_{rec}) - i\omega]} \\ &= \frac{i\omega\,(k_{tr} + k_{rec}) - i^2\omega^2 + k_{tr}\,(k_{tr} + k_{rec}) - i\omega k_{tr}}{(k_{tr} + k_{rec})^2 - i^2\omega^2} \\ &= \frac{\omega^2 + i\omega k_{rec} + k_{tr}\,(k_{tr} + k_{rec})}{(k_{tr} + k_{rec})^2 + \omega^2} \\ &= \frac{\omega^2 + k_{tr}\,(k_{tr} + k_{rec})}{(k_{tr} + k_{rec})^2 + \omega^2} + \frac{i\omega k_{rec}}{(k_{tr} + k_{rec})^2 + \omega^2} \end{aligned} \tag{4.28}$$

Therefore, the IMPS response has real and imaginary components given by

$$\mathrm{Re}\left(\frac{j_{photo}}{qg}\right) = \frac{\omega^2 + k_{tr}\,(k_{tr} + k_{rec})}{(k_{tr} + k_{rec})^2 + \omega^2} \tag{4.29}$$

$$\mathrm{Im}\left(\frac{j_{photo}}{qg}\right) = \frac{i\omega k_{rec}}{(k_{tr} + k_{rec})^2 + \omega^2} \tag{4.30}$$

These equations describe a semicircle in the complex plane as shown in Fig 4.2.

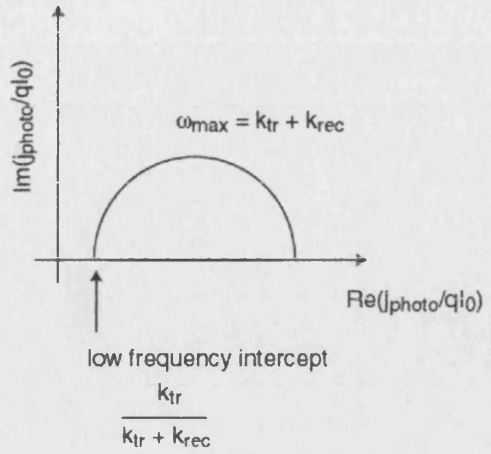

Figure 4.2: IMPS plot in the complex form.

Maximum of the semicircle

The imaginary part becomes maximum at one point, and in order to find out this point, the imaginary part can be differentiated with respect to ω

$$\frac{d\,Im\left(\frac{j_{photo}}{qg}\right)}{d\omega} = \frac{k_{rec}\left[(k_{tr}+k_{rec})^2+\omega^2\right]-2\omega^2 k_{rec}}{\left[(k_{tr}+k_{rec})^2+\omega^2\right]^2} = 0$$

at the maximum

Hence

$$\begin{aligned} \omega_{max}^2 &= (k_{tr}+k_{rec})^2 \\ \omega_{max} &= k_{tr}+k_{rec} \qquad \text{since } \omega > 0 \end{aligned}$$

Low frequency intercept

The low frequency intercept on the x axis also gives an useful information

If $\omega \rightarrow 0$, eq 4.29 can be reduced to

$$Re\left(\frac{j_{photo}}{qg}\right) = \frac{k_{tr}}{k_{tr}+k_{rec}} \tag{4.31}$$

4.3.2 Light Modulated Microwave Reflectivity (LMMR) response

Since reflected microwave response is a linear function of the change in the charge that accumulates at the semiconductor|electrolyte interface, microwave response can be expressed as

$$\frac{\Delta P}{P_r} = S'Q(t)$$

where S′ is modified sensitivity factor.

Eq 4.26 can be rearranged as

$$Q = \frac{qg}{(k_{tr} + k_{rec}) + i\omega} \tag{4.32}$$

Multiplying the complex conjugate, eq 4.32 becomes

$$\begin{aligned} Q &= \frac{qg\left[(k_{tr} + k_{rec}) - i\omega\right]}{\left[(k_{tr} + k_{rec}) + i\omega\right]\left[(k_{tr} + k_{rec}) - i\omega\right]} \\ &= \frac{qg\left[(k_{tr} + k_{rec}) - i\omega\right]}{(k_{tr} + k_{rcc})^2 + \omega^2} \end{aligned} \tag{4.33}$$

Separating the real and imaginary parts of eq 4.33

$$Q = \frac{qg\,(k_{tr} + k_{rec})}{(k_{tr} + k_{rcc})^2 + \omega^2} - \frac{i\omega qg}{(k_{tr} + k_{rcc})^2 + \omega^2} \tag{4.34}$$

Therefore, the microwave response is given by

$$\mathrm{Re}\left(\frac{\Delta P}{P_r}\right) = \frac{S'qg\,(k_{tr} + k_{rec})}{(k_{tr} + k_{rcc})^2 + \omega^2} \tag{4.35}$$

$$\mathrm{Im}\left(\frac{\Delta P}{P_r}\right) = -\frac{S'\omega qg}{(k_{tr} + k_{rec})^2 + \omega^2} \tag{4.36}$$

These equations describe a semicircle in the complex plane as shown in Fig 4.3.

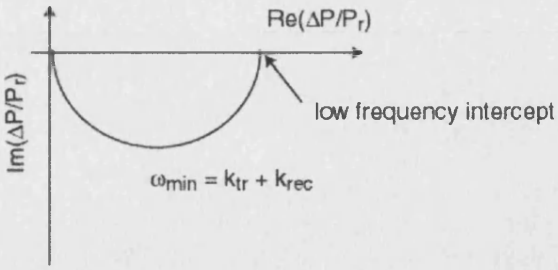

Figure 4.3: LMMR plot in the complex form.

Minimum of the semicircle

In order to find out the minimum of the semicircle, the imaginary part of the eq 4.36 needs to be differentiated with respect with ω

$$\frac{d\,\mathrm{Im}\left(\frac{\Delta P}{P_r}\right)}{d\omega} = \frac{qg\left[(k_{tr}+k_{rec})^2+\omega^2\right]-2\omega^2 qg}{\left[(k_{tr}+k_{rec})^2+\omega^2\right]^2} = 0$$

at the minimum

Therefore,

$$\begin{aligned} \omega_{min}^2 &= (k_{tr}+k_{rec})^2 \\ \omega_{min} &= k_{tr}+k_{rec} \qquad \text{since } \omega > 0 \end{aligned}$$

Low frequency intercept

If $\omega \rightarrow 0$, eq 4.35 can be reduced to

$$\mathrm{Re}\left(\frac{\Delta P}{P_r}\right) = \frac{S'qg}{k_{tr}+k_{rec}} \tag{4.37}$$

The low frequency intercept of the microwave response does not give an useful information.

4.4 Time resolved responses

4.4.1 Time dependent photocurrent response

The photocurrent is given by

$$j_{photo} = j_{ch} + j_{tr} \tag{4.38}$$

or

$$j_{photo} = qg - j_{rec} \tag{4.39}$$

The transfer, recombination and charging components of the time dependent photocurrent are [13]

$$j_{tr}(t) = \frac{qgk_{tr}\left[1 - \exp(-(k_{tr} + k_{rec})t)\right]}{k_{tr} + k_{rec}} \tag{4.40}$$

$$j_{rec}(t) = \frac{qgk_{rec}\left[1 - \exp(-(k_{tr} + k_{rec})t)\right]}{k_{tr} + k_{rec}} \tag{4.41}$$

$$j_{ch}(t) = qg\exp(-(k_{tr} + k_{rec})t) \tag{4.42}$$

Eq 4.40, eq 4.41 and eq 4.42 are shown in Fig 4.4

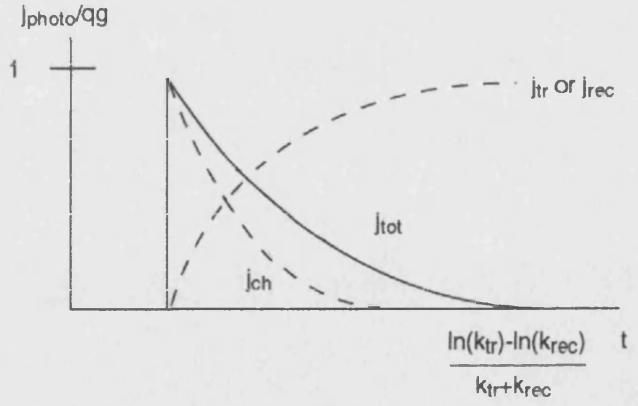

Figure 4.4: Components of the current density.

From eq (4.39) and (4.41), the time dependent j_{photo} becomes

$$j_{photo}(t) = \frac{qg(k_{tr} + k_{rec}\exp(-(k_{tr} + k_{rec})t))}{k_{tr} + k_{rec}} \tag{4.43}$$

From eq (4.38), (4.40), and (4.42), the same answer is obtained.

If $k_{rec} = 0$, eq 4.43 can be reduced to

$$j_{photo} = qg \tag{4.44}$$

and no kinetic information is obtained.

4.4.2 Time dependent microwave response

The photogenerated flux of minority carriers towards the surface shows 3 processes: surface charge storage, charge transfer and recombination. Each current density can be written in terms of charge

$$j_{ch} = \frac{dQ}{dt} \tag{4.45}$$

$$j_{tr} = k_{tr}Q \tag{4.46}$$

$$j_{rec} = k_{rec}Q \tag{4.47}$$

From eq 4.46, the charge is given by

$$Q = \frac{j_{tr}}{k_{tr}} \tag{4.48}$$

Inserting eq 4.40 to eq 4.48, time dependent charge is given by

$$\begin{aligned} Q &= \frac{j_{tr}(t)}{k_{tr}} \\ &= \frac{qg\,[1 - \exp(-(k_{tr} + k_{rec})t)]}{k_{tr} + k_{rec}} \end{aligned} \tag{4.49}$$

Therefore, the time dependent microwave response is

$$\begin{aligned} \frac{\Delta P}{P_r} &= \frac{S\mu_n Q}{Rd} \\ &= \frac{S\mu_n}{Rd}\frac{qg\,[1 - \exp(-(k_{tr} + k_{rec})t)]}{k_{tr} + k_{rec}} \end{aligned} \tag{4.50}$$

If $k_{rec} = 0$, eq 4.50 can be reduced to

$$\frac{\Delta P}{P_r} = \frac{S\mu_n}{Rd}\frac{qg\left[1-\exp(-k_{tr}t)\right]}{k_{tr}} \tag{4.51}$$

Fig 4.5 shows that the microwave response and photocurrent in the case of $k_{rec} = 0$.

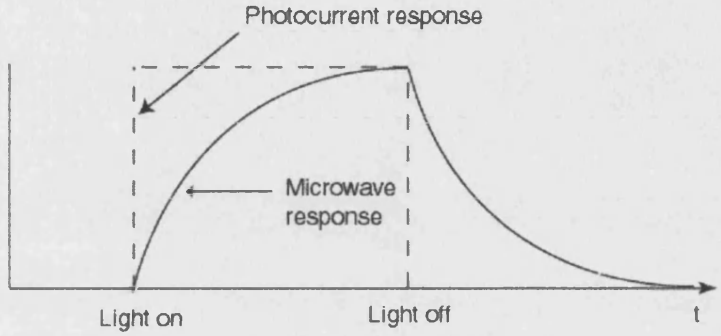

Figure 4.5: Comparison of photocurrent and microwave responses

4.5 Potential dependence of the LMMR response

The Gärtner equation is given by

$$j_{photo} = -qg\left(1 - \frac{\exp(-\alpha W)}{1+\alpha L}\right) \tag{4.52}$$

From eq 4.26

$$qg = i\omega Q + (k_{tr} + k_{rec})\,Q \tag{4.53}$$

Inserting eq 4.53 into eq 4.52,

$$j_{photo} = -\left[i\omega Q + (k_{tr} + k_{rec})\,Q\right]\left(1 - \frac{\exp(-\alpha W_{sc})}{1+\alpha L}\right) \tag{4.54}$$

Eq 4.54 can be rearranged as

$$\begin{aligned} Q &= \frac{j_{photo}}{\left[i\omega + (k_{tr} + k_{rec})\right]\left(1 - \frac{\exp(-\alpha W)}{1+\alpha L}\right)} \\ &= \frac{j_{photo}\left[(k_{tr} + k_{rec}) - i\omega\right]}{\left[(k_{tr} + k_{rec})^2 + \omega^2\right]\left(1 - \frac{\exp(-\alpha W)}{1+\alpha L}\right)} \end{aligned} \tag{4.55}$$

Therefore, the Gärtner like potential dependent microwave response is

$$\frac{\Delta P}{P_r} = \frac{S\mu}{Rd} \frac{j_{photo}\left[(k_{tr} + k_{rec}) - i\omega\right]}{\left[(k_{tr} + k_{rec})^2 + \omega^2\right]\left(1 - \frac{\exp(-\alpha W)}{1+\alpha L}\right)} \tag{4.56}$$

4.6 Frequency resolved potential modulated responses under accumulation condition

For anodic dissolution of p-Si, the following equivalent circuit is used

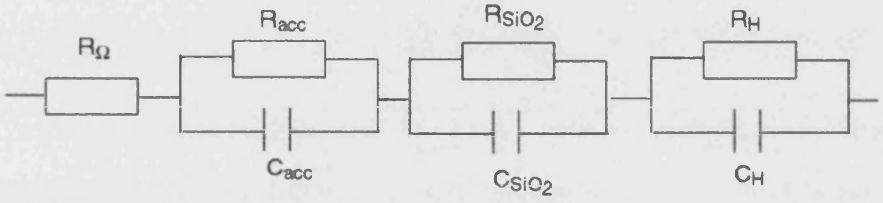

Figure 4.6: Equivalent circuit for anodic dissolution of p-Si

where R_Ω = contact and solution resistance

R_{acc} = charge transfer resistance at accumulation layer

C_{acc} = accumulation capacitance

C_{SiO_2} = oxide layer capacitance = $\frac{\varepsilon_{SiO_2}\varepsilon_0}{d_{SiO_2}}$

R_{SiO_2} = charge transfer resistance at oxide layer

C_H = Helmholtz capacitance = $\frac{\varepsilon_H\varepsilon_0}{d_H}$

R_H = charge transfer resistance at Helmholtz layer

The equivalent circuit in Fig 4.6 contains too many elements to allow reliable fitting of the impedance response, which is typically a single semicircle at frequencies above a few Hz. A more satisfactory approach is minimise the number of a priori assumptions by reducing the equivalent circuits to only 3 elements as shown in Fig 4.7. The reason for this approach is discussed in Chapter 8.

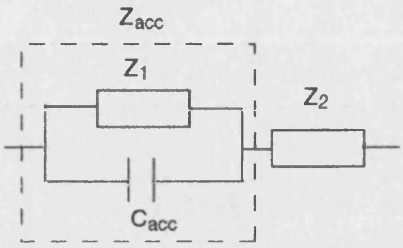

Figure 4.7: Mimimised equivalent circuit for anodic dissolution of p-Si

The total impedance of the 3 elements is given by

$$\begin{aligned} Z_{tot} &= Z_{acc} + Z_2 \\ &= \frac{Z_1}{1 + i\omega C_{acc} Z_1} \end{aligned} \tag{4.57}$$

It follows that the fraction of the total applied ac voltage that appears across C_{acc} is

$$\begin{aligned} f_{acc} &= \frac{Z_{acc}}{Z_{tot}} \\ &= \frac{Z_1}{Z_{tot}\,(1 + i\omega C_{acc} Z_1)} \end{aligned} \tag{4.58}$$

Under accumulation conditions, the PMMR response depends on the modulation of the hole density in the accumulation layer. This depends on the accumulation capacitance and the fraction of the total applied ac modulation that appears across the accumulation layer.

$$\begin{aligned} \frac{\Delta P}{P_r} &= \frac{S\mu_p C_{acc} \Delta\phi_{acc}}{Rd} \\ &= f_{acc} \frac{S\mu_p C_{acc} \Delta\phi_{tot}}{Rd} \\ &= f_{acc} S' Q_{acc} \end{aligned} \tag{4.59}$$

where S′ is modified sensitivity factor = $\frac{S\mu_p}{Rd}$

References

[1] Schlichthörl, G.; Peter, L. M. Journal of the Electrochemical Society **1994**, 141, L171-L173.

[2] Schlichthörl, G.; Peter, L. M. Journal of Electroanalytical Chemistry **1995**, 381, 55-61.

[3] Schlichthörl, G.; Peter, L. M. Journal of the Electrochemical Society **1995**, 142, 2665-2669.

[4] Schlichthörl, G.; Ponomarev, E. A.; Peter, L. M. Journal of the Electrochemical Society **1995**, 142, 3062-3067.

[5] Natarajan, A,; Oskam, G.; Searson, P. C. Journal of Applied Physics, **1998**, 83, 2112-2121.

[6] Natarajan, A.; Nellore, A.; Searson, P. C. Journal of Applied Physics, **1999**, 85, 1631-1636.

[7] Kunst, M.; Beck, G.; Tributsch, H. Journal of the Electrochemical Society **1984**, 131, 954-956.

[8] Kunst, M.; Tributsch, H. Chemical Physics Letters **1984**, 105, 123-126.

[9] Messer, B.; Tributsch, H. Journal of the Electrochemical Society **1986**, 133, 2212-2213.

[10] Messer, B.; Tributsch, H. Chemical Physics Letters **1987**, 142, 546-550.

[11] Schlichthörl, G.; Tributsch, H. Electrochimica Acta **1992**, 37, 919-931.

[12] Tributsch, H.; Schlichthörl, G.; Elstner, L. Electrochimica Acta **1993**, 38, 141-152.

[13] Peter, L. M. in Comprehensive chemical kinetics, Vol. 37, Elsevier, New York, 1999.

[14] Peter, L. M.; Vammaekelbergh, D. in Advances in electrochemical science and engineering, Vol.6, VCH, New York, 1999.

[15] Macdonald, J. R. Impedance spectroscopy, John Wiley, New York, 1987.

[16] Vijh, A. K. Electrochemistry of metals and semiconductors, Mercel Dekker, New York, 1973.

Chapter 5

Experimental

Sample preparation

Boron doped p-type Si wafers with (111) orientation (8-12 Ωcm, ITME) were degreased in isopropanol and then etched by flowing CP-4A etching solution (3:5:3 by volume 48% HF: conc.HNO_3: 100% CH_3COOH) over them for 30 s. The etching rate of silicon in CP-4A solution is 34.8 μm/min at room temperature [1]. The sample was then rinsed with Milli-Q water and dried under a nitrogen stream. Ohmic contact was made around the periphery of the wafer using Ga/In eutectic (Ga:In=75.5:24.5 by weight), the sample was mounted in the PTFE flow cell and dried overnight.

Electrolyte

The 1M fluoride (pH 3) solution contained 0.5 M NH_4F (40%, BDH, Aristar), 0.15 M NH_4Cl (Aldrich, ACS reagent) and 0.5 M HF (48%, BDH, AnalaR). Hexaamine ruthenium (III) (98%, Aldrich) was used as electron acceptor. 0.1M fluoride (pH 4.5) solution contained 0.1M NH_4F (40%, BDH, Aristar), 0.86 M NH_4Cl (Aldrich, ACS reagent), 0.06M CH_3COOH, (BDH, Aristar) and 0.04M CH_3COONH_4 (Aldrich, ACS reagent). The electrolyte was degassed with nitrogen for 15 min before starting experiments and was circulated continuously through the flow cell via a gravity-fed and nitrogen bubble lift system during the measurement as shown in Fig 5.1.

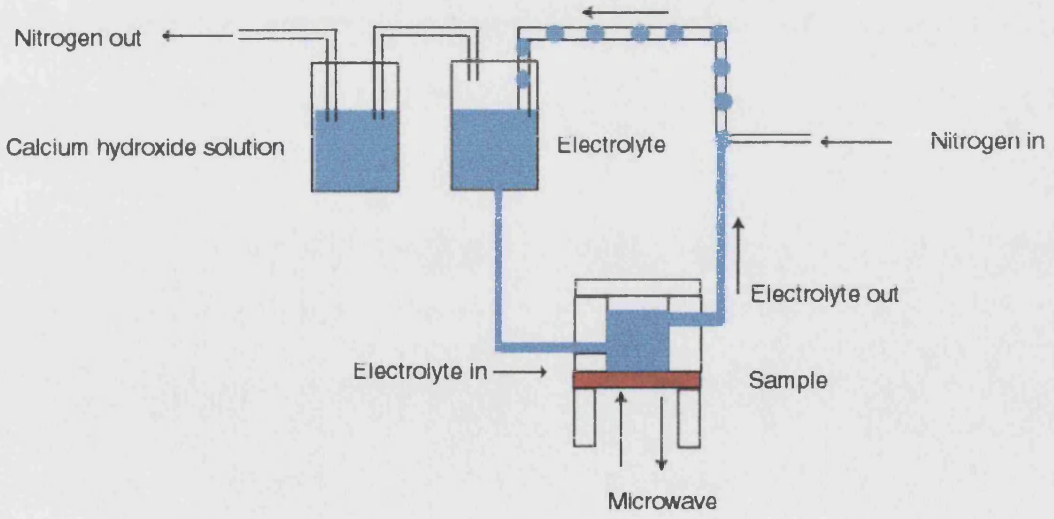

Figure 5.1: Gravity fed nitrogen lift system.

Electrochemical and microwave measurements

Measurements were made in three-electrode configuration with Pt wire counter and Ag/AgCl reference electrodes. Electrochemical measurements were carried out using an operational amplifier based potentiostat constructed in house (See Appendix A.6 for details of operational amplifier circuits) and a function generator (Hi-Tek PPR1) or the analogue output of a computer controlled Stanford Research SR830 lock in amplifier. Dc current-voltage curves were recorded in the dark and illumination from -0.35 V to -1.0 V with a sweep rate of 10 mVs^{-1}. For the microwave measurements, a Gunn diode (33 GHz, Atlantic Microwave Limited) was mounted on a rectangular Ka-band waveguide. The reflected microwave power was measured using a crystal detector (R422C, Agilent technology) via directional coupler (Flann Microwave).

Capacitance and PMMR measurements

The microwave response was recorded as a function of potential at a fixed modulation frequency (f = 270 Hz), and the capacitance was simultaneously recorded. A delay of 10 s was employed between potential increments to allow the system to equilibrate and the integration time of 10 s provided an adequate signal/noise ratio. The measurement was controlled by QBasic program written by Dr. M. Bailes. The experimental set-up for PMMR and capacitance measurements is shown in Fig 5.2.

IMPS and LMMR measurements

A sample was illuminated by a red light emitting diode, LED, (λ = 626 nm). The microwave response was recorded as a function of modulation frequency at a fixed dc potential (Light Modulated Microwave Reflectivity experiment), and the photocurrent was recorded simultaneously (Intensity Modulated Photocurrent Spectroscopy experiment). The measurement was controlled by QBasic program written by Dr. M. Bailes. The modulation depth was set to 100 % and the experimental set-up for LMMR and IMPS is shown in Fig 5.3. The IMPS and LMMR data were fitted using a nonlinear least squares program (Solartron ZView).

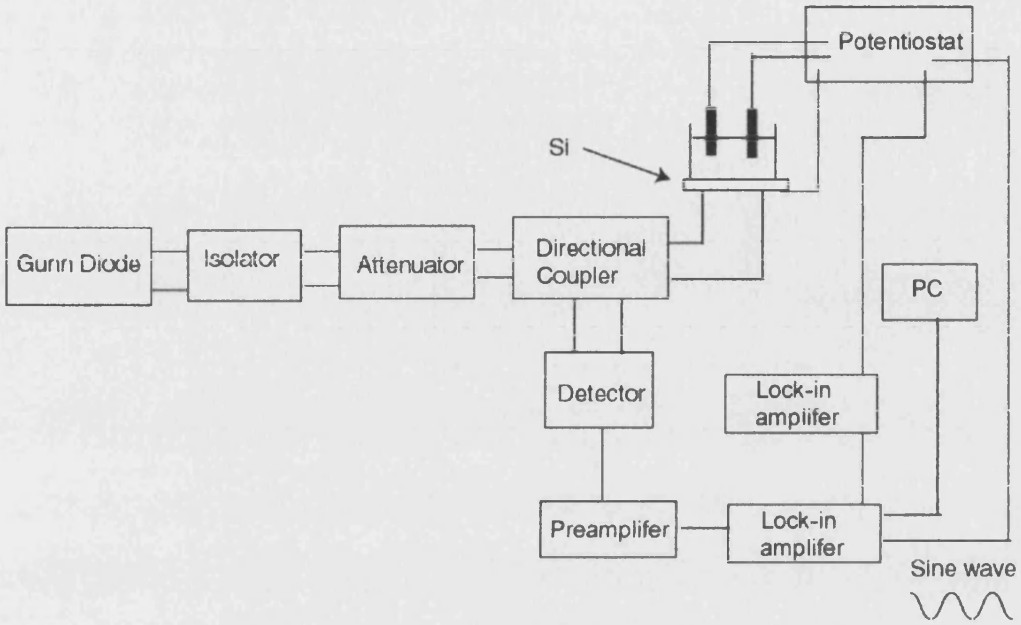

Figure 5.2: Experimental set-up for capacitance and PMMR measurement

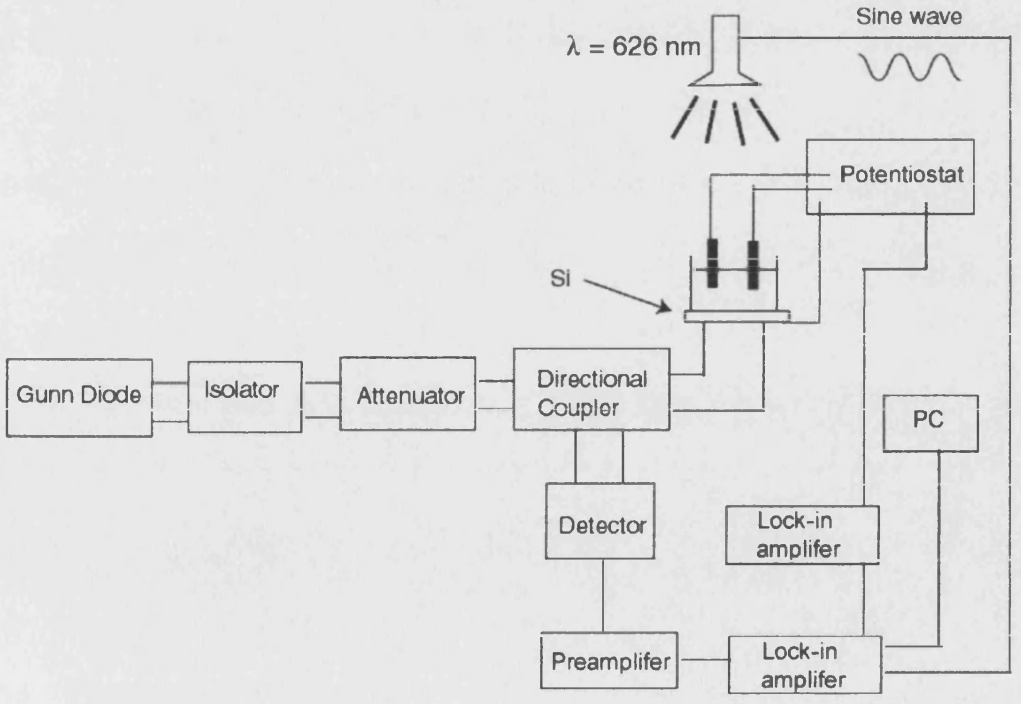

Figure 5.3: Experimental set-up for IMPS and LMMR measurements

Potential dependence of the LMMR measurements

The sample was illuminated by a red LED ($\lambda = 626$ nm) driven sinusoidally. Photocurrent and the microwave signals were recorded as a function of potential at a modulation frequency of 10 Hz. A delay of 10 s was employed between potential increments to allow the system to equilibrate and the integration time of 10 s provided an adequate signal/noise ratio. The measurement was controlled by QBasic program written by Dr. M. Bailes.

Time resolved photocurrent and microwave measurements

The red LED (λ = 626 nm) was used to provide rectangular illumination pulse and the light was on for 2 s and off for 12 s. The microwave signal was then averaged using a digital oscilloscope (Tektronix TDS 3012). The experimental set up is shown in Fig 5.4.

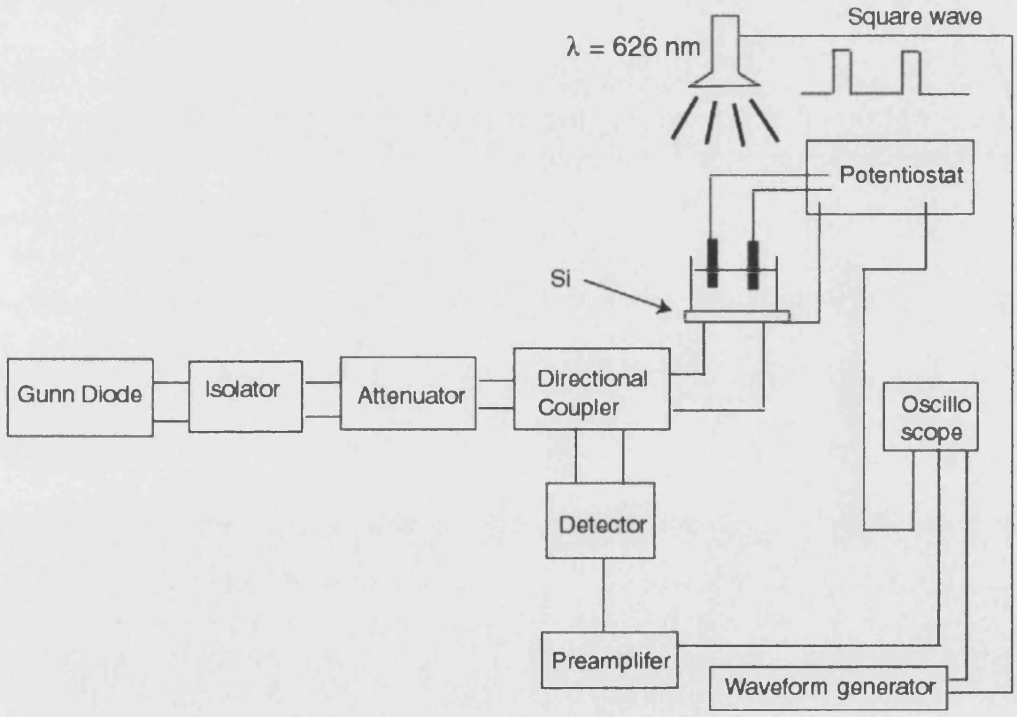

Figure 5.4: Experimental set-up for time resolved measurement

Transient capacitance and microwave measurements

The capacitance was measured in the dark and under illumination (λ = 626 nm) at 10 kHz with 40 mV rms. For the time resolved capacitance measurements, the light was on for 2 s and off for 10 s. The microwave signal was then averaged using a digital oscilloscope (Tektronix TDS 3012). The experimental set up is shown in Fig 5.5.

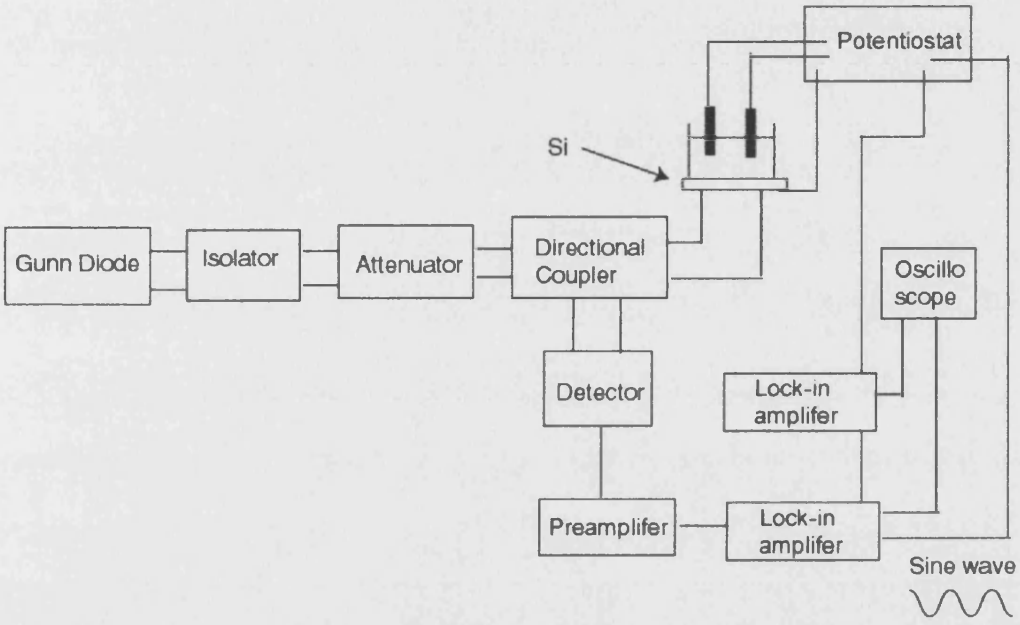

Figure 5.5: Experimental set-up for transient capacitance and PMMR measurements

Impedance and frequency resolved PMMR measurement

The impedance and frequency resolved PMMR were recorded from 45 kHz to 0.45 Hz with 40 mV rms, and the data was fitted using a non-linear least square program (Solartron ZView). The measurement was controlled by QBasic program written by Dr. M. Bailes. The impedance was derived from the measured admittance values. The admittance is expressed as the sum of real and imaginary parts

$$Y = Y_1 + iY_2$$

where Y_1 is real component and Y_2 is imaginary component.

Since impedance is the reciprocal of admittance, impedance can be expressed in terms of admittance.

$$\begin{aligned} Z &= \frac{1}{Y} \\ &= \frac{1}{Y_1 + iY_2} \\ &= \frac{Y_1 - iY_2}{(Y_1 + iY_2)(Y_1 - iY_2)} \\ &= \frac{Y_1}{Y_1^2 + Y_2^2} - \frac{iY_2}{Y_1^2 + Y_2^2} \end{aligned}$$

The phase is given by

$$\theta = \arctan\left(\frac{Z_2}{Z_1}\right) \tag{5.1}$$

The magnitude is given by

$$| Z | = \sqrt{Z_1^2 + Z_2^2} \tag{5.2}$$

where Z_1 is real component and Z_2 is imaginary component.

References

[1] Sze, S. M. Semiconductor devices: Physics and technology, John Wiley, New York, 1985.

[2] Macdonald, J. R. Impedance spectroscopy, John Wiley, New York, 1987.

[3] Bailes, M.; Böhm, S.; Peter, L. M.; Riley, D. J.; Greef, R. Electrochimica acta, **1998**, 43, 1757-1772.

[4] Schlichthörl, G.; Peter, L. M. Journal of Electroanalytical Chemistry **1995**, 381, 55-61.

[5] Schlichthörl, G.; Peter, L. M. Journal of the Electrochemical Society **1995**, 142, 2665-2669.

[6] Scroggie, M. G. Radio laboratory handbook, 6th edition, Iliffe, London, 1954.

Chapter 6

Characterisation of Si/fluoride interface in the dark

6.1 p-type silicon

It is necessary to know the position of the energy levels in semiconductors relative to redox species in electrolyte if semiconductor electrodes are used in electrochemical and photoelectrochemical systems. The energy gap and the flat band potential of the semiconductor as well as redox potential in the electrolyte are important parameters which characterise the semiconductor|electrolyte interface energetically. The most common method to determine the flat band potential is based on the measurement of potential dependence of the capacitance, which obeys the Mott-Schottky relation. A microwave measurement with a simultaneous capacitance measurement provides the sensitivity factor which can be used for an quantitative analysis. The capacitance-voltage curve for p-Si in 1M fluoride (pH 3) is shown in Fig 6.1 and the corresponding microwave response is also plotted. It is seen that the microwave response follows the capacitance.

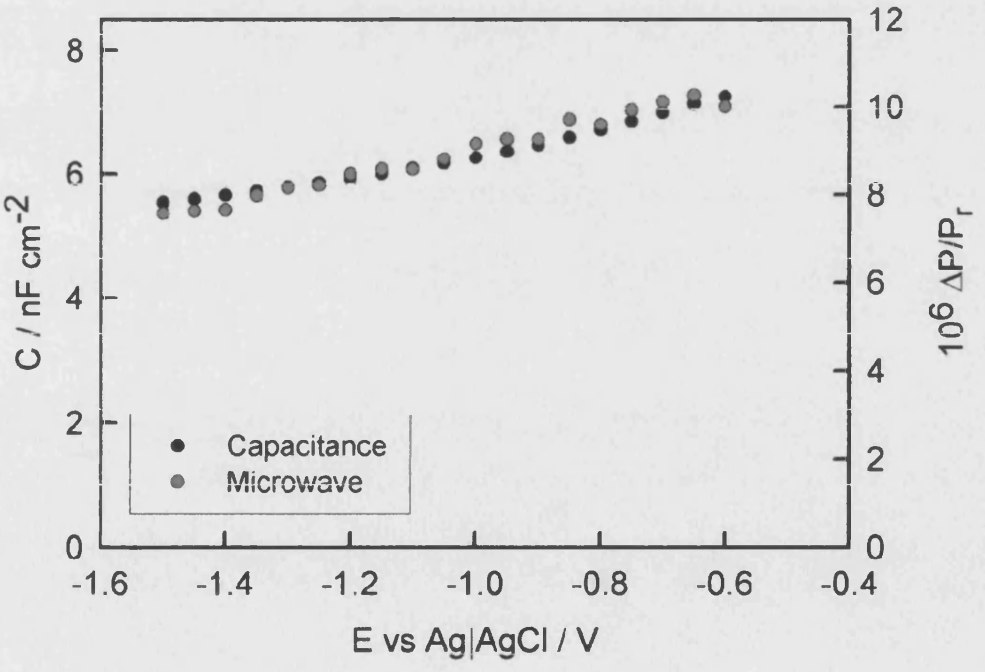

Figure 6.1: Capacitance-Voltage curve and the microwave-voltage curve for p-Si in 1 M fluoride (pH 3)

Fig 6.2 shows the microwave response as a function of capacitance from Fig 6.1. It is seen that microwave response is linearly proportional to capacitance.

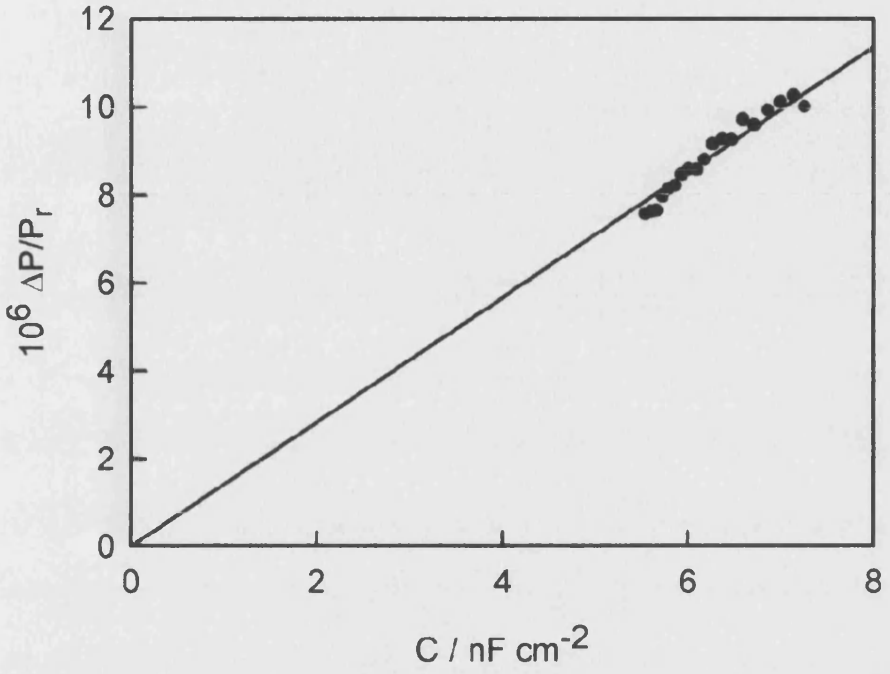

Figure 6.2: Capacitance-microwave plot.

The sensitivity factor can be calculated from the slope

$$\begin{aligned} S &= \frac{R \times d \times \text{slope}}{\mu_p \times \Delta\phi} \\ &= \frac{0.5 \times 350 \times 10^{-4} \times 1421}{460 \times 0.1} \\ &= 0.54 \ \Omega \text{ cm} \end{aligned} \tag{6.1}$$

This indicates that the sensitivity factor in the dark is different from that under illumination and the sensitivity factor under illumination is discussed later. Fig 6.3 shows the Mott-Schottky plot of p-Si in 1M fluoride (pH 3). From the slope, the doping density can be obtained

$$\begin{aligned} N_A &= \frac{2}{q\varepsilon_0\varepsilon_r A^2 \text{slope}} \\ &= \frac{2}{1.6 \times 10^{-19} \times 8.854 \times 10^{-14} \times 11.9 \times (0.21)^2 \times 3.67 \times 10^{17}} \\ &= 7.3 \times 10^{14} \text{cm}^{-3} \end{aligned}$$

The doping density of 7.3×10^{14} cm^{-3} was obtained from the slope and the flat band potential of 0.6 V were obtained from the intercept with x axis.

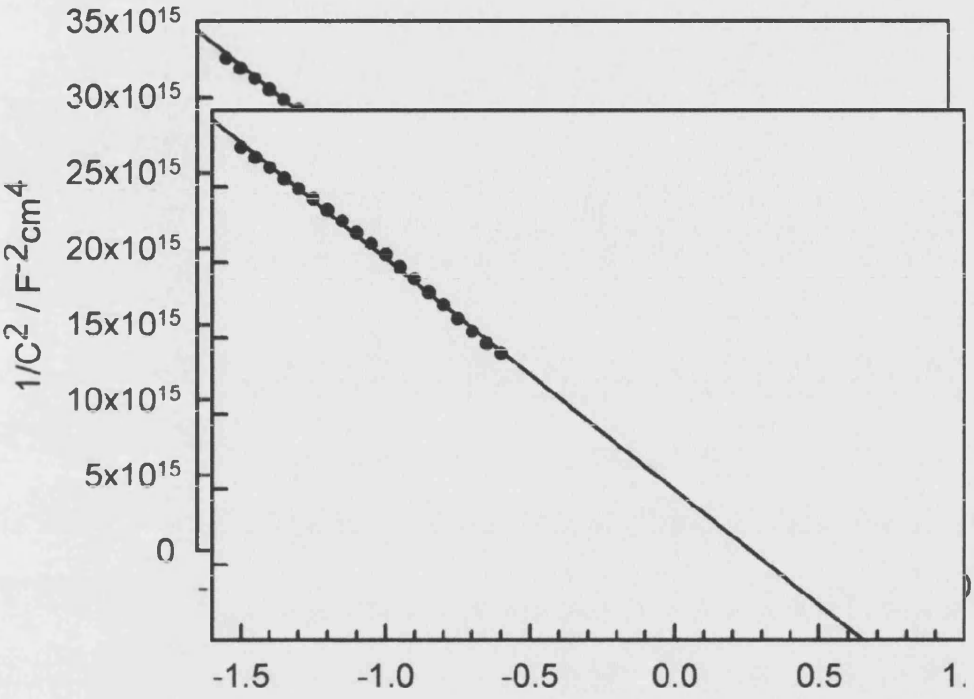

Figure 6.3: Mott-Schottky plot for p-Si in 1 M fluoride (pH 3).

The reported flat band potentials of p-Si are generally less positive than 0.6 V.

Orientation	N_A / cm^{-3}	Electrolyte	V_{fb} vs SCE / V	Reference
111	7×10^{16}	5% HF	0.15-2	[1]
111	-	10M NH_4F	0.3	[5]
111	2.7×10^{15}	0.5M HF+0.5M NH_4F	0.14	[6]
100	3×10^{15}	0.5 M HF	0.16	[7]

Table 6.1: Flat band potential of p-Si.

The flat band potential values vary considerably and the least positive flat band potential in the present work is 0.2 V, which is in good agreement with Table 6.1. The problem with p-type Si in HF media is that the flat band potential is affected by surface preparation and hydrogen incorporation. The effect of surface preparation on the flat band potential was studied by de Mierry [1–4] and hydrogen incorporation was studied

by Allongue [5].

de Mierry *et al.* prepared Si (111) sample ($N_A = 7 \times 10^{16}$ cm^{-3} for p-type and $N_D = 2.5 \times 10^{15}$ cm^{-3}) by 3 methods

1. Mechanical etching (MC)

Si was mechanically polished with diamond paste (0.1 mm, grain size), then the surface was polished, using 0.4M $Cu(NO_3)^{2+}$ in 7M NH_4F solution. Cu ion free silicon surface was obtained according to the following chemical reaction

$$Si + 2Cu^{2+} + 6F^{-} \longrightarrow SiF_6^{2-} + 2Cu$$

2. Chemical etching (C)

Si was mechanically polished with diamond paste and etched in HNO_3 : CH_3COOH : HF = 16:3:1 by volume. The etch rate is 2 μm min^{-1}.

3. Annealing (MC_A and C_A)

The sample prepared by mechanical etching and chemical etching was annealed at 450°C for 24 h in a 10^{-6} bar vacuum.

Fig 6.4 shows the Mott-Schottky plots of n- and p-type Si in 5% HF.

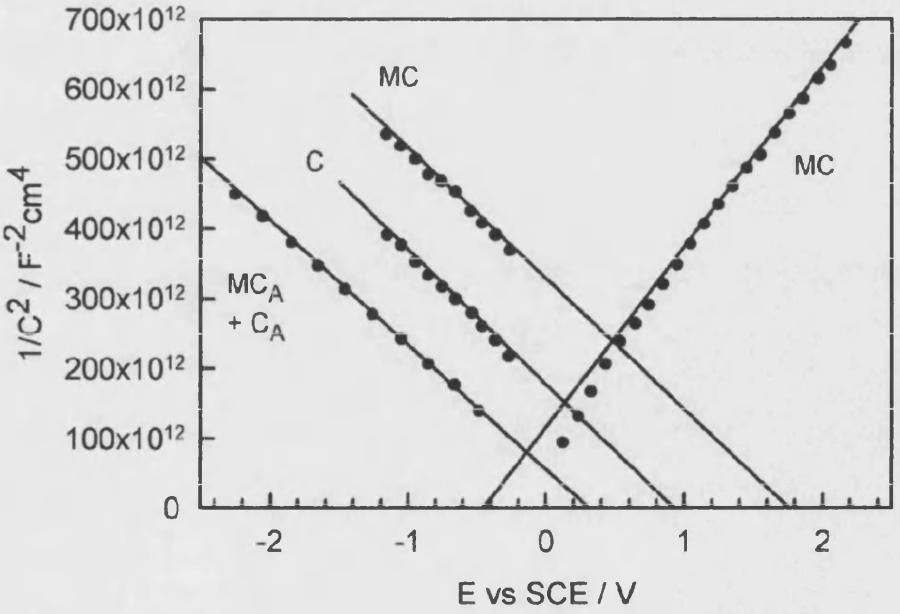

Figure 6.4: The effect of surface preparation on flat band potential in 5 % HF [1].

It can be seen that the preparation process of Si electrode affects the flat band potential significantly. In our case, CP-4A etching solution (HNO_3 : CH_3COOH : HF = 5:3:3 by volume) was used to smooth the surface.

It is known that hydrogen interacts with impurities in semiconductors. In the case of Si, electrical energy levels associated with metallic impurities can be neutralised by hydrogen. In addition, the incorporation of hydrogen causes a strong increase in the resistivity of p-Si due to the electrical neutralisation of dopants (boron in our case) by reaction with hydrogen and the subsequent formation of neutral dopant-H complex. Allongue *et al.* [5] reported that the flat-band potential shifts around 0.5 V after 8 min immersing in 10 M NH_4F solution (pH 4), as shown in Fig 6.5.

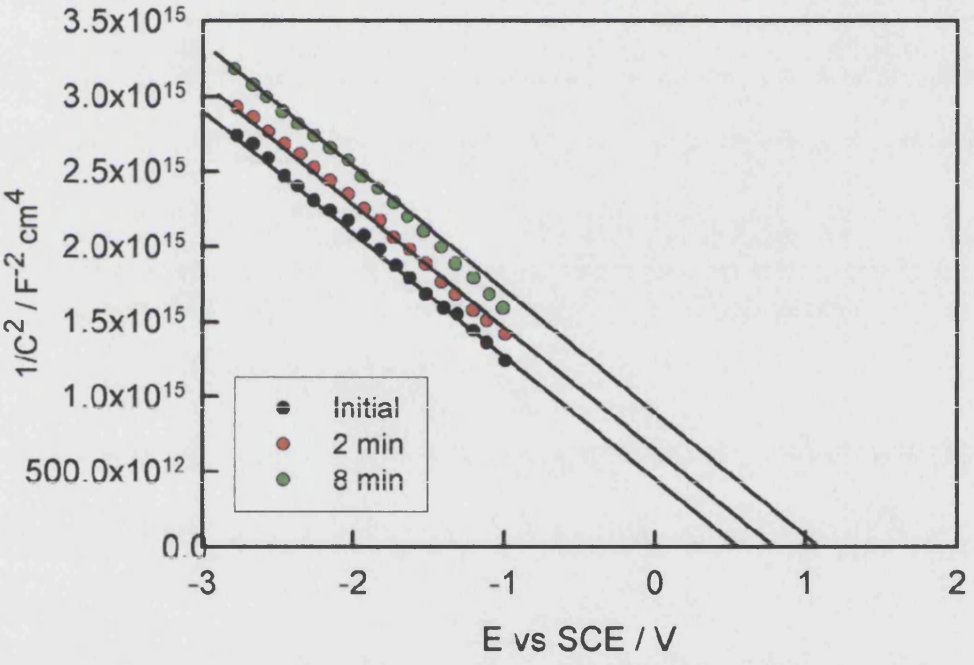

Figure 6.5: The effect of time on flat band potential [5].

The initial condition of Si surface is hydrogen terminated and the presence of hydrogen in the near surface region of Si was confirmed by infra-red spectroscopy. de Mierry *et al.* [4] reported that the diffusion length of hydrogen into Si lattice is 100 nm for the low doped p-type Si ($N_A = \sim 10^{16}$ cm^{-3}). The bond length of Si-H bond and Si-Si bond can be approximated to a few Angstroms. Taking into account hydrogen terminated surface and hydrogen incorporation, we suppose that silicon crystal at the

surface is as shown in Fig 6.6.

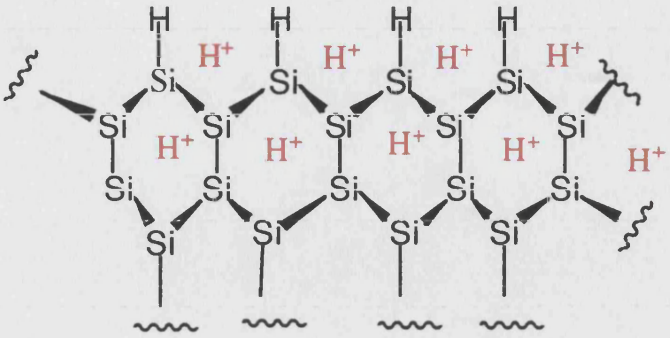

Figure 6.6: Hydrogen terminated Si (111) surface. Note that the bond behind the Si is not shown.

Using 0.2 V vs. Ag/AgCl for the flat band potential leads to the following energy diagram

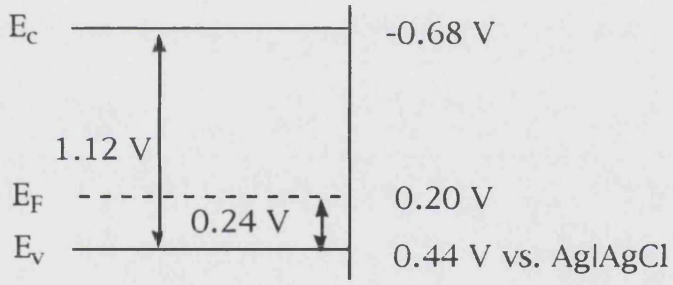

Figure 6.7: Band diagram of p-Si.

The microwave Mott-Schottky plot corresponding to Fig 6.3 is shown in Fig 6.8. It is seen that the flat band potential obtained from microwave Mott-Schottky is in good agreement with that from the conventional capacitance measurements.

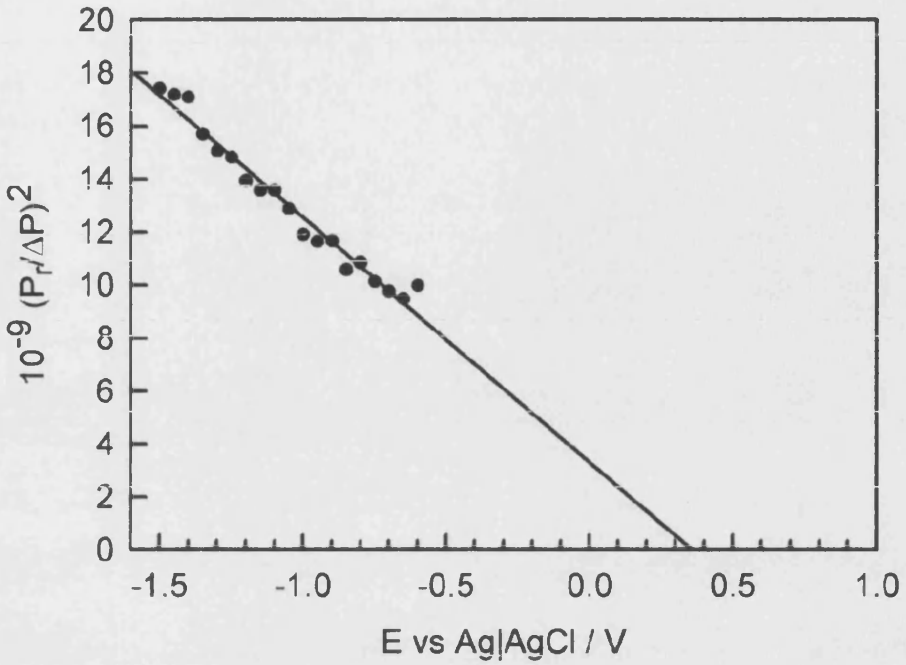

Figure 6.8: The microwave Mott-Schottky plot corresponding to Fig 6.3 for p-Si in 1 M fluoride (pH 3).

The time dependent microwave reflectance with 100 mV rms of modulation amplitude was calculated, applying from eq 3.46 to eq 3.49 and shown in Fig 6.9. The relationship between instantaneous maximum potential and root mean square potential is given by

$$\phi_{\text{rms}} = \frac{\phi_{\text{max}}}{\sqrt{2}} \tag{6.2}$$

For 100 mV rms, the instantaneous potential is

$$\begin{aligned} \phi_{\text{max}} &= \phi_{\text{rms}}\sqrt{2} \\ &= 0.1 \times \sqrt{2} \\ &= 0.14 \quad \text{V} \end{aligned}$$

The details are shown in Appendix A3.

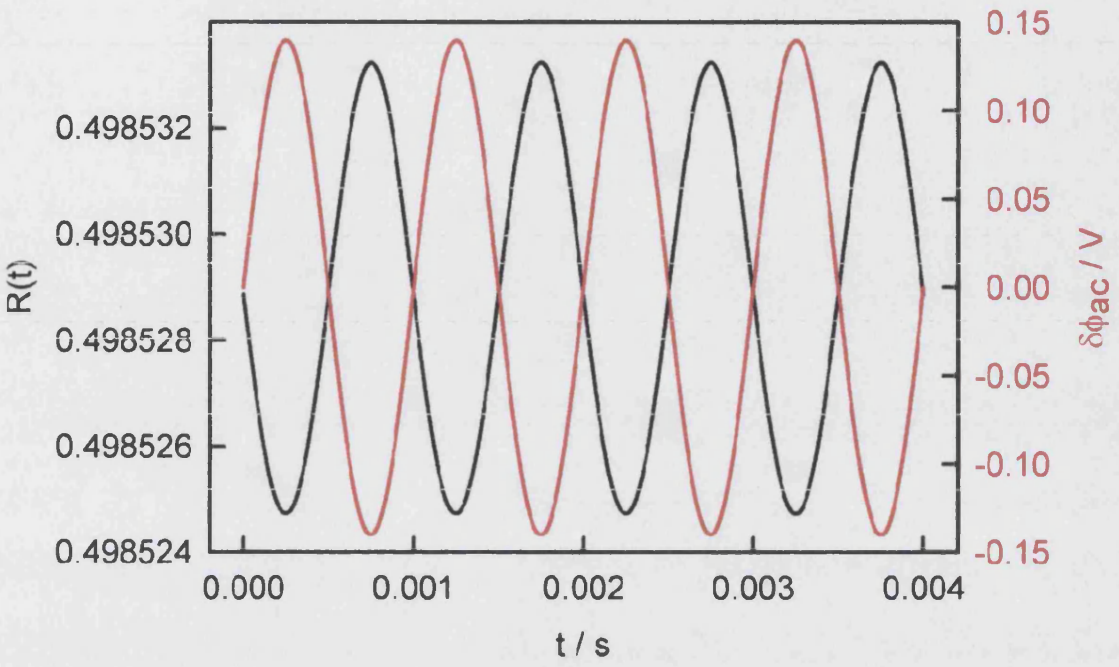

Figure 6.9: Microwave reflection at $E - E_{fb}$ = -1.2 V with the modulation amplitude of 100 mV rms.

From Fig 6.9 the normalised reflectance is

$$\begin{aligned} \frac{\Delta R}{R} &= \frac{0.49853311 - 0.49852467}{0.498529} \\ &= \frac{8.44 \times 10^{-6}}{0.498529} \\ &= 1.69 \times 10^{-5} \text{ at } E - E_{fb} = \text{-1.2 V} \end{aligned} \tag{6.3}$$

This value is reasonably in good agreement with the experimental (1.4×10^{-5} at -0.6 V in peak to peak value).

The theoretical value of the sensitivity factor is

$$S = \frac{\Delta R d}{R \mu_p C_{sc} \Delta \phi}$$

Space-charge capacitance is

$$\begin{aligned} C_{sc} &= \sqrt{\frac{\varepsilon_0 \varepsilon_r q N_A}{2(E - E_{fb})}} \\ &= \sqrt{\frac{11.9 \times 8.854 \times 10^{-14} \times 1.6 \times 10^{-19} \times 7.3 \times 10^{14}}{2 \times 1.2}} \end{aligned}$$

$$= 7.16 \times 10^{-9}\ \mathrm{F\,cm^{-2}}$$

This value can be used to obtain the sensitivity factor

$$S = \frac{8.44 \times 10^{-6} \times 350 \times 10^{-4}}{0.498529 \times 460 \times 7.16 \times 10^{-9} \times 0.283}$$
$$= 0.64$$

The theoretical value of sensitivity factor is in good agreement with the experimental (0.54).

6.2 n-type silicon

The capacitance-voltage curve for n-Si in 1M fluoride (pH 4.5) is shown in Fig 6.10. It is seen that the microwave response is almost superimposable with the capacitance. Again the microwave response is linearly proportional to capacitance as shown in Fig 6.11.

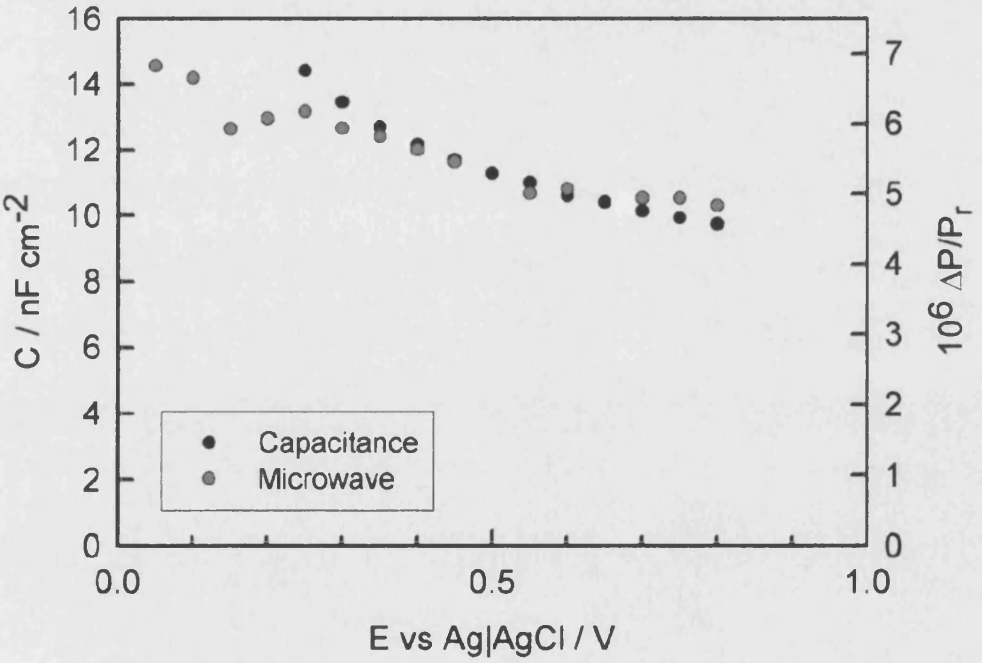

Figure 6.10: Capacitance-Voltage curve and the microwave-voltage curve for n-Si in 1 M fluoride (pH 4.5).

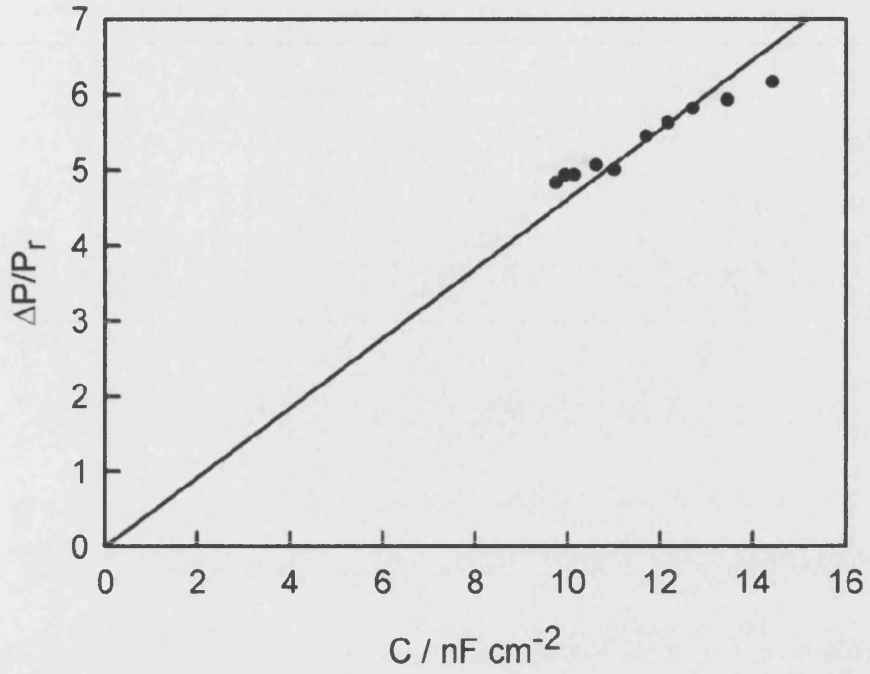

Figure 6.11: Capacitance-microwave plot.

The sensitivity factor can be calculated from the slope.

$$\begin{aligned} S &= \frac{R \times d \times \text{slope}}{\mu_p \times \Delta\phi} \\ &= \frac{0.5 \times 350 \times 10^{-4} \times 462}{460 \times 0.04} \\ &= 0.43 \ \Omega\,\text{cm} \end{aligned} \tag{6.4}$$

This value is quite similar to the sensitivity factor for p-Si in 1M fluoride (pH 3). Mott-Schottky plot is shown in Fig 6.12. The doping density can be obtained from Mott-Schottky relation

$$\begin{aligned} N_D &= \frac{2}{q\varepsilon_0\varepsilon_r A^2 \text{slope}} \\ &= \frac{2}{1.6 \times 10^{-19} \times 8.854 \times 10^{-14} \times 11.9 \times 1 \times 10^{16}} \\ &= 1.23 \times 10^{15}\,\text{cm}^{-3} \end{aligned}$$

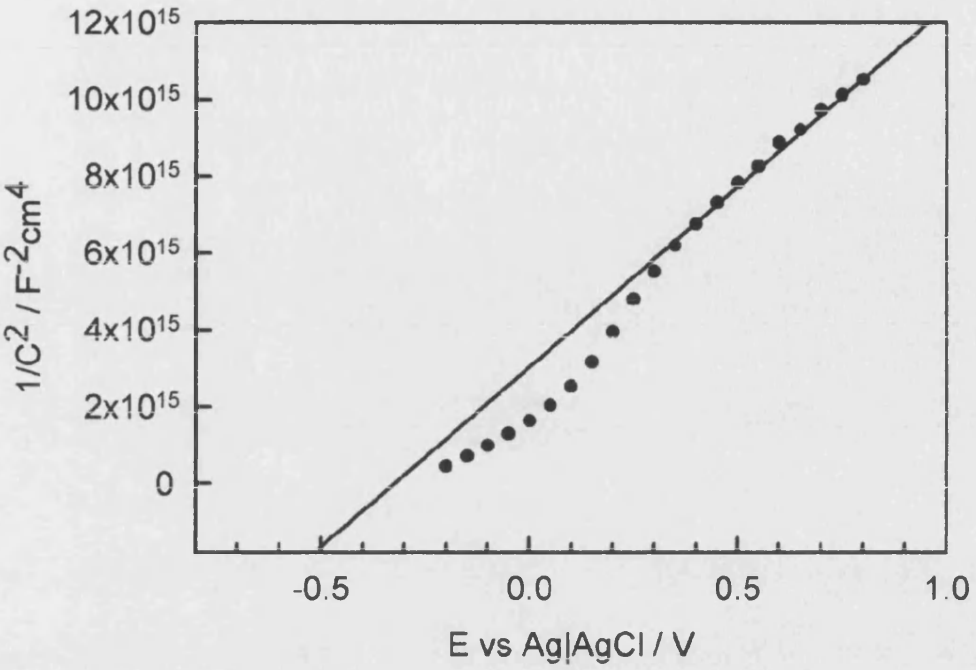

Figure 6.12: Mott-Schottky plot for n-Si in 1 M fluoride (pH 4.5).

The doping density of $1.23 \times 10^{15}\text{cm}^{-3}$ and the flat band potential of -0.5 V were obtained from the capacitance measurement. This value agrees with the literature [8, 9]. It should be noted that the determination of flat band potential involves a substantial extrapolation since the electrode capacitance increases very steeply between 0.2 V and 0.3 V. Probably it indicates the presence of a high density of surface state.

In order to draw the energy diagram for n-Si, it is necessary to know the energy difference between the conduction band and Fermi level. The carrier densities can be expressed as

$$n = N_C \exp\left(-\frac{E_C - E_F}{k_B T}\right) \tag{6.5}$$

Therefore, the energy difference between the conduction band and Fermi level is

$$\begin{aligned} E_C - E_F &= -k_B T \ln\left(\frac{n}{N_C}\right) \\ &= 0.0259 \ln\left(\frac{1 \times 10^{15}}{2.8 \times 10^{19}}\right) \\ &= 0.27 \text{ eV} \end{aligned}$$

A similar energy diagram for n-Si can be drawn as

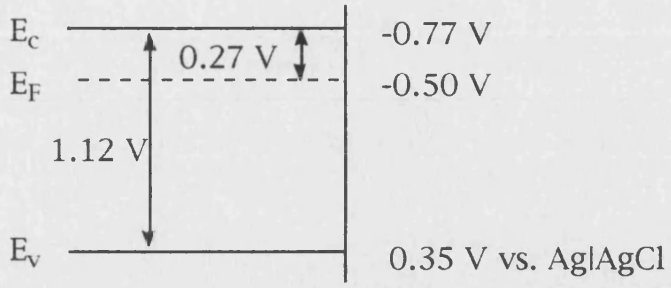

Figure 6.13: Band diagram of n-Si based on the experimental value of flat band potential.

Schlichthörl *et al.* [8] reported that the pH dependence of flat band potential of n-Si in fluoride media was Nernstian, i.e. -59 mV pH^{-1} as shown in Fig 6.14

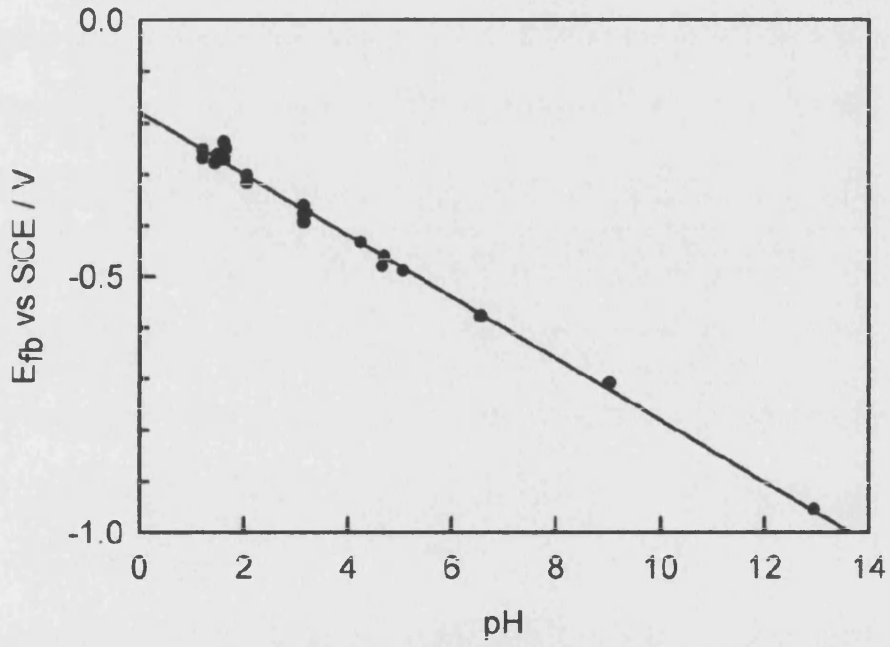

Figure 6.14: pH dependence of the flat band potential of n-Si [8].

If Si surface is covered by oxide, the pH dependence of the flat band potential is understandable since oxide layer changes dipoles, as shown in Fig 6.15.

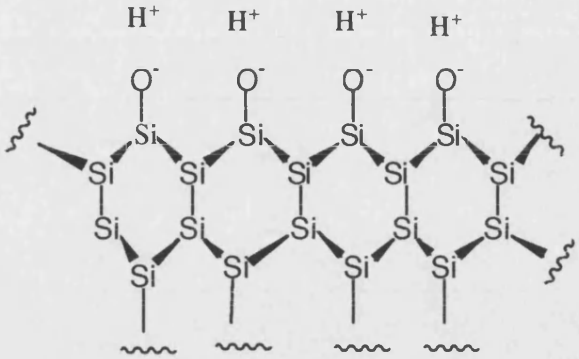

Figure 6.15: Oxygen terminated Si surface.

However, it is known that the surface of Si in fluoride solutions remains hydrogen terminated for pH up to at least 7 and hydrogen termination has been also established for alkaline solutions [17, 18]. A possible explanation for pH dependence of flat band potential is that protons diffuse into the silicon lattice and change the surface dipole, which supports Fig 6.6.

The microwave Mott-Schottky plot is shown in Fig 6.16. It is seen that the flat-band potential is similar to that obtained from the conventional capacitance measurement.

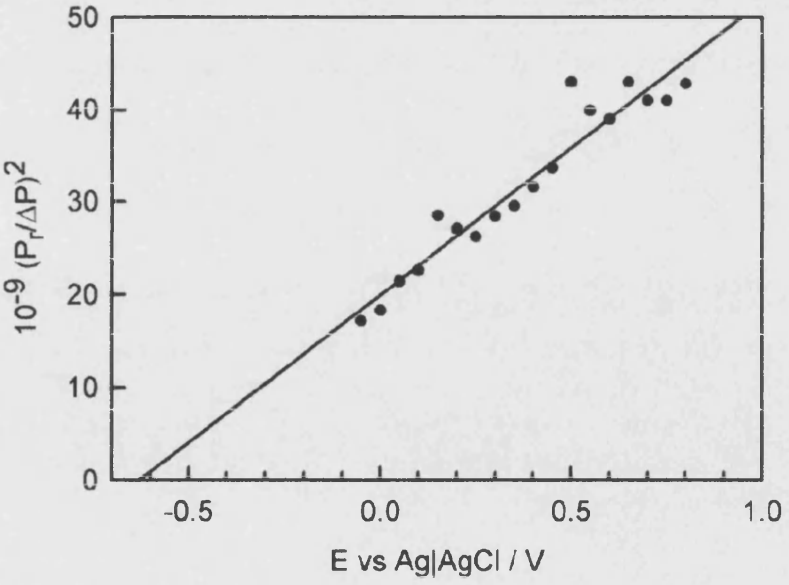

Figure 6.16: The microwave Mott-Schottky plot corresponding to Fig 6.12 for n-Si in 1 M fluoride (pH 4.5).

The theoretical microwave reflectance is shown in Fig 6.17. For 40 mV rms, the instantaneous potential is

$$\begin{aligned} \phi_{max} &= \phi_{rms}\sqrt{2} \\ &= 0.04 \times \sqrt{2} \\ &= 0.056 \text{ V} \end{aligned}$$

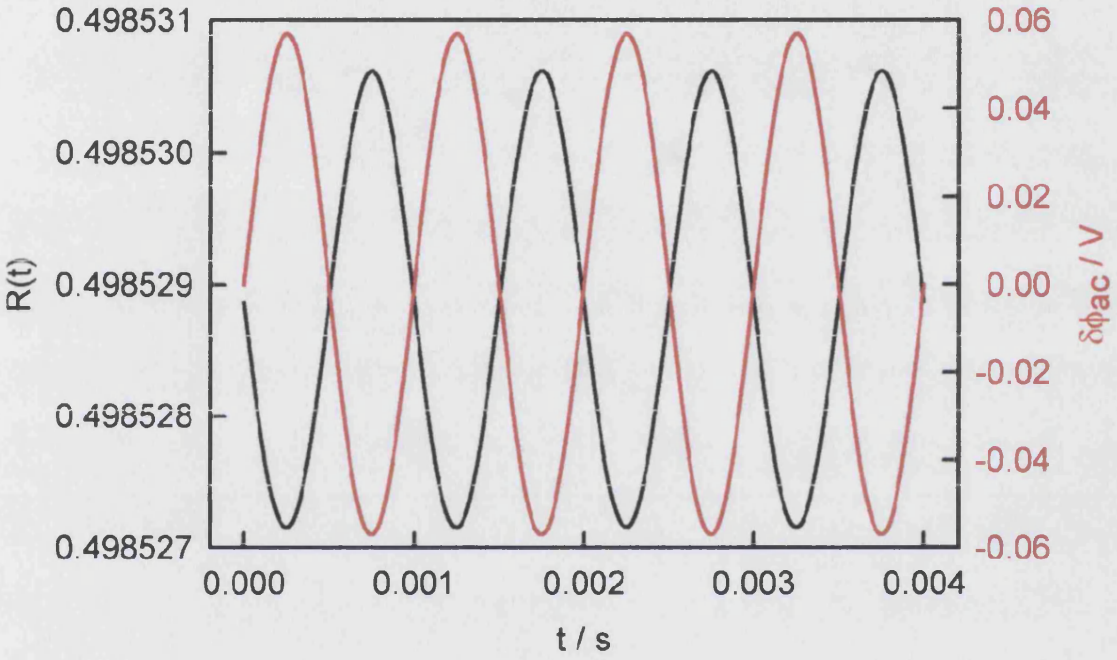

Figure 6.17: Time dependence of microwave reflectivity and modulation amplitude.

From Fig 6.17 the normalised reflectance is

$$\begin{aligned} \frac{\Delta R}{R} &= \frac{0.49853063 - 0.49852718}{0.498529} \\ &= \frac{3.45 \times 10^{-6}}{0.498529} \\ &= 6.92 \times 10^{-6} \text{ at } E - E_{fb} = \text{-}1.2 \text{ V} \end{aligned} \tag{6.6}$$

The theoretical value of the normalised reflectance is 6.92×10^{-6} whereas the experimental value is 7.2×10^{-6} at 0.6 V in peak to peak value.

Space-charge capacitance is

$$C_{sc} = \sqrt{\frac{\varepsilon_0 \varepsilon_r q N_A}{2(E - E_{fb})}}$$

$$= \sqrt{\frac{11.9 \times 8.854 \times 10^{-14} \times 1.6 \times 10^{-19} \times 1.23 \times 10^{15}}{2 \times 1.2}}$$
$$= 9.3 \times 10^{-9}\ \mathrm{F\,cm^{-2}}$$

The theoretical value of the sensitivity factor is

$$S = \frac{\Delta R d}{R \mu_p C_{sc} \Delta\phi}$$
$$= \frac{3.45 \times 10^{-6} \times 350 \times 10^{-4}}{0.498529 \times 460 \times 9.3 \times 10^{-9} \times 0.113}$$
$$= 0.50$$

6.3 Conclusion

p- and n-Si were energetically characterised by capacitance and PMMR measurements. The energy diagram was completed for both p- and n-type Si, based on the flat band potentials. The flat band potentials obtained from the capacitance measurement are consistent to that from the microwave measurement. The doping densities for p- and n-Si were $7.3 \times 10^{14}\mathrm{cm^{-3}}$ and $1.3 \times 10^{15}\mathrm{cm^{-3}}$, respectively and agree with the data sheet. The theoretical microwave reflectance was compared with the experimental, which reasonably agree. About 0.5 of sensitivity factor was obtained for both p-Si in 1M fluoride (pH 3) and n-Si in 1M fluoride (pH 4.5), which are in good agreement of theoretical values.

References

[1] Demierry, P.; Ballutaud, D.; Aucouturier, M.; Etcheberry, A. Journal of the Electrochemical Society **1990**, 137, 2966-2973.

[2] Demierry, P.; Etcheberry, A.; Aucouturier, M. Physica B **1991**, 170, 124-128.

[3] Demierry, P.; Etcheberry, A.; Aucouturier, M. Journal of Applied Physics **1991**, 69, 1099-1101.

[4] Demierry, P.; Etcheberry, A.; Rizk, R.; Etchegoin, P.; Aucouturier, M. Journal of the Electrochemical Society **1994**, 141, 1539-1546.

[5] Allongue, P.; Devilleneuve, C. H.; Pinsard, L.; Bernard, M. C. Applied Physics Letters **1995**, 67, 941-943.

[6] Ottow, S.; Popkirov, G. S.; Foll, H. Journal of Electroanalytical Chemistry **1998**, 455, 29-37.

[7] Searson, P. C.; Zhang, X. G. Electrochimica Acta **1991**, 36, 499-503.

[8] Schlichthörl, G.; Peter, L. M. Journal of Electroanalytical Chemistry **1995**, 381, 55-61.

[9] Schlichthörl, G.; Peter, L. M. Journal of the Electrochemical Society **1994**, 141, L171-L173.

[10] Schlichthörl, G.; Peter, L. M. Journal of the Electrochemical Society **1995**, 142, 2665-2669.

[11] Schlichthörl, G.; Ponomarev, E. A.; Peter, L. M. Journal of the Electrochemical Society **1995**, 142, 3062-3067.

[12] Natarajan, A,; Oskam, G.; Searson, P. C. Journal of Applied Physics, **1998**, 83, 2112-2121.

[13] Natarajan, A.; Nellore, A.; Searson, P. C. Journal of Applied Physics, **1999**, 85, 1631-1636.

[14] Peter, L. M. in Comprehensive chemical kinetics, Vol. 37, Elsevier, New York, 1999.

[15] Peter, L. M.; Vammaekelbergh, D. in Advances in electrochemical science and engineering, Vol.6, VCH, New York, 1999.

[16] daFonseca, C.; Ozanam, F.; Chazalviel, J. N. Surface Science **1996**, 365, 1-14.

[17] Bitzer, T.; Lewerenz, H. J.; Gruyters, M.; Jacobi, K. Journal of Electroanalytical Chemistry **1993**, 359, 287-292.

[18] Dumas, P.; Chabal, Y. J.; Jakob, P. Surface Science **1992**, 270, 867-878.

Chapter 7

Photocathodic reactions at p-Si

7.1 Hydrogen evolution reaction on p-Si

The reduction of H^+ to H_2 is a two-electron process involving an adsorbed hydrogen intermediate. There are many possible mechanisms and two possible mechanisms are shown here;

$$h\nu \rightarrow h^+_{vb} + e^-_{cb}$$
$$H^+ + e^-_{cb} \rightarrow H^{\cdot}_{ads}$$

followed either by

$$H^+ + H^{\cdot}_{ads} + e^-_{cb} \rightarrow H_2 \qquad \text{Electrochemical route}$$

or

$$H^{\cdot}_{ads} + H^{\cdot}_{ads} \rightarrow H_2 \qquad \text{Chemical route}$$

When an electron-hole pair is generated under illumination, the electron is either transferred to the electrolyte or recombines with holes. If the electron is transferred to the surface, H^+ is reduced to H_2 in acidic media, as illustrated in Fig 7.1.

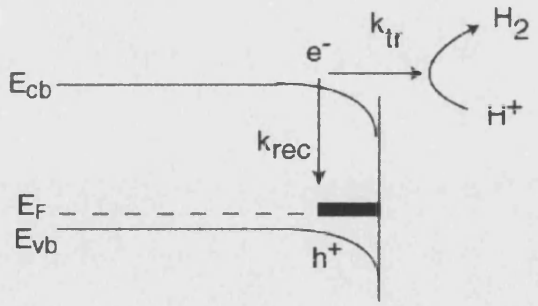

Figure 7.1: Electron transfer and recombination at p-Si. k_{tr} and k_{rec} are the rate constants for the electron transfer and recombination, respectively.

The current-voltage curve was recorded under sinusoidal modulation of the light intensity as shown in Fig 7.2.

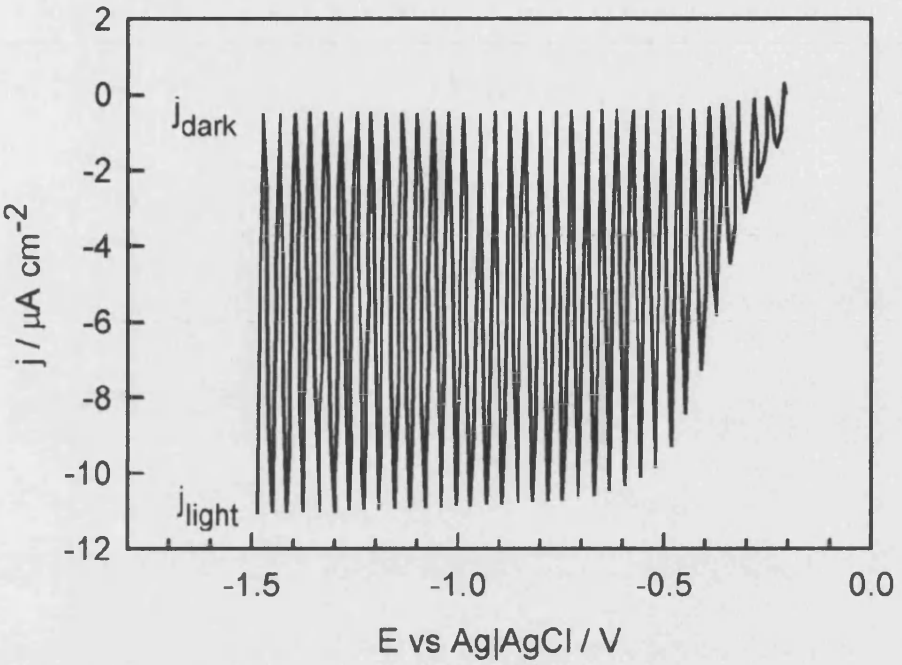

Figure 7.2: Current-voltage curve for p-Si in 1 M fluoride (pH 3) at 0.5 Hz.

It is noted that the recorded current contains both dc and ac components. The bottom points of the sinusoidal curve represents the current under illumination, j_{light}, and the top of the sinusoidal curve represents the current in the dark, j_{dark}. Photocurrent, j_{photo}, is the difference between j_{light} and j_{dark}

$$j_{photo} = j_{light} - j_{dark} \tag{7.1}$$

The photocurrent can be measured, using a lock-in amplifier under sinusoidal modulation of the light intensity. The normalised photocurrent-voltage curves for three light intensities recorded at modulation frequency of 10 Hz are shown in Fig 7.3. The assumption for the Gärtner model is that all carriers reaching the space charge region are immediately transferred to the surface and contribute to the photocurrent. This means that the Gärtner model ignores the recombination process and predicts the almost constant photocurrent as shown in Fig 7.3 (1). However, the reduction of photocurrent observed from Fig 7.3 (2)-(4) results from the space charge recombination. In general, the saturation region in the current-voltage curve is due to the charge transfer reaction and there is no surface recombination, whereas on the onset region, the electrons are

either transferred to redox species or recombine with holes. It is noted that the same information is obtained from Fig 7.2 as well.

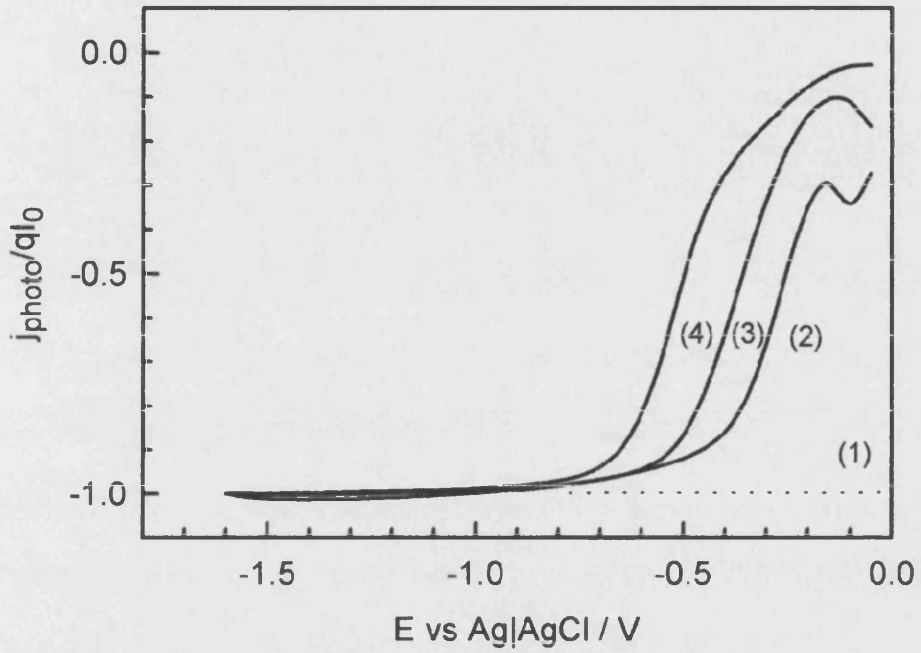

Figure 7.3: Normalised photocurrent-voltage curve for p-Si in 1 M fluoride (pH 3). (1) Gärtner model (2) j_{photo} = -0.7 μAcm^{-2} (3) j_{photo} = -7.6 μAcm^{-2} (4) j_{photo} = -91 μAcm^{-2} in saturation region.

The light induced microwave response recorded simultaneously is shown in Fig 7.4. The general shape of the microwave response curves follows the predictions of the model. The microwave response curves shift along the potential axis with increasing illumination intensity, which follows the behaviour of the photocurrent voltage plots. This shift could be caused by recombination or it could indicate that the accumulation of electrons near the surface alters the potential distribution across the system.

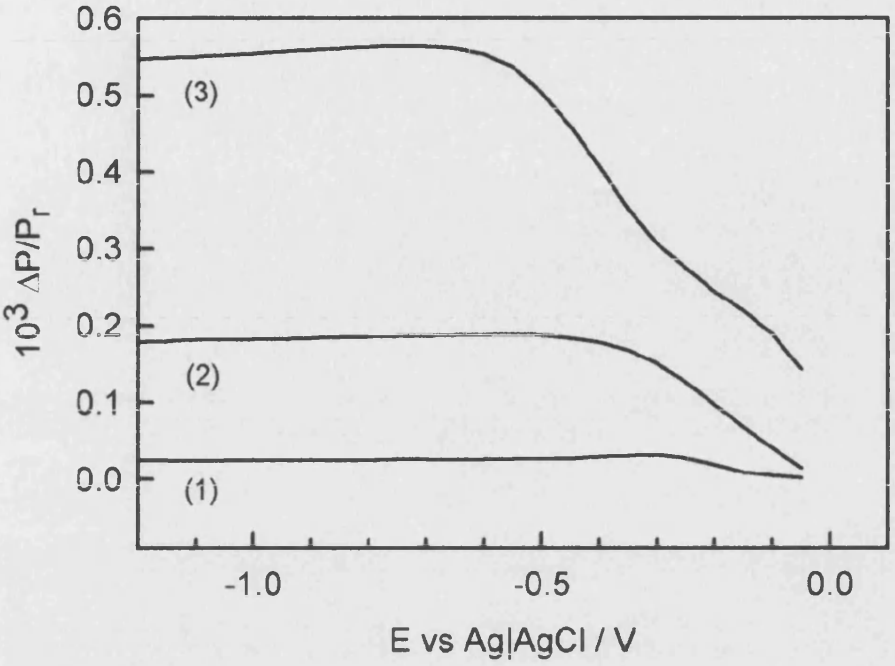

Figure 7.4: Microwave response for p-Si in 1 M fluoride (pH 3). (1) j_{photo} = -0.7 μAcm^{-2} (2) j_{photo} = -7.6 μAcm^{-2} (3) j_{photo} = -91 μAcm^{-2}. Note that microwave response is not normalised.

It is interesting to note that the microwave response is not linearly proportional to the photocurrent as shown in Fig 7.5. The reason is not clearly understood at present, but we believe that a large concentration of electrons are accumulated at the surface and results in the reduction of carrier mobility, which gives non-linear response (see Fig 2.28 and Fig 2.31). The details of the reduction of carrier mobility is discussed in Chapter 8.

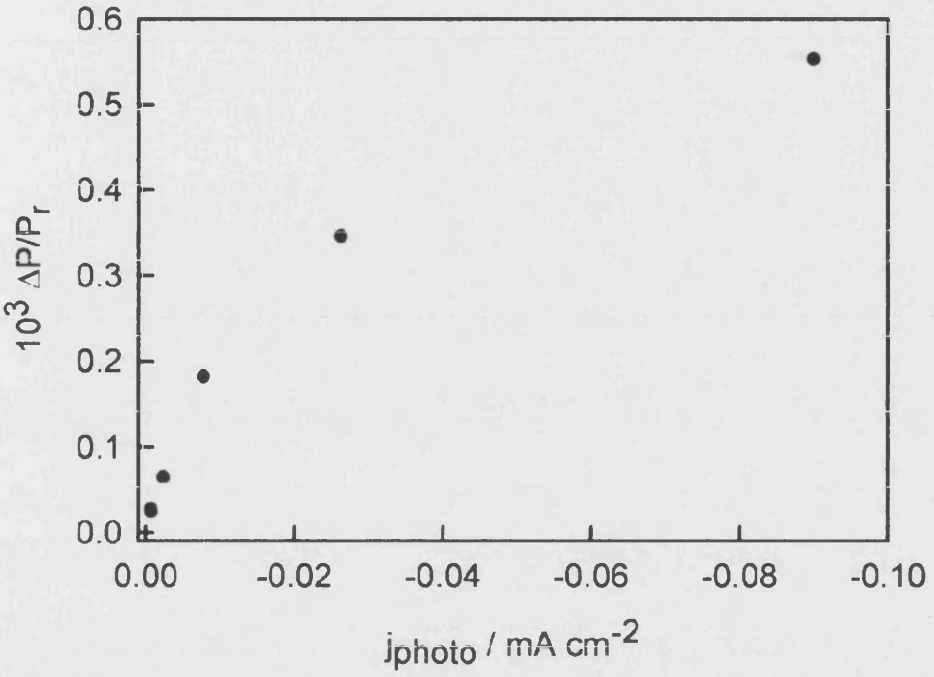

Figure 7.5: Microwave response as a function of photocurrent at -1.0 V.

7.2 Time- and frequency-resolved analysis

Light Modulated Microwave Reflectivity (LMMR) and Intensity Modulated Photocurrent Spectroscopy (IMPS) were used to study kinetics of charge transfer at p-Si|fluoride interface. It is already seen that there is no surface recombination in the saturation region of the current-voltage curve. It is predicted that IMPS response gives a small semicircle in this potential. On the other hand, a large semicircle is expected in the onset region since the competition between electron transfer and surface recombination is observed. Fig 7.6 illustrates these behaviour corresponding to theoretical predictions as discussed in Section 4.3. in Chapter 4. It can be seen that diameters of the IMPS semicircles decrease with increasing a band bending. The high frequency intercept is almost constant, whereas the low frequency intercept moves away from the origin as the band bending is increased. On the other hand, the diameters of LMMR semicircle increase with increasing the band bending, tending towards a limiting value in the saturation photocurrent region. This is due to the decrease in recombination rate with increasing band bending.

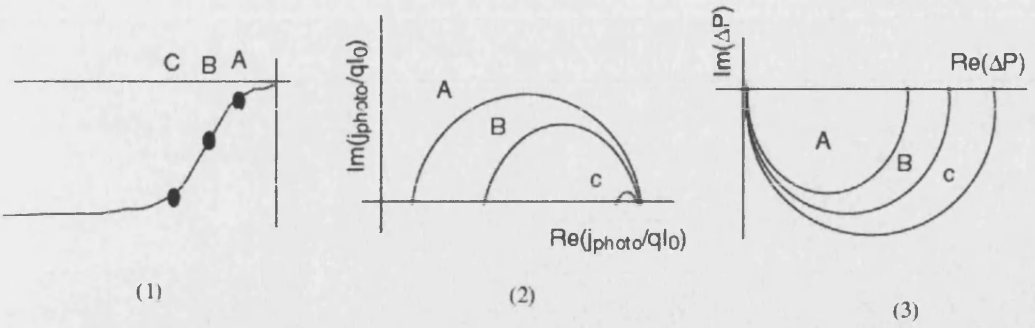

Figure 7.6: (1) i-V curve at cathodic potentials (2) theoretical prediction of IMPS responses (3) theoretical prediction of LMMR responses.

LMMR and IMPS responses were recorded at several potentials as illustrated in Fig 7.8 and Fig 7.9, respectively. It is seen from Fig 7.8 that the response becomes in-phase with increasing the band bending. The phase is given by

$$\theta = \arctan\left(\frac{\mathrm{Im}(\Delta \mathrm{P})}{\mathrm{Re}(\Delta \mathrm{P})}\right) \tag{7.2}$$

If Re(ΔP) is positive and Im(ΔP) is negative, which gives θ_1, no correction is required. On the other hand, if both Re(ΔP) and Im(ΔP) are negative, which gives θ_2, θ_3 can be obtained, subtracting θ_2 from 180°.

$$\theta_3 = -(180 - \theta_2) \tag{7.3}$$

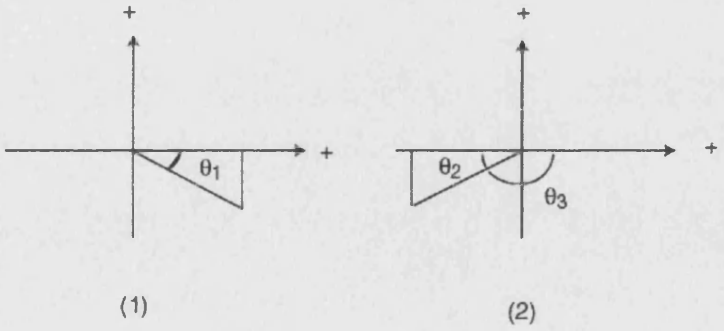

Figure 7.7: (1) In the case of real component is positive and imaginary component is negative (2) in the case of both real and imaginary components are negative.

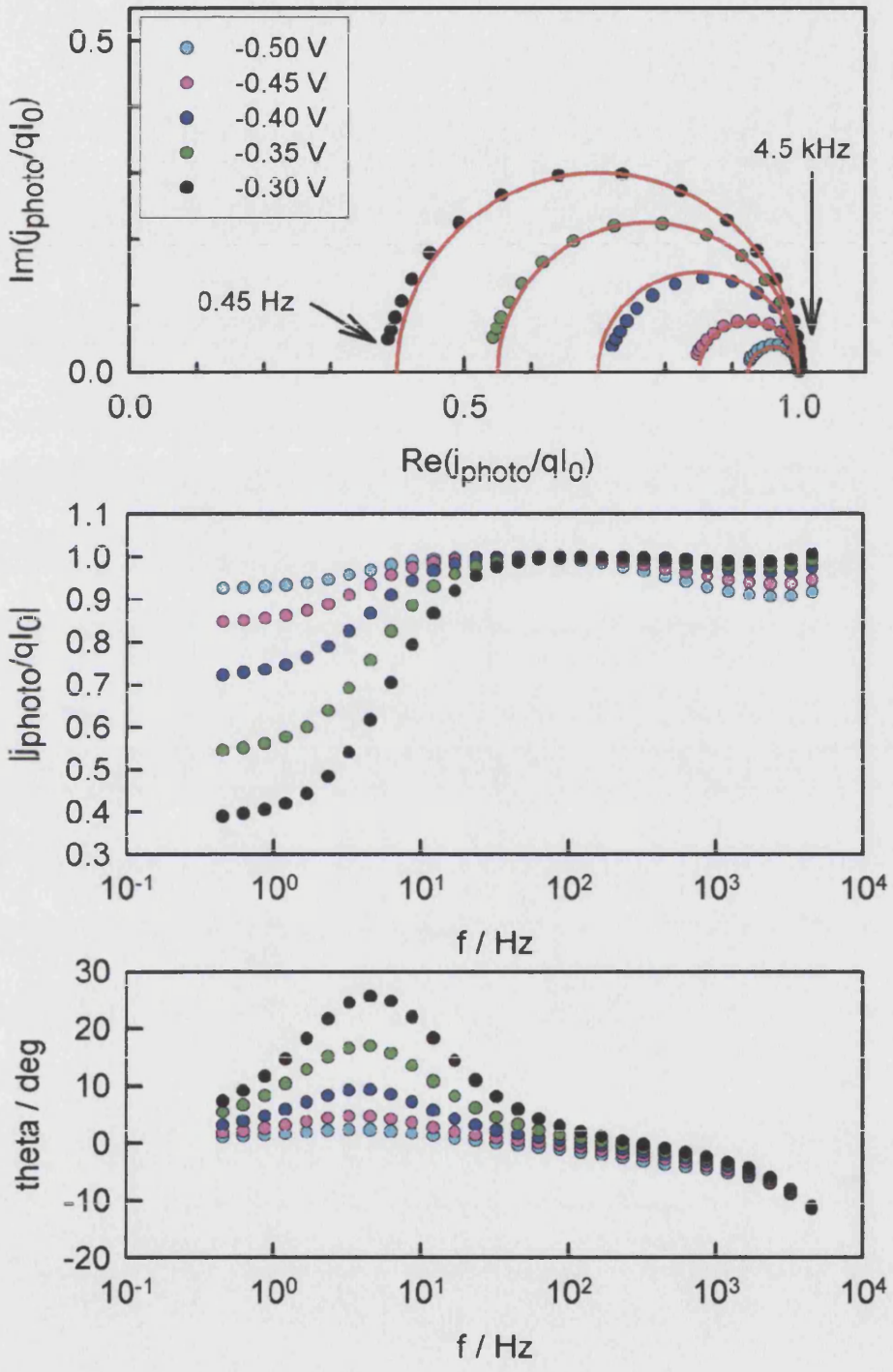

Figure 7.8: Complex and Bode plots of IMPS of p-Si in 1M fluoride (pH 3). j_{photo} = -3.4 μA cm^{-2} at the saturation region on current-voltage curve.

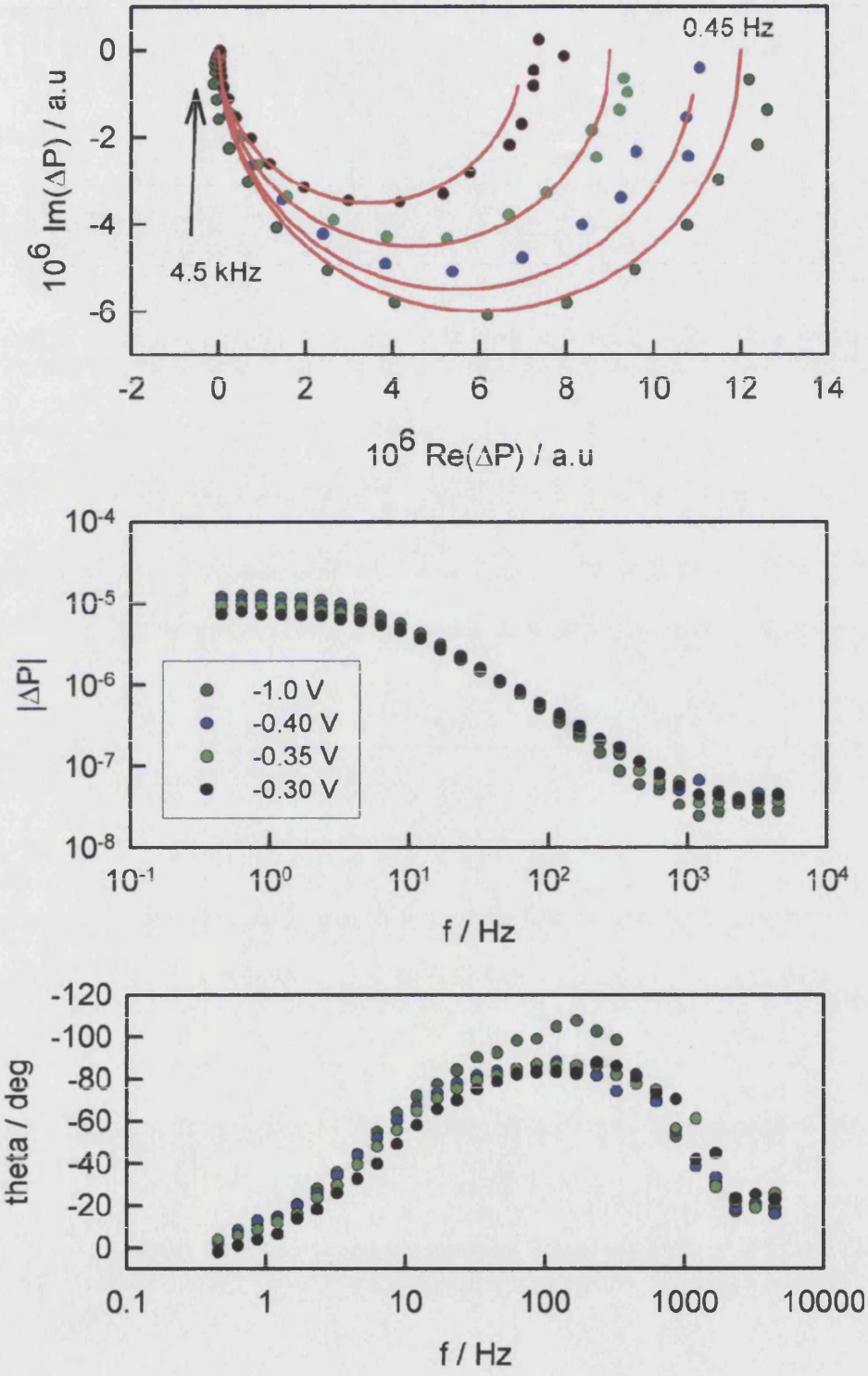

Figure 7.9: Complex and Bode plot of LMMR of p-Si in 1M fluoride (pH 3). j_{photo} = -3.4 μA cm^{-2} at the saturation region on current-voltage curve.

Since $\omega_{max} = 2\pi f = k_{tr} + k_{rcc}$ and low frequency intercept = $\frac{k_{tr}}{k_{tr}+k_{rec}}$ from the IMPS semicircle, k_{tr} and k_{rec} are separated. The rate constants are summarised in Table 7.1.

E / V	$k_{tr} + k_{rec}$ / s^{-1}		k_{tr} / s^{-1}	k_{rec} / s^{-1}
	LMMR	IMPS		
-0.55	25	19	18	1
-0.50	25	23	21	2
-0.45	26	26	22	4
-0.40	28	29	20	9
-0.35	32	35	19	16
-0.30	45	47	17	30

Table 7.1: The rate constants derived from IMPS and LMMR

The value of electron transfer rate constant is about 20 s^{-1} and almost independent of potential, whereas k_{rec} depends strongly on potential as shown in Fig 7.10.

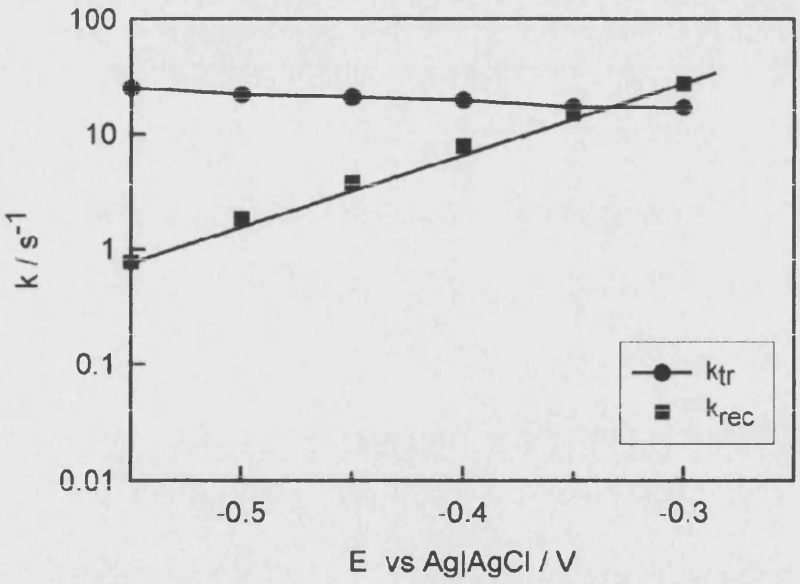

Figure 7.10: The potential dependence of the rate constants of p-Si in 1M fluoride (pH 3) at j = 4 $\mu A\,cm^{-2}$. A slope is 5.6 for k_{rec}.

Close to the flat band potential, electron-hole pairs are located near the surface, and have a large probability to recombine as illustrated in Fig 7.11 (1). On the other

hand, as the band bending is increased, holes are depleted from the surface (for p-type semiconductor in depletion condition), which reduces the probability to recombine with electrons as shown in Fig 7.11 (2). Therefore, the recombination is potential dependent.

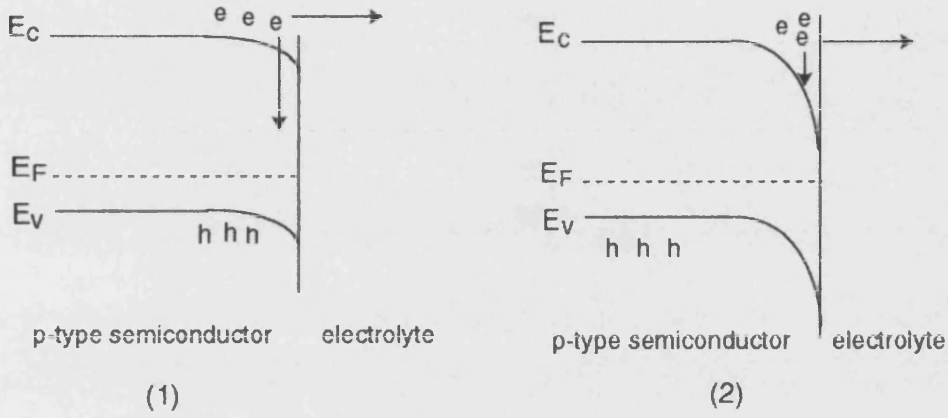

Figure 7.11: The effect of band bending on the recombination. (1) weakly depleted p-type semiconductor (2) deeply depleted p-type semiconductor. Note that the length of vector indicates the probability that the event occurs.

The quantitative analysis of potential dependent k_{rec} can be considered as follows. Electron-hole recombination via surface state is considered. In this case, the rate depends on the concentration of holes at surface.

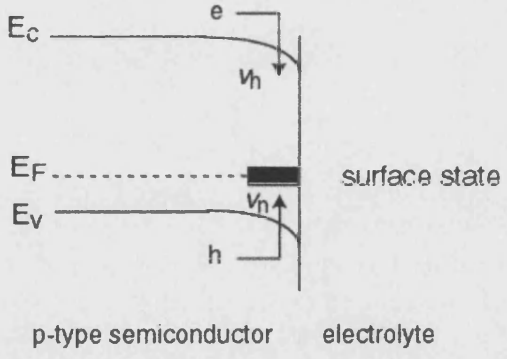

Figure 7.12: A recombination via surface state. v_h and v_n are the rate of electron and holes, respectively.

The rate of electron capture, v_h, is equal to the rate of hole capture, v_n, at steady state.

The rate of capture of electrons by surface state is given by

$$v_h = \nu_{th}\sigma_h N_{ss} f_{ss} p(0) \tag{7.4}$$

Here ν_{th} is thermal velocity in $cm\,s^{-1}$, σ_h is hole capture cross section in cm^{-2}, N_{ss} is density of surface state in cm^{-3}, f_{ss} is occupation of electrons, and p(0) is concentration of holes at x = 0 in cm^{-2}, so that v_h is in $cm^{-2}s^{-1}$.

Eq 7.4 can be simplified as

$$v_h = kp(0) \tag{7.5}$$

where $k = \nu_{th}\sigma_h N_{ss}$.

The concentration of holes depends on the potential drop in the semiconductor

$$p(0) = p_{bulk} \exp\left(-\frac{q\Delta\phi}{k_B T}\right) \tag{7.6}$$

Inserting eq 7.6 into eq 7.5

$$v_h = kp_{bulk} \exp\left(-\frac{q\Delta\phi}{k_B T}\right) \tag{7.7}$$

It is seen from eq 7.7 that electron capture rate depends exponentially on potential.

As discussed before, assuming the tunneling distance as 1.5 nm, first order heterogeneous rate constant is

$$\begin{aligned} k_{tr} &= k_{observed} \times \delta \\ &= 20 \times 15 \times 10^{-8} \\ &= 3 \times 10^{-6}\ cm\,s^{-1} \end{aligned}$$

This confirms that the hydrogen evolution reaction is a slow process.

The time-dependent microwave response of p-Si in NH_4F was studied using light pulses with a small ratio of light period to dark period in order to allow the system to return to its initial state between pulses. The photocurrent response is square in the saturation region as illustrated in Fig 7.13.

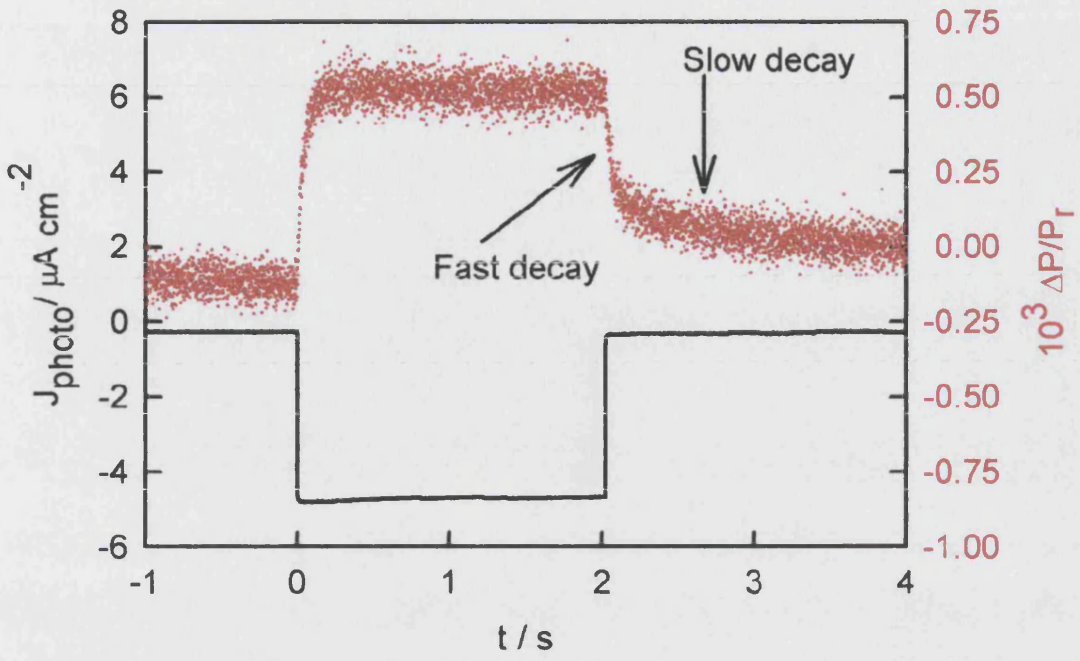

Figure 7.13: Transient photocurrent and the corresponding microwave response for p-Si in 1 M fluoride (pH 3) at -1.0 V.

It is interesting to note from Fig 7.13 that the microwave response does not decay to the initial level when the light is switched off. Instead, an initial decay, which has the same time constant as the rising part of the response, is followed by a much slower relaxation to the initial dark value. The origin of this phenomenon is not clearly understood at present, but we attribute it to the incorporation of hydrogen into the near the surface region of the silicon, modifying its dielectric properties [7–9]. The slow return to the baseline reflectivity could be caused by hydrogen diffusing back out of the silicon in the dark period.

The measured photocurrent responses are related to the electron and holes fluxes as shown in Fig 7.14. The electron displacement current is instantaneous whereas the hole current builds up to a steady state. The measured photocurrent is the sum of the electron and hole contributions. No kinetic information is obtained from the transient photocurrent measurement at the saturation region. On the other hand, the microwave response is determined by the rate constant for electron transfer, so that kinetic information can be obtained in the photocurrent saturation region.

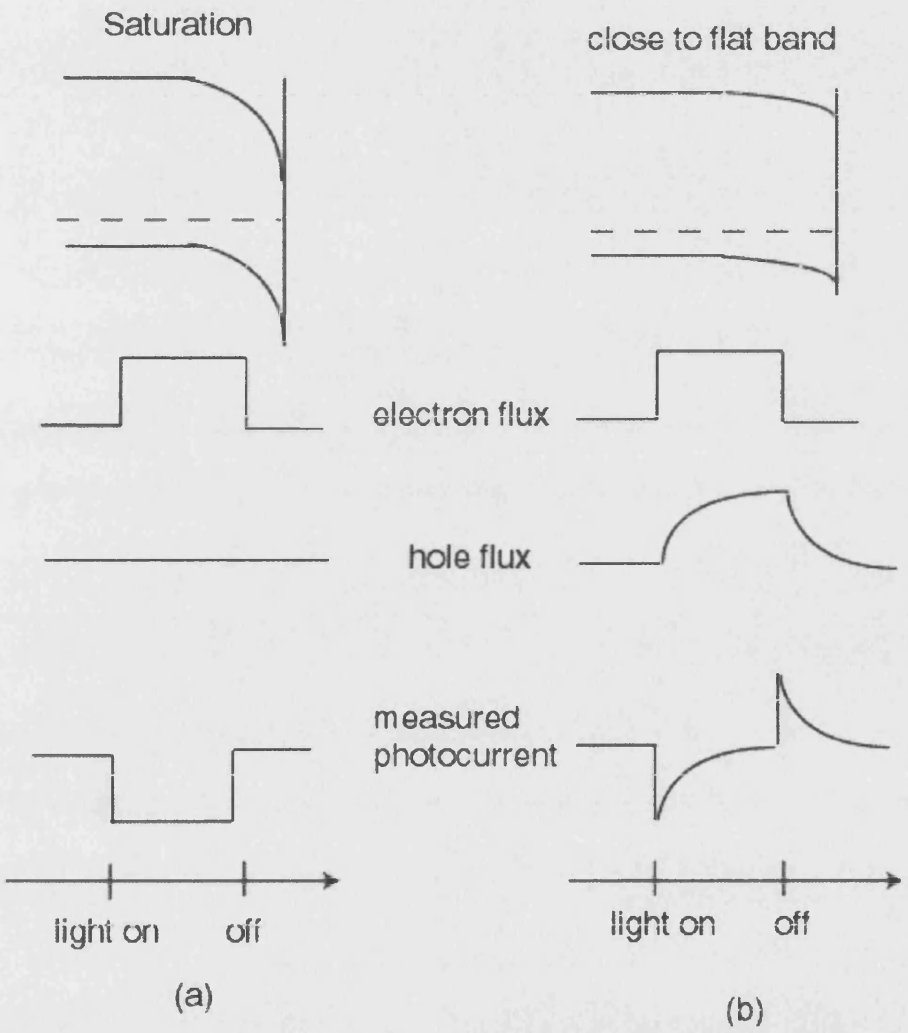

Figure 7.14: Photocurrent response at (a) saturation region (b) onset region. Note that the electron flux is negative components of current and hole flux is positive.

The difference between the rise times of the photocurrent and the microwave signal can be seen clearly in Fig 7.15.

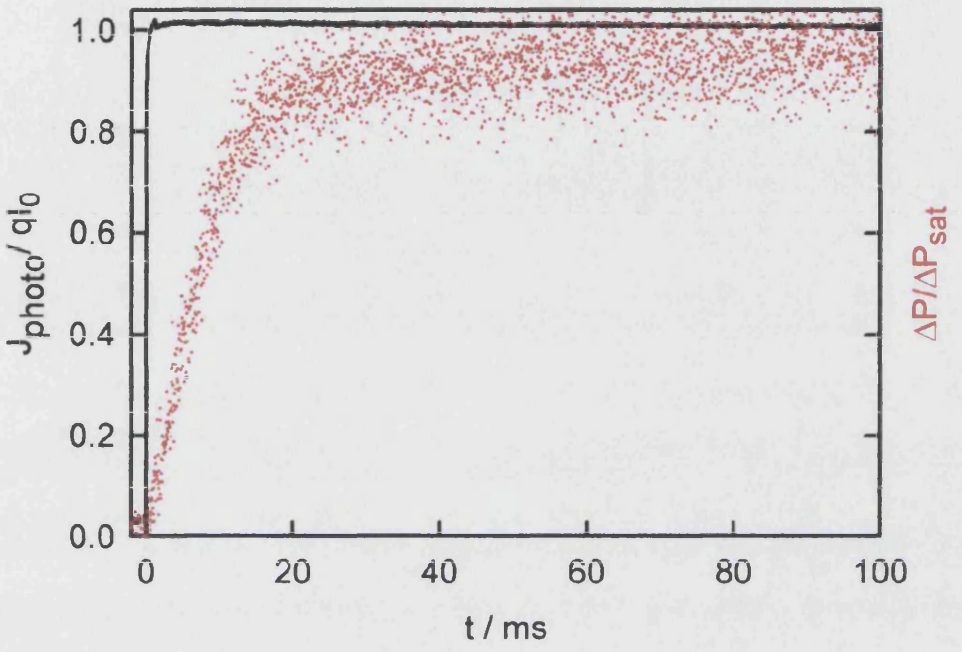

Figure 7.15: Normalised plots of photocurrent and microwave response of p-Si in 1M fluoride (pH 3) at -0.8 V.

Since photocurrent at the saturation region does not give useful information, only the microwave response is fitted, using y = A[1-exp(k(t-a))]+b and y = A[exp(k(t-a))]+b for light on and off, respectively. Here A is the height of the exponential, a is the shift on x coordinate and b on y coordinate as graphically shown in Fig 7.16.

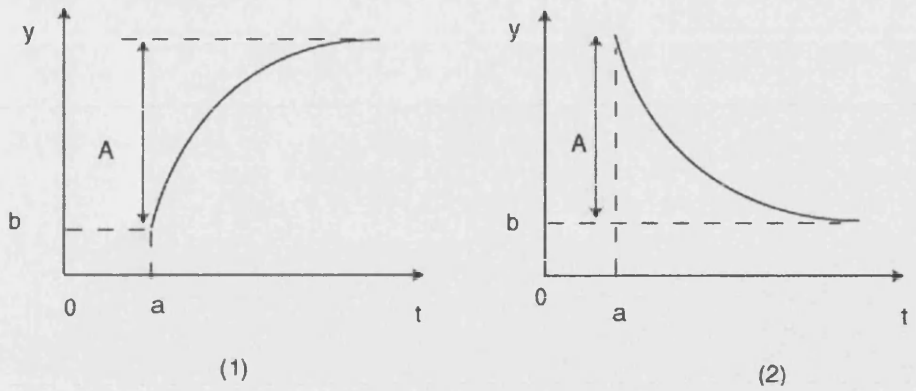

Figure 7.16: Time dependence of exponential form (1) y = A[1-exp(k(t-a))]+b (2) y = A[exp(k(t-a))]+b.

The following values are used to fit the data

$$y = 0.8 \times 10^{-3}[1 - \exp(-28(t + 0.005))] - 0.25 \times 10^{-3} \quad \text{for light on} \quad (7.8)$$

$$y = 0.8 \times 10^{-3}[\exp(-28(t - 2.015))] + 0.15 \times 10^{-3} \quad \text{for light off} \quad (7.9)$$

From eq 7.8 and eq 7.9, We obtain k = 28 s^{-1} for both light on and off, which is reasonably consistent with the values obtained from IMPS and LMMR (25 s^{-1}).

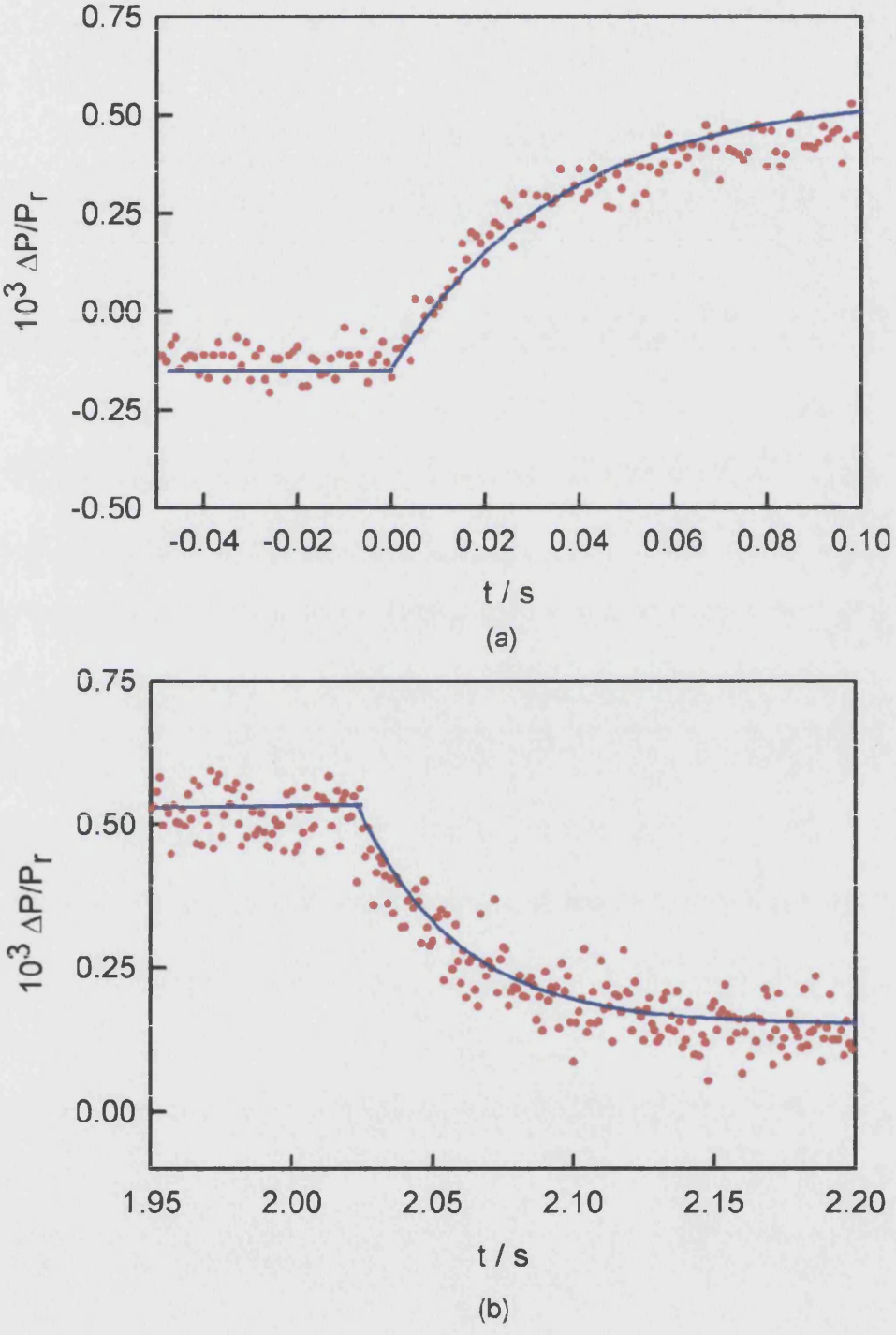

Figure 7.17: Expanded microwave response at -1.0 V a) light on b) light off. Blue line indicates the fitting.

When measurements are carried out at potentials in the photocurrent onset region, the photocurrent exhibits the decay and overshoot that are characteristic features of recombination as shown in Fig 7.18 and the expanded graph is shown in Fig 7.19.

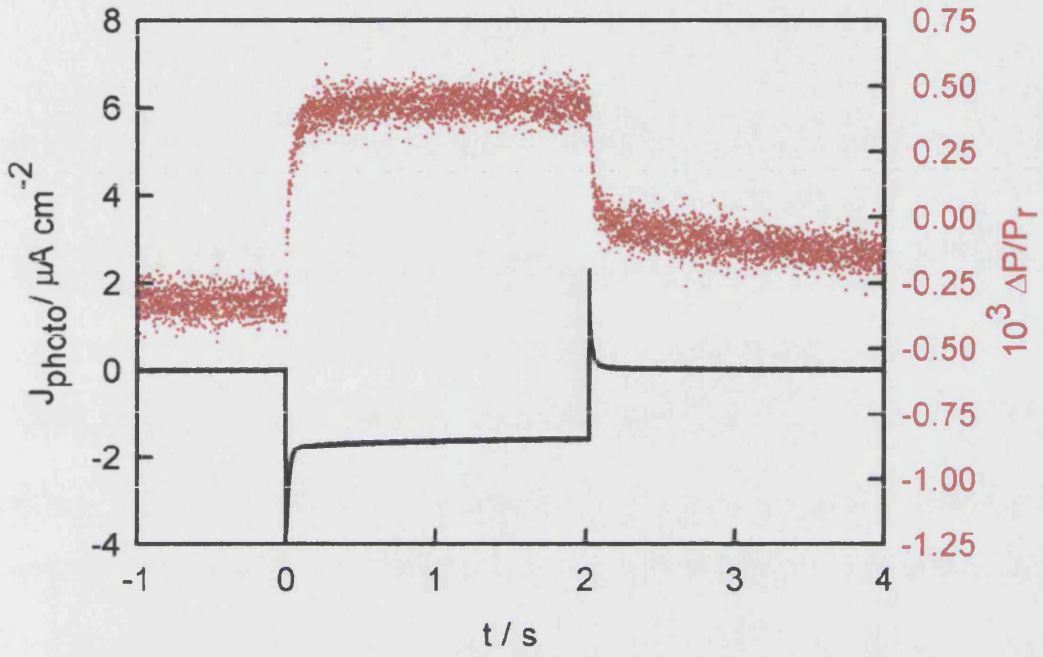

Figure 7.18: Transient photocurrent and the corresponding microwave response for p-Si in 1 M fluoride (pH 3) at -0.35 V.

The following values are used to fit the data

$$y = 0.8 \times 10^{-3}[1 - \exp(-55(t + 0.005))] - 0.5 \times 10^{-3} \quad \text{for light on} \quad (7.10)$$

$$y = 0.8 \times 10^{-3}[\exp(-49(t - 2.015))] \quad \text{for light off} \quad (7.11)$$

We obtain k = 58 and 60 s^{-1} for light on and off, respectively at -0.35 V, which is reasonably consistent with the values obtained from IMPS and LMMR (47 s^{-1}).

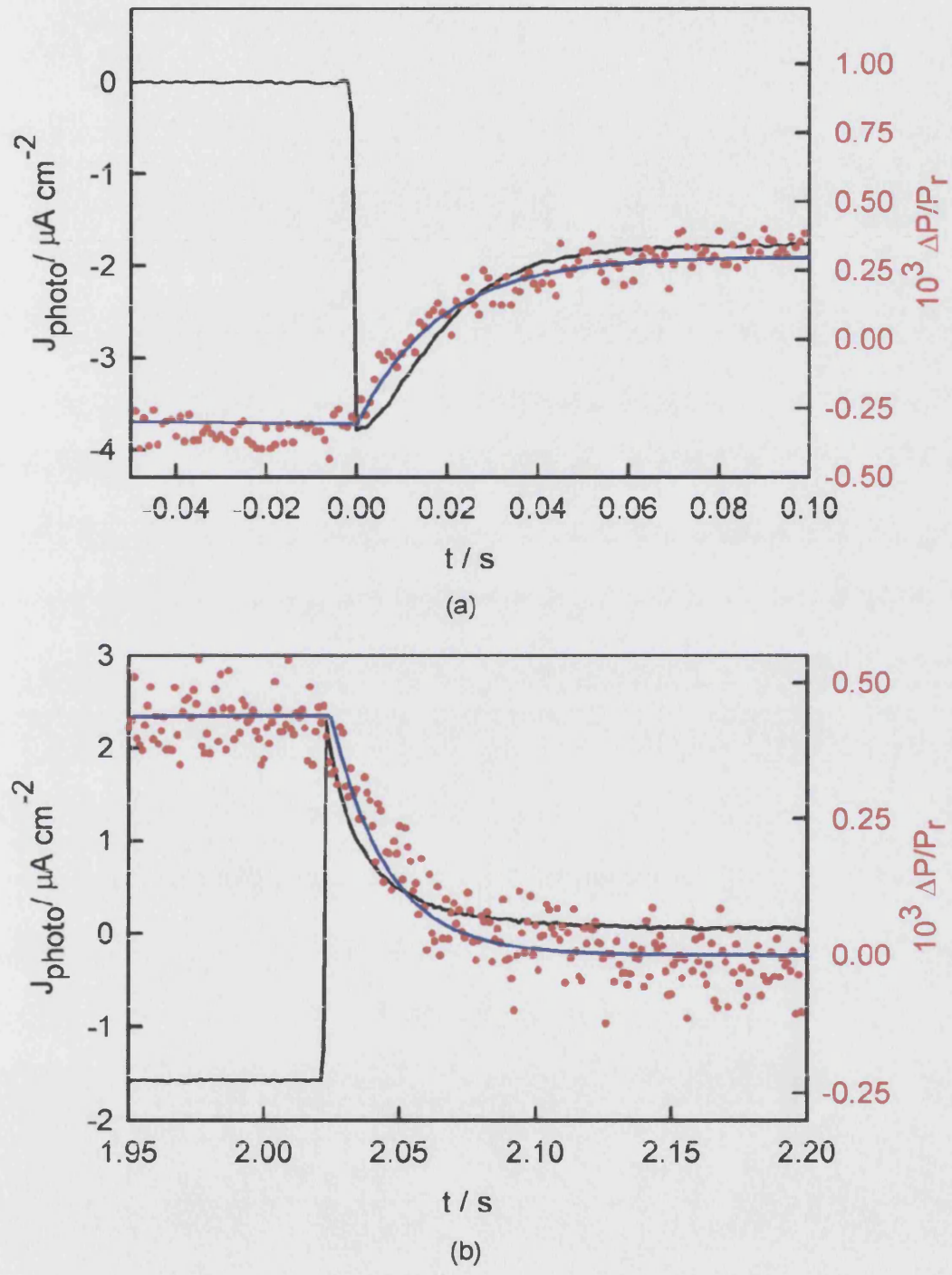

Figure 7.19: Expanded microwave response at -0.35 V a) light on b) light off. Blue line indicates the fitting.

7.3 Transient capacitance

When the light is switched off, the microwave response shows 2 components of the decay: one is fast and the other is slow as illustrated in Fig 7.20.

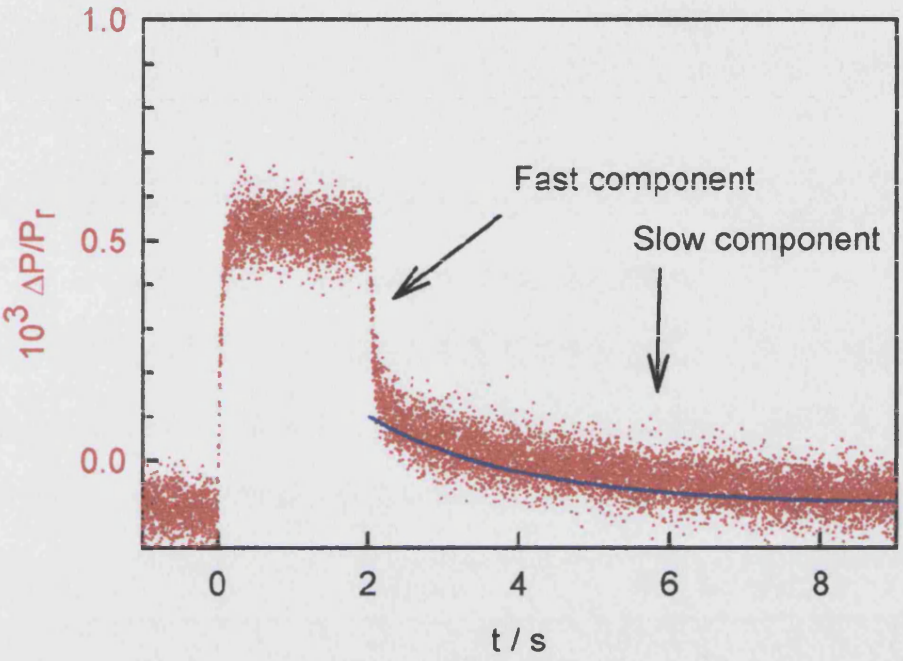

Figure 7.20: Time resolved microwave response at -1.0 V. Blue line indicates the fitting.

The slow component on the microwave responses was fitted, applying

$$y = 0.2 \times 10^{-3} \exp(-0.5(t - 2.015)) - 0.1 \times 10^{-3} \tag{7.12}$$

and k = 0.5 s^{-1} was obtained. The fast decay corresponds to the consumption of electrons by hydrogen evolution reaction but it is not clear what causes the slow component. There are two possibilities; (a) change of band-bending or (b) hydrogen incorporation. Photogenerated electrons accumulated at the surface change the quasi-Fermi level and hence the band bending. The easiest way to detect whether it occurs is to measure the capacitance. Mott-Schottky plots for p-Si in 1M fluoride (pH 3) in the dark and under illumination are shown in Fig 7.21.

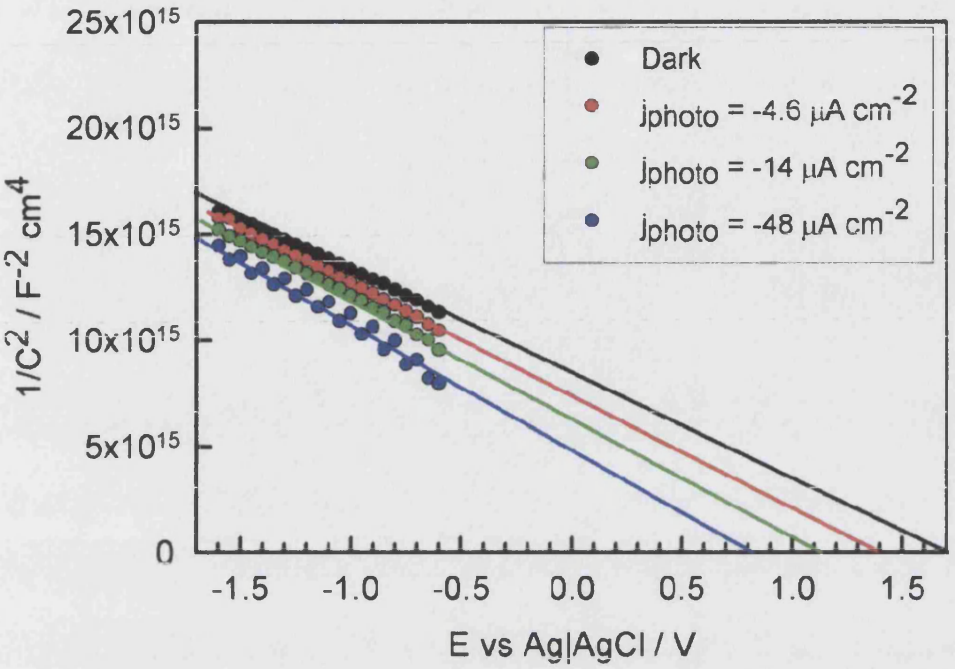

Figure 7.21: Mott-Schottky plot for p-Si in 1 M fluoride (pH 3).

As the light intensity increases, accumulation of electrons near the surface changes the potential distribution at Si|electrolyte interface and reduces the band bending. Fig 7.22 (a) shows the transient capacitance at several potentials under illumination (j_{photo} = -4 μA cm^{-2} at the saturation region on current-voltage curve). At -1.0 V the capacitance changed from 8.5 nF cm^{-2} to 8.75 nF cm^{-2}, which corresponds to 150 mV from Fig 7.22 (2). This potential shift is consistent with the change of potential distribution from Fig 7.21.

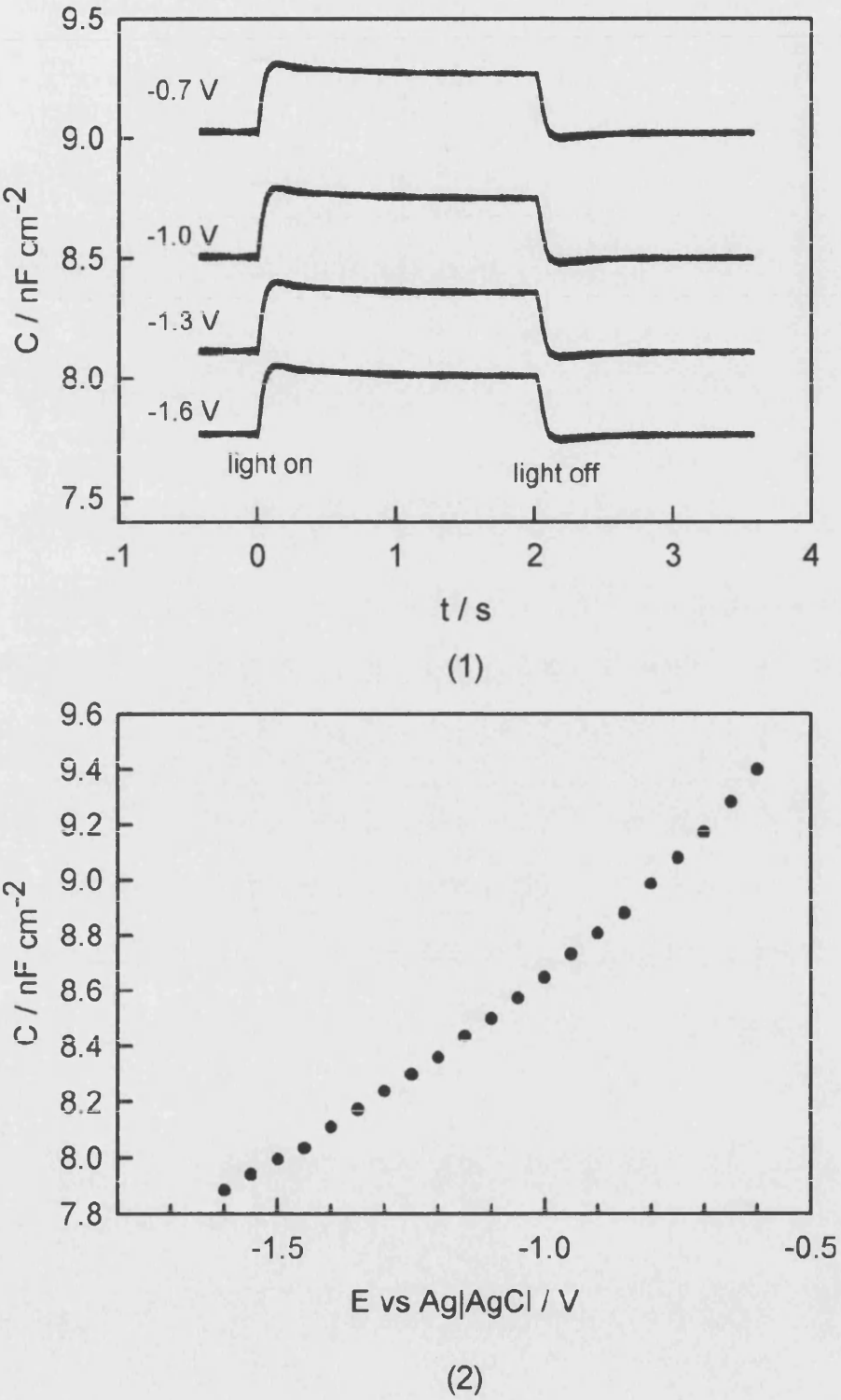

Figure 7.22: (1) Transient capacitance for p-Si in 1 M fluoride (pH 3) at j_{photo} = -3 μA cm^{-2}. (2) Capacitance-voltage curve in the dark can be used to obtain the change of potential from the change of capacitance.

The corresponding time resolved PMMR result is shown in Fig 7.23. Each curve was expanded as shown from Fig 7.24 to Fig 7.27.

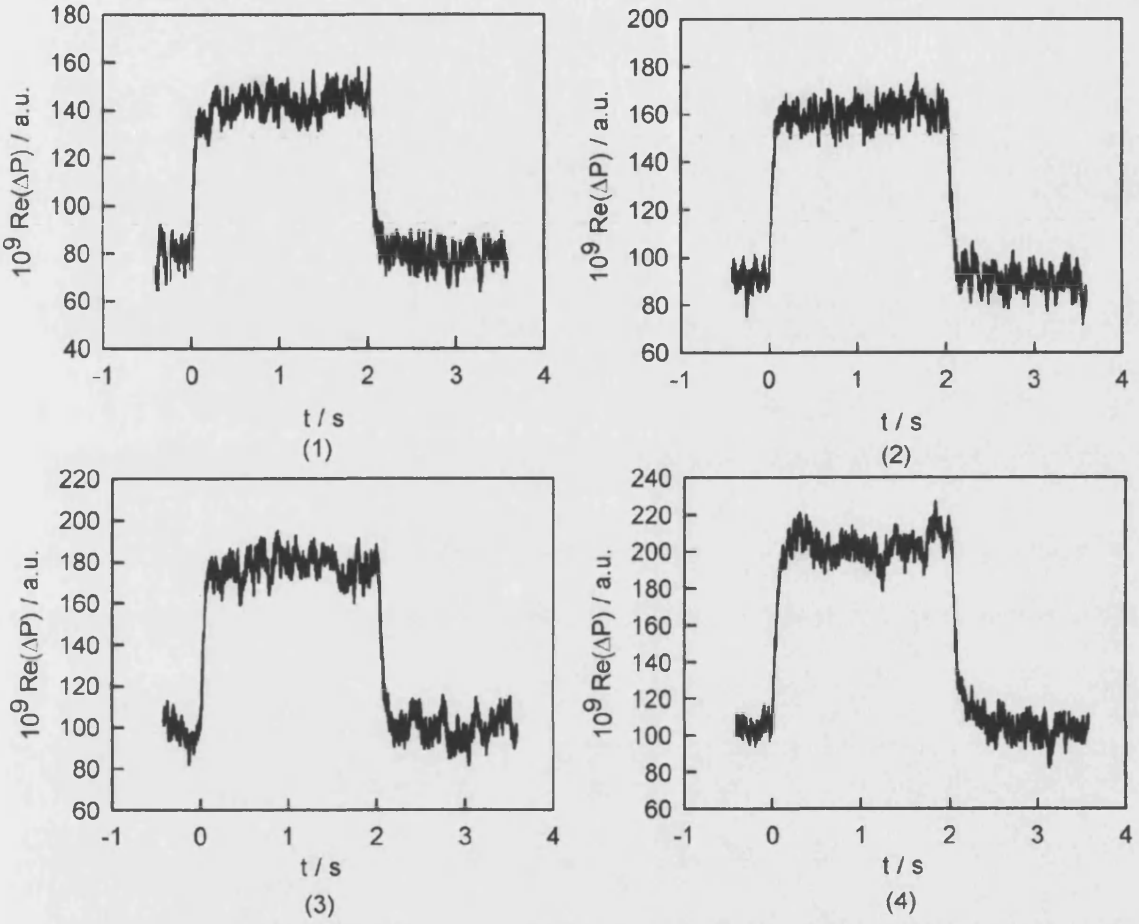

Figure 7.23: Time resolved PMMR for p-Si in 1 M fluoride (pH 3) at (1) -1.6 V (2) -1.3 V (3) -1.0 V and (4) -0.7 V under illumination (j_{photo} = -3 μA cm^{-2}). Note that the microwave response is not normalised.

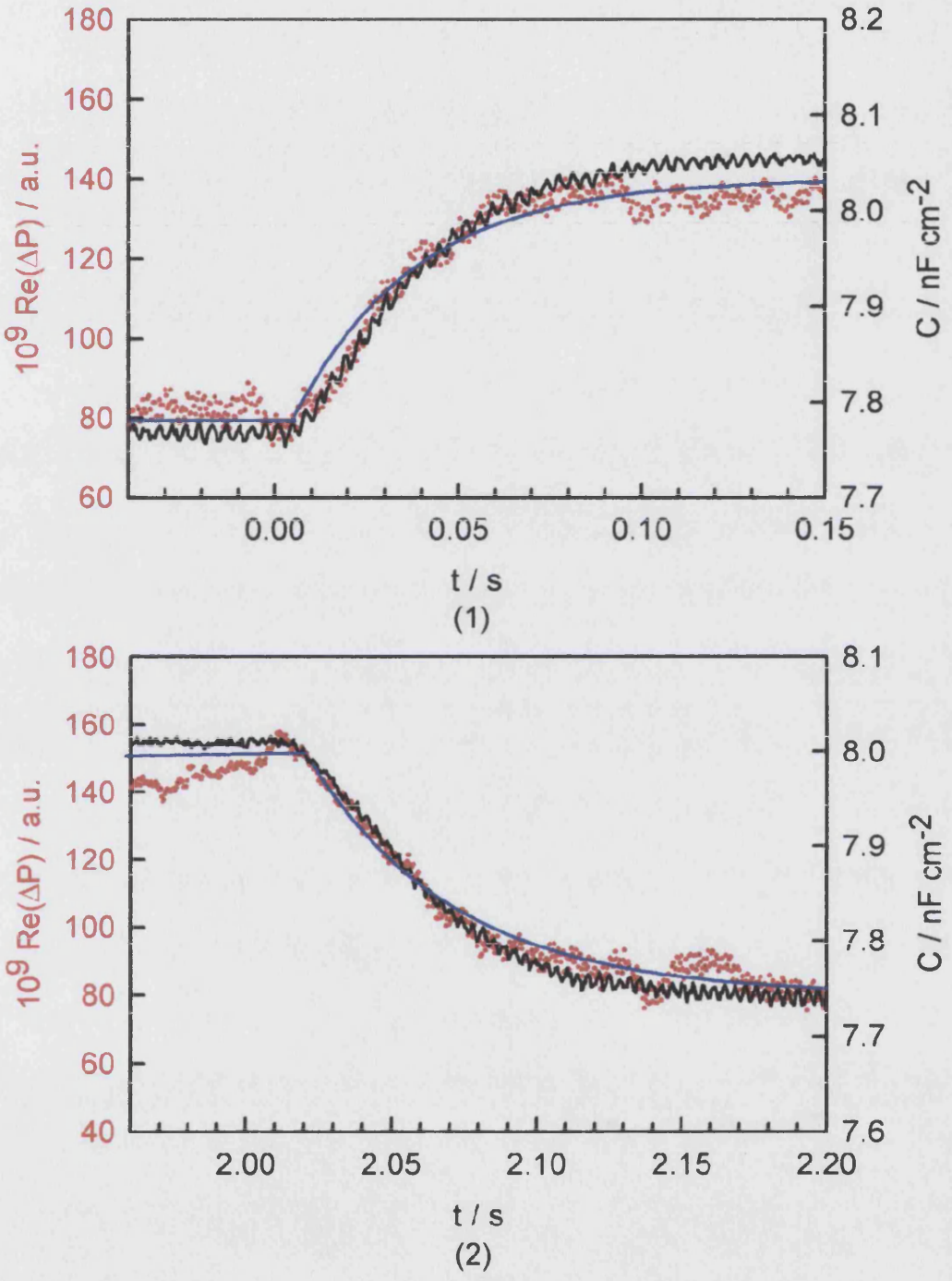

Figure 7.24: Time resolved PMMR for p-Si in 1 M fluoride (pH 3) at -1.6 V (1) light on (2) light off. Blue line indicates the fitting ($k_{light\ on} = 30\ s^{-1}$ and $k_{light\ off} = 20\ s^{-1}$).

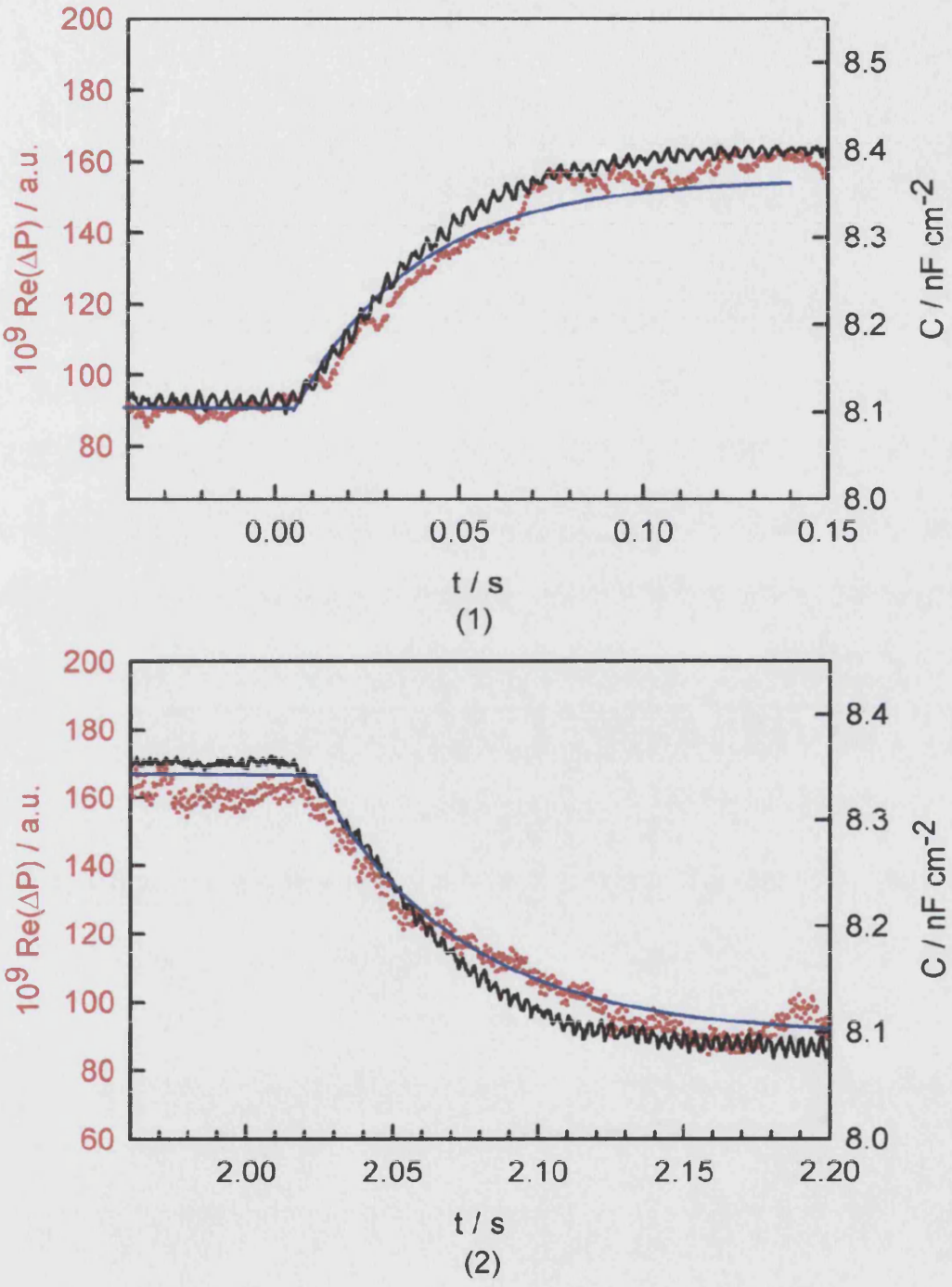

Figure 7.25: Time resolved PMMR for p-Si in 1 M fluoride (pH 3) at -1.3 V (1) light on (2) light off. Blue line indicates the fitting ($k_{light\ on} = 30\ s^{-1}$ and $k_{light\ off} = 20\ s^{-1}$).

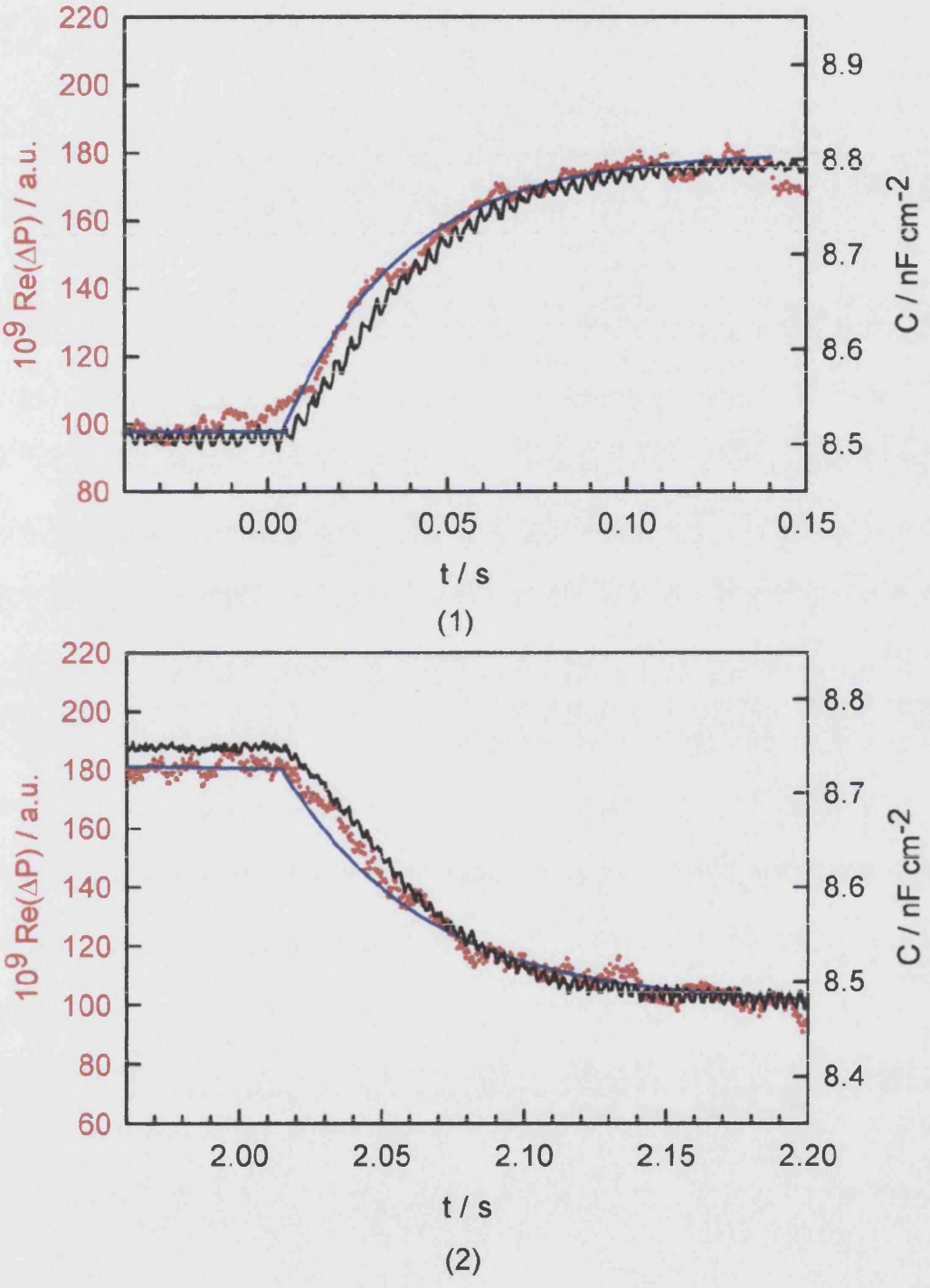

Figure 7.26: Time resolved PMMR for p-Si in 1 M fluoride (pH 3) at -1.0 V (1) light on (2) light off. Blue line indicates the fitting ($k_{light\ on} = 30\ s^{-1}$ and $k_{light\ off} = 20\ s^{-1}$).

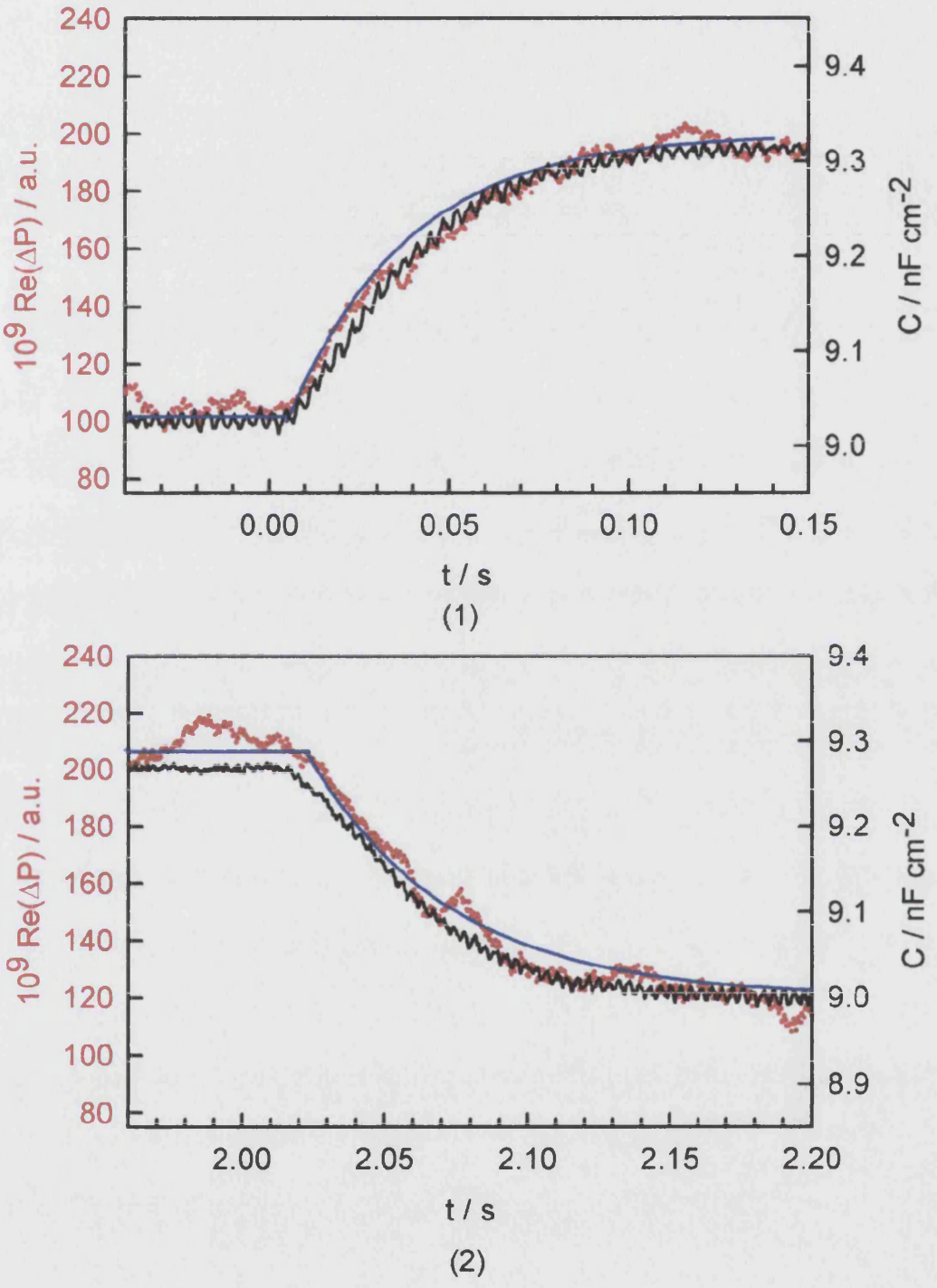

Figure 7.27: Time resolved PMMR for p-Si in 1 M fluoride (pH 3) at -0.7 V (1) light on (2) light off. Blue line indicates the fitting ($k_{light\ on} = 30\ s^{-1}$ and $k_{light\ off} = 20\ s^{-1}$).

The following values are used to fit the data at -1.6 V

$$y = 60 \times 10^{-9}[1 - \exp(-30(t - 0.005))] + 80 \times 10^{-9} \quad \text{for light on} \quad (7.13)$$

$$y = 80 \times 10^{-9}[\exp(-20(t - 2.015))] + 80 \times 10^{-9} \quad \text{for light off} \quad (7.14)$$

At -1.3 V

$$y = 65 \times 10^{-9}[1 - \exp(-30(t - 0.005))] + 90 \times 10^{-9} \quad \text{for light on} \quad (7.15)$$

$$y = 90 \times 10^{-9}[\exp(-20(t - 2.015))] + 90 \times 10^{-9} \quad \text{for light off} \quad (7.16)$$

At -1.0 V

$$y = 80 \times 10^{-9}[1 - \exp(-30(t - 0.005))] + 100 \times 10^{-9} \quad \text{for light on} \quad (7.17)$$

$$y = 80 \times 10^{-9}[\exp(-20(t - 2.015))] + 100 \times 10^{-9} \quad \text{for light off} \quad (7.18)$$

At -0.7 V

$$y = 100 \times 10^{-9}[1 - \exp(-30(t - 0.005))] + 100 \times 10^{-9} \quad \text{for light on} \quad (7.19)$$

$$y = 100 \times 10^{-9}[\exp(-20(t - 2.015))] + 120 \times 10^{-9} \quad \text{for light off} \quad (7.20)$$

It is seen that transient microwave is superimposable with capacitance. k = 30 s^{-1} and 20 s^{-1} were obtained from light on and off respectively. It is interesting to note that the rising part is slightly faster than decay part. Both the transient capacitance and microwave signal show the quick decay after the light off and therefore the slow components observed from time resolved LMMR measurements are not due to the change of the band bending.

The rate constant of the elementary reactions responsible for the competing processes of interfacial charge transfer and electron-hole recombination was measured to understand photoelectrochemical processes at the illuminated semiconductor|electrolyte interface. In the previous sections, these rate constants were determined by measuring the response of the semiconductor electrode to a time dependent perturbation. There are two types of perturbation; one is illumination by intensity modulated light at a fixed electrode potential and the other is modulation of the electrode potential under constant illumination. The first method is referred to as intensity modulated photocurrent spectroscopy (IMPS) and light modulated microwave reflectance measurement (LMMR),

and the second is photoelectrochemical impedance spectroscopy (PEIS), which is analogous with electrochemical impedance spectroscopy (EIS). In the case where the only processes involving photogenerated minority carriers are surface recombination and interfacial charge transfer, the frequency dependent IMPS exhibits a semicircle in the upper complex plane, and the rate constants of recombination, k_{rec}, and charge transfer, k_{tr}, can be found from the frequency of the maximum and the values of the low frequency intercepts.

The frequency dependent PEIS behaviour is generally more complicated than the corresponding IMPS response, and the complex plane impedance plot of Im(Z) vs Re(Z) may exhibit two semicircles. An equivalent circuits with two capacitors and two resistors have been proposed by Schefold to explain this type of behaviour [18].

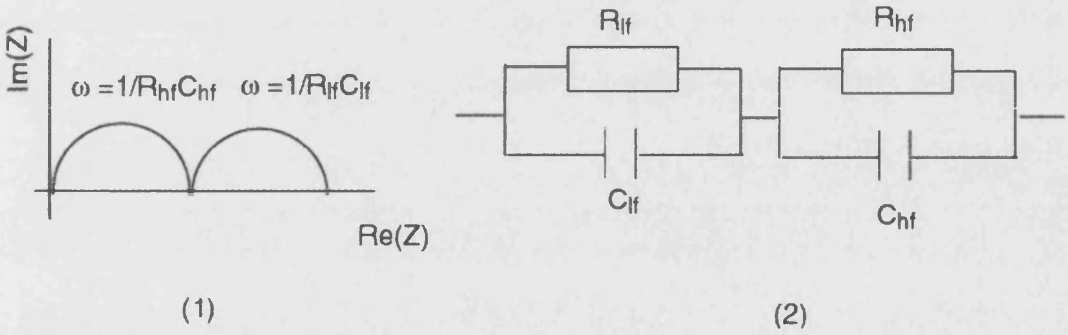

Figure 7.28: (1) PEIS response (2) equivalent circuit

In this approach, the capacitances represent depletion layer capacitance, C_{sc}, and Helmholtz capacitance, C_H. Although the physical significance of the resistance elements in the equivalent circuits is not clear, it can be called charge transfer resistance and recombination resistance. These resistances only have meaning in combination with the capacitors C_H and C_{sc} and the inverse of the RC product are used to represent the first order rate constant associated with charge transfer and recombination respectively. Schefold [18] has discussed the equivalent circuit approach and has proposed that the PEIS and IMPS measurements provide basically the same information, which means that it is possible in principle to derive the IMPS response from PEIS data. On the other hand, Ponomarev *et al.* [17] also showed that photoelectrochemical

impedance and Intensity modulated photocurrent spectroscopy should give the same information about the rate constants of charge transfer and recombination using a different approach from Schefold.

The R and C values for the low frequency semicircle are given by

$$R_{lf} = \left(\frac{k_B T}{q^2 I_0}\right) \frac{k_{tr} + k_{rec}}{k_{tr}} \tag{7.21}$$

$$C_{lf} = \left(\frac{q^2 I_0}{k_B T}\right) \frac{1}{k_{tr} + k_{rec}} \tag{7.22}$$

so that

$$\omega_{max} = \frac{1}{R_{lf} C_{lf}} = k_{tr} \text{ at low frequency semicircle} \tag{7.23}$$

The R and C values for the high frequency semicircle are

$$R_{hf} = \left(\frac{k_B T}{q^2 I_0}\right) \frac{k_{tr} + k_{rec}}{k_{rec}} \tag{7.24}$$

$$C_{hf} = C_{sc} \tag{7.25}$$

so that

$$\omega_{max} = \left(\frac{q^2 I_0}{k_B T}\right) \frac{k_{rec}}{k_{tr} + k_{rec}} \text{ at high frequency semicircle} \tag{7.26}$$

Since PEIS measurement is not performed, it is not possible to compare the results. However it is shown that the frequency- and time resolved IMPS measurements provide the same kinetic information as well as LMMR measurements. Taking into account the fact that PEIS and IMPS give the same information about the rate constants of charge transfer and recombination, it can be predicted that frequency- and time-resolved PEIS should provide the same kinetic information as well as the microwave measurements. Therefore, the rate constant obtained from the transient photocapacitance and time resolved PMMR measurements could corresponds to the charge transfer rate constant. Further study is required.

The sensitivity factor under illumination can be obtained as follows: Microwave response in the dark is

$$\left(\frac{\Delta P}{P_r}\right)_{dark} = S \frac{\mu_p C_{dark} \Delta\phi}{Rd} \tag{7.27}$$

Microwave response under illumination is

$$\left(\frac{\Delta P}{P_r}\right)_{light} = S\frac{\mu_p C_{light}\Delta\phi}{Rd} \tag{7.28}$$

Therefore, the change of microwave response is

$$\begin{aligned}\left(\frac{\Delta P}{P_r}\right)_{light} - \left(\frac{\Delta P}{P_r}\right)_{dark} &= S\frac{\mu_p \Delta\phi(C_{light} - C_{dark})}{Rd} \\ \Delta\left(\frac{\Delta P}{P_r}\right) &= S\frac{\mu_p \Delta\phi \Delta C}{Rd}\end{aligned} \tag{7.29}$$

If we plot $\Delta\left(\frac{\Delta P}{P_r}\right)$ as a function of ΔC, we expect the straight line and from the slope, and the sensitivity factor can be obtained. Fig 7.29 shows that the microwave response as a function of photoinduced change of the capacitance at -1.0 V.

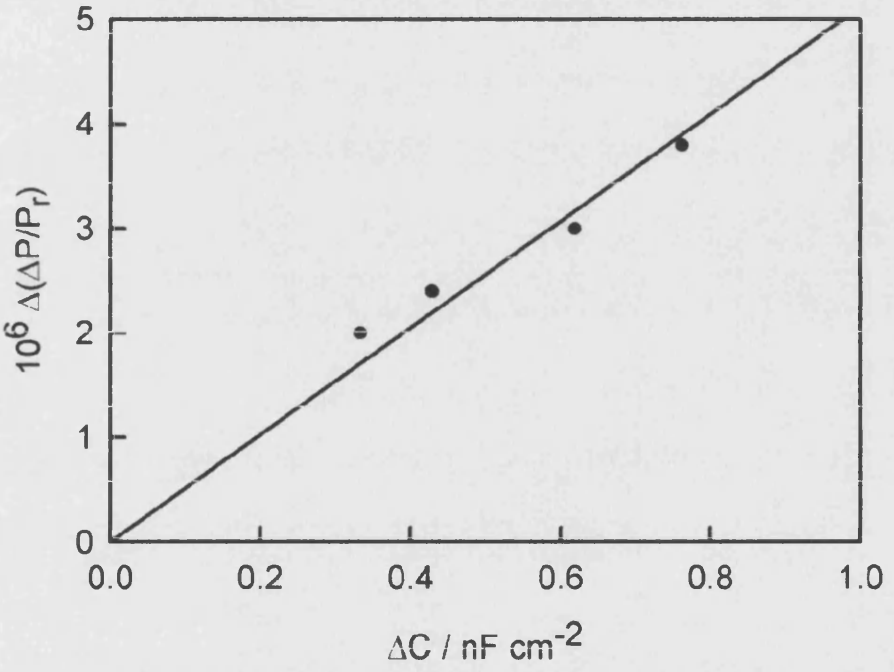

Figure 7.29: Normalised PMMR response under illumination as a function of photoinduced change of capacitance at -1.0 V.

From Fig 7.29 the sensitivity factor is

$$\begin{aligned}S &= \frac{R \times d \times \text{slope}}{\mu_p \times \Delta\phi} \\ &= \frac{0.5 \times 350 \times 10^{-4} \times 5123}{460 \times 0.04} \\ &= 4.87\,\Omega\text{cm}\end{aligned}$$

This is 10 times larger than the the theoretical value. The reason for this is no clear at present but it suggests that the microwave detects not only the change of conductivity due to the electrons but also the change of conductivity due to holes.

7.4 Photoelectrochemical reduction of $Ru(NH_3)_6^{3+}$

The hydrogen evolution reaction is a complicated reaction since it is a two step process. For this reason, a simple outer sphere redox system was studied in order to compare the rate of electron transfer with theoretical models, especially Marcus theory. A cyclic voltammogram of 1 mM $Ru(NH_3)_6Cl_3$ in 1M fluoride (pH 3) was obtained using a glassy carbon electrode, as shown in Fig 7.30.

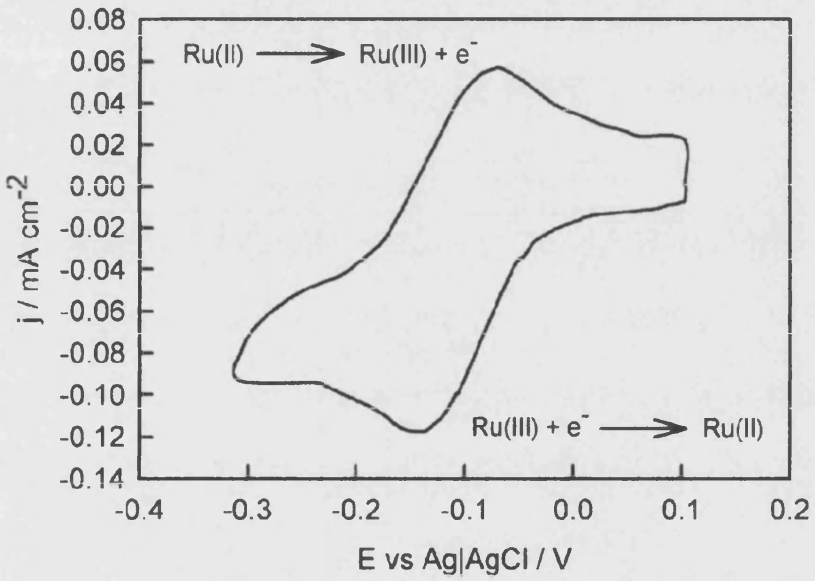

Figure 7.30: Cyclic Voltammogram of 1 mM $Ru(NH_3)_6Cl_3$ in 1 M fluoride (pH 3). Sweep rate = 2 mV s^{-1}.

The redox potential of $Ru(NH_3)_6^{2+/3+}$ was -0.13 V vs Ag | AgCl, which corresponds to 0.06 V vs SHE. It appears that $Ru(NH_3)_6Cl_3$ is stable in the acidic fluoride electrolyte used here.

Fig 7.31 shows the difference of electron transfer reactions at metal and semiconductor electrodes. It is seen that for metals electron transfer occurs near the Fermi

level whereas it occurs far from the Fermi level for semiconductor electrodes if E^{o} lies in the band gap of the semiconductor. In this case reduction process on semiconductor electrodes occurs at the potential in which the oxidised species is more probable, whereas for metal electrodes the reduction process takes place at the potential in which the oxidised species are less probable. It is predicted that the rate at semiconductors can be faster than that at metals.

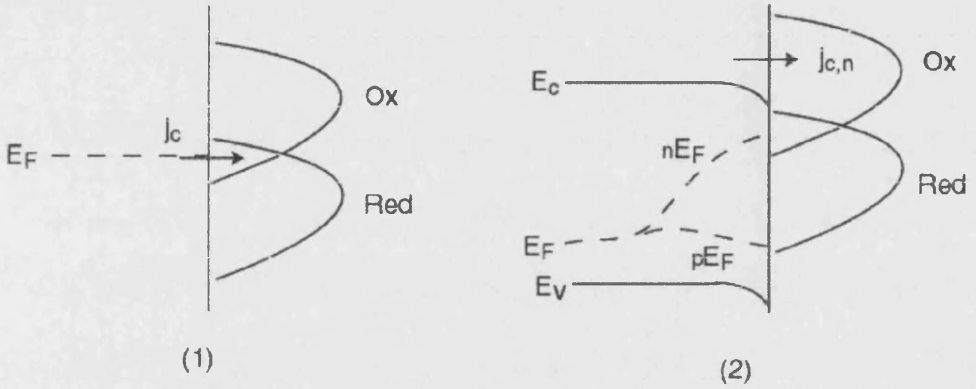

Figure 7.31: Energy diagram for electron transfer at (1) metal (2) p-type semiconductor.

The redox potential of $Ru(NH_3)_6^{2+/3+}$ is located above the Fermi level for p-Si, so Ru(III) accepts electrons from the conduction band as shown in Fig 7.32. If the redox potential is below the Fermi level, electrons in the valence band flow to the electrolyte and a large dark current is observed.

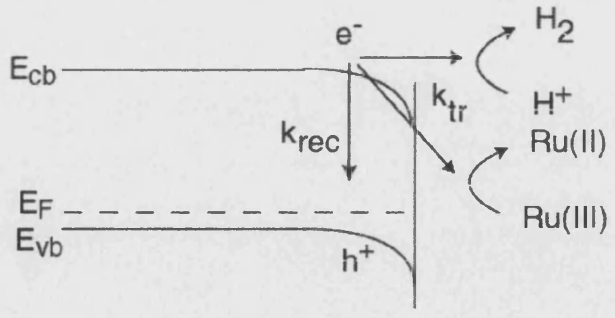

Figure 7.32: Schematic diagram for reduction of $Ru(NH_3)_6^{3+}$ at p-Si surface showing the competition with hydrogen evolution.

We predict that there is a competition between hydrogen evolution and reduction of

$Ru(NH_3)_6^{3+}$. The reversible hydrogen potential can be obtained from the Nernst equation

$$E = E^{\circ} + \frac{RT}{nF} \ln \frac{c_{Ox}}{c_{Red}}$$

For pH 3 electrolyte the reversible hydrogen potential is given by

$$\begin{aligned} E &= \frac{RT}{nF} \ln \frac{[H^+]}{P_{H_2}} \\ &= \frac{8.314 \times 298}{9.6485 \times 10^4} \ln[H^+] \\ &= 0.02568 \ln[H^+] \\ &= 0.02568 \frac{\log[H^+]}{\log e} \\ &= -0.059 \times pH \\ &= -0.059 \times 3 \\ &= -0.18 \text{ V vs SHE} \end{aligned}$$

It is noted that

$$AgCl + e^- \rightleftharpoons Ag + Cl^- \quad E^{\circ} = 0.22 \text{ V vs. SHE}$$

The potential of the reference electrode vs. SHE can be calculated as

$$\begin{aligned} E_{Ag/AgCl} &= 0.22 - 0.059 \log[Cl^-] \quad \text{at } 25^{\circ}C \\ &= 0.22 - 0.059 \log(3) \\ &= 0.19 \text{ V at 3M } [Cl^-] \end{aligned}$$

Therefore, -0.18 V vs. SHE corresponds to -0.37 V vs. Ag/AgCl. The redox potential for $Ru(NH_3)_6^{2+/3+}$ is -0.09 V vs. Ag/AgCl, which is used later to draw an energy diagram. In order to complete the energy diagram, it is necessary to know the value of reorganaisaiton energy of redox species.

The reorganisation energy is the free energy to reorganise atoms or molecules in the environment of the reactant from their positions at equilibrium. This consists of inner and outer terms.

$$\lambda_{re} = \lambda_o + \lambda_i \tag{7.30}$$

λ_o is the free energy required to reorganise the solvent molecules around the reactant (the outer coordination shell), given by

$$\lambda_o = \frac{q^2}{8\pi\varepsilon_0 a}\left(\frac{1}{\varepsilon_{opt}} - \frac{1}{\varepsilon_s}\right) \tag{7.31}$$

where ε_0 is permittivity in vacuum, a is ionic radius, ε_{opt} is optical dielectric constant (1.8 for water), and ε_s is static dielectric constant (78.5 for water).

λ_i is the free energy to reorganise the inner coordination shell of the reactant given by

$$\lambda_i = \sum_j \frac{f_j^{ox} f_j^{red}}{f_j^{ox} + f_j^{red}} (\Delta x_j)^2 \tag{7.32}$$

where f_j^{ox} and f_j^{red} are force constants of the oxidised and reduced species in the jth coordinate, respectively, and Δx is the change in bond length. Reorganisation energy is related to the heterogeneous rate constant, given by

$$k^o = Z \exp\left(-\frac{\lambda_{re}}{4RT}\right) \tag{7.33}$$

where Z is heterogeneous pre-exponential factor = $\sim 10^4$ cm s^{-1}.

The standard heterogeneous rate constant for $Ru(NH_3)_6^{2+/3+}$ is around 0.6 cm s^{-1}, and hence

$$\begin{aligned} 0.6 &= 1 \times 10^4 \exp\left(-\frac{\lambda_{re}}{4 \times 8.314 \times 298}\right) \\ 0.6 \times 10^{-4} &= \exp\left(-\frac{\lambda_{re}}{4 \times 8.314 \times 298}\right) \end{aligned} \tag{7.34}$$

Taking natural logarithm for both sides

$$\begin{aligned} \ln 0.6 \times 10^{-4} &= -\frac{\lambda_{re}}{4 \times 8.314 \times 298} \\ \lambda_{re} &= 9.63 \times 10^4 \ \text{J mol}^{-1} \end{aligned} \tag{7.35}$$

Dividing by Avogadro's constant

$$\begin{aligned} \lambda_{re} &= \frac{9.63 \times 10^4}{6 \times 10^{23}} \\ &= 1.6 \times 10^{-19} \ \text{J} \end{aligned} \tag{7.36}$$

Since 1 eV is 1.6×10^{-19} J, the reorganisation energy of $Ru(NH_3)_6^{2+/3+}$ is 1 eV. Therefore, the following energy diagram can be drawn.

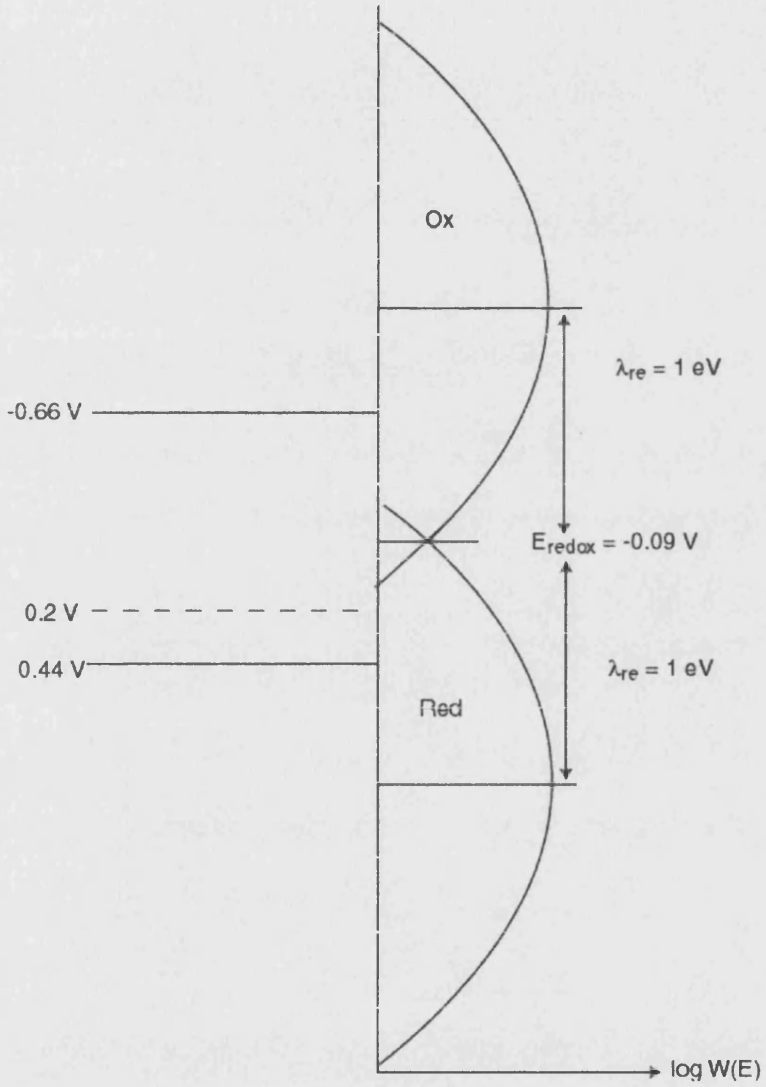

Figure 7.33: Distribution function of $Ru(NH_3)_6^{2+/3+}$ at Si|electrolyte interface at pH 3. Note that potential is against Ag/AgCl.

7.4.1 Potential dependence of photocurrent and microwave response

Normalised photocurrent-voltage curves for three light intensities are shown in Fig 7.34 in the presence of 0.33 mM $Ru(NH_3)_6^{3+}$. For the hydrogen evolution reaction (the absence of $Ru(NH_3)_6^{3+}$), the normalised photocurrent-voltage curve shifts to the left with increasing the light intensity whereas the photocurrent-voltage curve shifts only at the highest light intensity (j_{photo} = -444 $\mu A.cm^{-2}$) if $Ru(NH_3)_6^{3+}$ is present. At this light intensity we assume that the photocurrent is greater than the limiting current by the reduction of $Ru(NH_3)_6^{3+}$.

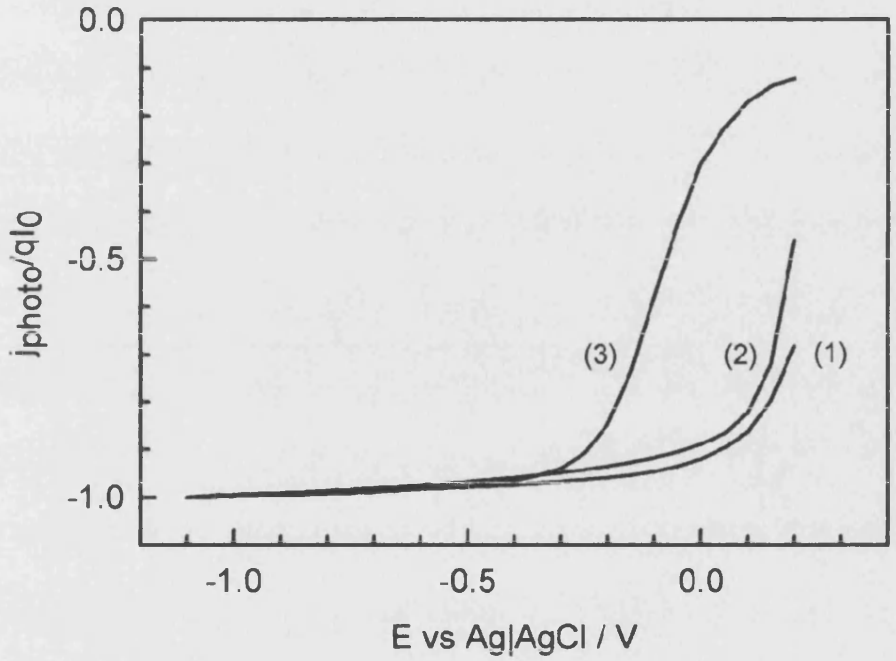

Figure 7.34: Normalised photocurrent response for p-Si in 1 M fluoride (pH 3) containing 0.33 mM $Ru(NH_3)_6^{3+}$. (1) j_{photo} = -3.8 $\mu A\ cm^{-2}$ (2) j_{photo} = -40 $\mu A\ cm^{-2}$ (3) j_{photo} = -444 $\mu A\ cm^{-2}$.

The microwave response should be reduced by increasing the charge transfer rate constant, as discussed before. It is known that the electron transfer at $Ru(NH_3)_6^{2+/3+}$ couples is fast. The reduction of $Ru(NH_3)_6^{3+}$ is expected to be faster reaction than the hydrogen evolution, and the theoretical value of the charge transfer rate constant for the reduction of $Ru(NH_3)_6^{3+}$ can be obtained as follows.

The electron capture cross section for interfacial electron transfer to Ru(III) can be expressed as [11]

$$\sigma[\mathrm{X}] = \sigma\delta c_{ox}\sqrt{\frac{k_B T}{\pi\lambda_{re}}}\exp\left(-\frac{(E_c - E_{redox} - \lambda_{re})^2}{4k_B T}\right) \tag{7.37}$$

where [X] is effective surface density of accessible oxidising agent, δ is the tunnelling distance, c_{ox} is concentration of oxidised species, $k_B T$ is thermal voltage, E_c is conduction band edge potential, E_{redox} is standard redox potential.

Fig 7.35 illustrates the capture cross section as a function of $E_{cs} - E_{redox}$ in the case of 1 eV of reorganisation energy and 10 mM of oxidised species.

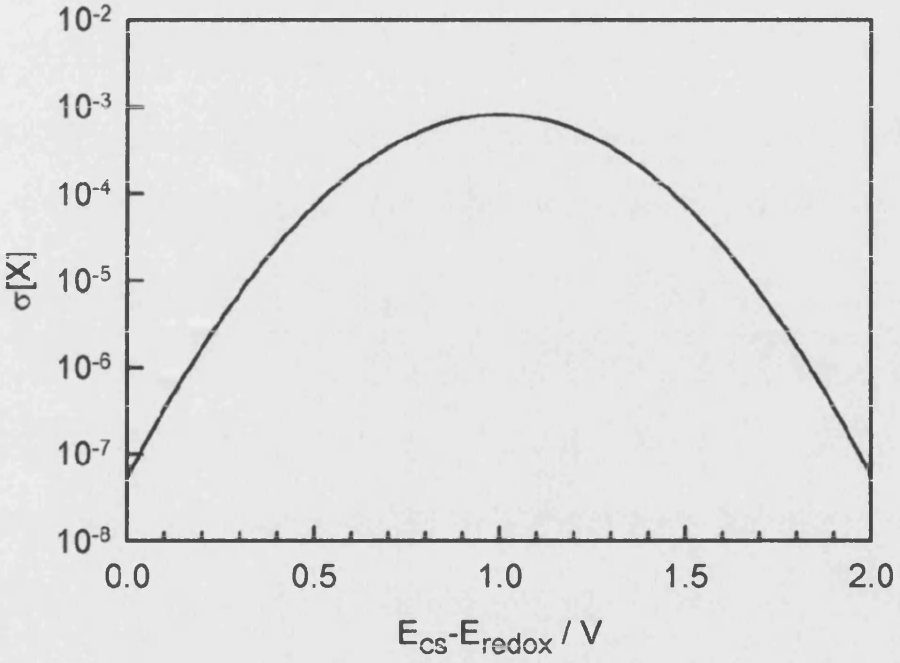

Figure 7.35: Capture cross section as a function of $E_{cs} - E_{redox}$ at λ_{re} = 1 eV for 10 mM of oxidised species.

In the case of $E_{cs} - E_{redox}$ = 0.54 eV, λ_{re} = 1 eV and c_{Ox} = 10 mM, the capture cross section is

$$\begin{aligned}\sigma[X] &= 1\times10^{-14}\times1.5\times10^{-7}\times6\times10^{18}\sqrt{\frac{0.026}{\pi}}\exp\left(-\frac{(0.54-1)^2}{4\times0.026}\right)\\ &= 9\times10^{-3}\times0.09\times0.13\\ &= 1.06\times10^{-4}\end{aligned}$$

It is seen that the capture cross section becomes maximum at 1 eV of $E_{cs} - E_{redox}$. 0.54 eV of $E_{cs} - E_{redox}$ is quite close to the maximum.

Fig 7.36 illustrates the capture cross section as a function of reorganisation energy in the case of 1 eV of $E_{cs} - E_{redox}$ and 10 mM of oxidised species. It is seen that the capture cross section becomes maximum at 0.8 eV of reorganisation energy.

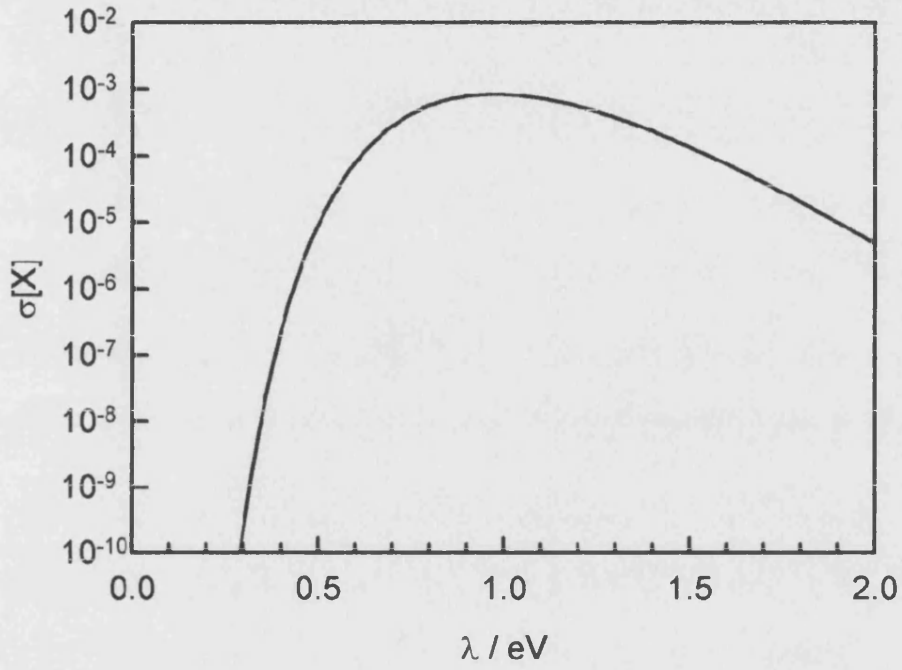

Figure 7.36: Capture cross section as a function of reorganisation energy at 1 eV of $E_{cs} - E_{redox}$ for 10 mM of oxidised species.

The rate constant for charge transfer is given by

$$k_{tr} = \nu_{th}\sigma[X] \tag{7.38}$$

where ν_{th} is thermal velocity of electrons. For Si, ν_{th} is 5.2×10^6 cms^{-1}, and the electron transfer rate constant is

$$\begin{aligned} k_{tr} &= 5.2 \times 10^6 \times 1.06 \times 10^{-4} \\ &= 550 \quad cms^{-1} \end{aligned}$$

This value is close to the upper limit ($\sim$ 100 cms^{-1}) discussed by Lewis [20]. It is predicted that the presence of $Ru(NH_3)_6^{3+}$ should almost eliminate the microwave sig-

nal due to the faster charge transfer reaction. However, the microwave response is still observed in the presence of 0.33 mM $Ru(NH_3)_6^{3+}$, as shown in Fig 7.37. It suggests that the charge transfer via reduction of $Ru(NH_3)_6^{3+}$ is slower than the expected.

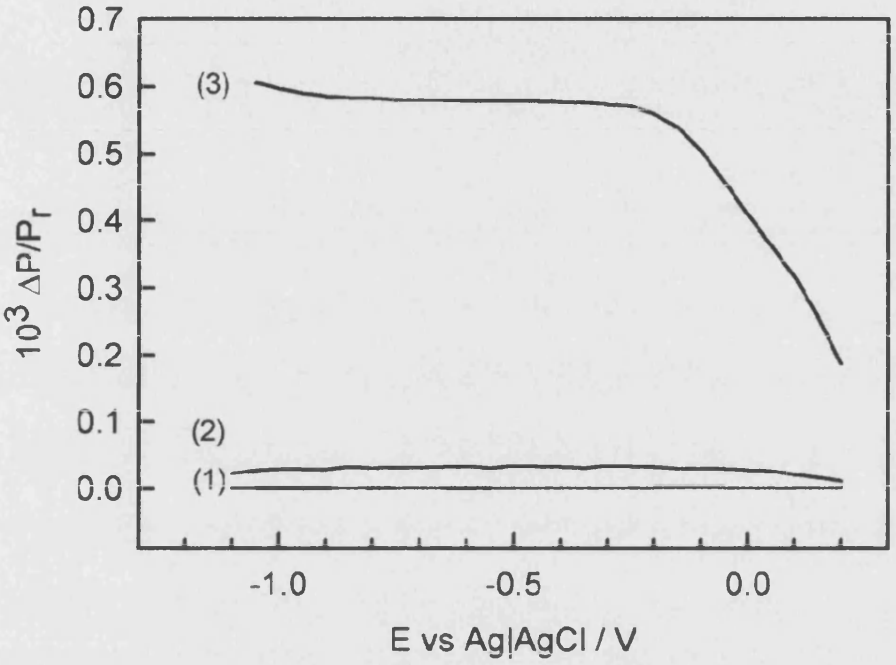

Figure 7.37: Microwave response for p-Si in 1 M fluoride (pH 3) containing 0.33 mM $Ru(NH_3)_6^{3+}$. (1) j_{photo} = -3.8 μA cm^{-2} (2) j_{photo} = -40 μA cm^{-2} (3) j_{photo} = -444 μA cm^{-2}.

The microwave response in the presence of 0.33 mM $Ru(NH_3)_6^{3+}$ at -1.0 V are tabulated in Table 7.2. The microwave response for hydrogen evolution (absence of $Ru(NH_3)_6^{3+}$) is tabulated in Table 7.3 as a comparison.

j_{photo} / μAcm^{-2}	$\Delta P/P_r$
3.8	3.96×10^{-7}
40	2.9×10^{-5}
444	5.96×10^{-4}

Table 7.2: Microwave response at -1.0 V in the presence of 0.33 mM $Ru(NH_3)_6^{3+}$.

j_{photo} / μAcm^{-2}	$\Delta P/P_r$
0.7	2.5×10^{-4}
7.62	1.82×10^{-4}
91	5.53×10^{-4}

Table 7.3: Microwave response at -1.0 V for the hydrogen evolution. Data is taken from Fig 7.4.

It is interesting to note that the microwave response is linearly proportional to the photocurrent if $Ru(NH_3)_6^{3+}$ is present whereas it is not linearly proportional in the case of the hydrogen evolution (cf. Fig 7.4). This result suggests that the increased rate constant via presence of $Ru(NH_3)_6^{3+}$ reduces the build up of electrons and the mobility of electrons are not reduced.

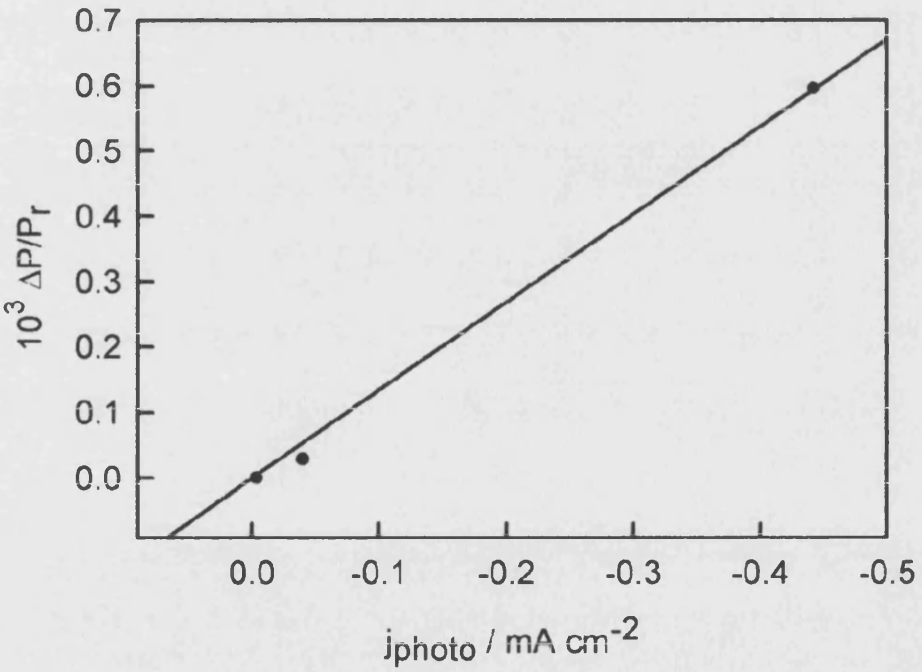

Figure 7.38: Microwave response as a function of photocurrent at -1.0 V.

7.4.2 Frequency resolved results

The IMPS and LMMR plots in the presence of 0.1 mM, 0.33 mM and 1 mM $Ru(NH_3)_6^{3+}$ are shown from Fig 7.39 to Fig 7.44.

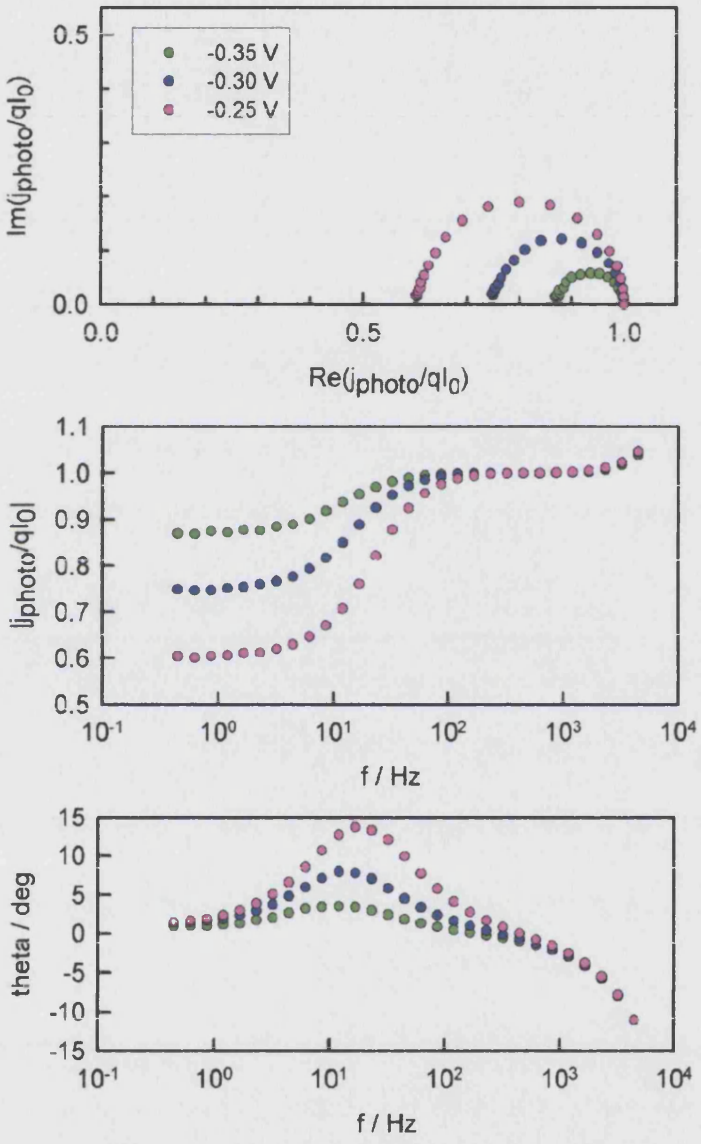

Figure 7.39: IMPS plots for p-Si in 1 M fluoride (pH 3) containing 0.01 mM $Ru(NH_3)_6^{3+}$. j_{photo} = -3.6 μA cm^{-2} at the saturation region on current-voltage curve.

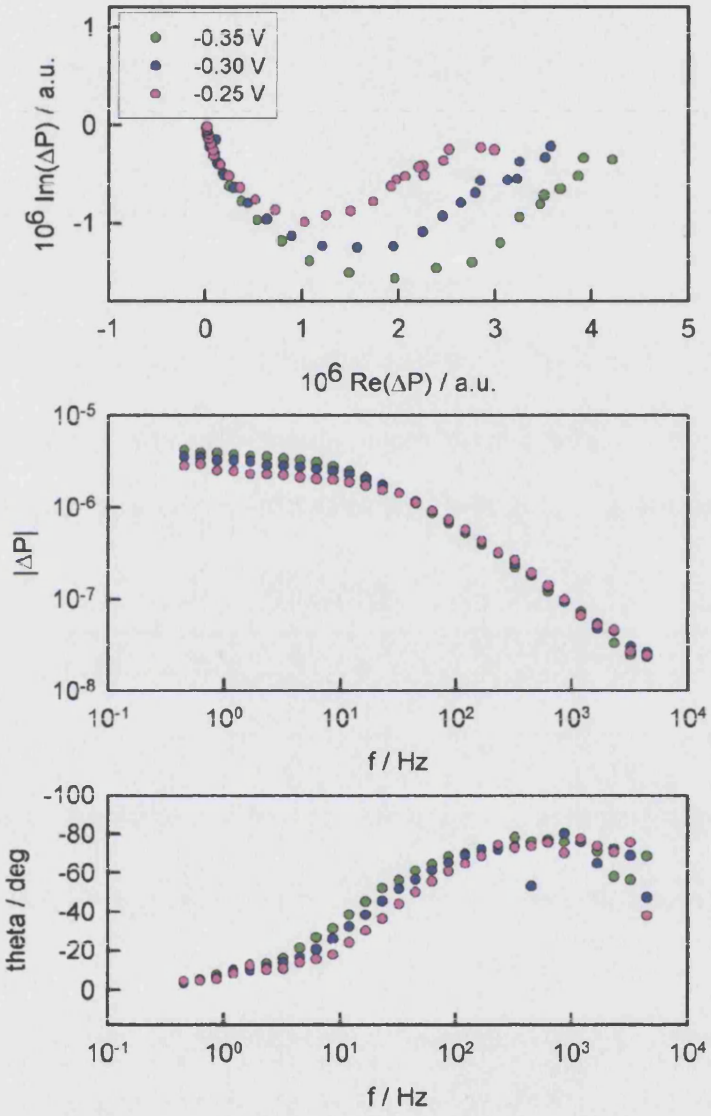

Figure 7.40: LMMR plots for p-Si in 1 M fluoride (pH 3) containing 0.01 mM $Ru(NH_3)_6^{3+}$. j_{photo} = -3.6 μA cm^{-2} at the saturation region on current-voltage curve.

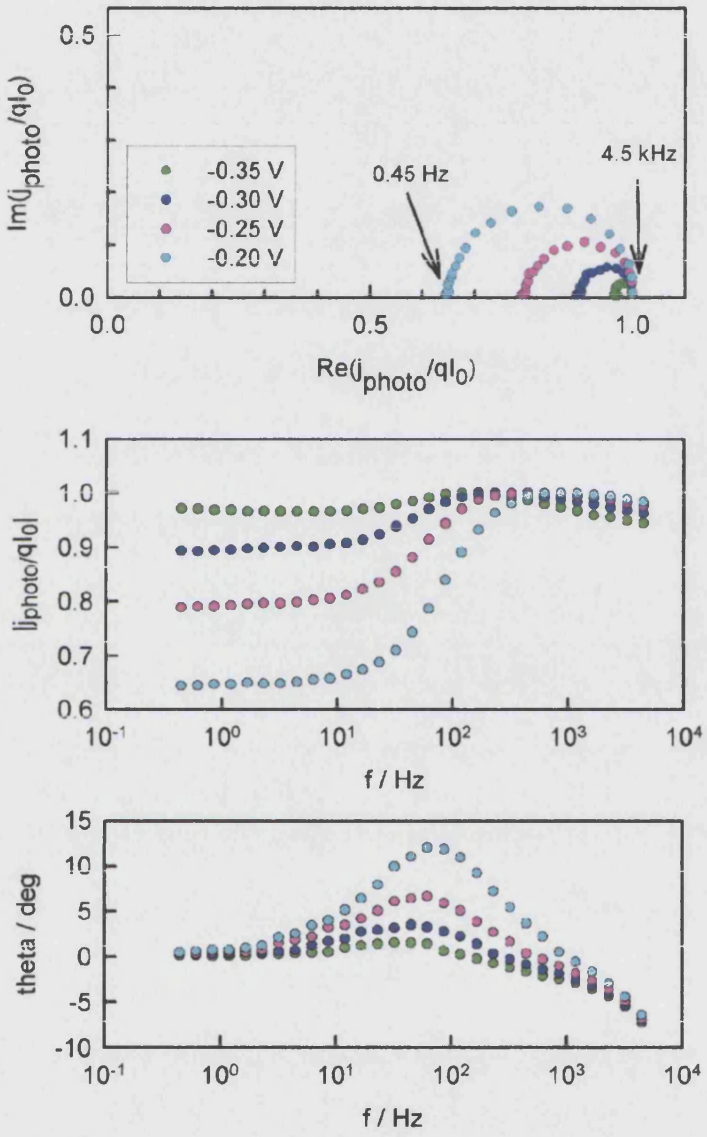

Figure 7.41: IMPS plots for p-Si in 1 M fluoride (pH 3) containing 0.33 mM $Ru(NH_3)_6^{3+}$. j_{photo} = -3.9 μA cm^{-2} at the saturation region on current-voltage curve.

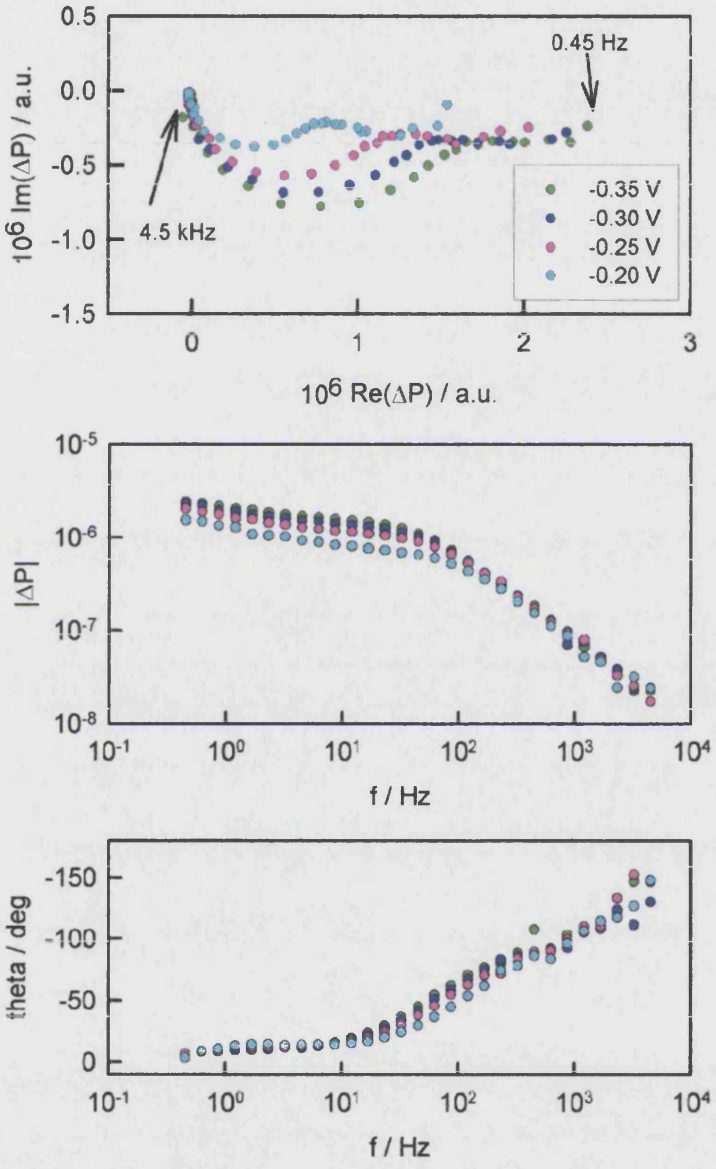

Figure 7.42: LMMR plots for p-Si in 1 M fluoride (pH 3) containing 0.33 mM $Ru(NH_3)_6^{3+}$. j_{photo} = -3.9 μA cm^{-2} at the saturation region on current-voltage curve.

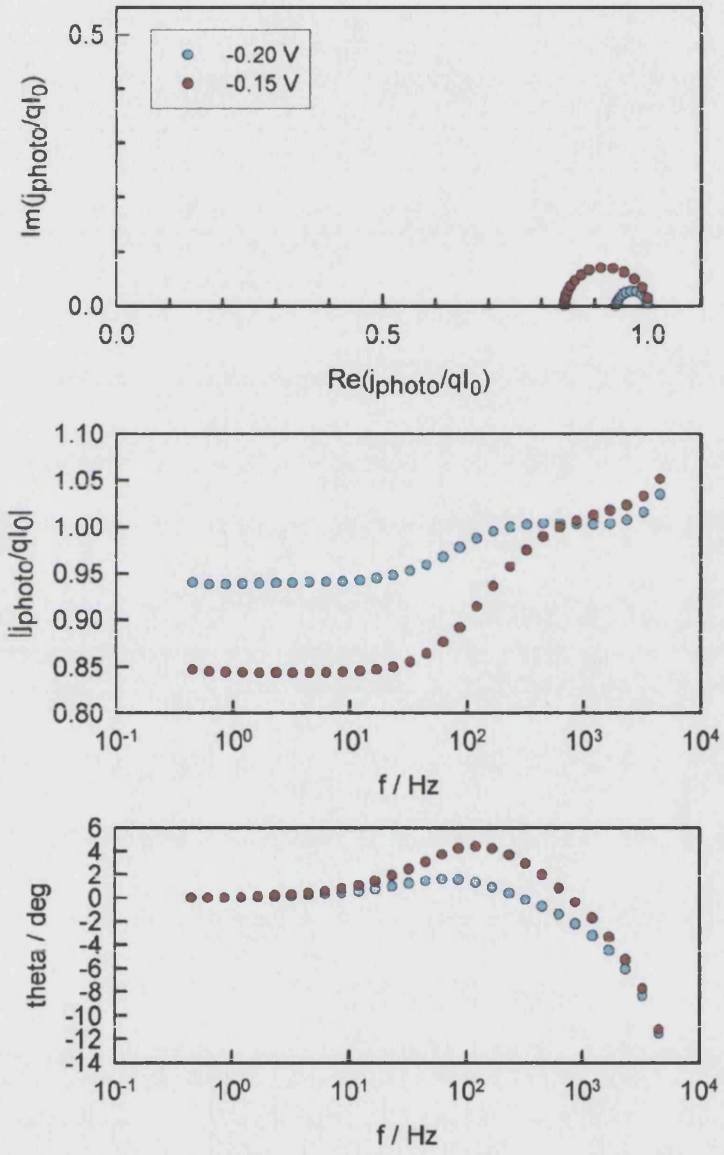

Figure 7.43: IMPS plots for p-Si in 1 M fluoride (pH 3) containing 1 mM $Ru(NH_3)_6^{3+}$. j_{photo} = -3.7 μA cm^{-2} at the saturation region on current-voltage curve.

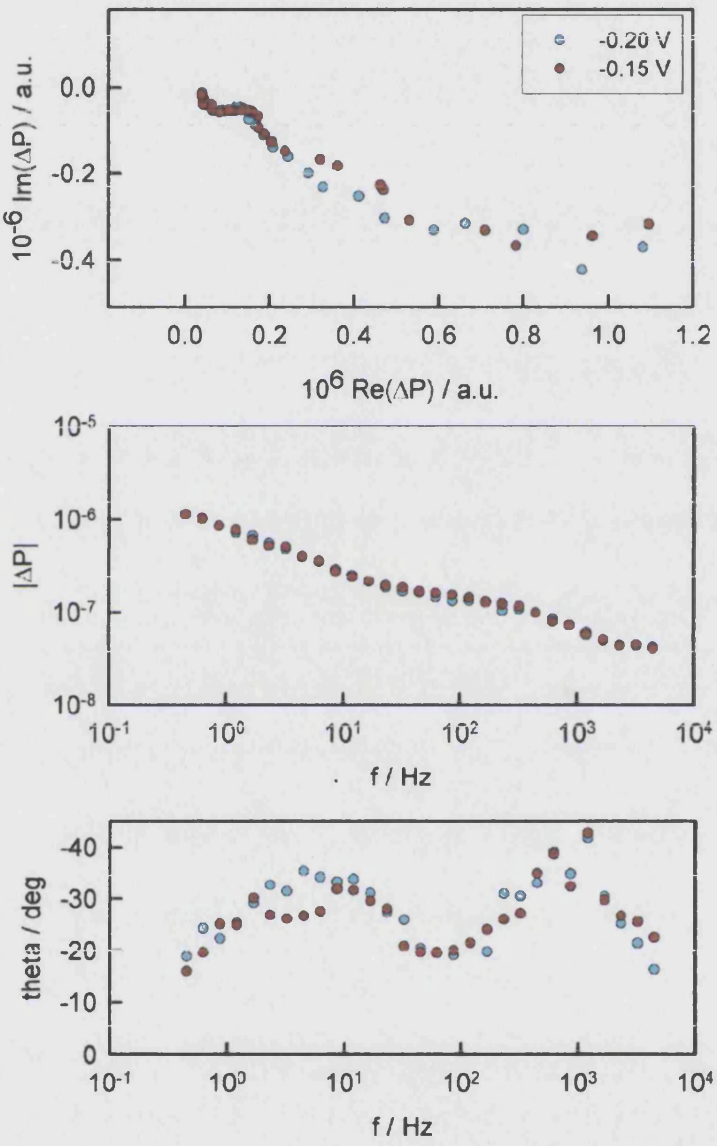

Figure 7.44: LMMR plots for p-Si in 1 M fluoride (pH 3) containing 1 mM $Ru(NH_3)_6^{3+}$. j_{photo} = -3.7 μA cm^{-2} at the saturation region on current-voltage curve.

The LMMR plot in Fig 7.42 at low frequencies shows flattened line, which could indicate the possibility of hydrogen evolution. Fig 7.45 illustrates the time resolved LMMR for p-Si in 1 M fluoride (pH 3) containing 0.33 mM $Ru(NH_3)_6^{3+}$. It is seen that the signal is reduced but the microwave response is still in the same time scale as the hydrogen evolution reaction (cf. Fig 7.20). This result suggests that hydrogen evolution reaction still takes place even though $Ru(NH_3)_6^{3+}$ is present.

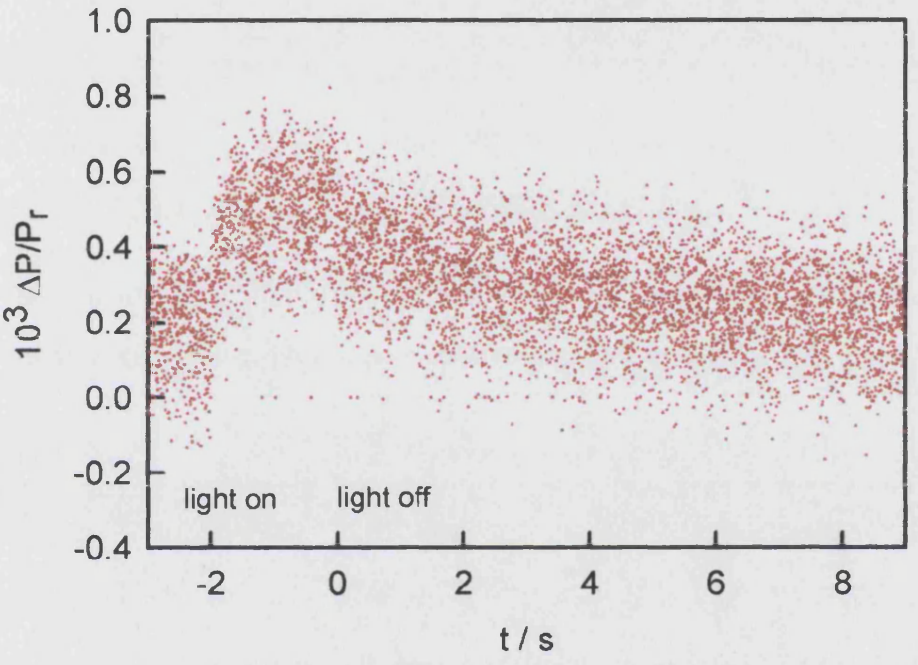

Figure 7.45: Time resolved LMMR plots for p-Si in 1 M fluoride (pH 3) containing 0.33 mM $Ru(NH_3)_6^{3+}$ at -0.45 V.

The photocurrent corresponding to Fig 7.45 is shown in Fig 7.46.

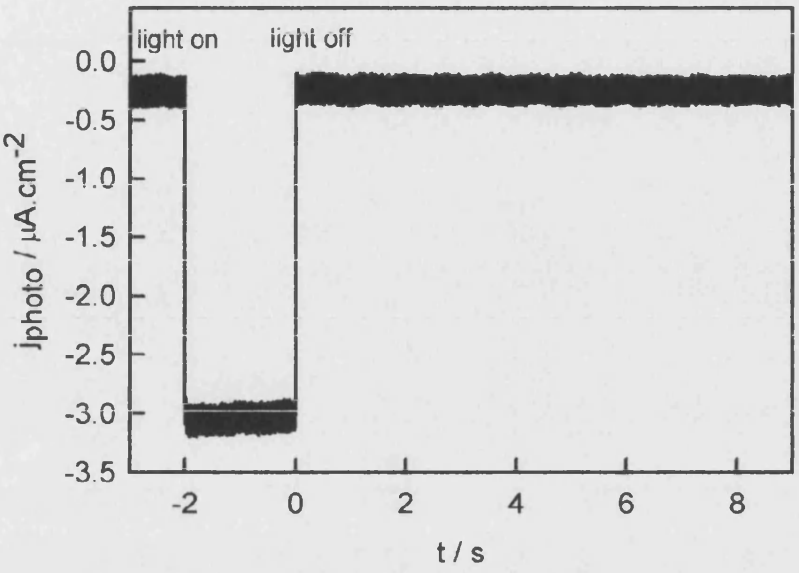

Figure 7.46: Transient photocurrent response corresponding to Fig 7.45, for p-Si in 1 M fluoride (pH 3) containing 0.33 mM $Ru(NH_3)_6^{3+}$ at -0.45 V.

The interpretation of IMPS and LMMR data has been previously described and the rate constants obtained from IMPS and LMMR for 0.1 mM $Ru(NH_3)_6^{3+}$ are summarised in Table 7.4 and the rate constants are derived from IMPS results as shown in Table 7.4 as well as in Fig 7.47.

E / V	$k_{tr} + k_{rec}$ / s^{-1}		k_{tr} / s^{-1}	k_{rec} / s^{-1}
	LMMR	IMPS		
-0.45	100	65	64	1
-0.40	104	67	64	3
-0.35	113	74	65	9
-0.30	146	99	74	25
-0.25	208	147	89	58

Table 7.4: 1M fluoride (pH 3) containing 0.1 mM $Ru(NH_3)_6^{3+}$. k_{tr} and k_{rec} derived from IMPS results.

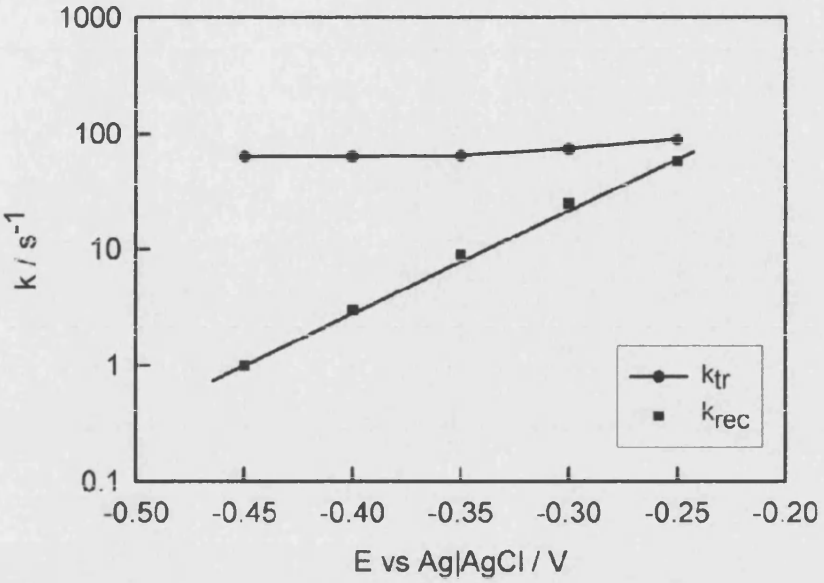

Figure 7.47: Rate constant as a function of potential at 0.1mM $Ru(NH_3)_6^{3+}$.

It is seen again that the k_{tr} is almost constant over the potential. On the other hand k_{rec} depends strongly on the potential.

We studied the hydrogen evolution reaction on p-Si at several light intensity as well as at several potentials by IMPS and LMMR. IMPS and LMMR results agree only at low light intensity (j_{photo} = ~-3 μA cm^{-2}). In the case of reduction of $Ru(NH_3)_6^{3+}$, IMPS and LMMR results are not consistent even for the low light intensity. In the case of hydrogen evolution, increasing the light intensity increases build up of electrons at the surface and electron mobility could be reduced, which results in the disagreement between IMPS and LMMR responses. However, in the case of reduction of $Ru(NH_3)_6^{3+}$, it is seen that microwave response is linearly proportional to the photocurrent, which predicts IMPS and LMMR responses should agree. In fact, IMPS and LMMR results are not good agreement and get worse at high concentration of $Ru(NH_3)_6^{3+}$. The reason for this is not clear at present.

The same trend is observed for 0.33 mM $Ru(NH_3)_6^{3+}$ as shown in Table 7.5 and Fig 7.48, i.e. k_{tr} is almost constant over the potential and k_{rec} varies.

E / V	$k_{tr} + k_{rec}$ / s^{-1}		k_{tr} / s^{-1}	k_{rec} / s^{-1}
	LMMR	IMPS		
-0.35	300	235	228	7
-0.30	324	264	237	27
-0.25	406	340	269	71
-0.20	551	527	342	185

Table 7.5: 1M fluoride (pH 3) containing 0.33 mM $Ru(NH_3)_6^{3+}$. k_{tr} and k_{rec} derived from IMPS results.

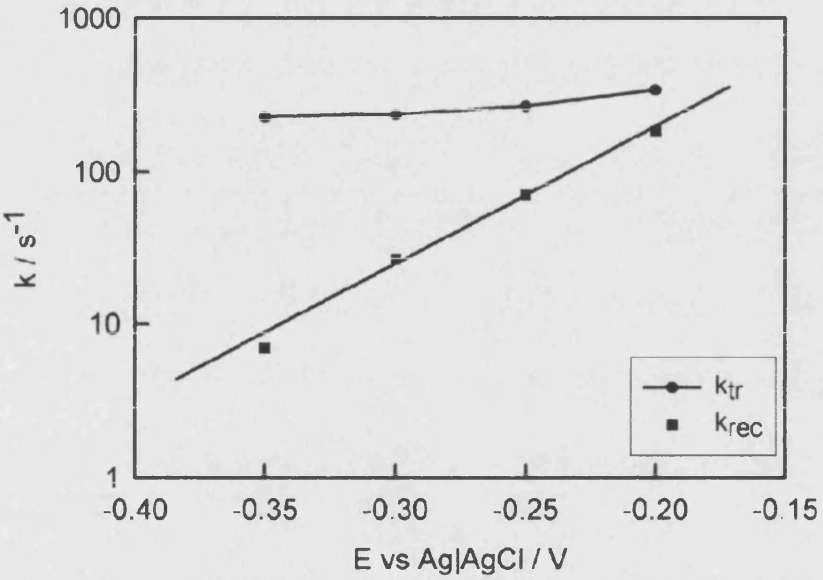

Figure 7.48: Rate constant as a function of potential at 0.33 mM $Ru(NH_3)_6^{3+}$.

It is interesting to note that k_{rec} is linearly proportional to the potential in logarithmic scale of k at 0.1 mM and 0.33 mM of $Ru(NH_3)_6^{3+}$. However, k_{tr} is no longer linearly proportional to the potential at 1 mM of $Ru(NH_3)_6^{3+}$ and k_{tr} slightly varies and is not constant any more, as shown in Table 7.6 and Fig 7.49.

E / V	$k_{tr} + k_{rec}$ / s^{-1}		k_{tr} / s^{-1}	k_{rec} / s^{-1}
	LMMR	IMPS		
-0.25	1460	465	457	8
-0.20	1528	992	875	117
-0.15	1799	1368	993	375
-0.10	1270	1340	708	632

Table 7.6: 1M fluoride (pH 3) containing 1 mM $Ru(NH_3)_6^{3+}$. k_{tr} and k_{rec} derived from IMPS results.

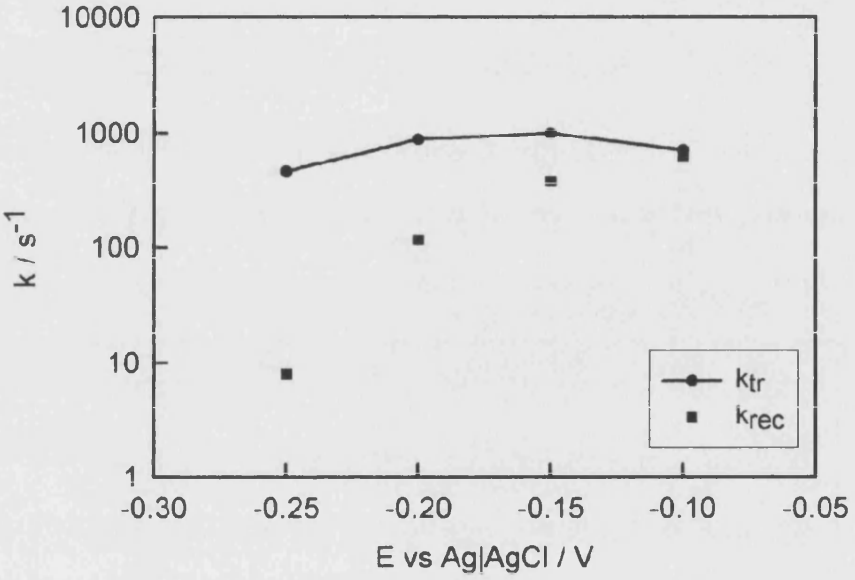

Figure 7.49: Rate constant as a function of potential at 1 mM $Ru(NH_3)_6^{3+}$.

Table 7.7 summarise the slope obtained from Fig 7.10, Fig 7.47, and Fig 7.48. 5.6 of the slope for hydrogen evolution and 9 for the presence of $Ru(NH_3)_6^{3+}$ were obtained. The slope becomes steeper when $Ru(NH_3)_6^{3+}$ is added. This means that the potential range that the recombination takes place in the hydrogen evolution is wider than that in the reduction of $Ru(NH_3)_6^{3+}$.

$[Ru(NH_3)_6^{3+}]$ / mol dm^{-3}	slope
0.0	5.6
0.1	8.9
0.33	8.9

Table 7.7: Slope from k_{rec} vs. potential plot.

Fig 7.50 illustrates the concentration dependence of the rate constant of charge transfer. It is seen that the charge transfer rate constant is linearly proportional to the concentration of $Ru(NH_3)_6^{3+}$, and 7.6×10^5 $M^{-1}s^{-1}$ is obtained from the slope. This value is quite similar to the rate constant for reaction with hydrogen (1.8×10^6 $M^{-1}s^{-1}$) studied by Navon *et al.*[16].

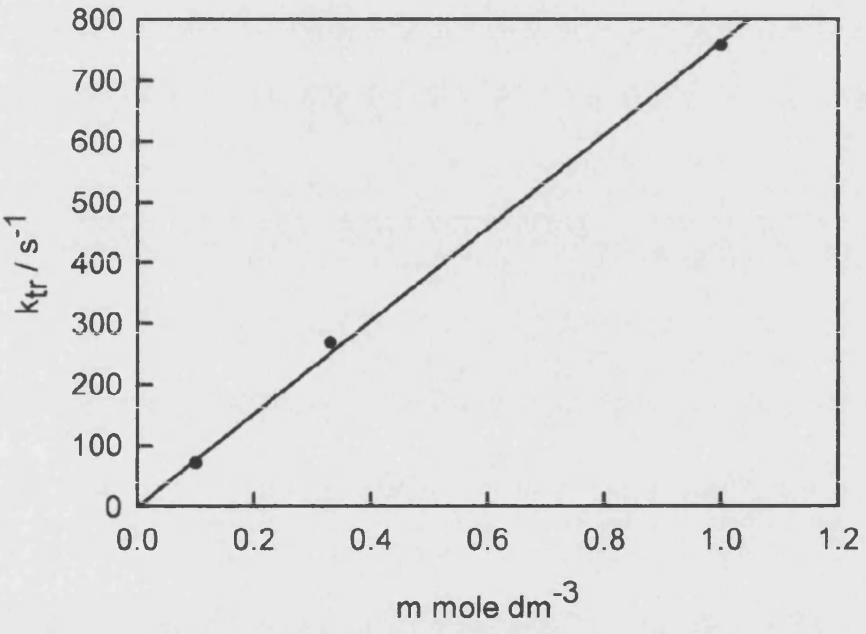

Figure 7.50: Rate constant as a function of the concentration of $Ru(NH_3)_6^{3+}$.

The first order rate constant for the reduction of 0.33 mM $Ru(NH_3)_6^{3+}$ was found to be 4×10^{-5} $cm\,s^{-1}$, assuming the tunnelling distance as 1.5 nm.

$$\begin{aligned} k_{tr} &= k_{observed} \times \delta \\ &= 269 \times 15 \times 10^{-8} \\ &= 4 \times 10^{-5}\ cm\,s^{-1} \end{aligned}$$

This value is much lower than the expected (550 $cm\,s^{-1}$). This result suggests that the reaction does not occur by direct electron transfer.

Navon *et al.* [16] studied the reaction of hydrogen atoms with $Ru(NH_3)_6^{3+}$. In this experiment, hydrogen atom was produced by a high frequency discharge in pure H_2 gas at pressures of ~30 mm, and introduced into the aqueous solution by bubbling. These authors compared with Marcus theory, using the following relations

$$k_{12} = \sqrt{k_{11}k_{22}K_{12}f} \tag{7.39}$$

where k_{12} is the rate constant of a reaction, k_{11} and k_{22} are self exchange rate constant for oxidised and reduced species, respectively, K_{12} is equilibrium constant of the reaction, f is correction factor obtained from

$$\ln f = \frac{(\ln K_{12})^2}{4} \ln\left(\frac{k_{11}k_{22}}{Z^2}\right) \tag{7.40}$$

Here Z is collision frequency ($1 \times 10^{11}\ M^{-1}s^{-1}$).

They discussed that the reaction with hydrogen is about 1000 times slower than Marcus type outer-sphere electron transfer and proposed the reaction scheme as

$$Ru(NH_3)_6^{3+} + H \longrightarrow Ru(NH_3)_5NH_2^{3+} + H_2 \tag{7.41}$$

followed by

$$Ru(NH_3)_5NH_2^{3+} + H_2 + H_2O \longrightarrow Ru(NH_3)_5^{2+} + H_3O^+ \tag{7.42}$$

Our experimental result is in good agreement with their analysis and we propose an indirect route that electrons are transferred via a reaction intermediate.

$$H^+ + e \longrightarrow H^{\cdot} \tag{7.43}$$

$$H^{\cdot} + Ru(III) \longrightarrow H^+ + Ru(II) \tag{7.44}$$

Schematic diagram of the reaction scheme for the reduction of $Ru(NH_3)_6^{3+}$ is illustrated in Fig 7.51.

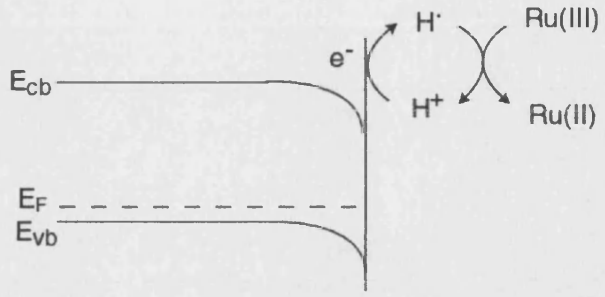

Figure 7.51: Reduction of Ru(III) via reaction intermediate.

7.5 Conclusion

The kinetics of hydrogen evolution and reduction of $Ru(NH_3)_6^{3+}$ were studied by frequency- and time resolved microwave and photocurrent measurements. It is shown that the time resolved measurements give the same kinetic information as frequency resolved measurements. It is also shown that the combination of microwave and photocurrent measurements are powerful tool to study kinetics of interfacial electron transfer reactions at semiconductor|electrolyte interface. Hydrogen evolution reaction at p-Si is kinetically hindered. The reduction of $Ru(NH_3)_6^{3+}$ is slightly faster than the hydrogen evolution reaction, but not faster than the expected. It could indicate that $Ru(NH_3)_6^{3+}$ could be reduced via hydrogen, which is a different route from Marcus type outer-sphere electron transfer.

References

[1] Schlichthörl, G.; Ponomarev, E. A.; Peter, L. M. Journal of the Electrochemical Society **1995**, 142, 3062-3067.

[2] Peter, L. M. in Comprehensive chemical kinetics, Vol. 37, Elsevier, New York, 1999.

[3] Peter, L. M.; Vammaekelbergh, D. in Advances in electrochemical science and engineering, Vol.6, VCH, New York, 1999.

[4] Iwasita, T.; Schmickler, W.; Schultze, J. W. Berichte Der Bunsen-Gesellschaft-Physical Chemistry Chemical Physics **1985**, 89, 138-142.

[5] Chen, P; McCreery, R. L. Analytical Chemistry **1996**, 68, 3958-3965.

[6] Iwasita, T.; Schmickler, W.; Herramnn, J.; Vogel, U. Journal of the Electrochemical Society **1983**, 130, 2026-2032.

[7] Demierry, P.; Etcheberry, A.; Aucouturier, M. Physica B **1991**, 170, 124-128.

[8] Demierry, P.; Etcheberry, A.; Aucouturier, M. Journal of Applied Physics **1991**, 69, 1099-1101.

[9] Demierry, P.; Ballutaud, D.; Aucouturier, M.; Etcheberry, A. Journal of the Electrochemical Society **1990**, 137, 2966-2973.

[10] Meyer, T. J.; Taube, H. Inorganic Chemistry **1968**, 7, 2369-2379.

[11] Morrison, S. R. Electrochemistry at semiconductor and oxidized metal electrodes; Plenum press: New York, 1980.

[12] Hale, J. M. in Reactions of molecules at electrodes; John Wiley: London, 1971.

[13] Sato, N. Electrochemistry at metal and semiconductor electrodes; Elsevier: Oxford, 1998.

[14] Schmickler, W. Interfacial electrochemistry; Oxford : Oxford University Press: Oxford, 1996.

[15] Southampton Electrochemistry Group Instrumental methods in electrochemistry; Horwood: Chichester, 2001.

[16] Navon, G.; Meyerstein, D. Journal of Physical Chemistry **1970**, 74, 4067-4070.

[17] Ponomarev, E. A.; Peter, L. M. Journal of Electroanalytical Chemistry **1995**, 397, 45-52.

[18] Schefold, J. Journal of Electroanalytical Chemistry **1992**, 341, 111-136.

[19] Vanmaekelbergh, D.; Cardon, F. Journal of Physics D-Applied Physics **1986**, 19, 643-656.

[20] Lewis, N. S. Solar Energy Materials and Solar Cells **1995**, 38, 323-325.

[21] Pomykal, K. E.; Fajardo, A. M.; Lewis, N. S. Journal of Physical Chemistry **1996**, 100, 3652-3664.

[22] Fajardo, A. M.; Lewis, N. S. Journal of Physical Chemistry B **1997**, 101, 11136-11151.

[23] Pomykal, K. E.; Lewis, N. S. Journal of Physical Chemistry B **1997**, 101, 2476-2484.

[24] Lewis, N. S. Journal of Physical Chemistry B **1998**, 102, 4843-4855.

[25] Czapski, G.; Jortner, J.; Stein, G. Journal of Physical Chemistry 65, **1961**, 956-964.

[26] G. Czapski, G.; Stein, G. Journal of Physical Chemistry 63, **1959**, 850-853.

[27] Atwater, H. A. Journal of Applied Physics, 31, **1960**, 938-939.

[28] Schofthaler, M.; Brendel, R. Journal of Applied Physics, 77, **1995**, 3162-3173.

[29] Marcus, R. A. Journal of Physical Chemistry 67, **1963**, 853-857.

Chapter 8

Anodic dissolution of p-Si

8.1 Introduction

Anodic dissolution of Si in fluoride media is of great interest for both science and technology. For instance, removal of oxide layer via dissolution in aqueous fluoride solution is a key process step in silicon based microfabrication technologies [1]. Fig 8.1 illustrates the atomically flat Si (111) surface. It is seen that all dangling bonds at the surface have reacted with hydrogen atom. A dangling bond is the unsaturated bond at the first layer of the surface. The dissolution normally starts at the kink site for Si (111).

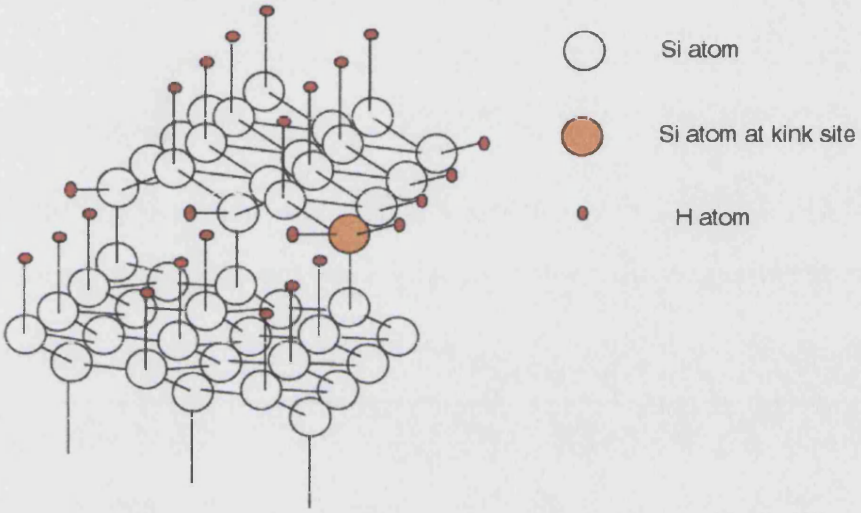

Figure 8.1: Atomically flat Si (111) surface shows a kink site.

In porous silicon formation region, the Si surface is hydrogen terminated and the etching mechanism is divalent reaction mechanism. The overall etching reaction in this region is

$$Si + 6HF + 2h^+ \longrightarrow SiF_6^{2-} + H_2 + 4H^+ \tag{8.1}$$

In the electropolishing region, it is assumed that the thickness of the inner oxide layer is constant at a given potential under controlled hydrodynamic conditions, i.e. the rates of oxide growth and dissolution are equal. The tetravalent reaction mechanism is generally accepted in this region. The overall oxidation reaction is

$$Si + 2H_2O + 4h^+ \longrightarrow SiO_2 + 4H^+ \tag{8.2}$$

HF is present in several forms such as HF, HF_2^-, and F^- and depends on pH. Searson [2] calculated for the case of 1M of the total concentration of fluoride as shown in Fig 8.2. It is seen that at low pH, HF molecules are dominant whereas at high pH F^- is dominant. At intermediate pH, HF_2^- is the dominant species.

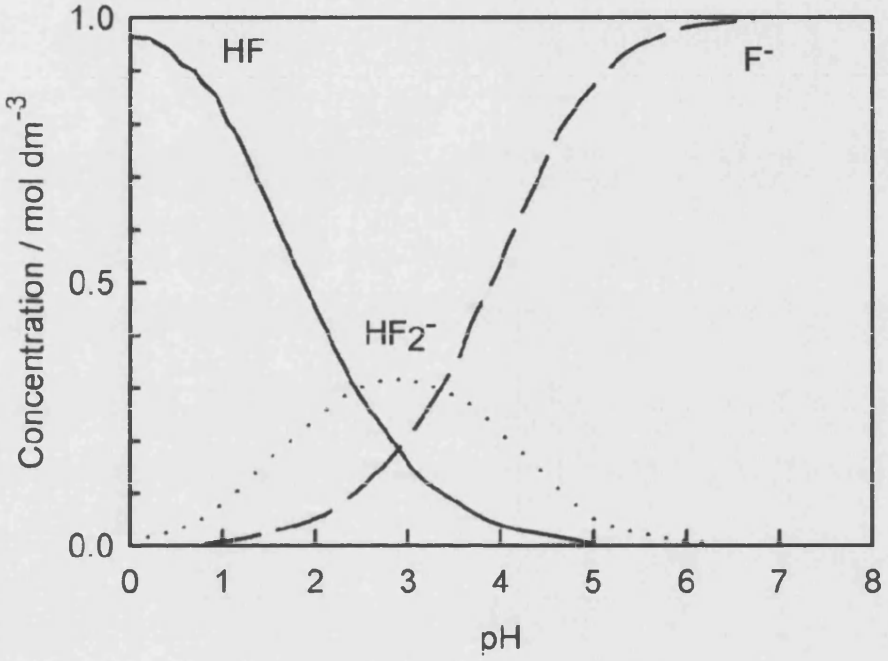

Figure 8.2: The total concentration of fluoride ion is 1M [2]

The formed oxide layer dissolve in fluoride solutions and its dissolution process depends on the presence of HF

$$SiO_2 + 6HF \longrightarrow SiF_6^{2-} + 2H_2O + 2H^+ \text{ at low pH} \tag{8.3}$$

or

$$SiO_2 + 3HF_2^- \longrightarrow SiF_6^{2-} + H_2O + OH^- \text{ at intermediate pH} \tag{8.4}$$

If the electrolyte contains NH_4F, the overall reaction for the etching is proposed as

$$SiO_2 + 6NH_4F + 4H_2O \longrightarrow SiF_6^{2-} + 6NH_4^+ + 2H^+ + 6OH^- \tag{8.5}$$

We used 0.1M fluoride (pH 4.5) and (pH 3), therefore, eq 8.4 and eq 8.5 are probable reaction mechanism.

8.2 Single frequency capacitance and PMMR results

The anodic dissolution of p-Si was studied in 0.01M fluoride (pH 3) and capacitance and PMMR response are shown in Fig 8.8. Inversion conditions are not observed in aqueous solutions since electron transfer prevents the establishment of thermal equilibrium between holes and electrons. Instead, a deep depletion layer is formed.

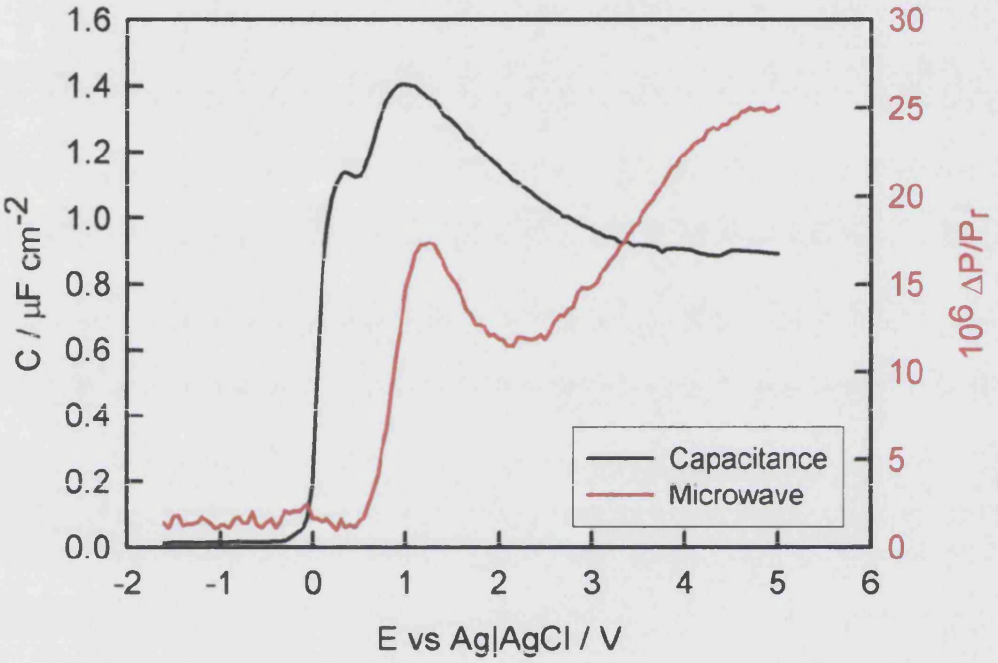

Figure 8.3: Capacitance and PMMR measured for p-Si in 0.01M NH_4F (pH 3) at 1 kHz with 40 mV rms.

Semiconductor|oxide is extensively studied in Metal Oxide Semiconductor (MOS) devices. The electric field and capacitance can be obtained by solving Poisson's equation [9]

$$\frac{d^2\phi}{dx^2} = -\frac{\rho(x)}{\varepsilon_0\varepsilon_r} \tag{8.6}$$

$$\rho(x) = q[p(x) - n(x) + N_D - N_A] \tag{8.7}$$

From eq 8.6 and eq 8.7

$$\frac{d^2\phi}{dx^2} = -\frac{q[p(x) - n(x) + N_D - N_A]}{\varepsilon_0\varepsilon_r} \tag{8.8}$$

The charge neutrality should be balanced in the bulk, and therefore eq 8.7 becomes

$$N_D - N_A = n(\infty) - p(\infty) \tag{8.9}$$

Since $n = n_i \exp(u)$ and $p = n_i \exp(-u)$, eq 8.9 becomes

$$\begin{aligned} N_D - N_A &= n_i[\exp(u_{bulk}) - \exp(-u_{bulk})] \\ &= 2n_i \sinh u_{bulk} \end{aligned} \tag{8.10}$$

where $u_{bulk} = -\ln\left(\frac{N_A}{n_i}\right)$

Similarly,

$$\begin{aligned} n(x) - p(x) &= n_i[\exp u(x) - \exp -u(x)] \\ &= 2n_i \sinh u(x) \end{aligned} \tag{8.11}$$

where $u(x)$ is dimensionless potential given by

$$u(x) = \frac{q\phi(x)}{k_B T} \tag{8.12}$$

Hence eq 8.8 can be rewritten as

$$\begin{aligned} \frac{d^2\phi}{dx^2} &= \frac{2qn_i}{\varepsilon_0\varepsilon_r}(\sinh u(x) - \sinh u_{bulk}) \\ \frac{d^2u}{d\phi^2}\frac{d^2\phi}{dx^2} &= \frac{q}{k_B T}\frac{2qn_i}{\varepsilon_0\varepsilon_r}(\sinh u(x) - \sinh u_{bulk}) \\ \frac{d^2u(x)}{dx^2} &= \frac{2q^2n_i}{k_B T\varepsilon_0\varepsilon_r}(\sinh u(x) - \sinh u_{bulk}) \\ &= \frac{1}{\lambda_i^2}[\sinh u(x) - \sinh u_{bulk}] \end{aligned} \tag{8.13}$$

where λ_i is intrinsic Debye length, given by

$$\begin{aligned} \lambda_i &= \sqrt{\frac{\varepsilon_0\varepsilon_{Si}k_B T}{2q^2n_i}} \\ &= \sqrt{\frac{8.854 \times 10^{-14} \times 11.9 \times 1.38 \times 10^{-23} \times 298}{2 \times (1.6022 \times 10^{-19})^2 \times 1 \times 10^{10}}} \\ &= 2.9 \times 10^{-3} \text{ cm at } 298 \text{ K} \end{aligned} \tag{8.14}$$

Since $\frac{d}{dx}\left(\frac{du}{dx}\right)^2 = 2\frac{du}{dx}\left(\frac{d^2u}{dx^2}\right)$, $2\frac{du}{dx}$ can be multiplied to eq 8.13

$$2\frac{du}{dx}\left(\frac{d^2u}{dx^2}\right) = \frac{2}{\lambda_i^2}(\sinh u(x) - \sinh u_{bulk})\frac{du}{dx} = \frac{d}{dx}\left(\frac{du}{dx}\right)^2 \tag{8.15}$$

Integrating from the surface to the bulk

$$\int_{du_s}^{0} d\left(\frac{du}{dx}\right)^2 = \frac{2}{\lambda_i^2}\int_{u_s}^{u_b}(\sinh u(x) - \sinh u_{bulk})du$$

$$-\left(\frac{qF_s}{k_B T}\right)^2 = \frac{2}{\lambda_i^2}(\cosh u_{surf} - \cosh u_{bulk})(u_{bulk} - u_{surf})\sinh u_{bulk} \qquad (8.16)$$

The final solution for the electric field at the surface of the silicon is given by

$$F_{Si}^{surf} = \mathrm{sgn}(u_{bulk} - u_{surf})\frac{k_B T}{q\lambda_i}F(u_{surf}, u_{bulk}) \qquad (8.17)$$

where $F(u_{surf}, u_{bulk}) = \sqrt{2\left[(u_{bulk} - u_{surf})\sinh u_{bulk} - (\cosh u_{bulk} - \cosh u_{surf})\right]}$

It is noted that $\mathrm{sgn}(u_{bulk} - u_{surf})$ is +1 if $u_{bulk} - u_{surf} > 0$ and $\mathrm{sgn}(u_{bulk} - u_{surf})$ is -1 if $u_{bulk} - u_{surf} < 0$.

The electric field is plotted as a function of the potential as shown in Fig 8.4.

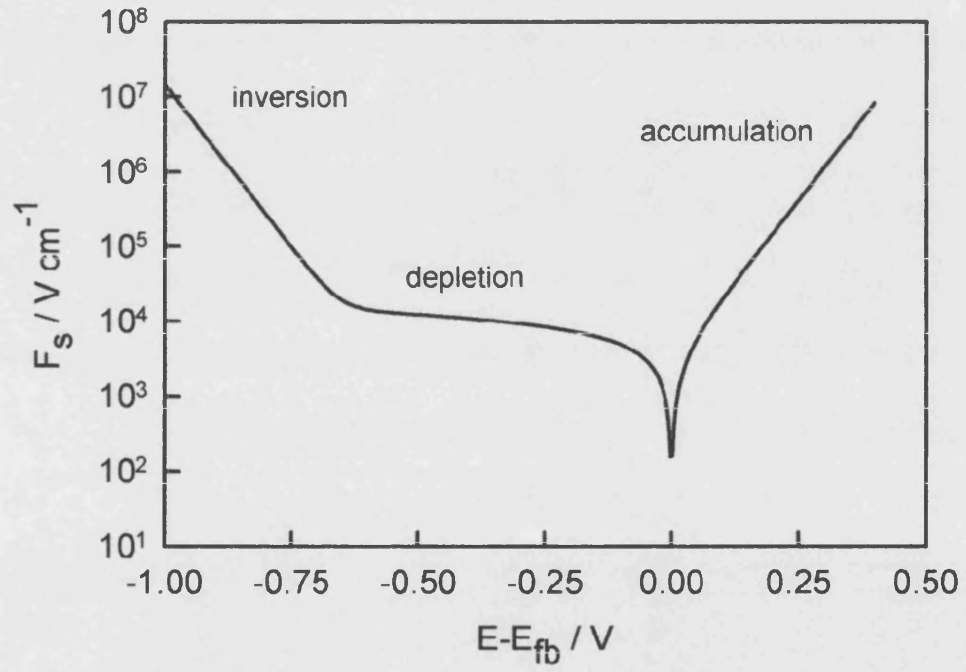

Figure 8.4: Potential dependence of the electric fields for p-Si.

Using Gauss's law, the total charge is

$$Q = \varepsilon_0\varepsilon_r F_{Si}^{surf}$$

$$= \mathrm{sgn}(u_{bulk} - u_{surf})\frac{\varepsilon_0\varepsilon_r}{\lambda_i}\left(\frac{k_B T}{q}\right)F(u_{surf}, u_{bulk}) \qquad (8.18)$$

The capacitance of the silicon space charge region depends on the potential difference across the semiconductors, expressed as

$$\begin{aligned} C &= \left(\frac{dQ}{du_s}\right)\left(\frac{du}{d\phi}\right) \\ &= \frac{q}{k_B T}\left(\frac{dQ}{du_s}\right) \end{aligned} \tag{8.19}$$

From eq 8.18 and eq 8.19

$$\begin{aligned} C_{Si} &= -\mathrm{sgn}(u_{bulk} - u_{surf})\frac{\varepsilon_0\varepsilon_r}{\lambda_i}\left(\frac{k_B T}{q}\right)\left(\frac{q}{k_B T}\right)\frac{d}{du}[F(u_{surf}, u_{bulk})] \\ &= -\mathrm{sgn}(u_{bulk} - u_{surf})\frac{\varepsilon_0\varepsilon_r}{\lambda_i}\frac{\sinh u_{surf} - \sinh u_{bulk}}{F(u_{surf}, u_{bulk})} \end{aligned} \tag{8.20}$$

The potential dependence of the capacitance of the Si|electrolyte interface in the absence of surface oxide is illustrated in Fig 8.5. It can be seen that the Helmholtz layer, C_H, determines the total capacitance when the inversion or accumulation capacitances become larger than C_H. In the depletion region, the capacitance is determined by the space charge capacitance, which is much smaller than C_H. In the case of p-Si in fluoride solutions, accumulation of holes causes dissolution of silicon lattice. Initially, a porous silicon layer is formed and at higher applied voltages electropolishing occurs and a thin oxide film is present. Under the latter conditions, the total capacitance is determined by the dielectric capacitance of oxide layer. We may expect the thickness of this insulating oxide to be determined by the anodising ratio, as illustrated in Fig 8.6.

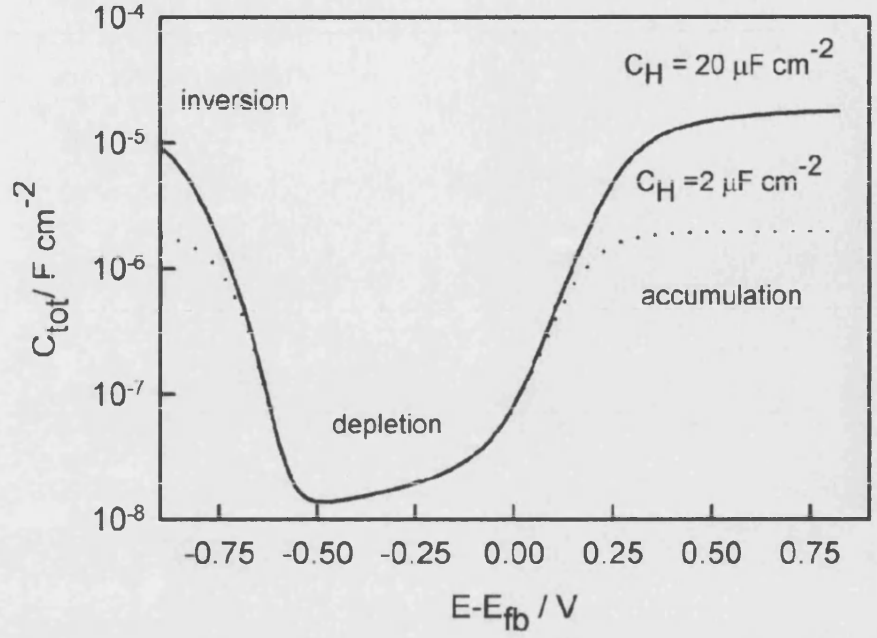

Figure 8.5: Calculated capacitance of the p-Si|electrolyte interface showing inversion, depletion and accumulation. Note that $1/C_{tot}=1/C_{Si}+1/C_H$.

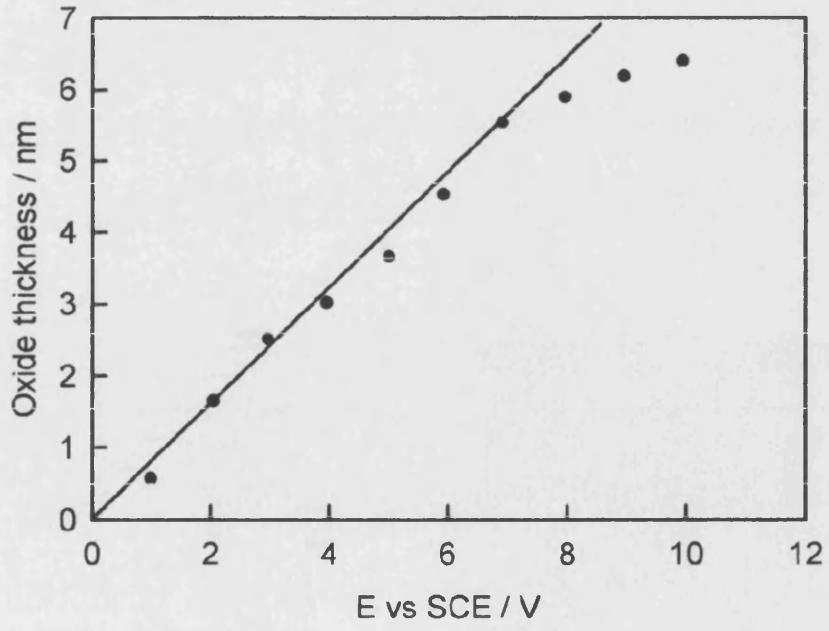

Figure 8.6: Oxide growth at Si in 0.1M fluoride (pH 4.5) and anodising ratio is 0.85 nm V^{-1} [3].

It is seen that the oxide growth is almost linearly proportional to the applied potential and the anodising ratio is 0.85 nm V^{-1}. Taking into account the oxide capacitance, the total capacitance was calculated as shown in Fig 8.7

$$\frac{1}{C_{tot}} = \frac{1}{C_{acc}} + \frac{1}{C_{ox}} + \frac{1}{C_H} \tag{8.21}$$

where C_{acc} is accumulation capacitance, C_{ox} is (dry) oxide capacitance, and C_H is Helmholtz capacitance. Oxide capacitance is given by

$$C_{ox} = \frac{\varepsilon_0 \varepsilon_{SiO_2}}{d} \tag{8.22}$$

$$d = \text{anodising ratio} \times E \tag{8.23}$$

It is seen that the total capacitance is reduced with increasing the potential in the range of 0.4 V to 2.5 V (cf. Fig 8.5). In practice, the anodising ratio may not be constant since changes in oxide structure and composition affect the kinetic growth. Fig 8.7 explains the reduction of capacitance observed in Fig 8.3.

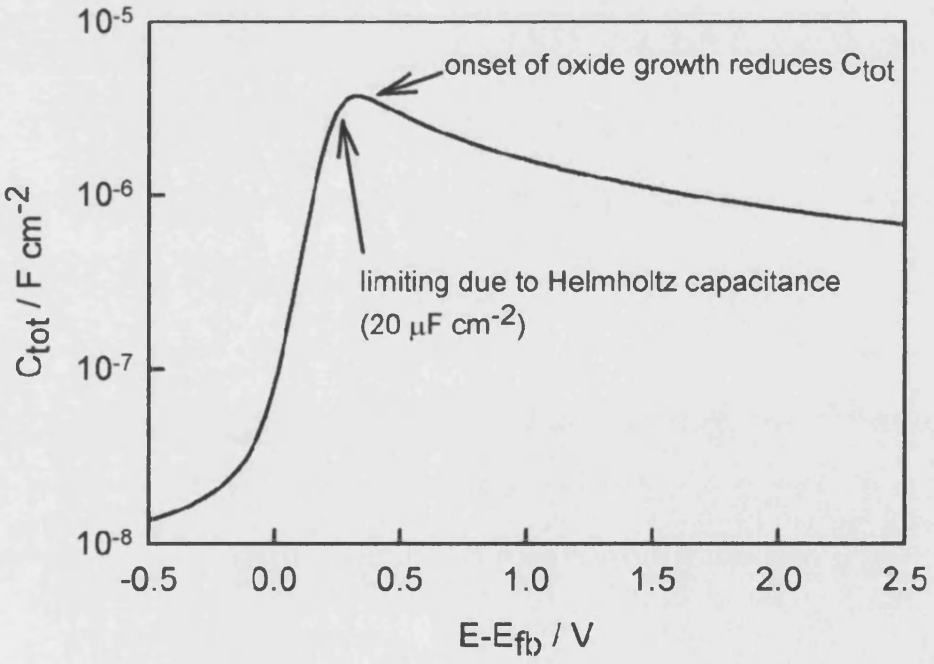

Figure 8.7: Calculated capacitance for p-Si under accumulation conditions, showing the predicted effect of oxide growth in the case of anodising ratio = 1 nmV^{-1}.

Fig 8.8 shows the cyclic voltammogram of p-Si in 10 mM fluoride (pH 3). It is seen that the 10 mM fluoride does not etch oxide layer properly and the reverse direction is quite different from the forward scan.

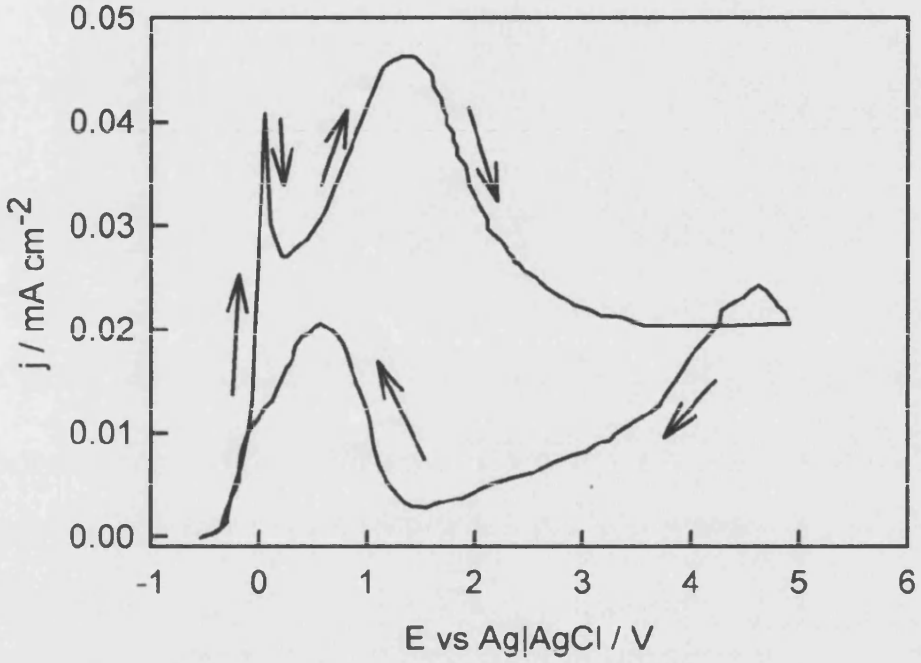

Figure 8.8: Cyclic voltammogram of p-Si in 0.01 M fluoride (pH 3). Sweep rate = 2 mV s^{-1},

Bailes *et al.*[5] measured the etch rate of oxide layer at several concentration of fluoride as well as at different pH, as summarised in Table 8.1.

$[F^-]$ / mol dm^{-3}	pH	Etch rate / nm s^{-1}
0.01	3.0	0.0011
0.1	3.0	0.0143
0.1	4.5	0.0023

Table 8.1: The effect of fluoride concentration on etching rate [5].

It is seen that the etch rate in 0.1 M fluoride (pH 4.5) is quite similar to that in 0.01M fluoride (pH 3) and 0.1M fluoride (pH 4.5) has the faster etching rate of oxide layer than 10 mM (pH 3). Fig 8.9 shows the potential dependence of the dark current and

capacitance of the p-Si in 0.1M fluoride (pH 4.5) at 1k Hz, and Fig 8.10 shows the corresponding PMMR response. It is interesting to note that the microwave response falls in the porous silicon region before rising again in the electropolishing region. This indicates a sharp reduction in the modulation of the hole density in the silicon under conditions where porous silicon is formed. The reason for this is not clear but we speculate it points to Fermi level pinning as the result of raid hole consumption at the interface. The rise in the microwave response in the electropolishing region indicates that the modulated hole density increases. This increase can be related to the changes in accumulation capacitance and the changes in the potential distribution across the system due to the formation of the inner dielectric layer oxide.

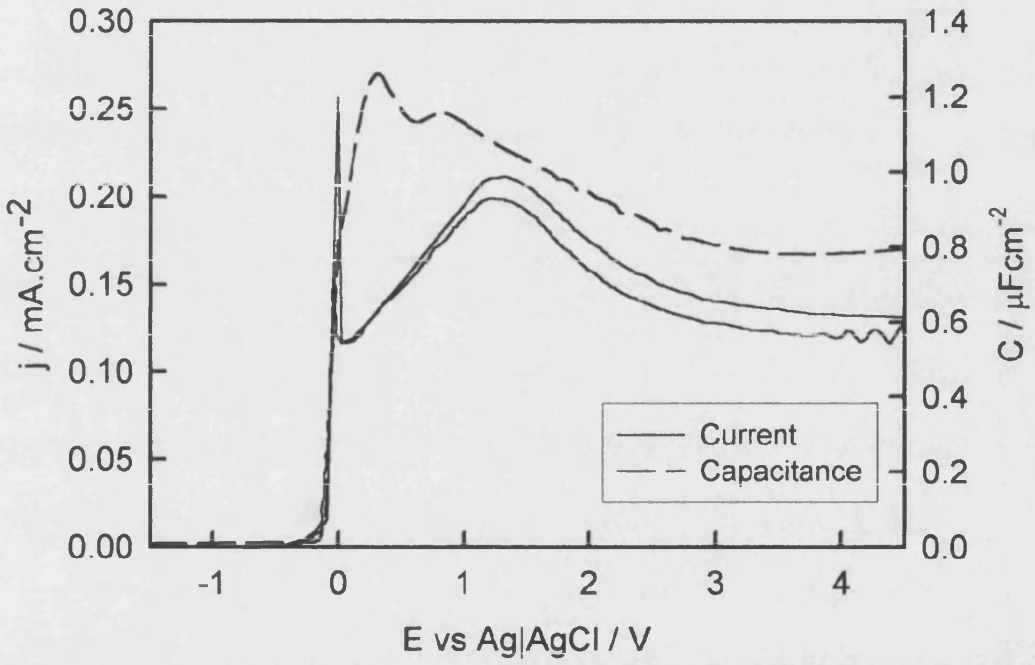

Figure 8.9: Current density and capacitance measured for p-Si in 0.1M NH_4F (pH 4.5). Sweep rate = 2 mV s^{-1}, at 1 kHz with 40 mV rms.

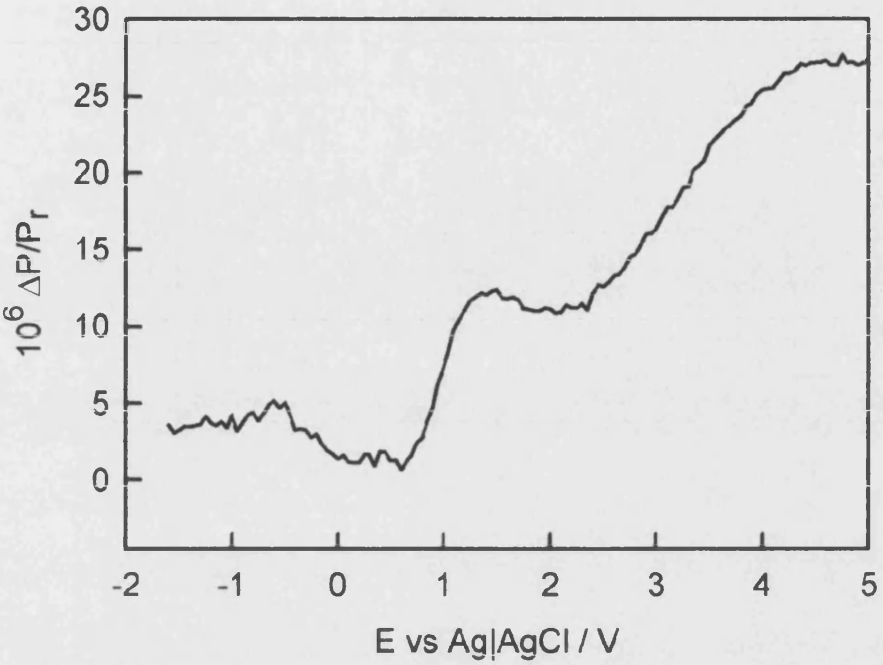

Figure 8.10: PMMR response of the same system.

In the depletion region, the dark current is small and for the low doped samples used in this study ($N_A = \sim 10^{15}$ cm^{-3}), the total capacitance of the system is determined predominantly by the depletion layer capacitance. Under these conditions, the microwave response can be related to the Mott-Schottky relationship, and the sensitivity factor can be determined from the linear relationship between capacitance and PMMR responses as shown in Fig 8.11.

$$\frac{\Delta P}{P_r} = S\frac{\mu_p C \Delta\phi}{Rd} \tag{8.24}$$

The sensitivity factor is

$$\begin{aligned} S &= \frac{R \times d \times \text{slope}}{\mu_p \times \Delta\phi} \\ &= \frac{0.5 \times 350 \times 10^{-4} \times 440}{460 \times 0.04} \\ &= 0.42 \ \ \Omega\,\text{cm} \end{aligned}$$

0.42 of sensitivity factor was obtained for 0.1M fluoride (pH 4.5).

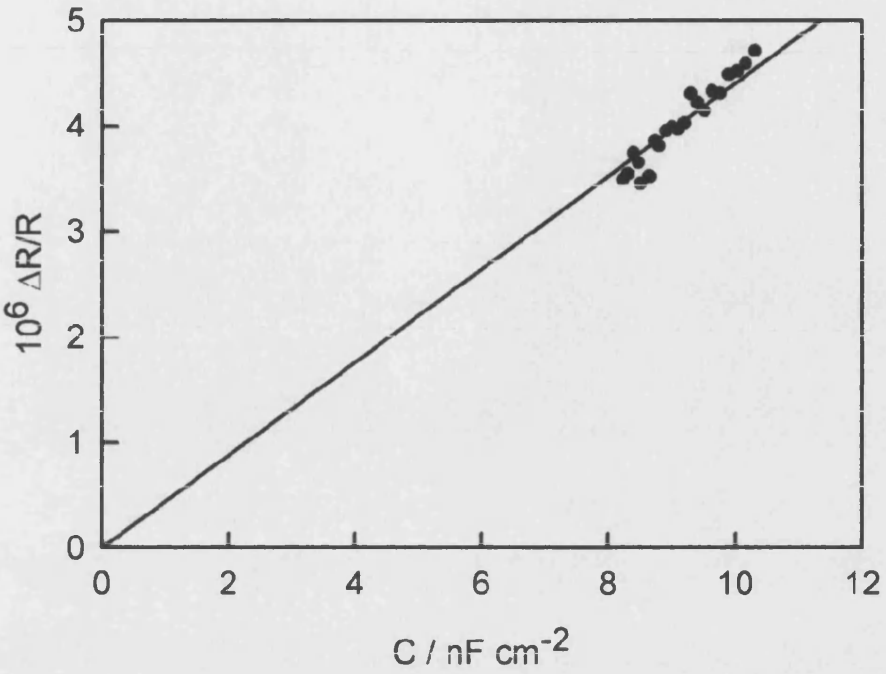

Figure 8.11: Normalised PMMR response as a function of capacitance of p-Si in 0.1M fluoride (pH 4.5) at 10 kHz with 40 mV rms.

The mobility in the depletion and inversion layers is extensively studied. The carrier mobility is variable and is reduced with increasing concentration of dopants as shown in Fig 8.12.

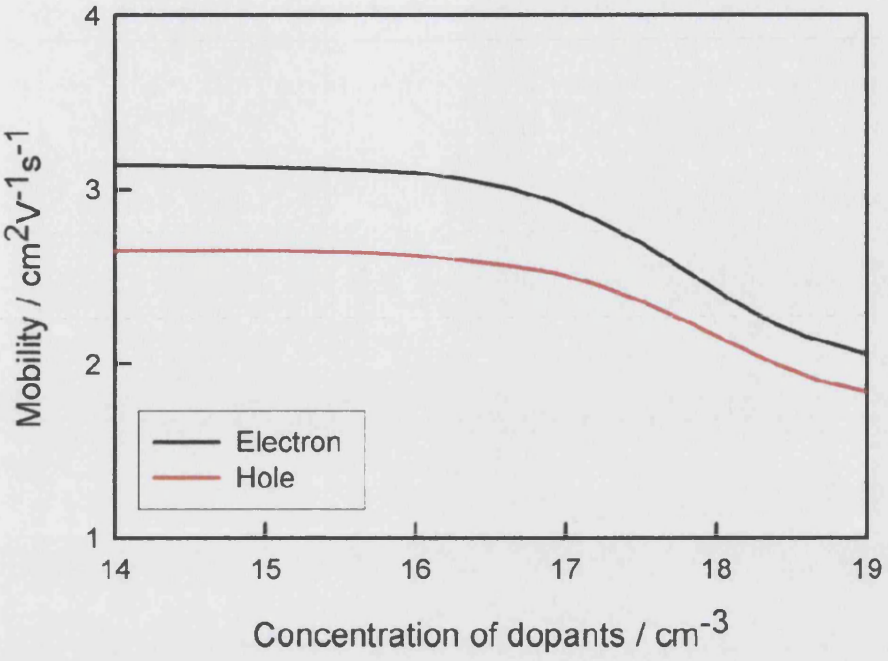

Figure 8.12: Bulk mobility of electrons and holes of Si at room temperature [20].

The hole mobility in accumulation region can be related to different scattering processes given by [18]

$$\frac{1}{\mu_{\text{acc}}} = \frac{1}{\mu_{\text{c}}} + \frac{1}{\mu_{\text{ph}}} + \frac{1}{\mu_{\text{sr}}} \tag{8.25}$$

where μ_{c} is mobility limited by ionised impurity (coulomb) scattering, μ_{ph} is mobility limited by phonon scattering, and μ_{sr} is mobility limited by surface roughness scattering. For low doping levels, the coulomb scattering is large, so that the phonon and surface roughness scattering are dominated. At higher doping levels, the coulomb scattering is dominant, i.e. surface roughness and phonon scattering terms are large. In accumulation region, the carrier mobility is reduced as increasing the electric field, which also reduce the microwave response. Fig 8.13 shows the accumulation layer mobility for electron and holes. It is seen that the mobility approaches the bulk mobility values as decreasing the electric field. This could be due to ionised impurity (coulomb) scattering by the large carrier concentration.

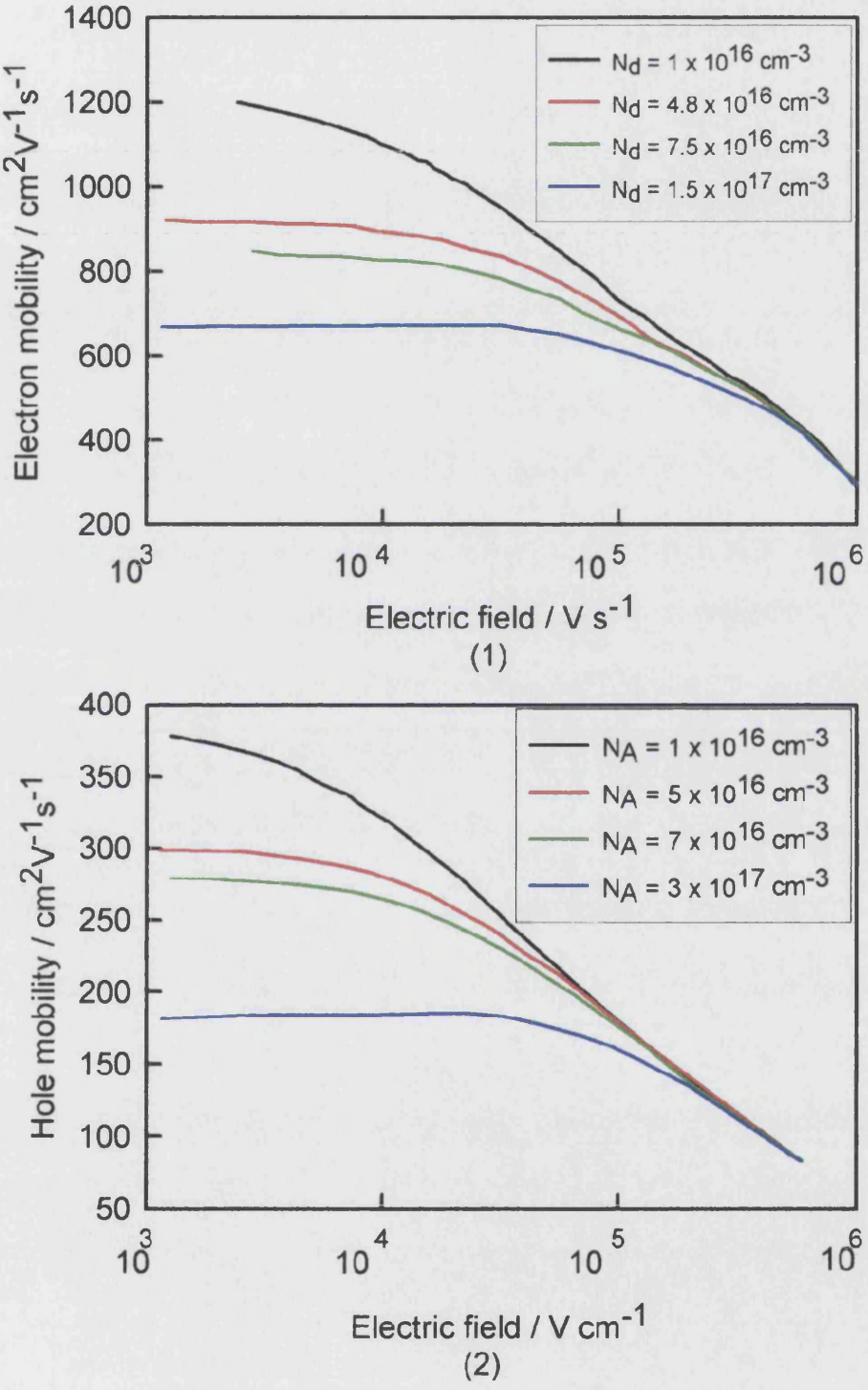

Figure 8.13: Mobility of electrons and holes for Si in accumulation region [18].

The various scattering in the case of doping density of 5×10^{19} cm^{-3} is plotted as a function of the electric field as shown in Fig 8.14. It is seen that the reduction in mobility is dominated by the surface roughness scattering term at high electric field.

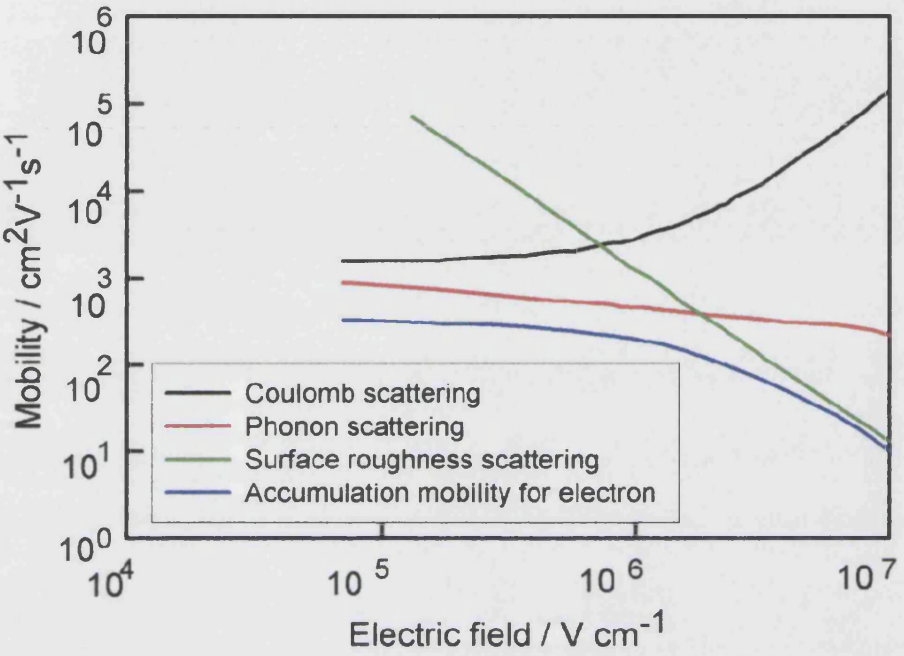

Figure 8.14: Mobility of electrons in accumulation layer in the case of doping density of 5×10^{19} cm^{-3} [10].

From eq 8.24, the hole mobility can be expressed as

$$\mu_p = \frac{\Delta P}{P_r} \times \frac{Rd}{SC\Delta\phi} \tag{8.26}$$

The hole mobility was calculated applying eq 8.26 as shown in Fig 8.15. It is seen that in depletion region the mobility is bulk mobility whereas in accumulation region, the mobility is reduced compared with the bulk mobility, which could be due to the surface roughness scattering.

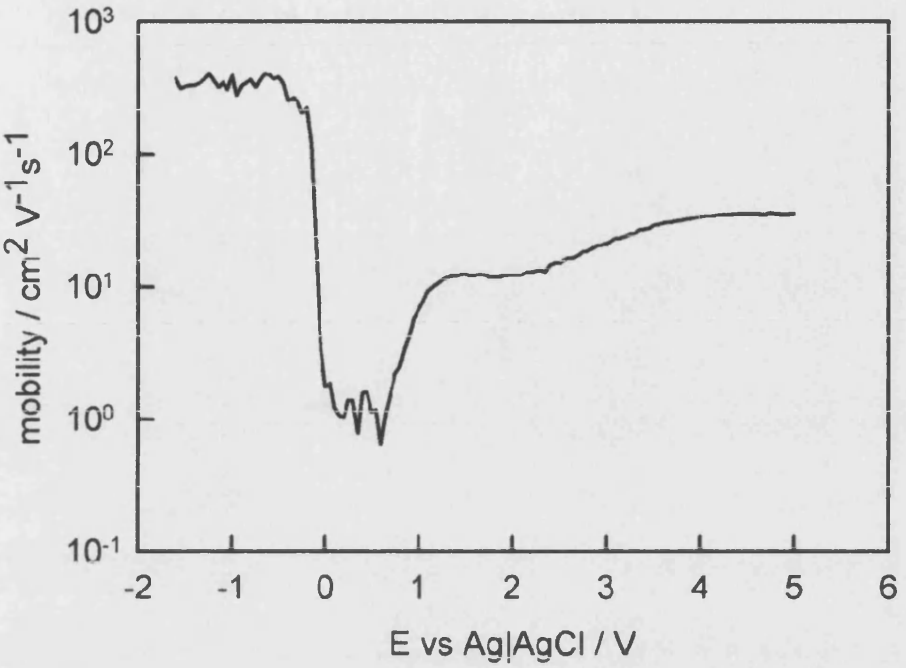

Figure 8.15: Mobility of holes for p-Si. S = 0.42

It is shown from Table 8.1 that the dissolution rate is faster in 0.1M fluoride (pH 3) than in 0.1M fluoride (pH 4.5) and we studied the anodic dissolution of p-Si in 0.1M fluoride (pH 3). The potential dependence of the current and capacitance of p-Si in 0.1M NH_4F (pH 3) is shown in Fig 8.16, and the corresponding microwave response is shown in Fig 8.17. It is seen that the large current in pH 3 electrolyte confirms that the dissolution rate is increased as decreasing pH. It is interesting to note that the two peaks are observed from 0.1M pH 4.5 and 0.01M pH 3 electrolyte whereas single peak is observed from 0.1M pH 3 electrolyte. The obtained current density is similar to the reported value [5]. Fig 8.17 shows the negative response in depletion region and the reason is not clear at present.

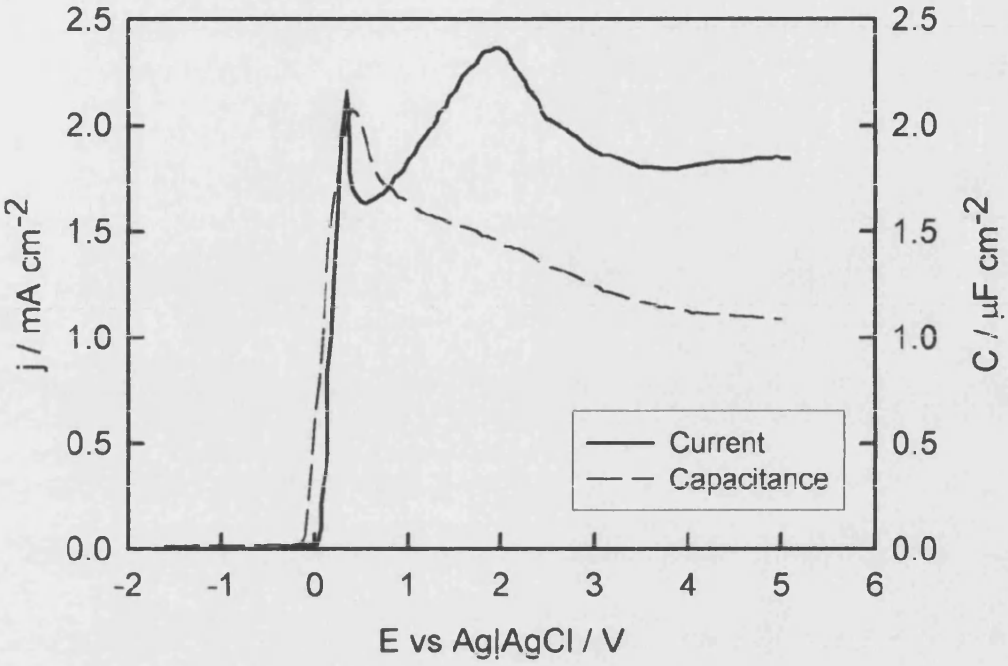

Figure 8.16: Current density and capacitance of p-Si in 0.1M NH_4F (pH 3).

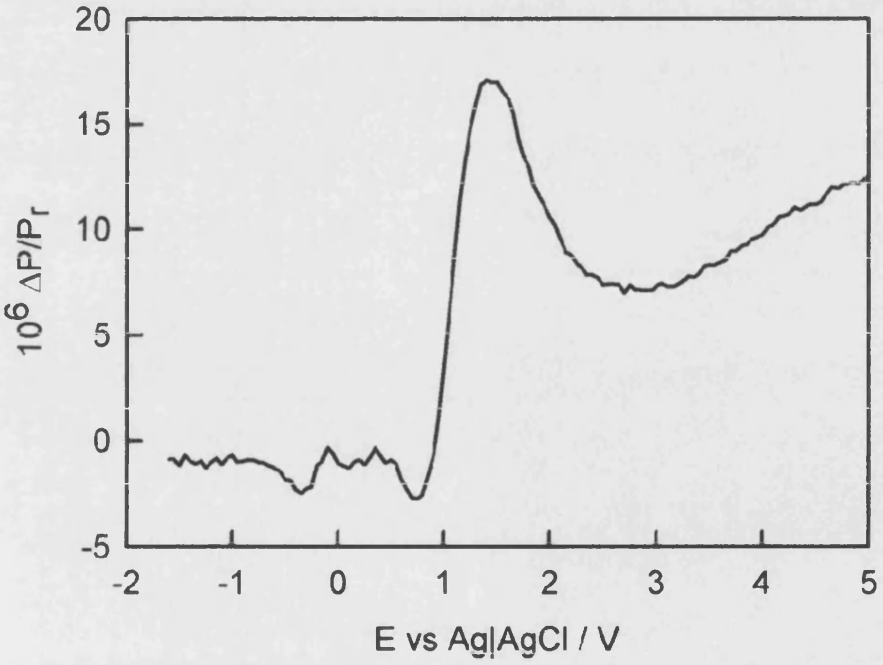

Figure 8.17: PMMR response of p-Si in 0.1M fluoride (pH 3) at 1kHz with 40 mV rms.

8.3 Frequency resolved EIS and PMMR results

The impedance of p-Si|NH_4F system under electropolishing conditions has been studied by a number of authors [5, 8, 14, 15]. In general, the impedance response in the electropolishing region exhibits two semicircles and the high frequency response is interpreted in terms of the capacitance of the oxide layer in parallel with a charge transfer resistance as illustrated in Fig 8.18. The low frequency response is characterised by a pseudocapacitance that has been attributed to slow relaxation of the oxide thickness associated with the balance between film growth and dissolution.

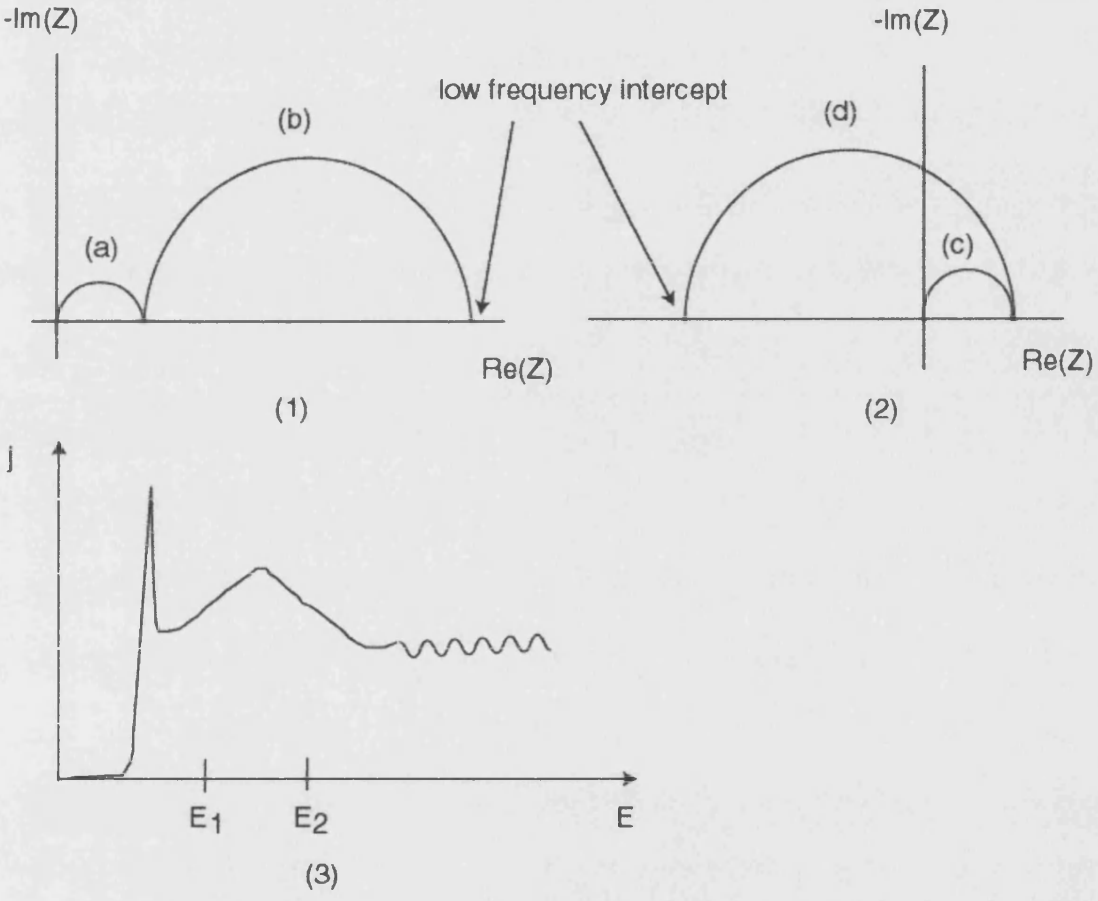

Figure 8.18: Impedance in the electropolishing region (1) dE/dj is positive, corresponding to E_1 on current-voltage curve (2) dE/dj is negative, corresponding to E_2. Note that (a) and (c) are high frequency semicircle and (b) and (d) are low frequency semicircle.

Both Fig 8.18 (1) and (2) are in the electropolsihing region. The difference can

be explained, defining a Faradaic resistance. A Faradaic resistance is defined using Ohms law, V = IR, Faradaic resistance is obtained by the inverse of the slope of the current voltage plot

$$R_F = \frac{dE}{dj} \tag{8.27}$$

Therefore Fig 8.18 (1) corresponds to the potential at E_1 and Fig 8.18 (2) corresponds to the potential at E_2 on the current-voltage curve in Fig 8.18 (3).

Impedance for p-Si in 0.1M fluoride (pH 4.5) at 1V is shown in Fig 8.19. It is noted that an inductive loop is observed at low frequency. This low frequency loop is related to the existence of reactions involving adsorbed intermediate. This could explain that the existence of the second current maximum as a transition from a hydrated form of oxide to a dry one.

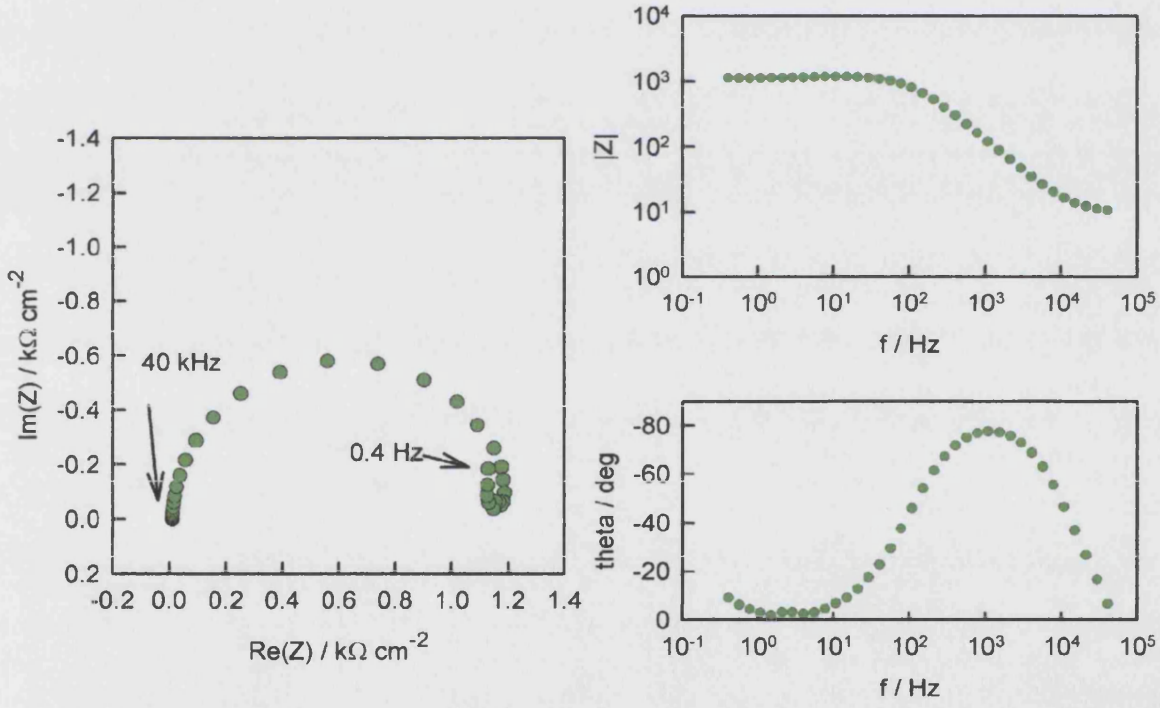

Figure 8.19: Impedance plot in 0.1M fluoride (pH 4.5) at 1 V with 40 mv rms of modulation amplitude.

In order to fit both impedance and microwave response, it is necessary to model the electropolishing region. Chazalviel and co workers [3, 4] reported that a thin inner layer of SiO_2 and a much thicker outer layer of porous hydrated oxide exist. Dissolution of this layer in fluoride solutions gives rise to an anodic current peak attributed to electron injection [6]. The inner oxide layer is an electronic insulator and acts as a dielectric. The structure of the interface under electropolishing conditions generally consists of the 5 regions as shown in Fig 8.20.

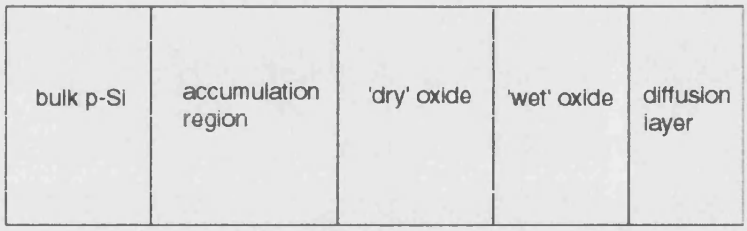

Figure 8.20: Structure of the silicon|electrolyte interface under electropolishing conditions.

Assuming that the outer hydrated layer is sufficiently porous and that it does not influence the impedance response, Fig 8.20 can be rewritten in terms of capacitors. Here C_{acc} is accumulation capacitance, C_{SiO_2} is (dry) oxide capacitance, and C_H is Helmholtz capacitance.

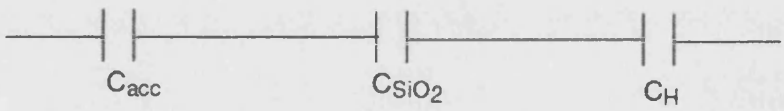

Figure 8.21: Total capacitance in the electropolishing region.

Fig 8.22 illustrates the equivalent circuit used for the initial study of the anodic dissolution in the electropolishing region. Here R_c is contact resistance, C_{ss} is surface state capacitance, R_{ss} is surface state resistance, and R is charge transfer resistance. It is noted that Fig 8.22 (2) takes into account the surface state whereas Fig 8.22 (1) does not.

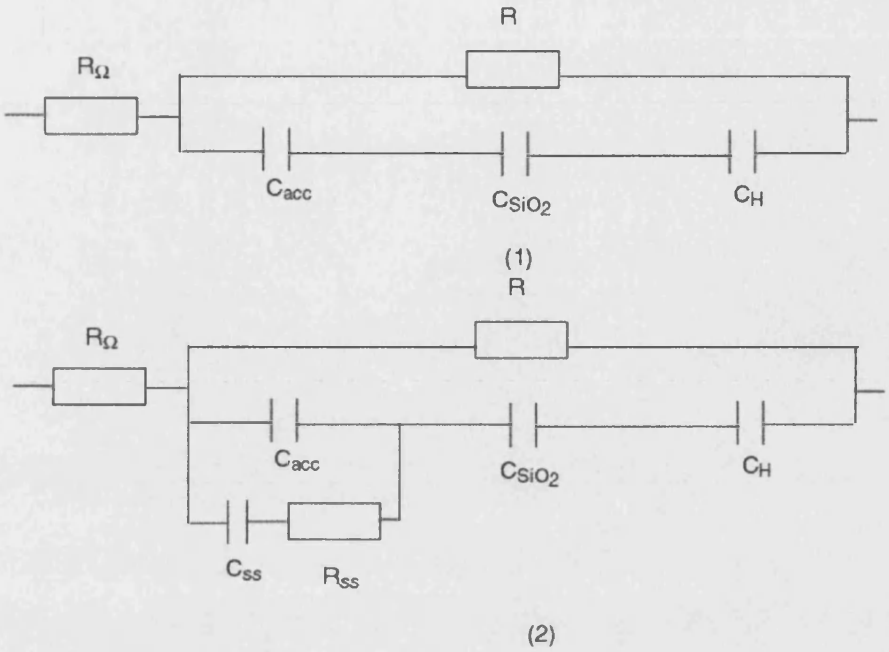

Figure 8.22: Equivalent circuit for initial study of anodic dissolution of p-Si (1) without surface state (2) with surface state.

It is seen that the equivalent circuit in Fig 8.22 uses single resistance for charge transfer. However, charge transfer process at each layer is different process i.e. the charge transfer at Si is electronic, ionic at SiO_2 and another ionic transfer at electrolyte, hence, the charge transfer resistance should be different, as shown in Fig 8.23

electrolyte & wet SiO_2	dry SiO_2	p-Si
ionic transfer 1	ionic transfer 2	charge transfer

Figure 8.23: Charge transfer at Si| SiO_2 |electrolyte.

Therefore we separated the resistances for each component, and used the following equivalent circuit for the simple case, i.e. the surface state is neglected

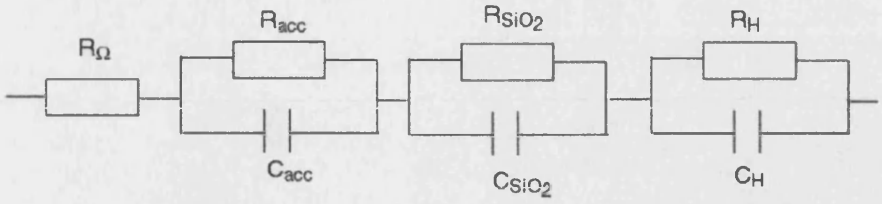

Figure 8.24: Equivalent circuit for anodic dissolution of p-Si

We neglected the surface state but Kirah [17] takes into account the surface state as shown in Fig 8.25.

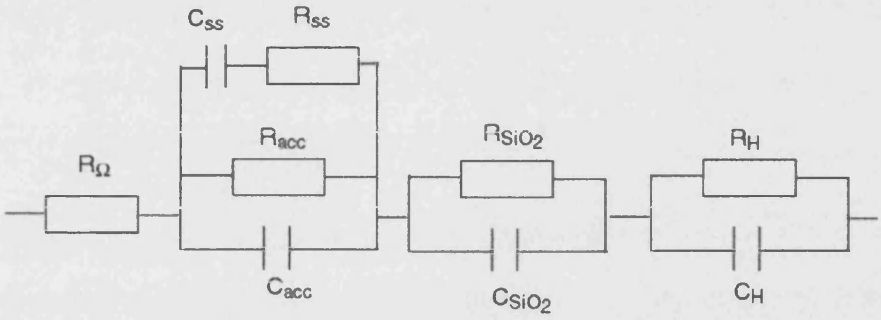

Figure 8.25: Equivalent circuit for anodic dissolution of p-Si

The problem is that it is unable to fit the impedance and microwave simultaneously. Therefore, we used the general equivalent circuit to obtain accumulation impedance as shown in Fig 8.26. Here Z_1 is the unknown impedance in parallel with accumulation capacitance, C_{acc}, and Z_2 is unknown impedance in series. The details are discussed later.

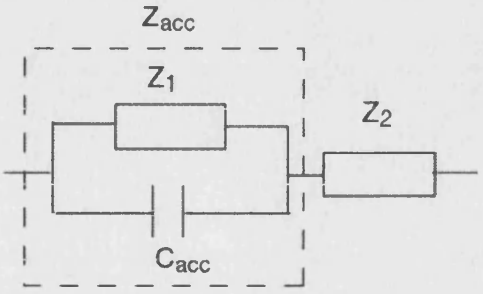

Figure 8.26: Generalised equivalent circuit.

Fig 8.27 illustrates the impedance response at 2 V in 0.1M NH_4F (pH 4.5). It is seen that the second semicircle starts at low frequency. We were not able to apply further low frequency due to the practical limitations. For this measurement, the microwave is simultaneously recorded. Since the microwave response is small and requires the signal to be amplified using a preamplifier. If the frequency below 0.4 Hz is applied, the signal is filtered off.

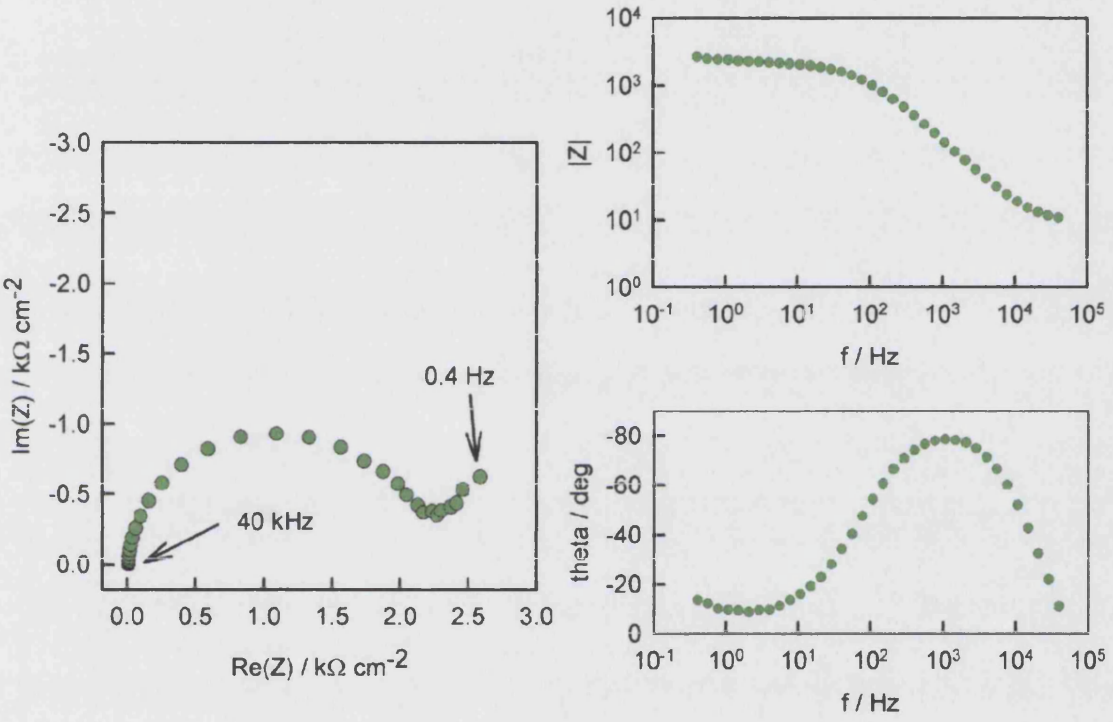

Figure 8.27: Impedance plot in 0.1M fluoride (pH 4.5) at 2 V with 40 mv rms of modulation amplitude.

Impedance at several potentials are summarised in Fig 8.28. It is seen that the semicircle becomes larger with increasing the potential.

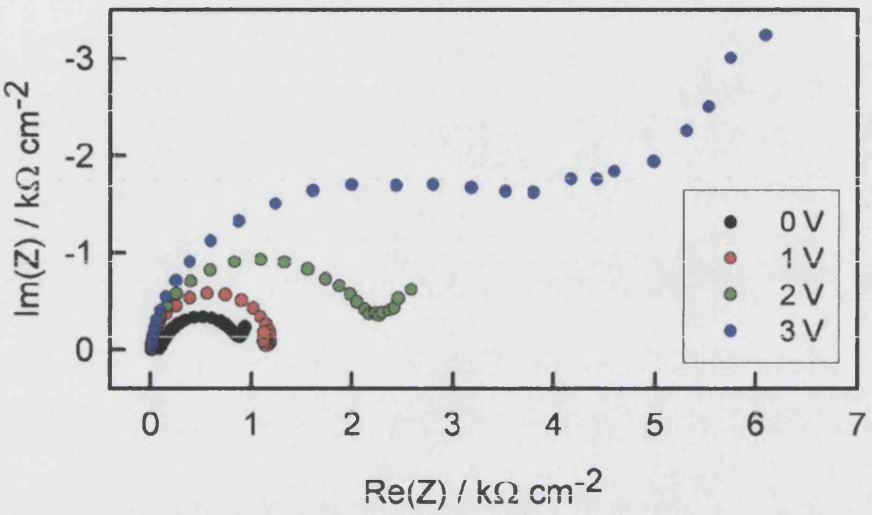

Figure 8.28: Impedance of p-Si in 0.1M fluoride (pH 4.5) with 40 mv rms of modulation amplitude.

We also studied impedance and frequency resolved PMMR for anodic dissolution of p-Si in 0.1M fluoride (pH 3) in electropolishing region. Impedance in 0.1M fluoride (pH 3) at 1 V and 2 V are shown in Fig 8.29 and Fig 8.30, respectively. The impedance response in 0.1M fluoride (pH 3) is similar to that in 0.1M fluoride pH (4.5). At 1V, the capacitive loop is again observed at low frequency. At 2 V, the capacitive loop is not observed and the low frequency semicircle seems to start.

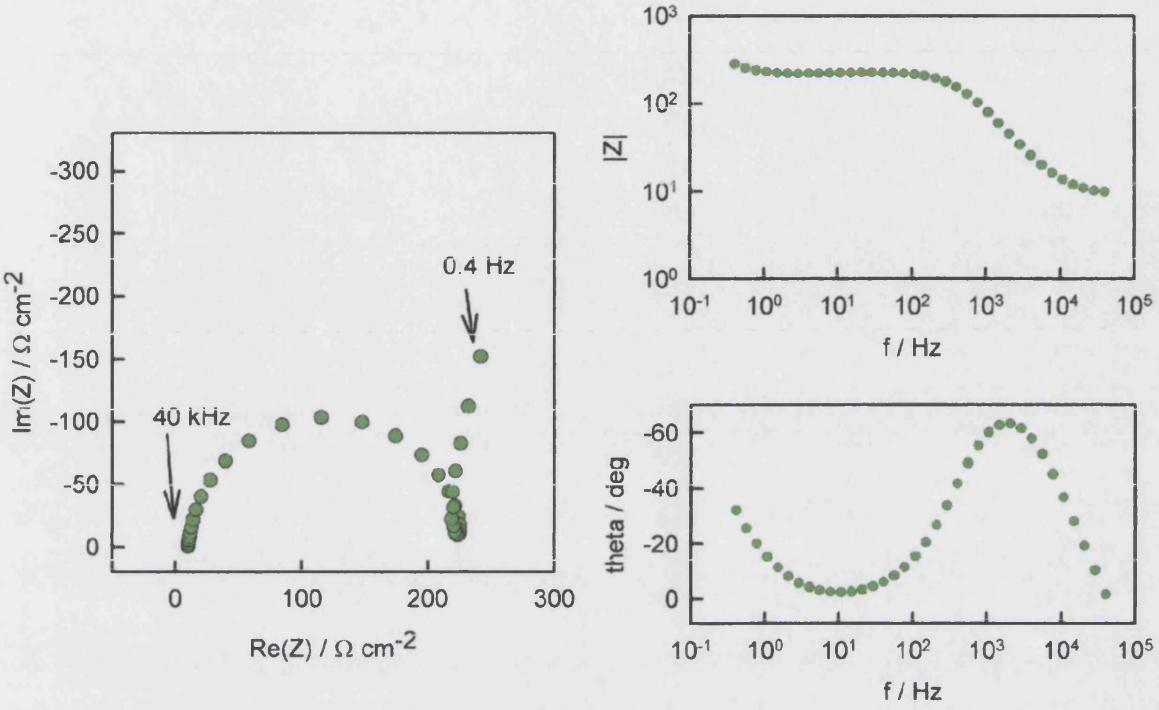

Figure 8.29: Impedance in 0.1M fluoride (pH 3) at 1 V with 40 mV rms.

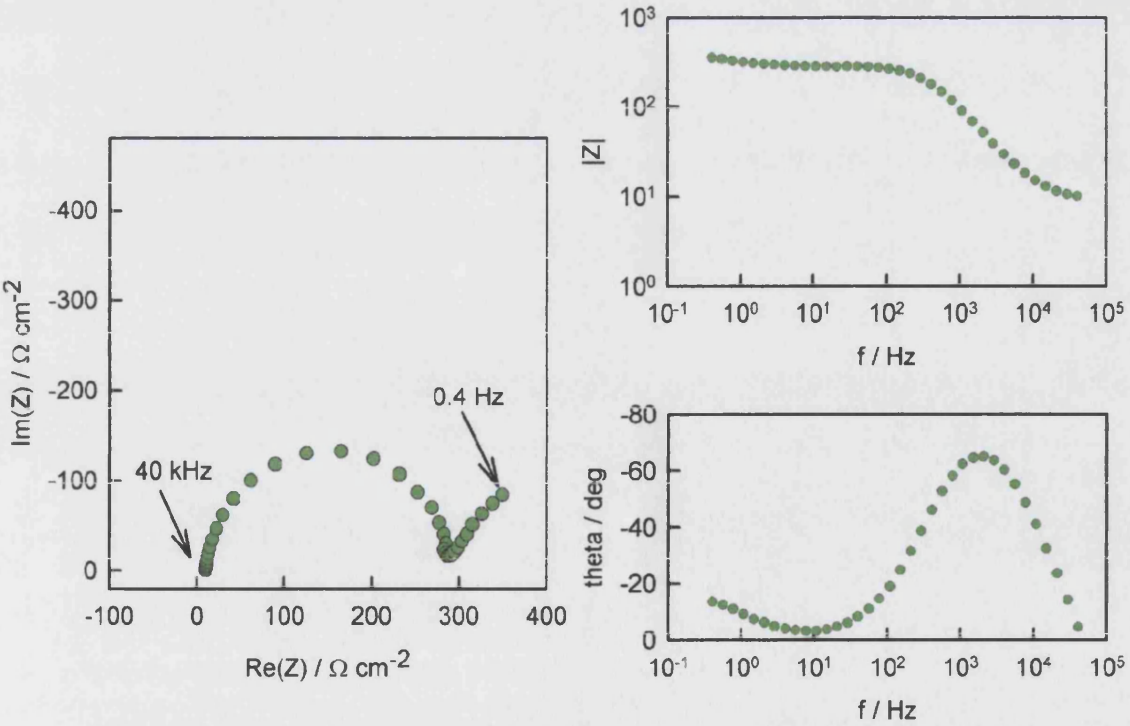

Figure 8.30: Impedance in 0.1M fluoride (pH 3) at 2 V with 40 mV rms.

Impedance for p-Si in 0.1M fluoride (pH 3) at several potentials are summarised in Fig 8.31. As the potential increases, the semicircle becomes larger.

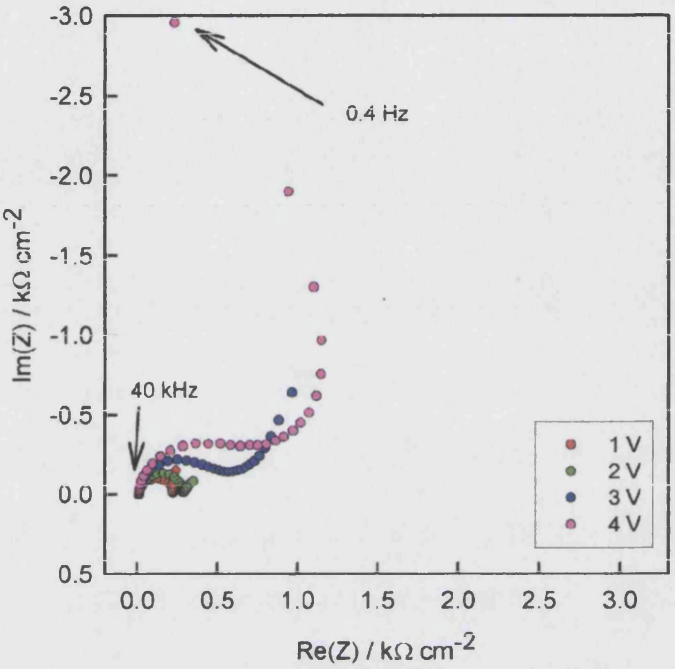

Figure 8.31: Impedance in 0.1 M fluoride (pH 3) at several potentials.

The corresponding PMMR response is shown from Fig 8.32 to Fig 8.35 for 0.1M fluoride (pH 4.5) and from Fig 8.36 to Fig 8.39 for 0.1M fluoride (pH 3). The high frequency semicircle in the lower complex plane corresponds to attenuation of the microwave signal due to the series combination of the ohmic resistance and the total capacitance. At low frequencies the PMMR response crosses into the upper complex plane and is attenuated as the frequency falls.

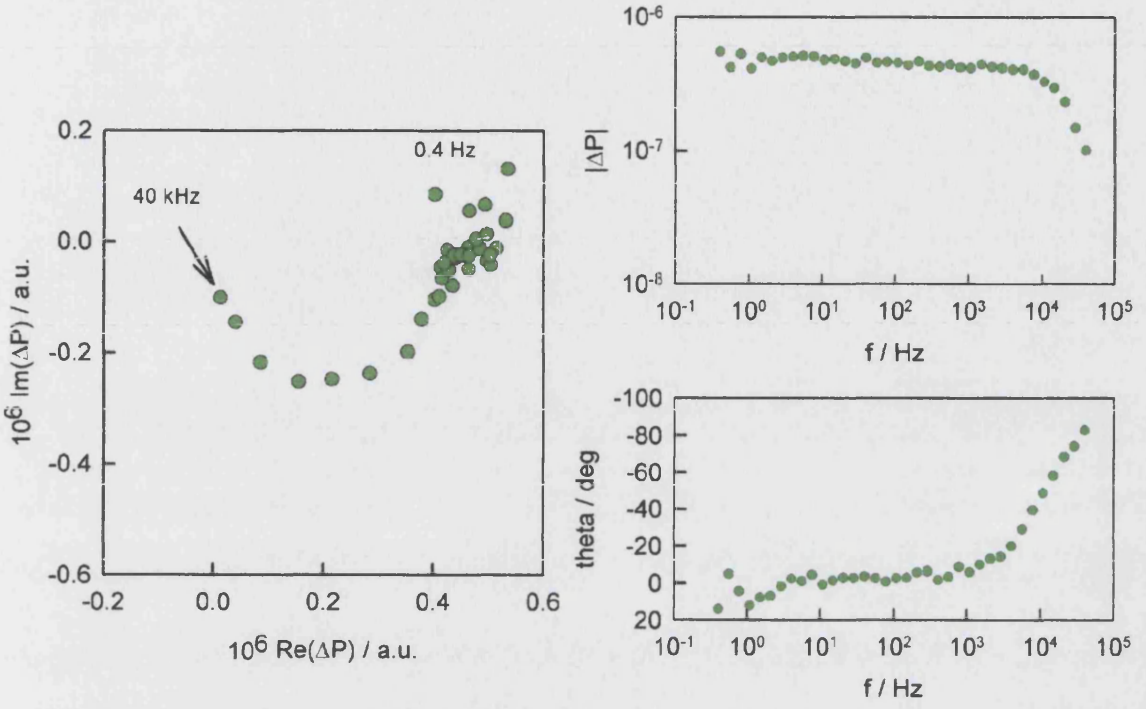

Figure 8.32: Microwave response in 0.1M fluoride (pH 4.5) at 1 V with 40 mV rms.

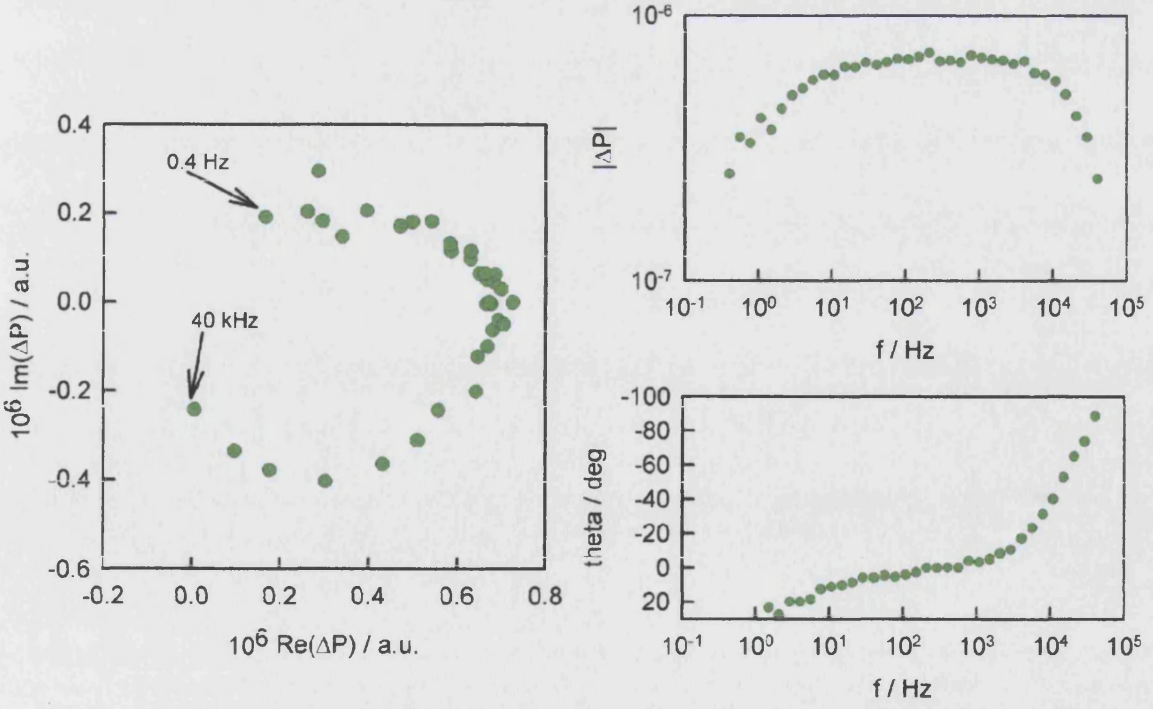

Figure 8.33: Microwave response in 0.1M fluoride (pH 4.5) at 2 V with 40 mV rms.

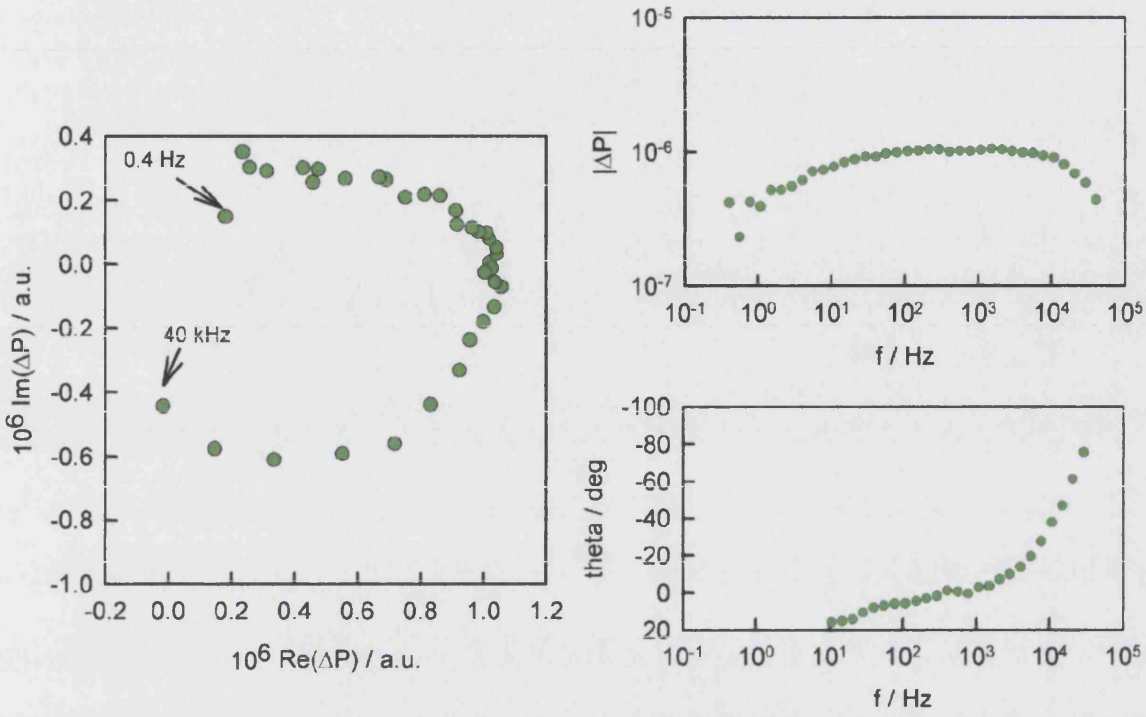

Figure 8.34: Microwave response in 0.1M fluoride (pH 4.5) at 3 V with 40 mV rms.

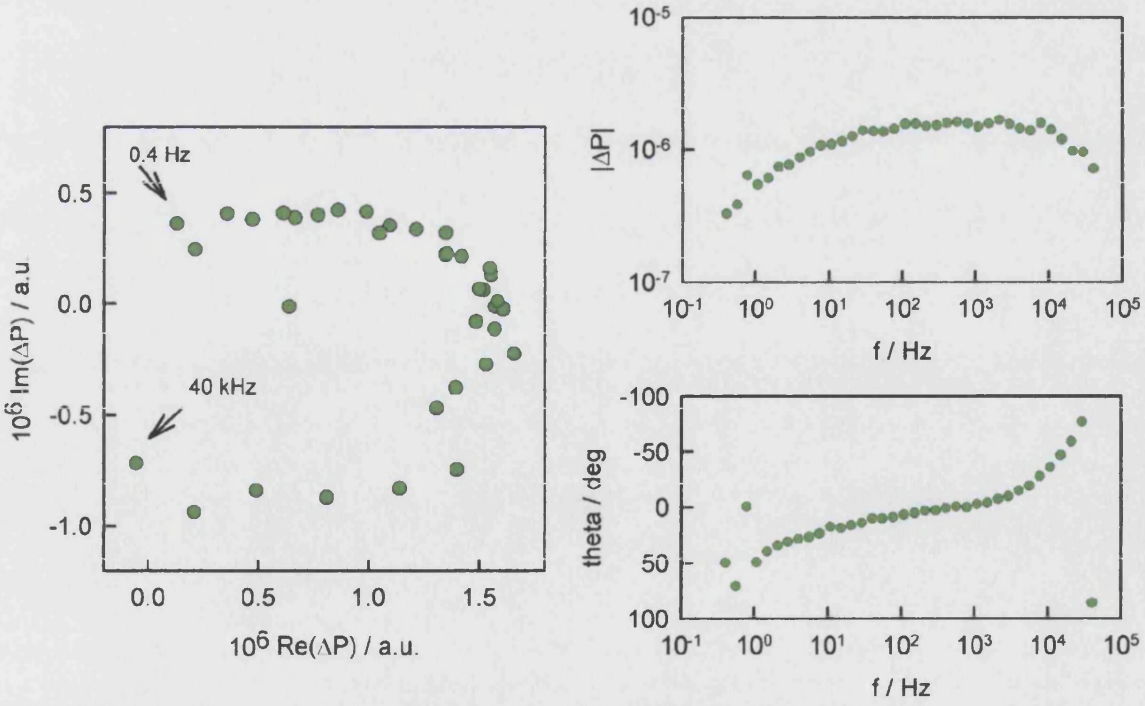

Figure 8.35: Microwave response in 0.1M fluoride (pH 4.5) at 4 V with 40 mV rms.

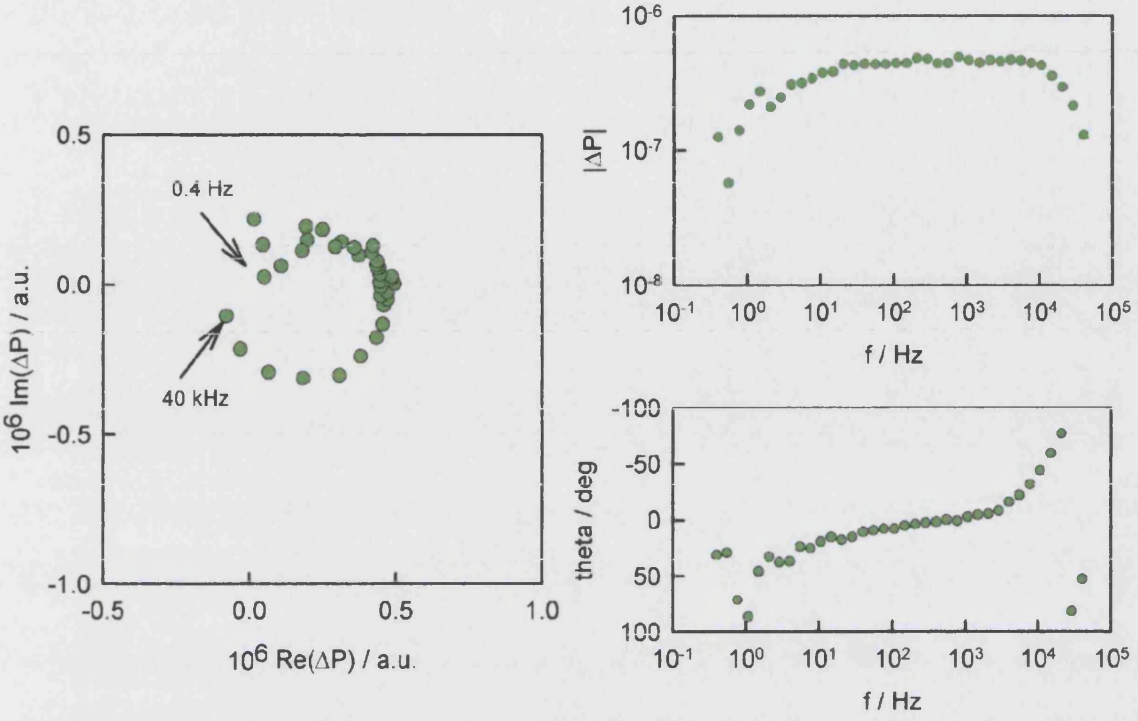

Figure 8.36: Microwave response in 0.1M fluoride (pH 3) at 1 V with 40 mV rms.

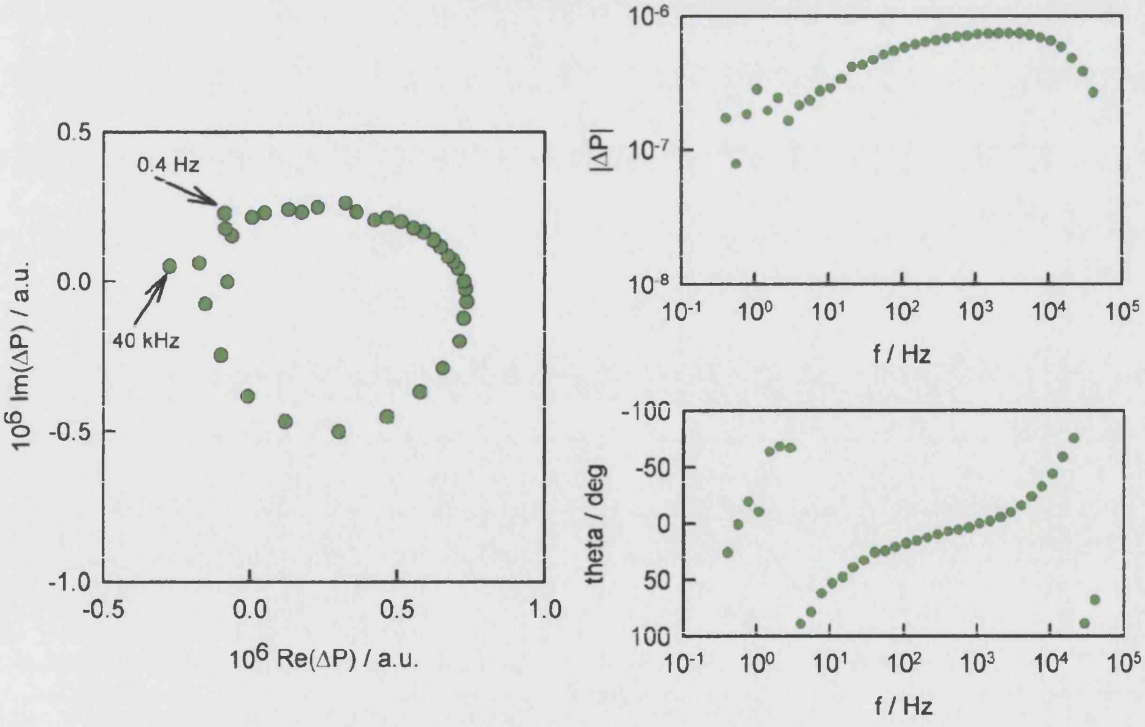

Figure 8.37: Microwave response in 0.1M fluoride (pH 3) at 2 V with 40 mV rms.

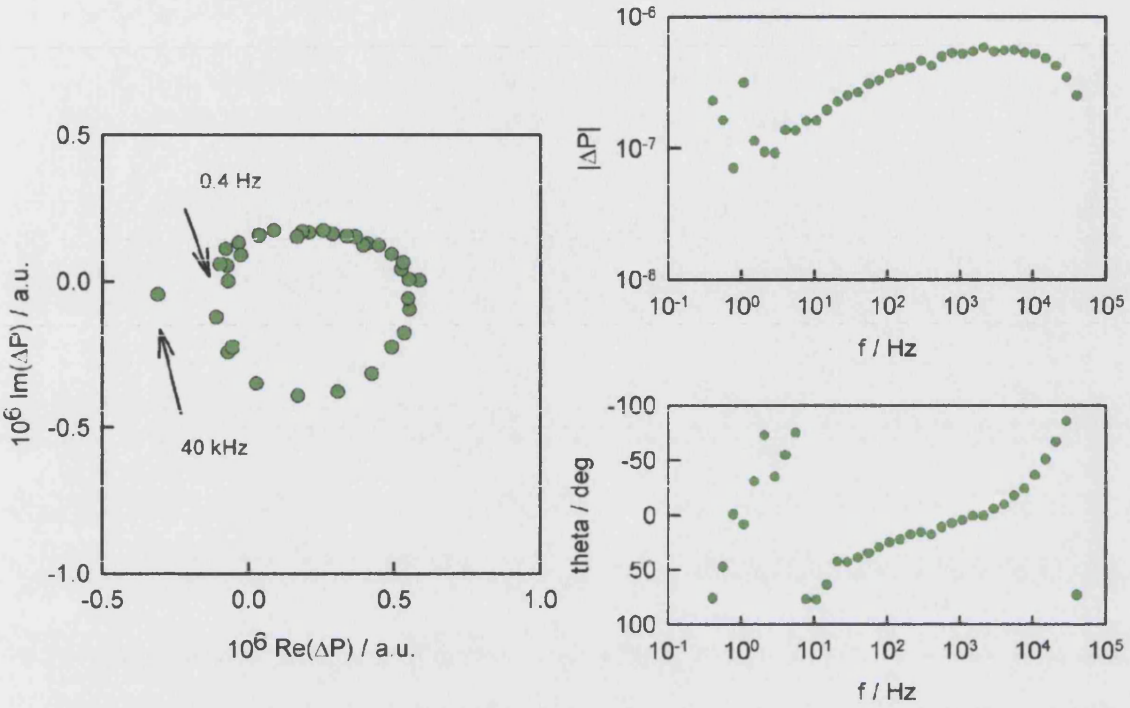

Figure 8.38: Microwave response in 0.1M fluoride (pH 3) at 3 V with 40 mV rms.

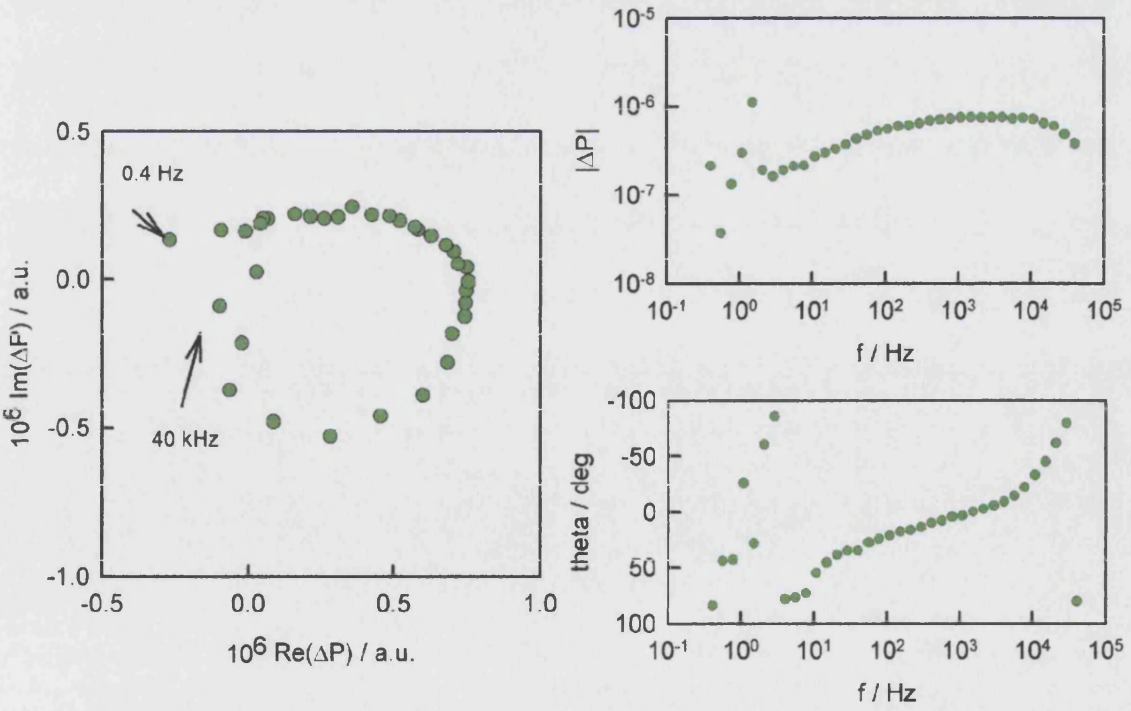

Figure 8.39: Microwave response in 0.1M fluoride (pH 3) at 4 V with 40 mV rms.

The PMMR response is determined by the accumulation capacitance and the fraction of the applied ac modulation that appears across the accumulation layer. If the ohmic series resistance is negligible, the impedance is determined by the capacitances of accumulation, oxide and Helmholtz layers. Under these conditions, the microwave response is given by

$$\begin{aligned} \frac{\Delta P}{P_r} &= \frac{S\Delta\sigma}{R} \\ &= S'C_{acc}\Delta\phi_{acc} \end{aligned} \tag{8.28}$$

where $S' = \frac{S\mu}{Rd}$

Since the fraction of potential across the accumulation layer is equivalent to the fraction of impedance, i.e. $\frac{\phi_{acc}}{\phi_{tot}} = \frac{Z_{acc}}{Z_{tot}}$, eq 8.28 becomes

$$\frac{\Delta P}{P_r} = S'\frac{Z_{acc}}{Z_{tot}}C_{acc}\Delta\phi_{tot} \tag{8.29}$$

As mentioned before, the accumulation impedance can be obtained by multiplying the impedance response by the frequency resolved microwave response. From eq 8.29

$$\begin{aligned} \frac{\Delta P}{P_r} &= S'\frac{Z_{acc}}{Z_{tot}}C_{acc}\Delta\phi_{tot} \\ \frac{\Delta P}{P_r}Z_{tot} &= S'Z_{acc}C_{acc}\Delta\phi_{tot} \\ \Delta P Z_{tot} &= KZ_{acc} \end{aligned} \tag{8.30}$$

where $K = S'RC_{acc}d\phi_{tot}$ and is treated as 1 for the rest of the calculation.

ΔP and Z_{tot} contain the real and imaginary component. Hence

$$\begin{aligned} \Delta P \times Z_{tot} &= (Re(\Delta P) + jIm(\Delta P))(Re(Z) + jIm(Z)) \\ &= Re(\Delta P)Re(Z) - Im(\Delta P)Im(Z) + j(Re(\Delta P)Im(Z) + Im(\Delta P)Re(Z)) \end{aligned}$$

Reminding that accumulation impedance consists of accumulation capacitance and unknown impedance as described in Fig 8.26, the accumulation impedance is given by

$$\begin{aligned} \frac{1}{Z_{acc}} &= \frac{1}{Z_1} + jC_{acc}\omega \\ &= \frac{1 + jC_{acc}\omega Z_1}{Z_1} \end{aligned} \tag{8.31}$$

Taking inverse of both sides on eq 8.31, the accumulation impedance can be expressed as

$$Z_{acc} = \frac{Z_1}{1 + jC_{acc}\omega Z_1} \tag{8.32}$$

Rearranging eq 8.32, and solving for Z_1

$$\begin{aligned} Z_{acc}(1 + jC_{acc}\omega Z_1) &= Z_1 \\ Z_1(1 - j\omega C_{acc}Z_{acc}) &= Z_{acc} \\ Z_1 &= \frac{Z_{acc}}{1 - j\omega C_{acc}Z_{acc}} \end{aligned} \tag{8.33}$$

Since Z_{acc} contains real and imaginary components and eq 8.33 can be rewritten as

$$\begin{aligned} Z_1 &= \frac{Re(Z_{acc}) + jIm(Z_{acc})}{1 - j\omega C_{acc}(Re(Z_{acc}) + jIm(Z_{acc}))} \\ &= \frac{Re(Z_{acc}) + jIm(Z_{acc})}{1 + \omega C_{acc}Im(Z_{acc}) - j\omega C_{acc}Re(Z_{acc})} \end{aligned} \tag{8.34}$$

Multiplying the complex conjugate, eq 8.34 becomes

$$\begin{aligned} Z_1 &= \frac{[Re(Z_{acc}) + jIm(Z_{acc})][1 + \omega C_{acc}Im(Z_{acc}) + j\omega C_{acc}Re(Z_{acc})]}{[1 + \omega C_{acc}Im(Z_{acc}) - j\omega C_{acc}Re(Z_{acc})][1 + \omega C_{acc}Im(Z_{acc}) + j\omega C_{acc}Re(Z_{acc})]} \\ &= \frac{Re(Z_{acc}) + j(Im(Z_{acc}) + \omega C_{acc}Im(Z_{acc})^2 + \omega C_{acc}Re(Z_{acc})^2)}{(1 + \omega C_{acc}Im(Z_{acc}))^2 + (\omega C_{acc}Re(Z_{acc}))^2} \end{aligned} \tag{8.35}$$

If the accumulation impedance is known, Z_1 can be worked out. In addition, if the accumulation impedance is known, Z_2 can be also worked out.

$$Z_2 = Z_{tot} - Z_{acc} \tag{8.36}$$

The accumulation impedance for p-Si in 0.1M fluoride (pH 4.5) at 1, 2, 3 and 4 V are shown in Fig 8.40 to Fig 8.43. Except at low frequencies the accumulation impedance can be fitted well by a single time constant, τ_{acc}.

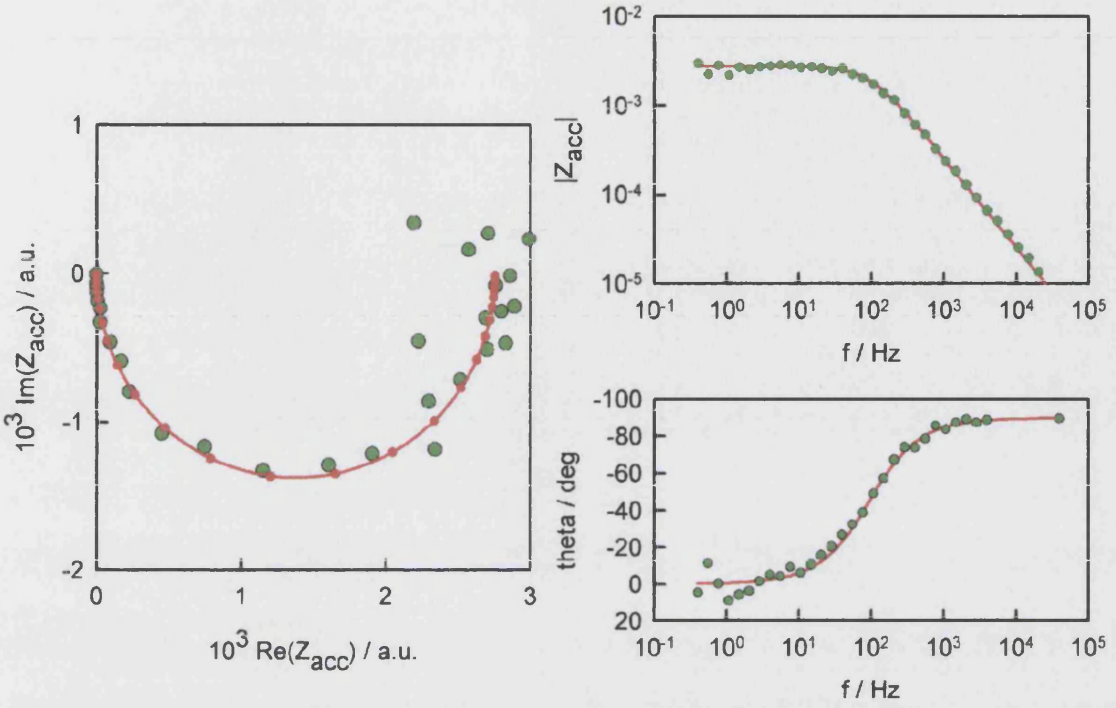

Figure 8.40: Deconvoluted accumulation impedance at 1V in 0.1M pH 4.5.

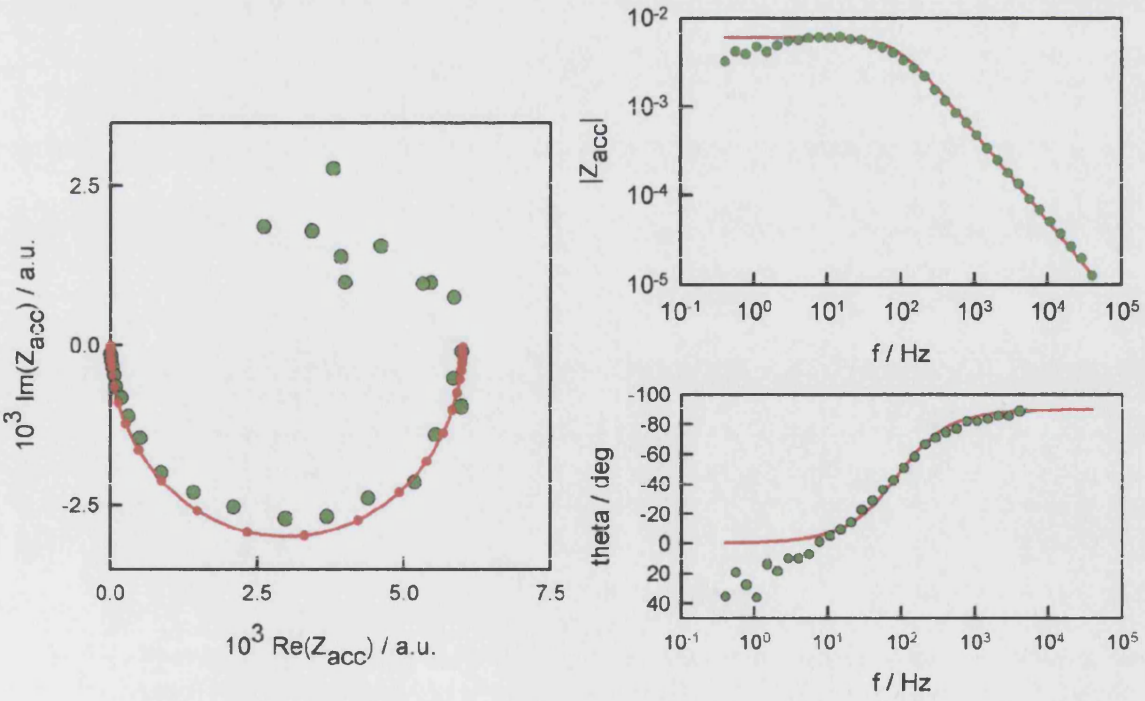

Figure 8.41: Deconvoluted accumulation impedance at 2V in pH 4.5.

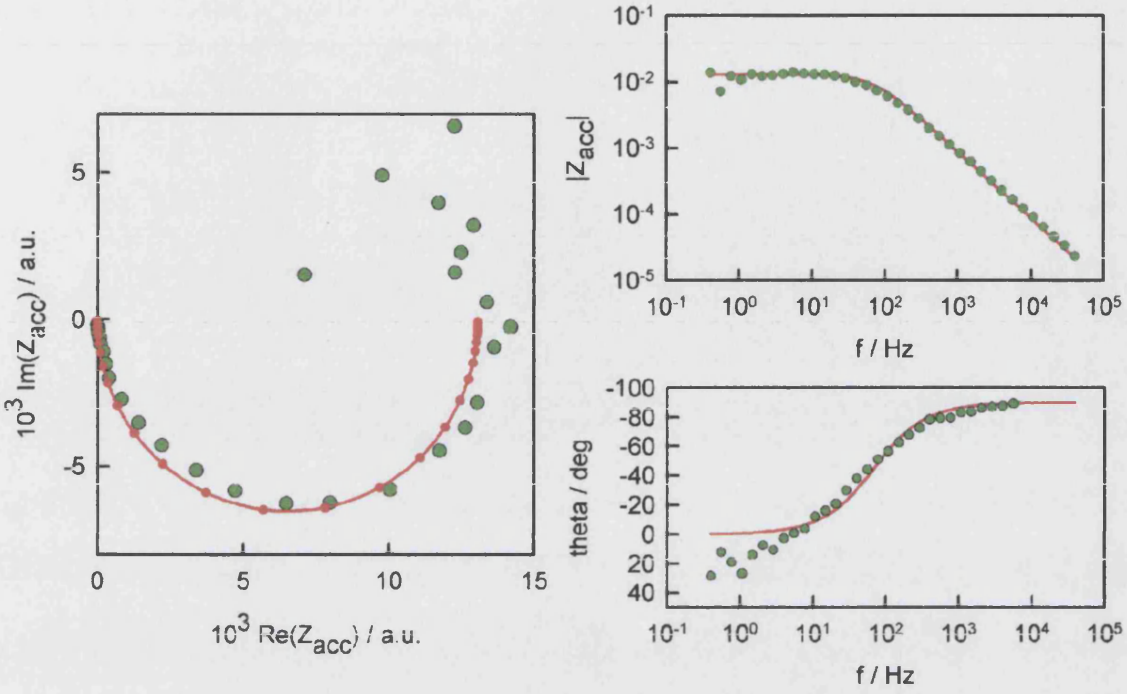

Figure 8.42: Deconvoluted accumulation impedance at 3V in pH 4.5.

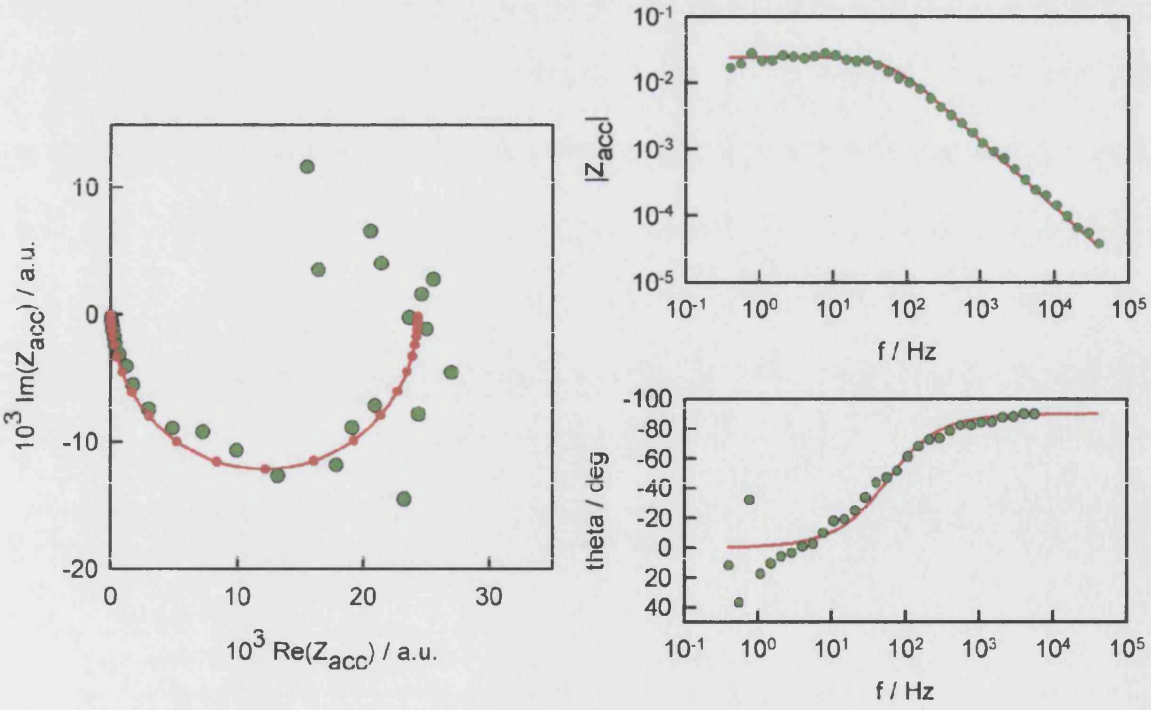

Figure 8.43: Deconvoluted accumulation impedance at 4V in pH 4.5.

Each time constant is summarised in Table 8.2.

E / V	τ_{tot} / ms	τ_{acc} / ms
1	1.49	1.68
2	2.11	1.86
3	3.25	2.35
4	4.09	2.84

Table 8.2: Comparison of τ_{tot} and τ_{acc}.

τ_{acc} at 1 V and 2 V are 1.68 ms and 1.86 ms, respectively. These are very close to the time constant for the total impedance, which are 1.49 ms and 2.11 ms. The error becomes significant with increasing the potential. The deviation of Z_{acc} at low frequencies arise from the pseudocapacitive behavior of the system that is associated with relaxation of the overall oxide thickness.

The accumulation impedance for 0.1M fluoride (pH 3) are shown from Fig 8.44 to Fig 8.47. The general shape of accumulation impedance for pH 3 solution is similar to that for pH 4.5 solution, but the fitting for pH 3 solution shows the large error at low frequency, compared with pH 4.5 solutions. The reason is not clear at the present. Each time constant is summarised in Table 8.3. Z_{acc} shows the signal semicircle but the time constant for Z_{acc} is quite different from that of Z_{tot}. Large error is observed for this system and requires the further study.

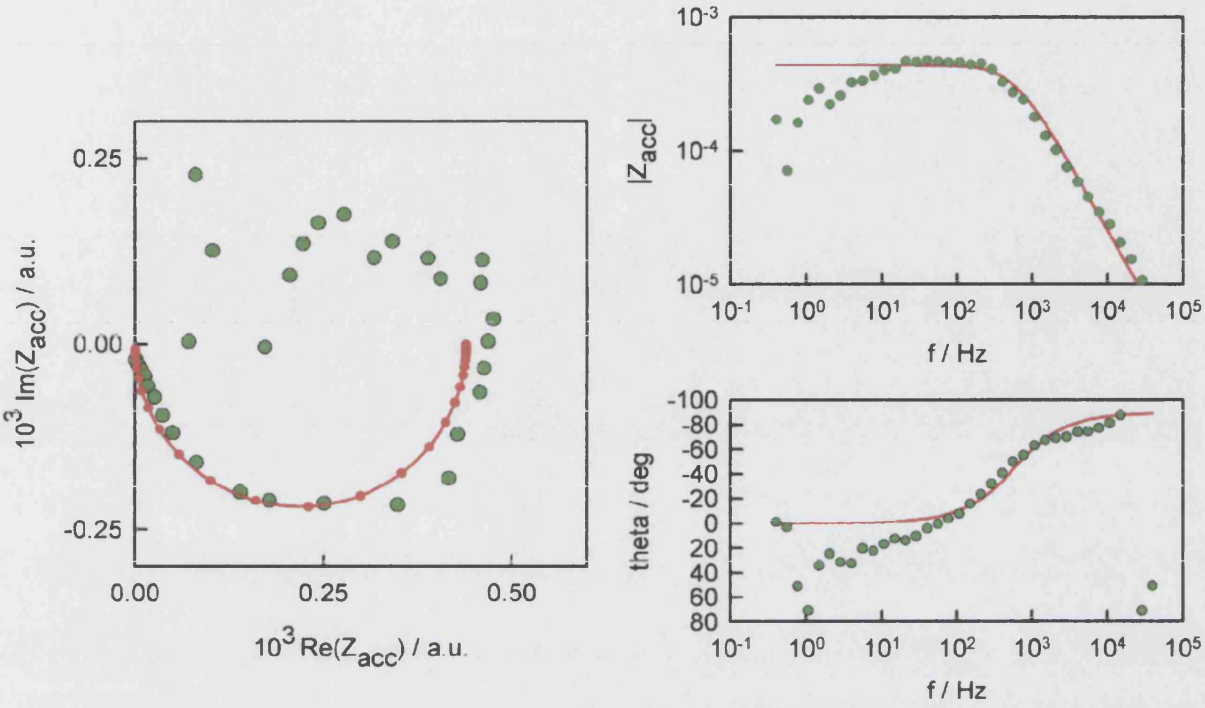

Figure 8.44: Deconvoluted accumulation impedance at 1V in 0.1 pH 3.

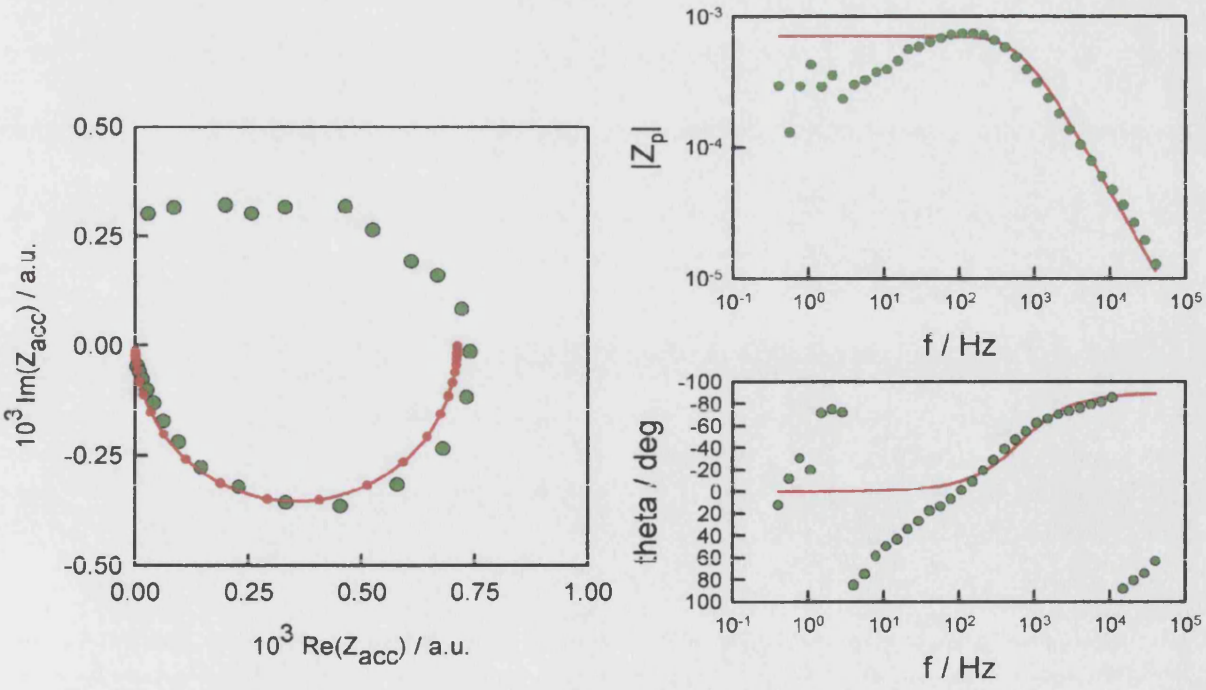

Figure 8.45: Deconvoluted accumulation impedance at 2V in 0.1M pH 3.

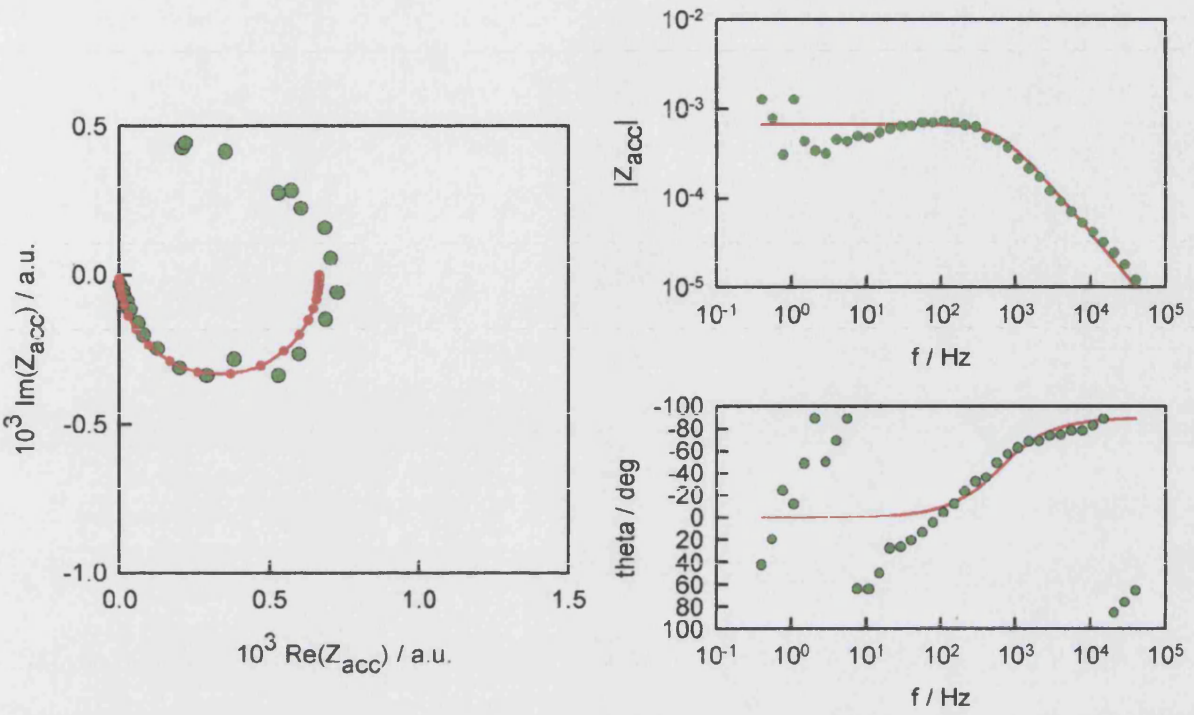

Figure 8.46: Deconvoluted accumulation impedance at 3V in 0.1M pH 3.

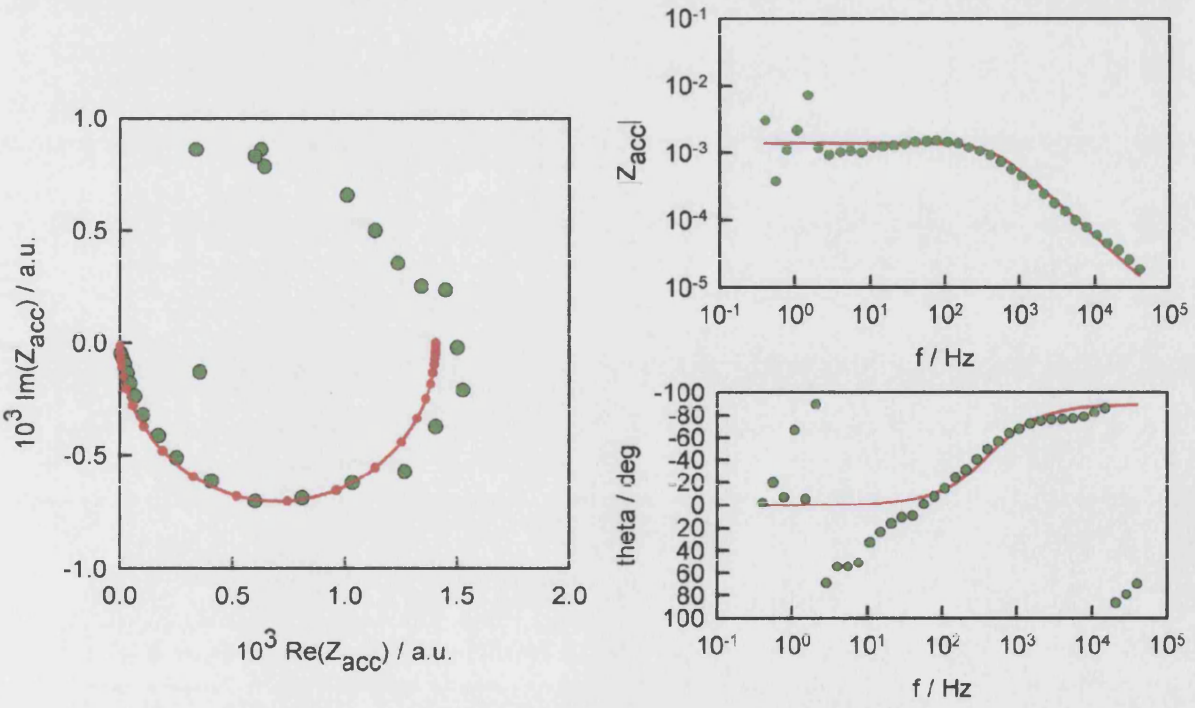

Figure 8.47: Deconvoluted accumulation impedance at 4V in 0.1M pH 3.

E / V	τ_{tot} / ms	τ_{acc} / ms
1	0.39	0.27
2	0.44	0.25
3	0.58	0.26
4	0.73	0.38

Table 8.3: Comparison of τ_{tot} and τ_{acc}.

8.4 Conclusion

This study has shown that analysis of the frequency dependence of the PMMR response of the semiconductor|electrolyte junction offers new insights into the potential distribution. Convolution of the impedance and PMMR responses give information about the accumulation impedance even under conditions where it is invisible in the total impedance response. The experiments outlined in this chapter show that the frequency resolved PMMR measurement is powerful tool to understand semiconductor|electrolyte interface.

References

[1] Mahajan, S.; Sree Harsha, K. S. Principles of growth and processing of semiconductors McGrawHill, 1999.

[2] Searson, P. C. in Advances in Electrochemical Science and Engineering Vol 4, VCH, New York, 1995.

[3] daFonseca, C.; Ozanam, F.; Chazalviel, J. N. Surface Science **1996**, 365, 1-14.

[4] Ozanam, F.; daFonseca, F.; Rao, A. V.; Chazalviel, J. N. Applied Spectroscopy **1997**, 51, 519-525.

[5] Bailes, M.; Böhm, S.; Peter, L. M.; Riley, D. J.; Greef, R. Electrochimica acta, **1998**, 43, 1757-1772.

[6] Cattarin, S.; Peter, L. M.; Riley; D. J. Journal of Physical Chemistry B 101 **1997**, 4071-4076.

[7] Sze, S. M. Physics of semiconductor devices, 2nd edition, John Wiley, New York, 1981.

[8] Ozanam, F; Chazalviel, J.N.; Radi, A.; Etman, M. Journal of the Electrochemical Society, **1992**, 139, 2491-2501.

[9] Nicollian, E. H.; Brews, J. R. MOS (Metal Oxide Semiconductor) Physics and Technology, John Wiley, New York, 1982.

[10] Mudanai, S.; Chindalore, G. L.; Shih, W. K.; Wang, H.; Ouyang, Q.; Tasch, A. F.; Maziar, C. M.; Banerjee, S. K. Ieee Transactions on Electron Devices **1999**, 46, 1749-1759.

[11] McKeon, J. B.; Chindalore, G.; Hareland, S. A.; Shih, W. K.; Wang, C.; Tasch, A. F.; Maziar, C. M. Ieee Electron Device Letters **1997**, 18, 200-202.

[12] Manzani, S.; Modelli, A. Journal of Applied Physics **1989**, 65, 2361-2370.

[13] Vanmaekelbergh, D.; Searson, P. C. Journal of the Electrochemical Society **1994**, 141, 697-702.

[14] Searson, P. C.; Zhang, X. G. Journal of the Electrochemical Society **1990**, 137, 2539-2546.

[15] Searson, P. C.; Zhang, X. G. Electrochimica Acta **1991**, 36, 499-503.

[16] Madou, M. J.; Gomes, W. P.; Fransen, F.; Cardon, F. Journal of the Electrochemical Society **1982**, 129, 2749-2752.

[17] K.A.W. Kirah , PhD thesis, in Engineering Physics and Mathematics Department, AIN Shams University, Cairo, 2000.

[18] McKeon, J. B.; Chindalore, G.; Hareland, S. A.; Shih, W. K.; Wang, C.; Tasch, A. F.; Maziar, C. M. Ieee Electron Device Letters **1997**, 18, 200-202.

[19] Chazalviel; J. -N. Electrochimica Acta **1992**, 37, 865-875.

[20] Pierret, R. F. Semiconductor fundamentals, 2nd edition, Addison-Wesley publishing, Reading, 1989.

Chapter 9

Further work

The present work has demonstrated the range of possibilities for the application of microwave reflectance techniques in semiconductor electrochemistry. The fundamental aspects of the methods are now well understood, and the studies of silicon photoelectrodes have provided a useful test of theory. The range of experimental systems studied was restricted than planned originally, and work included in the original plan, but not completed included the following topics;

- Photodissolution of n-Si in NH_4F (electron injection/ current multiplication)
- Electron transfer at H-terminated Si in dry aprotic solvent using simple one electron redox couples
- Effects of surface modification on electron transfer at silicon photoelectrodes (Pt nanodots, and derivation of alkyl groups)
- Pulse laser excitation (time resolved microwave reflectance on μs time scale)
- Extension of microwave methods to other semiconductor (ZnO, GaAs, GaP, CdS)
- Studies of nanocrystalline materials such as TiO_2
- Studies of porous systems (Si, GaP)
- Studies of conducting polymers such as poly(aniline)

Now that we have a basic understanding based on careful study of model system, microwave methods can be applied to study all of the systems listed above.

Appendix A

A.1 Proportionality constant

A.1.1 Proportionality constant for electron emission

The rate of electron capture is given by

$$R_a = \nu_{th}\sigma_n n N_t (1 - f(E)) \tag{A.1}$$

The rate of emission of electrons is given by

$$R_b = e_n N_t f(E) \tag{A.2}$$

At thermal equilibrium, the rate of capture and emission of electrons are equal

$$\begin{aligned} R_a &= R_b \\ \nu_{th}\sigma_n n N_t (1 - f(E)) &= e_n N_t f(E) \\ e_n &= \frac{\nu_{th}\sigma_n n (1 - f(E))}{f(E)} \end{aligned} \tag{A.3}$$

Since f(E) is the Fermi-Dirac distribution, 1-f(E) is

$$\begin{aligned} 1 - f(E) &= 1 - \frac{1}{1 + \exp\left(\frac{E_t - E_F}{k_B T}\right)} \\ &= \frac{\exp\left(\frac{E_t - E_F}{k_B T}\right)}{1 + \exp\left(\frac{E_t - E_F}{k_B T}\right)} \end{aligned} \tag{A.4}$$

Hence $\frac{1-f(E)}{f(E)}$ becomes

$$\begin{aligned} \frac{1 - f(E)}{f(E)} &= \frac{\exp\left(\frac{E_t - E_F}{k_B T}\right)}{1 + \exp\left(\frac{E_t - E_F}{k_B T}\right)} \div \frac{1}{1 + \exp\left(\frac{E_t - E_F}{k_B T}\right)} \\ &= \exp\left(\frac{E_t - E_F}{k_B T}\right) \end{aligned} \tag{A.5}$$

The concentration of electrons is given by

$$n = n_i \exp\left(\frac{E_F - E_i}{k_B T}\right) \tag{A.6}$$

Inserting A.5 and A.6 into A.3, the proportionality constant is obtained

$$\begin{aligned} e_n &= \nu_{th}\sigma_n n_i \exp\left(\frac{E_F - E_i}{k_B T}\right) \exp\left(\frac{E_t - E_F}{k_B T}\right) \\ &= \nu_{th}\sigma_n n_i \exp\left(\frac{E_t - E_i}{k_B T}\right) \end{aligned} \tag{A.7}$$

A.1.2 Proportionality constant for hole emission

The rate of hole capture is expressed as

$$R_c = \nu_{th}\sigma_p p N_t f(E) \tag{A.8}$$

The rate of hole emission is given by

$$R_d = e_p N_t\,(1 - f(E)) \tag{A.9}$$

Under thermal equilibrium condition, the rate of hole emission and capture is equal

$$\begin{aligned} R_c &= R_d \\ \nu_{th}\sigma_p p N_t f(E) &= e_p N_t\,(1 - f(E)) \\ e_p &= \frac{\nu_{th}\sigma_p p f(E)}{1 - f(E)} \end{aligned} \tag{A.10}$$

From A.5

$$\frac{f(E)}{1 - f(E)} = \exp\left(-\frac{E_t - E_F}{k_B T}\right) \tag{A.11}$$

The concentration of holes is given by

$$p = n_i \exp\left(\frac{E_i - E_F}{k_B T}\right) \tag{A.12}$$

Inserting A.11 and A.12 into A.10, the proportionality constant is

$$\begin{aligned} e_p &= \nu_{th}\sigma_p n_i \exp\left(\frac{E_i - E_F}{k_B T}\right) \exp\left(-\frac{E_t - E_F}{k_B T}\right) \\ &= \nu_{th}\sigma_p n_i \exp\left(\frac{E_i - E_t}{k_B T}\right) \end{aligned} \tag{A.13}$$

A.2 Propagation constant

Maxwell's equations are given by

$$\nabla \bullet \mathrm{E} = 0 \tag{A.14}$$

$$\nabla \bullet \mathrm{H} = 0 \tag{A.15}$$

$$\nabla \times \mathrm{E} = -\mathrm{j}\omega\mu\mathrm{H} \tag{A.16}$$

$$\nabla \times \mathrm{H} = (\sigma + \mathrm{j}\omega\varepsilon)\,\mathrm{E} \tag{A.17}$$

where E is electric field, H is magnetic field, σ is conductivity, μ is permeability, and ω is angular frequency.

Taking the rotation of eq A.16 gives

$$\begin{aligned} \nabla \times \nabla \times \mathrm{E} &= \nabla \times (-\mathrm{j}\omega\mu\mathrm{H}) \\ &= -\mathrm{j}\omega\mu\nabla \times \mathrm{H} \end{aligned} \tag{A.18}$$

Since the vector identity is

$$\nabla \times \nabla \times \mathrm{A} = \nabla(\nabla \bullet \mathrm{A}) - \nabla^2\mathrm{A} \tag{A.19}$$

eq A.18 becomes

$$\nabla(\nabla \bullet \mathrm{E}) - \nabla^2\mathrm{E} = -\mathrm{j}\omega\mu\nabla \times \mathrm{H} \tag{A.20}$$

Inserting eq A.17 into eq A.20 gives

$$\nabla(\nabla \bullet \mathrm{E}) - \nabla^2\mathrm{E} = -\mathrm{j}\omega\mu\,(\sigma + \mathrm{j}\omega\varepsilon)\,\mathrm{E} \tag{A.21}$$

Since $\nabla \bullet \mathrm{E} = 0$, eq A.21 can be reduced to

$$\nabla^2\mathrm{E} - \gamma^2\mathrm{E} = 0 \tag{A.22}$$

where $\gamma^2 = j\omega\mu(\sigma + j\omega\varepsilon)$.

For transverse electric waves, the electric field is perpendicular to the propagating direction (z axis), i.e. $E_z = 0$. The propagation constant for TE waves is given by

$$k^2 = \frac{d^2}{dx^2} + \frac{d^2}{dy^2} + \gamma^2 \tag{A.23}$$

Since $\frac{d^2E}{dx^2} = \left(\frac{m\pi}{a}\right)^2$ and $\frac{d^2E}{dy^2} = \left(\frac{n\pi}{b}\right)^2$, the propagation constant in a rectangular waveguide becomes

$$k = \sqrt{\left(\frac{m\pi}{a}\right)^2 + \left(\frac{n\pi}{b}\right)^2 + j\omega\mu(\sigma + j\omega\varepsilon)} \tag{A.24}$$

Since $n = 1$ and $m = 0$ for TE_{10} mode rectangular waveguide, the final solution is

$$k = \sqrt{\left(\frac{m\pi}{a}\right)^2 + j\omega\mu(\sigma + j\omega\varepsilon)} \tag{A.25}$$

Here k is a complex quantity, known as the propagation constant of the medium.

A.3 Alternating current

A.3.1 Root Mean Square (RMS)

The voltage in AC circuit is given by

$$v = v_{max} \cos \omega t$$

where V_{max} is maximum voltage.

Taking the square of both sides

$$v^2 = v_{max}^2 \cos^2 \omega t \tag{A.26}$$

Since $\cos^2 \theta = \frac{1+\cos 2\theta}{2}$, eq A.26 can be rewritten as

$$\begin{aligned} v^2 &= v_{max}^2 \cos^2 \omega t \\ &= v_{max} \left(\frac{1 + \cos 2\omega t}{2} \right) \\ &= \frac{v_{max}^2}{2} + \frac{v_{max}^2}{2} \cos 2\omega t \end{aligned} \tag{A.27}$$

The average value of $\cos 2\omega t$ is equal to 0 over any number of complete cycles, as shown below;

The angular frequency is given by

$$\omega = \frac{2\pi}{T}$$

and can be substituted into eq A.27

$$\cos 2\omega t = \cos \frac{4\pi}{T} t$$

and can be integrated with respect to t

$$\int_0^T \cos \frac{4\pi}{T} t dt = \frac{T}{4\pi} \left[\sin \frac{4\pi}{T} t \right]_0^T$$

$$= \frac{T}{4\pi}\left[\sin\frac{4\pi}{T}T - \sin\frac{4\pi}{T}0\right]$$
$$= \frac{T}{4\pi}\left[\sin 4\pi - \sin 0\right]$$
$$= 0$$

Hence,the root mean square voltage is

$$v^2 = \frac{v_{max}^2}{2}$$
$$v = \frac{v_{max}}{\sqrt{2}}$$

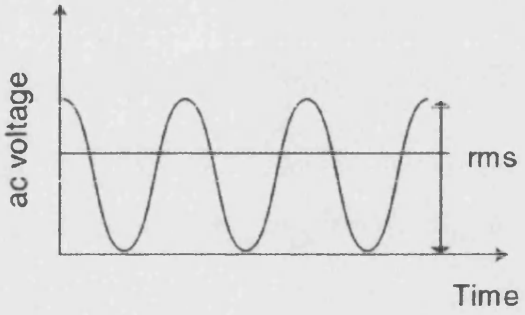

Figure A.1: Sine wave modulation of potential.

A.3.2 Modulation

A light emitting diode (LED) (λ = 626 nm) was used in all experiments, and sinusoidally modulated to produce ac signal. The ratio between peak-to-peak and dc is related to the modulation depth;

$$\frac{pk/pk}{dc} = 2 \text{ for } 100\% \text{ modulation}$$
$$= 1 \text{ for } 50\% \text{ modulation}$$

Both peak-to-peak and dc are shown in Fig A.2.

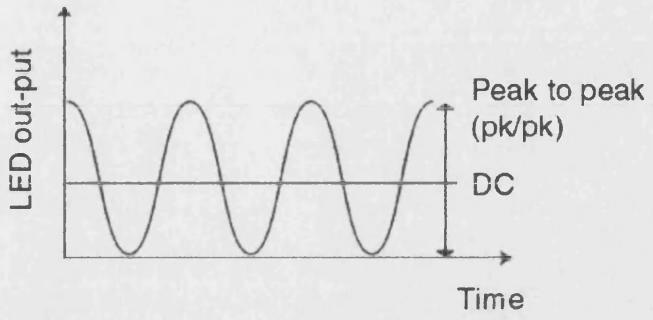

Figure A.2: Sine wave modulation of light intensity.

A.4 Useful Mathematics

A.4.1 Semicircle

The mathematical expression for a circle is

$$(x-a)^2 + (y-b)^2 = r^2 \tag{A.28}$$

where a is x-coordinate at the center of the circle, b is y-coordinate at the center of the circle, and r is radius of the circle.

Eq A.28 can be solved for y

$$\begin{aligned} (y-b)^2 &= r^2 - (x-a)^2 \\ y &= \pm\sqrt{r^2-(x-a)^2} + b \end{aligned} \tag{A.29}$$

Hence semicircle is

$$y = \sqrt{r^2-(x-a)^2} + b \tag{A.30}$$

and

$$y = -\sqrt{r^2-(x-a)^2} + b \tag{A.31}$$

The semicircles are sketched in Fig A.3.

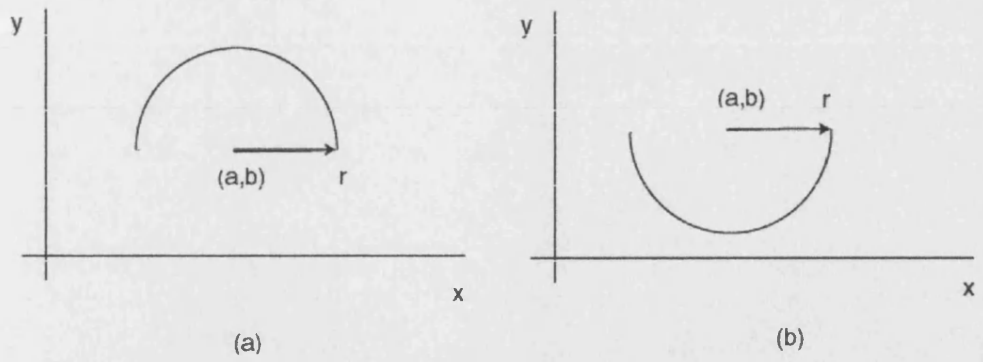

Figure A.3: Sketch for semicircles (a) $y = \sqrt{r^2 - (x-a)^2} + b$ (b) $y = -\sqrt{r^2 - (x-a)^2} + b$

A.4.2 Semi ellipse

The mathematical expression for an ellipse is

$$\frac{(x-a)^2}{\alpha^2} + \frac{(y-b)^2}{\beta^2} = 1 \tag{A.32}$$

where α is semimajor axis if $\alpha > \beta$

β is semiminor axis if $\alpha > \beta$

It is noted that the above expression is identical to that of circle if $\alpha = \beta$.

Eq A.32 can be solved for y

$$\begin{aligned} \frac{(y-b)^2}{\beta^2} &= 1 - \frac{(x-a)^2}{\alpha^2} \\ (y-b)^2 &= \beta^2 - \frac{\beta^2}{\alpha^2}(x-a)^2 \\ y &= \pm\sqrt{\beta^2 - \frac{\beta^2}{\alpha^2}(x-a)^2} + b \end{aligned} \tag{A.33}$$

Hence the semi-ellipse is

$$y = \sqrt{\beta^2 - \frac{\beta^2}{\alpha^2}(x-a)^2} + b \tag{A.34}$$

and

$$y = -\sqrt{\beta^2 - \frac{\beta^2}{\alpha^2}(x-a)^2} + b \tag{A.35}$$

The semiellipses are sketched in Fig A.4.

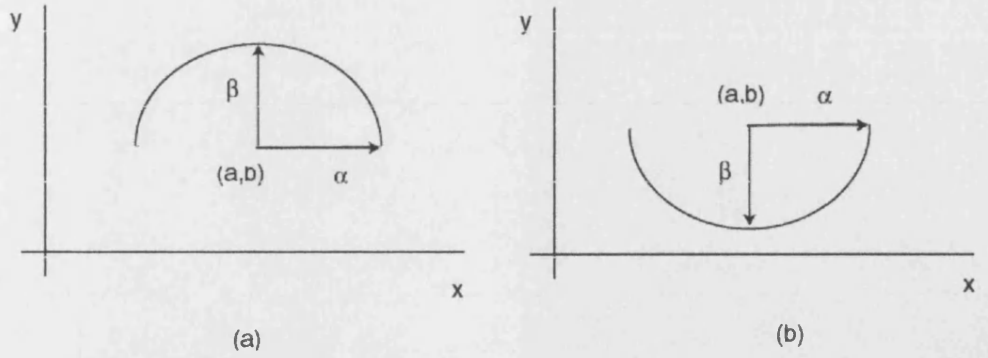

Figure A.4: Sketch for semicircles (a) $y = \sqrt{\beta^2 - \frac{\beta^2}{\alpha^2}(x-a)^2} + b$ (b) $y = -\sqrt{\beta^2 - \frac{\beta^2}{\alpha^2}(x-a)^2} + b$

A.5 Absorption coefficient

The energy of the electromagnetic waves is given by

$$\begin{aligned} E &= h\nu \\ &= \frac{hc}{\lambda} \end{aligned} \tag{A.36}$$

The above expression needs to be converted into eV.

$$\begin{aligned} E &= \frac{6.6261 \times 10^{-34}\text{J} \times 2.9979 \times 10^{8}\text{ms}^{-1}}{\lambda \times 1.6022 \times 10^{-19}\text{J.eV}^{-1}} \\ &= \frac{1.2398 \times 10^{-6}}{\lambda} \end{aligned} \tag{A.37}$$

The absorption coefficient is given by

$$\alpha = \frac{4\pi k_e}{\lambda} \tag{A.38}$$

where k_e is extinction coefficient.

The energy of the electromagnetic waves and absorption coefficient for Si are tabulated below [9]

λ / μm	E / eV	k_e	α / cm^{-1}	λ / μm	E / eV	k_e	α / cm^{-1}
0.2066	6.000968	2.909	1769389	0.2138	5.798877	3.045	1789738
0.2073	5.980704	2.928	1774932	0.2145	5.779953	3.061	1793271
0.2080	5.960577	2.944	1778625	0.2153	5.758477	3.073	1793612
0.2087	5.940585	2.937	1768444	0.2160	5.739815	3.086	1795362
0.2094	5.920726	2.963	1778135	0.2168	5.718635	3.102	1798011
0.2101	5.901000	2.982	1783575	0.2175	5.700230	3.112	1798002
0.2109	5.878615	2.987	1779789	0.2183	5.679340	3.135	1804653
0.2116	5.859168	3.005	1784591	0.2191	5.658603	3.150	1806667
0.2123	5.839849	3.015	1784626	0.2198	5.640582	3.169	1811776
0.2130	5.820657	3.025	1784661	0.2206	5.620127	3.190	1817168

Continued

λ / μm	E / eV	k_e	α / cm^{-1}	λ / μm	E / eV	k_e	α / cm^{-1}
0.2214	5.599819	3.206	1819683	0.2384	5.200503	3.354	1767937
0.2222	5.579658	3.228	1825574	0.2394	5.178780	3.363	1765276
0.2230	5.559641	3.245	1828604	0.2403	5.159384	3.376	1765463
0.2238	5.539768	3.267	1834421	0.2412	5.140133	3.389	1765648
0.2246	5.520036	3.285	1837958	0.2422	5.118910	3.408	1768216
0.2254	5.500444	3.302	1840912	0.2431	5.099959	3.429	1772525
0.2263	5.478568	3.319	1843031	0.2441	5.079066	3.451	1776589
0.2271	5.459269	3.334	1844838	0.2450	5.060408	3.477	1783399
0.2279	5.440105	3.350	1847185	0.2460	5.039837	3.504	1789942
0.2288	5.418706	3.359	1844862	0.2470	5.019433	3.533	1797449
0.2296	5.399826	3.366	1842265	0.2480	4.999194	3.565	1806416
0.2305	5.378742	3.368	1836162	0.2490	4.979116	3.598	1815815
0.2313	5.360138	3.368	1829811	0.2500	4.959200	3.632	1825642
0.2322	5.339363	3.364	1820554	0.2510	4.939442	3.670	1837394
0.2331	5.318747	3.358	1810291	0.2520	4.919841	3.709	1849550
0.2339	5.300556	3.353	1801413	0.2530	4.900395	3.749	1862108
0.2348	5.280239	3.346	1790761	0.2541	4.879181	3.789	1873828
0.2357	5.260076	3.344	1782857	0.2551	4.860055	3.835	1889143
0.2366	5.240068	3.344	1776075	0.2562	4.839188	3.880	1903104
0.2375	5.220211	3.347	1770932	0.2572	4.820373	3.928	1919156

Continued

λ / μm	E / eV	k_e	α / cm^{-1}	λ / μm	E / eV	k_e	α / cm^{-1}
0.2583	4.799845	3.979	1935795	0.2818	4.399574	5.344	2383062
0.2594	4.77941	4.031	1952777	0.2831	4.379371	5.381	2388543
0.2605	4.759309	4.088	1972028	0.2844	4.359353	5.414	2392206
0.2616	4.739297	4.149	1993038	0.2857	4.339517	5.435	2390557
0.2627	4.719452	4.211	2014350	0.2870	4.319861	5.439	2381480
0.2638	4.699773	4.278	2037867	0.2883	4.300382	5.395	2351563
0.2649	4.680257	4.350	2063560	0.2897	4.279600	5.301	2299425
0.2661	4.659151	4.426	2090145	0.2910	4.260481	5.158	2227400
0.2672	4.639970	4.506	2119164	0.2924	4.240082	4.989	2144105
0.2684	4.619225	4.590	2149018	0.2938	4.219877	4.812	2058182
0.2695	4.600371	4.678	2181279	0.2952	4.199864	4.639	1974776
0.2707	4.579978	4.764	2211533	0.2966	4.180040	4.480	1898090
0.2719	4.559765	4.849	2241057	0.2980	4.160403	4.335	1828027
0.2731	4.539729	4.933	2269861	0.2995	4.139566	4.204	1763907
0.2743	4.519869	5.011	2295665	0.3009	4.120306	4.086	1706420
0.2755	4.500181	5.082	2318051	0.3024	4.099868	3.979	1653492
0.2768	4.479046	5.148	2337127	0.3039	4.079631	3.885	1606461
0.2780	4.459712	5.206	2353256	0.3054	4.059594	3.798	1562773
0.2792	4.440544	5.257	2366096	0.3069	4.039752	3.720	1523196
0.2805	4.419964	5.3404	2392494	0.3084	4.020104	3.650	1487265

Continued

λ / μm	E / eV	k_e	α / cm^{-1}	λ / μm	E / eV	k_e	α / cm^{-1}
0.3100	3.999355	3.587	1454051	0.3444	3.599884	2.987	1089888
0.3115	3.980096	3.529	1423651	0.3463	3.580133	2.983	1082457
0.3131	3.959757	3.477	1395505	0.3483	3.559575	2.984	1076602
0.3147	3.939625	3.429	1369243	0.3502	3.540263	2.989	1072555
0.3163	3.919696	3.386	1345233	0.3522	3.520159	2.999	1070033
0.3179	3.899969	3.346	1322651	0.3542	3.500282	3.014	1069312
0.3195	3.880438	3.310	1301868	0.3563	3.479652	3.026	1067242
0.3212	3.859900	3.275	1281285	0.3583	3.460229	3.023	1060233
0.3229	3.839579	3.242	1261696	0.3604	3.440067	2.982	1039759
0.3246	3.819470	3.211	1243087	0.3625	3.420138	2.881	998723
0.3263	3.799571	3.182	1225443	0.3647	3.399506	2.705	932055
0.3280	3.779878	3.154	1208364	0.3668	3.380044	2.456	841412
0.3297	3.760388	3.128	1192223	0.3690	3.359892	2.169	738657
0.3315	3.739970	3.103	1176273	0.3712	3.339978	1.870	633058
0.3333	3.719772	3.079	1160872	0.3734	3.320300	1.577	530722
0.3351	3.699791	3.058	1146761	0.3757	3.299973	1.321	441847
0.3369	3.680024	3.039	1133547	0.3780	3.279894	1.110	369012
0.3388	3.659386	3.021	1120514	0.3803	3.260058	0.945	312259
0.3406	3.640047	3.007	1109427	0.3827	3.239613	0.815	267614
0.3425	3.619854	2.995	1098869	0.3850	3.220260	0.714	233049

Continued

λ / μm	E / eV	k_e	α / cm^{-1}	λ / μm	E / eV	k_e	α / cm^{-1}
0.3875	3.199484	0.630	204305	0.4428	2.799910	0.163	46258
0.3899	3.179790	0.561	180809	0.4460	2.779821	0.149	41982
0.3924	3.159531	0.505	161723	0.4492	2.760018	0.149	41683
0.3949	3.139529	0.456	145107	0.4525	2.739890	0.133	36935
0.3974	3.119779	0.416	131545	0.4558	2.720053	0.131	36117
0.4000	3.099500	0.387	121580	0.4592	2.699913	0.130	35576
0.4025	3.080248	0.355	110834	0.4626	2.680069	0.131	35586
0.4052	3.059724	0.329	102032	0.4661	2.659944	0.134	36127
0.4078	3.040216	0.313	96451	0.4696	2.640119	0.120	32112
0.4105	3.020219	0.291	89082	0.4732	2.620034	0.120	31867
0.4133	2.999758	0.269	81789	0.4769	2.599706	0.090	23715
0.4161	2.979572	0.255	77011	0.4806	2.579692	0.094	24578
0.4189	2.959656	0.244	73196	0.4843	2.559983	0.083	21536
0.4217	2.940005	0.228	67942	0.4881	2.540053	0.079	20339
0.4246	2.919925	0.211	62447	0.4920	2.519919	0.077	19667
0.4275	2.900117	0.203	59672	0.4959	2.500101	0.073	18499
0.4305	2.879907	0.194	56629	0.4999	2.480096	0.073	18351
0.4335	2.859977	0.185	53628	0.5040	2.459921	0.066	16456
0.4366	2.839670	0.185	53247	0.5081	2.440071	0.072	17807
0.4397	2.819650	0.170	48585	0.5123	2.420066	0.060	14718

Continued

λ / μm	E / eV	k_e	α / cm^{-1}	λ / μm	E / eV	k_e	α / cm^{-1}
0.5166	2.399923	0.060	14595	0.6199	2.000000	0.022	4460
0.5209	2.380111	0.056	13510	0.6262	1.979879	0.022	4415
0.5254	2.359726	0.053	12676	0.6326	1.959848	0.019	3774
0.5299	2.339687	0.043	10197	0.6391	1.939916	0.018	3539
0.5344	2.319985	0.045	10582	0.6458	1.919789	0.017	3308
0.5391	2.299759	0.048	11189	0.6526	1.899785	0.016	3081
0.5438	2.279882	0.044	10168	0.6595	1.879909	0.016	3049
0.5486	2.259934	0.044	10079	0.6666	1.859886	0.015	2828
0.5535	2.239928	0.032	7265	0.6738	1.840012	0.014	2611
0.5585	2.219875	0.038	8550	0.6812	1.820023	0.013	2398
0.5636	2.199787	0.032	7135	0.6888	1.799942	0.013	2372
0.5687	2.180060	0.034	7513	0.6965	1.780043	0.013	2345
0.5740	2.159930	0.030	6568	0.7045	1.759830	0.012	2140
0.5794	2.139800	0.027	5856	0.7126	1.739826	0.011	1940
0.5848	2.120041	0.030	6446	0.7208	1.720033	0.011	1918
0.5904	2.099932	0.030	6385	0.7293	1.699986	0.010	1723
0.5961	2.079852	0.027	5692	0.7380	1.679946	0.010	1703
0.6019	2.059811	0.025	5219	0.7469	1.659928	0.009	1514
0.6078	2.039816	0.025	5169	0.7560	1.639947	0.009	1496
0.6138	2.019876	0.024	4914	0.7653	1.620018	0.008	1314

Continued

λ / μm	E / eV	k_e	α / cm^{-1}
0.7749	1.599948	0.008	1297
0.7847	1.579967	0.007	1121
0.7948	1.559889	0.007	1107
0.8051	1.539933	0.006	937
0.8157	1.519922	0.006	924
0.8266	1.499879	0.005	760

A.6 Operational amplifiers

An operational amplifier (op-amp) is a device that can be used to amplify dc as well as ac inputs. Potentiostats are an example of the use of operational amplifiers. The purpose of a potentiostat is to control the potential of the working electrode in a cell and measure the resulting current through the cell. The basic circuit is shown below

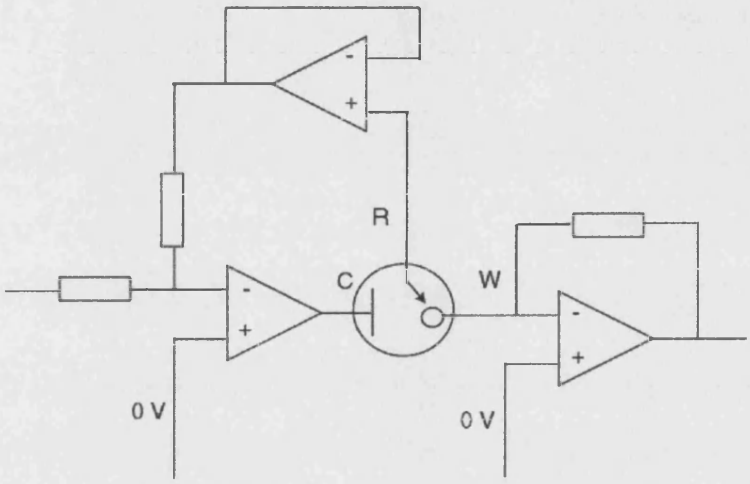

Figure A.5: Basic circuit of potentiostat.

The circuit uses a voltage follower, a current-voltage converter, and an inverting amplifier. Each op-amp circuit is described in the next section.

A.6.1 Inverting amplifier

The circuit of inverting amplifier is shown below

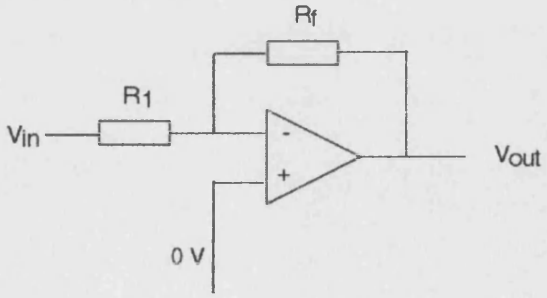

Figure A.6: Schematic diagram of inverting amplifier.

The noninverting input terminal is grounded. The relationship between output and

input is given by

$$V_{out} = -GV_{in} \tag{A.39}$$

where G is gain, given by

$$G = \frac{R_f}{R_1} \tag{A.40}$$

In the case of potentiostat,

$$R_f = R_1 \tag{A.41}$$

Otherwise the output is attenuated. In general, the voltage at the inverting terminal is close to that at noninverting terminal. Therefore, the inverting terminal is close to ground potential since noninverting input is grounded.

A.6.2 Current-to-Voltage converter

The circuit of current-voltage converter is shown below

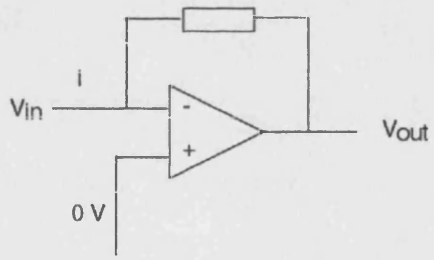

Figure A.7: Schematic diagram of current-voltage converter.

Since the noninverting input is grounded, the current flows across the resistor

$$V_{out} = iR_f \tag{A.42}$$

Therefore, the input current is converted into a proportional output voltage.

A.6.3 Voltage follower

The circuit of the voltage follower is shown below

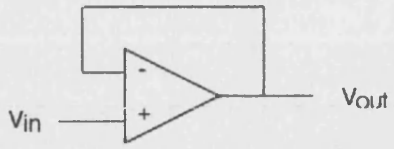

Figure A.8: Schematic diagram of voltage follower.

The open-loop voltage gain, A, is expressed as

$$A = \frac{V_{out}}{V_{in} - V_{out}} \tag{A.43}$$

A.43 can be solved for V_{out}

$$V_{out} = \frac{1}{1 + \frac{1}{A}} V_{in} \tag{A.44}$$

For the ideal op-amp, A = ∞ and A.44 can be reduced to

$$V_{out} = V_{in} \tag{A.45}$$

Therefore, for the voltage follower the output is equal to the input voltage.

A.6.4 Real op-amps

The common type is 741 op-amps containing 20 transistors and 11 resistors, and 741 op-amps are used to construct our potentiostat. A real op-amp has characteristics which are reasonable approximation of an ideal op-amp.

Parameter	Ideal op-amp	Typical op-amp
open loop gain	∞	$10^5 - 10^9$
Common mode voltage gain	0	10^{-5}
Gain bandwidth product	∞	1-20 MHz
Input resistance	∞	10^6 Ω for bipolar
		$10^9 - 10^{12}$ Ω for FET
Output resistance	0	100-1000 Ω

Table A.1: Real vs ideal op-amps. FET is Field Effect Transistor.

An open loop gain is generally given by

$$A = \frac{V_{out}}{V^+ - V^-} \tag{A.46}$$

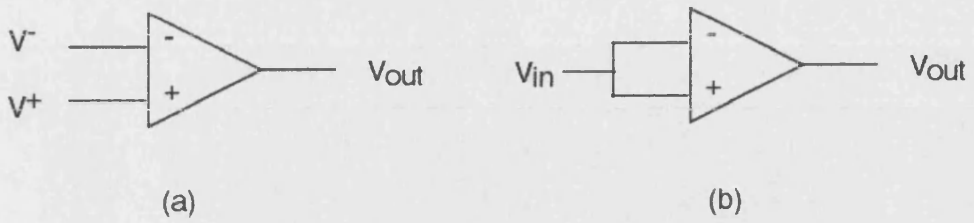

Figure A.9: Schematic diagram of op-amps for (a) differential voltage gain (b) common mode voltage gain.

Common mode voltage gain, G, is expressed as

$$G = \frac{V_{out}}{V^{in}} \tag{A.47}$$

The gain is dependent on the frequency if ac signal is applied. The change of gain with frequency is shown below

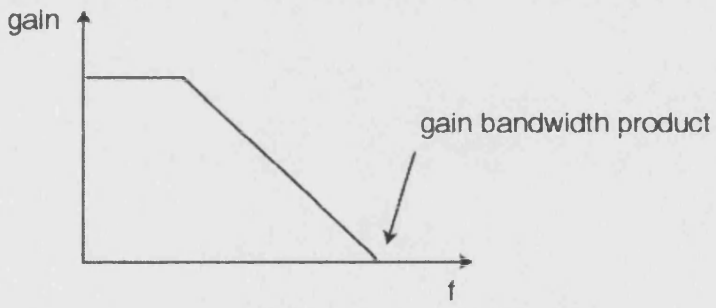

Figure A.10: Bode plot of gain shows the gain bandwidth product.

A.7 Wafer identification

Silicon wafers are usually circular and have characteristic flats, as illustrated below, provided for identification purposes.

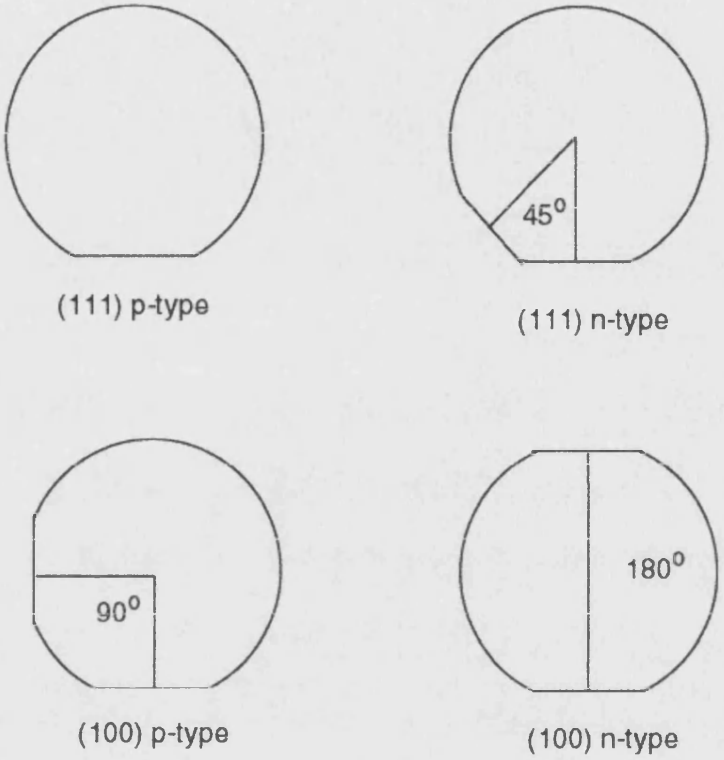

Figure A.11: Identification of silicon wafers.

References

[1] Collins, R. E. Foundations for microwave engineering, McGraw-Hill, New York, 1992.

[2] Grant, I. S.; Phillips, W. R. Electromagnetism, 2nd edition, John Wiley, New York, 1990.

[3] Chatterjee, R. Elements of microwave engineering, John Wiley, New York, 1986.

[4] Dunlop, J.; Smith, D. G. Telecommunications engineering, 2nd edition, Van Norstrand Reinhold, Hong Kong, 1989.

[5] Sadiku, M. N. O. Elements of electromagnetics, 2nd edition, Oxford University Press, Oxford, 1995.

[6] Peter, L. M. in Porous silicon science and technology, Springer-Verlag, 1995.

[7] Sze, S. M. Semiconductor devices: Physics and technology, John Wiley, New York, 1985.

[8] Sze, S. M. Physics of semiconductor devices, 2nd edition, John Wiley, New York, 1981.

[9] Palik, E. D. Handbook of optical constants of solids, Academic Press, 1985.

[10] Anton, H. Calculus; a new horizon, 6th edition, John Wiley, New York, 1998.

[11] Schroder, D. K. Semiconductor material and device characterisation, 2nd edition, John Wiley, New York, 1998.

[12] Sze, S. M. VLSI Technology, 2nd edition, McGraw-Hill, New York, 1988.

[13] Willard, H. H.; Merrit, L. L.; Dean, J. A.; Settle, F. A. Instrumental methods of analysis, 7th edition, Wadsworth, California, 1981.

[14] Simpson, R. E. Introductory electronics for scientists and engineers, 2nd edition, Allyn and Bacon, 1987.

Appendix B

B.1 Publication list

1 Cass, M.; Duffy, N. W.; Pennock, S. R.; Peter, L. M.; Ushiroda, S.; Walker, A., 'Application of microwave reflectance methods to the study of p-Si in fluoride solutions', Journal of Electroanalytical Chemistry in press.

2. Duffy, N. W.; Kirah, K.; Peter, L. M.; Ushiroda, S., 'Frequency response analysis of the potential modulate microwave reflectivity; Response of p-type silicon during anodic dissolution in ammonium fluoride solutions', Zeitschrift fuer Phyikalische Chemie in press.

3. Arimori, S.; Ushiroda, S.; Jenkins, A. T. A.; Peter, L. M.; James, T. D. 'A modular electrochemical sensor for saccharides', Chemical communications, 2368-2369, 2002.

4 Cass, M.; Duffy, N. W.; Pennock, S. R.; Peter, L. M.; Ushiroda, S.; Walker, A., 'Microwave reflectance studies of photoelectrochemical kinetics at semiconductor electrodes. Part 1: Steady state, transient and periodic responses', submitted to Journal of Physical Chemistry B, 2002.

5 Cass, M.; Duffy, N. W.; Pennock, S. R.; Peter, L. M.; Ushiroda, S.; Walker, A., 'Microwave reflectance studies of photoelectrochemical kinetics at semiconductor electrodes. Part 2. in preparation.

6 Cass, M.; Duffy, N. W.; Pennock, S. R.; Peter, L. M.; Ushiroda, S.; Walker, A., 'Microwave reflectance studies of photoelectrochemical kinetics at semiconductor electrodes. Part 3. in preparation.